AN ABSTRACT OF THE DISSERTATION OF

Troy Youngmin Ansell for the degree of Doctor of Philosophy in Materials Science
presented on December 12, 2014.
Title: Development of New High-Temperature Piezoelectric Perovskite Ceramics

Abstract approved: _____

David P. Cann

Lead zirconate titanate (PZT) is the dominant ferroelectric material in the market due to its excellent piezoelectric properties, relatively high Curie transition temperature (T_C), low cost, etc. However, because of emerging applications with requirements for high temperature (T_C > 400 ^oC) ferroelectrics, researchers are increasingly looking at alternative materials to replace PZT. A number of ternary Pb-based solid solutions were developed to find ferroelectric ceramics with a T_C above 400 ^oC, with piezoelectric properties similar to PZT.

For high temperature applications, $PbTiO_3$-$BiScO_3$ (PT-BS) based ternary solid solutions were developed. The best results were found in the PT-BS-$Bi(Ni_{1/2}Ti_{1/2})O_3$ (PT-BS-BNiT) ternary system where a number of compositions exhibited low field piezoelectric coefficients (d_{33}) between 300 and 450 pC/N, high field coefficients (d_{33}*) between 300 and 900 pm/V, Curie temperatures (T_C) between 300 and 450 ^oC, and electromechanical coupling factors (k_p) up to ≈ 0.3. Additionally, the low field d_{33} increased with increasing temperature in all compositions and with the highest recorded value of d_{33} ≈ 1200 pC/N. In a number of compositions (mainly those with diffuse phase transitions), the decrease in properties occurred not at T_C but at a lower temperature called the depolarization temperature (T_d). For the PT-BS-BNiT ternary, the value of T_C decreased as BNiT content increased while at the same time, the separation between T_d and T_C increased with increasing BNiT content. In PT-BS rich

compositions, a shift from a first order phase transition to more relaxor-like transitions were observed in BNiT rich compositions. This behavior is attributed to a break down in long-range order induced by poling treatment and to a large occupancy of Bi on the A-site of the perovskite unit cells allowing the persistence of a tetragonal distortion despite the loss of polarization (the order parameter of normal ferroelectric materials).

Development of New High-Temperature Piezoelectric Perovskite Ceramics

by
Troy Youngmin Ansell

A DISSERTATION

submitted to

Oregon State University

in partial fulfillment of
the requirements for the
degree of

Doctor of Philosophy

Presented December 12, 2014
Commencement June 2015

Doctor of Philosophy dissertation of Troy Youngmin Ansell presented on December 12, 2014

APPROVED:

Major Professor, representing Materials Science

Director of the Materials Science Program

Dean of the Graduate School

I understand that my dissertation will become part of the permanent collection of Oregon State University libraries. My signature below authorizes release of my dissertation to any reader upon request.

Troy Youngmin Ansell, Author

ACKNOWLEDGEMENTS

I would like to acknowledge this work was supported in part through NASA / Oregon Space Grant Consortium, grant NNX10AK68 and with the immense help of Dr. Alp Sehiriouglu and Ben Kowalski of Case Western Reserve University / NASA.

I would also like to thank Prof. Dr. Jürgen Rödel and his research group for taking me in for 10 weeks so that I could investigate the temperature dependent properties of my piezoelectric materials. Also thanks to the funding agency, Deutsche Forschungsgemeinschaft (DFG), through their SFB595, project D1 which funded my trip to Germany. I would especially like to thank Dr. Eva Sapper and Matias Acosta for showing me how to use all the equipment and helping with me with the data processing. Also I would to thank Martin Blömker and Dr. Robert Dittmer for showing me around Germany and for an awesome skiing trip to France. Vielen Dank!

I would like to thank Dr. Chris Holmes-Parker for helping me get into this exciting field and Jason Nikkel, Dr. Eric Patterson, Dr. Yu-hong Jeon, Dr. Nattaphon (Ton) Raengthon, and Joel Walenza-Slabe for their help in this project and thesis. I would like to thank Ashley Mason, Nitish Kumar, Sasiporn (Noon) Prasertpalichat, Dr. Narit (Sunny) Triamnak, and Dmitriy Khvostenko for helping me stay sane through these tough years. Also, thanks to Dr. Whitney Schmidt, Ashley Mason, and Nitish Kumar for proofreading my dissertation.

I would like to thank the members of my committee for your advice and help. Thank you Dr. Gambatese and Dr. McGuire for serving as Graduate Council Representative. Thank you Dr. Lerner for your helpful suggestions on compositional studies. I want to thank Dr. Brady Gibbons for keeping Dearborn Hall fun and interesting and helping me with my class. Thank you Dr. Warnes for your advise and especially for your help during my first attempt at teaching. I would especially like to thank Dr. David Cann for giving me this chance in my life, I hope I haven't disappointed.

Lastly and most importantly, I would like to thank all of my friends and family for their support, especially my beautiful wife Aleta and wonderful son Henry, I would not be here without you.

CONTRIBUTION OF AUTHORS

Dr. David Cann served as my advisor and mentor throughout my time as a Ph.D. student. He also served as the principle investigator in the four papers corresponding to Chap. 5 - 8. Jason Nikkel was an undergraduate student working for Dr. Cann during the first two years of my graduate employment. He fabricated many of the first BMT ternary compositions and helped in the initial solid solution batching and x-ray diffraction work. In my work shown in Chap. 5 on the BZT and BMT ternary compositions, many of the high temperature measurements were conducted at NASA Glenn Research Center in Cleveland, OH under the direction of Dr. Alp Sehirlioglu. Under the direction and guidance of Prof. Dr. Jürgen Rödel of the Institute of Materials Science, Technische Universität Darmstadt, Germany, high temperature d_{33}, polarization, and strain measurements were conducted on BNiT ternary compositions. Much of the underlying science of the BNiT ternary compositions were determined through discussions with Dr. Eva Sapper, Dr. Cann, and Prof. Jürgen Rödel with additional experiments.

TABLE OF CONTENTS

TABLE OF CONTENTS (Continued)

TABLE OF CONTENTS (Continued)

TABLE OF CONTENTS (Continued)

LIST OF FIGURES

LIST OF FIGURES (Continued)

LIST OF FIGURES (Continued)

LIST OF TABLES

LIST OF TABLES (Continued)

LIST OF SYMBOLS, ABBREVIATIONS AND/OR NOMENCLATURE

(In order of appearance)

$PbTiO_3$ - $PbZrO_3$ ..... PZT

$PbTiO_3$ - $BiScO_3$ ..... PT-BS

$PbTiO_3$ - $BiScO_3$ - $Bi(Zn_{1/2}Ti_{1/2})O_3$ .....PT-BS-BZT

$PbTiO_3$ - $BiScO_3$ - $Bi(Mg_{1/2}Ti_{1/2})O_3$ ..... PT-BS-BMT

$PbTiO_3$ - $BiScO_3$ - $Bi(Ni_{1/2}Ti_{1/2})O_3$ .....PT-BS-BNiT

$PbTiO_3$ - $BiScO_3$ - $Bi(Co_{1/2}Ti_{1/2})O_3$ ..... PT-BS-BCoT

$PbTiO_3$ - $(Bi_{1/2}Na_{1/2})TiO_3$ - $Bi(Zn_{1/2}Ti_{1/2})O_3$ ..... PT-BNT-BZT

T_C .....Curie Temperature

T_D, T_d .....Depolarization Temperature

d_{33} .....Low field piezoelectric coefficient along the polar axis

d_{33}* .....High field piezoelectric coefficient along the polar axis

t .....Tolerance factor

ΔEN .....Difference in electronegativity

P .....Polarization

χ_e .....Electric susceptability

ϵ ..... Electric Permittivity

LIST OF SYMBOLS, ABBREVIATIONS AND/OR NOMENCLATURE

(Continued)

ϵ_r ..... Relative Permittivity

$tan\delta$ ..... Loss tangent

k ..... Electromechanical coupling factor

k_p ..... Planar electromechanical coupling factor

K ..... Dielectric constant

P_{SAT} ..... Saturation polarization

P_S ..... Spontaneous polarization

P_R, P_r ..... Remanent polarization

E_C ..... Coercive field

E_{bias} ..... Internal bias field

γ_S ..... Asymmetry in strain loops

T_m ..... Temperature of maximum permittivity

T_B ..... Burn's temperature

T_f ..... Freezing temperature

T_t ..... Thermal depoling temperature

I dedicate this work to my parents, Wade & Heeyoung Ansell

Through hard work and sacrifice you made me the man I am today.

Development of New High-Temperature Piezoelectric Perovskite Ceramics

1 Introduction

1.1 Motivation

The ubiquitous perovskite ferroelectric ceramic lead zirconate titanate or $PbTiO_3$ - $PbZrO_3$ (PZT), is used in many piezoelectric and ferroelectric applications. Due to the ceramics excellent properties, stability in a large range of temperatures, and a relatively high phase transition temperature, this perovskite has been utilized in many applications. Lead zirconate titanate is used: as the ferroelectric material in ferroelectric random access memory (FeRAM) [1]; as an actuator in driving motors, operating robotic arms, steering and driving of probes or satellites, or a temperature sensor, or as an accelerometer, pressure sensor, and/or vibration sensor. Other applications include: a ceramic resonator in circuit boards, the transducer in medical ultrasound imaging, and for spark generation in push-button lighters. Despite the wide range of applications of PZT, emerging applications of piezoelectric sensors and actuators in extreme environments, especially temperatures exceeding 400 ^{o}C, has motivated development of alternative materials [2–4].

New perovskite solid solutions were developed to find piezoelectric ceramics with comparable piezoelectric and ferroelectric properties to PZT with higher transition temperatures: $PbTiO_3$ - $BiScO_3$ (PT-BS) [2], $PbTiO_3$ - $Bi(Zn_{1/2},Ti_{1/2})O_3$ (PT-BZT) [5], $PbTiO_3$ - $Bi(Mg_{1/2},Ti_{1/2})O_3$ (PT-BMT) [6, 7], $PbTiO_3$ - $Bi(Ni_{1/2},Ti_{1/2})O_3$ (PT-BNiT) [8, 9], and other PT-based solid solutions [10–12]. Among these piezoelectrics, PT-BS stood out as a potential candidate to replace PZT for high-temperature sensing and actuator applications. The solid solution has piezoelectric properties that ex-

ceed those of PZT with a Curie temperature (T_C) higher than PZT, and comparable ferroelectric properties [2, 3, 13]. Unfortunately, PT-BS contains scandium, a rare earth transition metal in the form of Sc_2O_3, which is expensive [14, 15]. Therefore researchers looked into alternative materials to both PT-BS and PZT [14–16], including ternary perovskite solid solutions. In this work, PT-based binary and ternary perovskites were investigated in order to find materials with piezoelectric and ferroelectric properties comparable to PT-BS and PZT, higher transition temperatures to PZT, and lower concentration of Sc_2O_3.

Effort and financial capital has also been directed toward lead-free or lead-reduced ferroelectric materials due to the toxicity of lead. The dangers of lead have been known since the roman citizen Vitruvius wrote about the metals dangers to human health over two thousand years ago. Society today is still grappling with lead caused poisoning and sickness. Lead uptake into the body occurs primarily through ingestion and inhalation. Lead absorption into the bloodstream depends on a number of factors including: nutrition and diet, age, exposure, and whether lead digested is inorganic or organic. Absorption of inorganic lead, such as PbO, depends on particle size and generally is not taken into the body through the skin, however, organic lead (e.g. tetraethyl lead in leaded gasoline) can be absorbed via cuts in the skin [17].

After lead absorption, the body accumulates lead in the blood (with a half-life of ≈ 30-40 days), in soft tissue (half-life of ≈ 40 days), and in the bones (half-life of ≈ 20 to 30 years) [17]. Blood being a transport system for the efficient distribution of nutrients throughout the body, transports lead to the major organs (heart, kidneys, liver, brain, etc.). Lead can also affect the hemopoietic system by inhibiting the function of several key enzymes [18] involved in the production of blood. Virtually all systems in the human body are effected by lead, with the most deleterious effects occurring in the: hemopoietic system, nervous, reproductive systems, the urinary tract, and cognitive systems [17, 19]. The effects of lead are most serious in newborns

and young children where lead disrupts cognitive and behavioral development. The previously cited papers provide brief reviews on lead uptake and the mechanisms of lead toxicity in the human body.

Because of the environmental dangers of lead, governments (European Union, Japan, California, etc.) around the world have outlawed lead in some commercial products such as in solder, automobile engines, and paints [17, 20]. The European Parliament has passed a directive known as the Restriction of the use of certain Hazardous Substances in electrical and electronic equipment (RoHS) which limits the use of hazardous materials like lead in electronic products developed for human use [20]. This directive and similar laws passed around the world applies to the application of lead based piezoelectrics such as PZT or $Pb(Mg_{1/3},Nb_{2/3})O_3$ (PMN) in a number of commercial products. An additional benefit of this work is development of materials with reduced Pb-content.

1.2 Research Objectives

The focus of this work was on developing high temperature piezoelectric ceramics. A number of PT-based ternary perovskite solid solutions were investigated to include: $xPbTiO_3$-(1-x)$Bi[Sc_{1/2}Zn_{1/4}Ti_{1/4}]O_3$ (PT-BS-BZT), $xPbTiO_3$-(1-x)$Bi[Sc_{1/2}Mg_{1/4}Ti_{1/4}]O_3$ (PT-BS-BMT), $xPbTiO_3$-$yBiScO_3$-$zBi(Ni_{1/2}Ti_{1/2})O_3$ (PT-BS-BNiT), $xPbTiO_3$-$yBiScO_3$-$zBi(Co_{1/2}Ti_{1/2})O_3$ (PT-BS-BCoT), and $xPbTiO_3$-$y(Bi_{1/2}Na_{1/2})TiO_3$-$zBi(Zn_{1/2}Ti_{1/2})O_3$ (PT-BNT-BZT). The measured properties were compared to PZT, PT-BS, and other PT-based piezoelectric solid solutions. Most of the solid solutions researched were based on the PT-BS binary system developed by Eitel *et. al.* [2]; however, solid solutions based on $xPbTiO_3$ - (1-x)$Bi_{1/2}Na_{1/2})TiO_3$ (PT-BNT) were studied more recently for low-lead and lower cost (as compared to PT-BS based solid solutions) ferroelectric materials.

As "high-temperature" implies, transition temperatures (T_C and depolarization

temperature, T_d) of these solid solutions were investigated. Other important properties of piezoelectrics, ferroelectrics, and insulators were investigated: piezoelectric coefficients, electromechanical strain, dielectric permittivity, dielectric and conductive losses, electromechanical coupling, phase purity (XRD), microstructure (SEM), density (shrinkage, Archimedes method), and frequency dependent impedance behavior. Polarization and strain were measured up to 200 ^{o}C. Impedance and the direct piezoelectric coefficient were measured up to high temperatures exceeding T_C. Difficulties with test equipment set-up prevented in-situ measurement of d_{33}, and therefore, d_{33} was measured via ex-situ and other indirect methods here at OSU. In order to measure electrical properties at high temperatures, samples were taken to NASA Glenn Research Center in Ohio (high temperature strain, d_{33}*, and impedance), and measurements were made at the Technische Universität Darmstadt in Darmstadt, Germany (in-situ d_{33}).

Before an in depth discussion of these solid solutions, some preliminary topics will be covered. The mathematics behind piezoelectric and ferroelectric properties, some basic information on crystal structures, and other relevant science behind these materials will be covered in Chap. 2. A full literature review of both PT-based and Pb-free materials, as well as device applications of piezoelectric materials will be covered in Chap. 3. Experimental designs will be the topic of Chap. 4. Chapters 5 - 8 will cover the results of PT-based solid solutions [PT-BS-BMT (Chap. 5), PT-BS-BZT (Chap. 5), PT-BS-BNiT (Chapters 6-8)].

1.3 References

1. Scott, J. F., Araujo, C. A., Meadows, H. B., McMillan, L. D. & Shawabkeh, A. Radiation effects on ferroelectric thin-film memories: Retention failure mechanisms. *J. Appl. Phys.* **66,** 1444–1453 (1989).

2. Eitel, R. E. *et al.* New High Temperature Morphotropic Phase Boundary Based on Bi(Me)O_3-$PbTiO_3$ Ceramics. *Jpn. J. Appl. Phys.* **40,** 5999–6002 (2001).

3. Eitel, R. E., Randall, C. A., Shrout, T. R. & Park, S.-E. Preparation and Characterization of High Temperature Perovskite Ferroelectrics in the Solid-Solution (1-x)$BiScO_3$-x$PbTiO_3$. *Jpn. J. Appl. Phys.* **41,** 2099–2104 (2002).

4. Bao, X., Bar-Cohen, Y., Sherrit, S., Badescu, M. & Shrout, T. R. in *Proceedings of the SPIE Smart Structures and Materials/NDE Symposium* (SPIE, 2012).

5. Suchomel, M. R. & Davies, P. K. Enhanced Tetragonality in (x)$PbTiO_3$-(1-x)Bi($Zn_{1/2}Ti_{1/2}$)O_3 and Related Solid Solution Systems. *Appl. Phys. Lett.* **86,** 2629051–2629053 (2005).

6. Randall, C. A. *et al.* Investigation of a high T_C piezoelectric system: (1-x)Bi($Mg_{1/2}$ $Ti_{1/2}$)O_3-(x)$PbTiO_3$. *J. Appl. Phys.* **95,** 3633–3639 (2004).

7. Sharma, S. & Hall, D. A. Ferroelectric and Antiferroelectric Polarization Switching Characteristics of Bi($Mg_{0.5}Ti_{0.5}$)O_3-$PbTiO_3$ Ceramics. *J. Mater. Sci.: Mater. Electron.* **21,** 405–409 (2010).

8. Takenaka, T. & Yamada, M. Solid-Solution ($Bi_{1-x}Pb_x$)($Ni_{(1+x)/2}Ti_{(1+x)/2}$)O_3 for New Piezoelectric Ceramics. *Jpn. J. Appl. Phys.* **32,** 4218–4222 (1993).

9. Choi, S. M., Stringer, C. J., Shrout, T. R. & Randall, C. A. Structure and Property Investigation of a Bi-based Perovskite Solid Solution: (1-x)Bi($Ni_{1/2}Ti_{1/2}$)O_3-x$PbTiO_3$. *J. Appl. Phys.* **98,** 0341081–0341084 (2005).

10. Woodward, D., Reaney, I., Eitel, R. E. & Randall, C. A. Crystal and domain structure of the $BiFeO_3$-$PbTiO_3$ solid solution. *J Appl Phys* **94,** 3313–3318 (2003).

11. Cheng, J. R., Zhu, W., Li, N. & Cross, L. Fabrication and characterization of x$BiGaO_3$-(1-x)$PbTiO_3$: a high temperature reduced Pb-content piezoelectric ceramic. *Mater. Lett.* **57,** 2090–2094 (2003).

12. Cheng, J. R., Li, N. & Cross, L. Structural and dielectric properties of Ga-modified $BiFeO_3$-$PbTiO_3$ crystalline solutions. *J. Appl. Phys.* **94,** 5153–5158 (2003).

13. Eitel, R. E., Zhang, S. J., Shrout, T. R. & Randall, C. A. Phase Diagram of the Perovskite System (1-x)$BiScO_3$-x$PbTiO_3$. *J. Appl. Phys.* **96,** 2828–2831 (2004).

14. Sterianou, I. *et al.* High-temperature (1-x)$BiSc_{1/2}Fe_{1/2}O_3$-x$PbTiO_3$ piezoelectric ceramics. *Appl. Phys. Lett.* **87,** 242901 (2005).

15. Sterianou, I., Sinclair, D. C., Reaney, I. M., Comyn, T. & Bell, A. J. Investigation of high Curie temperature (1-x)$BiSc_{1-y}Fe_yO_3$-x$PbTiO_3$ piezoelectric ceramics. *J. Appl. Phys.* **106** (2009).

16. Sebastian, T. *et al.* High temperature piezoelectric ceramics in the $Bi(Mg_{1/2}Ti_{1/2})O_3$-$BiFeO_3$-$BiScO_3$-$PbTiO_3$ system. *J. Electroceram.* **25,** 130–134 (2010).

17. Goyer, R. A. Lead Toxicity: Current Concerns. *Environ. Health Persp.* **100,** 177–187 (1993).

18. Piomelli, S. Childhood lead poisoning. *Pediatr. Clin. N. Am.* **49,** 1285–1304 (2002).

19. Papanikolaou, N. C., Hatzidaki, E. G., Belivanis, S., Tzanakakis, G. N. & Tsatsakis, A. M. Lead toxicity update. A brief review. *Med. Sci. Monit.* **11,** RA329–RA336 (2005).

20. Rödel, J., Jo, W., Seifert, K. T. P., Anton, E. M. & Granzow, T. Perspective on the Development of Lead-free Piezoceramics. *J. Am. Ceram. Soc.* **92,** 1153 (2009).

2 Background

2.1 Introduction

Ceramics are a class of inorganic and nonmetallic solids. Unlike metals, most ceramics are brittle, thermal insulators, and electrical insulators at standard temperature and pressure (STP); however ceramics are generally harder than metals and share comparable stiffness and strength to metals [1]. Throughout most of human history, ceramics were used as vessels for containing our food and drink, or shaped into statues for worship and trade. They were made of clays such as kaolin or a combination of different minerals like feldspar, and other silicates readily available from the earth. Today, the use of ceramics have expanded to include: electrical components in circuit boards, optical materials in optoelectronics and laser systems, structural materials in the form of concrete, ceramics like boron carbide for use as neutron moderators in nuclear power reactors, etc. In electronics, ceramics have found use as insulators, ionic conductors, superconductors, and both passive and active components in many different applications. These electronic ceramics include materials like: PZT, $BaTiO_3$, silicon carbide, and the high temperature superconductor yttrium barium copper oxide (YBCO).

This chapter will provide a brief review of some of the topics important to the study of ferroelectric ceramic materials. The basic science topics covered in this chapter include: crystal structure and x-ray diffraction, perovskite crystal structure, dielectric, piezoelectric, pyroelectric, and ferroelectric properties. Also included is a discussion of defect chemistry of ceramics and a brief review of impedance spectroscopy.

2.2 Crystallography

2.2.1 Crystal Structure

In the study of materials, microscopic structure deeply affects the observed macroscopic properties. In the study of ceramics, a distinction is made between single crystals and ceramics. Single crystals (sometimes called mono-crystals) exhibit long-range crystallographic order whereas ceramics are polycrystalline and are composed of many crystals and the ceramic exhibits medium-range order. Amorphous solids such as glass have short range order. Crystals are defined as solids made up of a periodic lattice of atoms or molecules. Every lattice exhibits translational symmetry. For a lattice to have rotational symmetry; however, the lattice must be consistent with translation when rotated. This restricts the possible number of rotations to two-fold (diad), three-fold (triad), four-fold (tetrad), and six-fold (hexad). Due to this restriction on rotational symmetry, crystals can be broadly grouped into seven crystal systems. One crystal system groups all crystals with the same axis of rotation, e.g. all crystals with orthorhombic symmetry exhibit three mutually perpendicular diad (two-fold) rotation axes.

The smallest repeat unit of a crystal is known as the unit cell. The unit cell is completely defined by three unit cell edge lengths (a, b, c) and three angles (α, β, γ). The points of the unit cell can be arranged in different ways, all of the possible combinations of points arranged according to the different combinations of rotational symmetry add up to 14 unique lattices known as the Bravais lattices (also called space lattices). Application of symmetry operations (i.e. rotation, translation, and/or inversion) to the seven crystal systems lead to 32 different crystallographic arrangements known as point groups. Finally, combining the 32 point groups with 14 Bravais lattices lead to 230 space groups [2].

The 32 point groups can be split up into two groups: 11 centrosymmetric point groups, and 21 non-centrosymmetric. Of the 21 non-centrosymmetric point groups,

20 are piezoelectric (colored red (pyroelectric) or blue (piezoelectric) in Table 2.1), ten of which are pyroelectric. More details about piezoelectricity, pyroelectricity, and ferroelectricity designations are described in Sections 2.6 through 2.9. It is, for now, adequate to establish that the 10 pyroelectric systems make up a subset of the 20 piezoelectric crystal systems and when an electric field is applied to a pyroelectric, crystals which maintain a polarization upon removal of the field are classified ferroelectric. Unless otherwise stated, the rest of this work will focus on polycrystalline ceramic materials.

TABLE 2.1: List of the seven crystal systems with the corresponding 32 point groups. Piezoelectric point groups in blue and pyroelectric point groups in red.

Crystal System	Axis Lengths and Angles	Point Groups
Cubic	$a = b = c$; $\alpha = \beta = \gamma = 90^o$	23, $m\bar{3}$, 432, $\bar{4}3m$, $m\bar{3}m$
Tetragonal	$a = b \neq c$; $\alpha = \beta = \gamma = 90^o$	4, $\bar{4}$, 4/m, 422, 4mm, $\bar{4}2m$, 4/mmm
Orthorhombic	$a \neq b \neq c$; $\alpha = \beta = \gamma = 90^o$	222, mm2, mmm
Trigonal	$a = b = c$; $\alpha = \beta = \gamma \neq 90^o$	3, $\bar{3}$, 32, 3m, $\bar{3}m$
Hexagonal	$a = b \neq c$; $\alpha = \beta = 90^o, \gamma = 120^o$	6, $\bar{6}$, 622, 6mm, $\bar{6}m2$, 6/mmm, 6/m
Monoclinic	$a \neq b \neq c$; $\alpha = \gamma = 90^o \neq \beta$	2, m, 2/m
Triclinic	$a \neq b \neq c$; $\alpha \neq \beta \neq \gamma \neq 90^o$	1, $\bar{1}$

2.2.2 X-ray Diffraction

X-ray diffraction is commonly used to determine the microscopic structure of a crystalline or polycrystalline material. The periodic lattice is bombarded with high energy photons in the x-ray portion of the electromagnetic spectrum. The atoms act as scattering sites of the x-rays due to photon interaction with the electrons. The incident x-rays contact the atoms of the specimen as plane waves and scatter off the atoms

generating spherical waves that propagate out from atomic scattering sites. Figure 2.1 is a representation of the bombardment of a crystalline lattice by x-rays and the generated spherical waves. The excited electrons (electron cloud) releases the absorbed energy by emission of x-rays with nearly the same wavelength as the incident wave in a process known as elastic scattering (also known as Rayleigh scattering). The atoms in the lattice acts like an optical grating for the x-rays and so generating the spherical waves. These spherical waves can be treated as plane waves as the distance from the specimen to a detector is large in comparison to the wavelength of the diffracted x-rays (Fraunhofer approximation) [3]. Constructive interference of these plane waves at a photographic plate or detector generates diffraction patterns characteristic of the material.

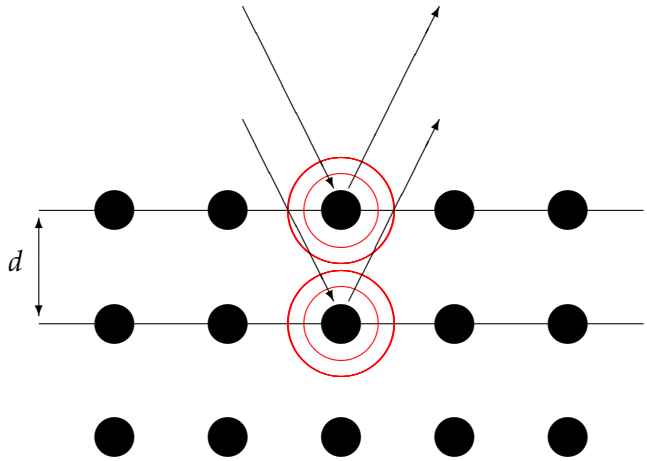

FIGURE 2.1: Lattice of atoms bombarded by x-rays.

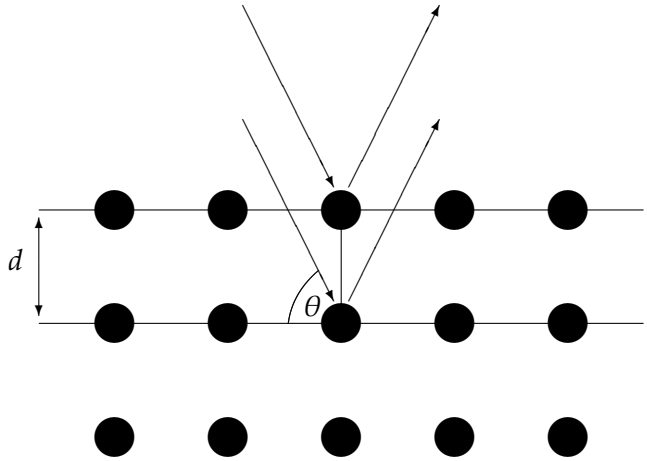

FIGURE 2.2: Lattice of atoms bombarded by x-rays with the Bragg condition for constructive interference.

X-ray diffraction by a crystalline material was discovered by Walter Friedrich, Paul Knipping, and Max Laue (later to be promoted to the nobility and given the title "von") in 1912 [4]. The model for x-ray diffraction was identified by William L. Bragg in 1915 in what is known as Bragg's law [5]. A graphical representation is shown in Fig. 2.2 and the corresponding law is Eq. 2.1:

$$2d \sin\theta = n\lambda \tag{2.1}$$

where d is known as the d-spacing and is the separation of the individual planes of atoms, θ is the angle between the line of incidence of the x-ray photon and a plane of atoms as seen in Fig. 2.2, n is an integer, and λ is the wavelength of the incident x-rays. For constructive interference, multiple x-ray beams must remain in phase after diffraction. The path difference of different x-ray beams must be an integer value, n, apart. This means that the difference between two path lengths must be equal to multiples of $2d \sin\theta$ (this is known as the Bragg condition for x-ray diffraction).

X-rays are best suited to the study of the microscopic structure of crystalline and polycrystalline materials since the distance between atoms in a crystal is on the order of one Å and the range of wavelengths of x-rays is 0.01 nm to 10 nm (0.1 Å to 100 Å). The x-ray diffraction pattern will depend on the crystal system and point group of the material. Next, the x-ray diffraction pattern of the highest symmetry crystal system, the cubic system and related point groups, will be discussed.

X-ray diffraction patterns are composed of a collection of intensity peaks. These peaks are a measure of the scattering sites (atoms) that occupy a plane under bombardment of x-rays. The more atoms that satisfy the Bragg condition for x-ray diffraction in a plane, the higher the intensity at that angle. As a result, close packed planes will generally have higher intensities. A set of three unit lengths called the Miller indices (sometimes four for non-cubic unit cells) are used to identify planes of atoms within a material. In the literature, these indices are h, k, and l for the unit lengths of x, y, and z respectively. For many metals, such as copper, that have a face-centered cubic (FCC) unit cell, the densest packed plane is the (111) plane. This plane has the Miller indices $h = 1$, $k = 1$, and $l = 1$ and compared to other planes, the highest intensity peak in a x-ray diffraction pattern. From interplanar geometry, a relationship between the inter-planar spacing and the lattice parameter for the cubic crystal systems is shown in Eq. 2.2 [6].

$$d_{hkl} = \sqrt{\frac{a}{h^2 + k^2 + l^2}} \tag{2.2}$$

The parameters a, b, and c in Eq. 2.2 are the unit cell edge lengths, i.e. lattice parameters. For cubic systems, a = b = c, and in addition, all three angles are equivalent leading to Eq. 2.2. Rearranging this equation for a and then combining this equation with Eq. 2.1,

$$a = \frac{\lambda}{2\,sin\theta}\sqrt{h^2 + k^2 + l^2} \tag{2.3}$$

Taking copper as an example, the lattice parameter can be indexed from XRD patterns found in numerous articles. In one article, on nano particles of copper, the (111) peak is observed at $2\theta \approx 43^{o}$ [7]. The wavelength is determined from the characteristic wavelength of the radiation source used to bombard the target specimen, in this case, the radiation source was Cu K$\alpha \approx 1.54$Å. So plugging into Eq. 2.3, $\lambda = 1.54$ Å, *h, k, and* $l = 1$, and $\theta = 21.5^{o} = 0.375$ radians, the calculated lattice parameter for copper is 0.364 pm. This value is close to the established lattice parameter of 0.361 pm for copper.

The procedure to find the lattice parameter of copper is called indexing. Lattice parameters are also calculated for some of the materials in this work. The unit cells; however, are tetragonal, and/or rhombohedral, or sometimes pseudo cubic. Indexing tetragonal and rhombohedral x-ray peaks is quite difficult in comparison to indexing cubic peaks and a review of the indexing procedure used in this thesis can be found in these references [6, 8]. Also important to note, there is a difference between single crystal x-ray diffraction, which has been assumed to this point, and powder diffraction. Diffraction experiments with single crystals lead to diffraction patterns shown in three-dimensional reciprocal space. Transformation of reciprocal space to the direct space results in no loss of information. In the x-ray diffraction of powders, three dimensional information is averaged and projected onto one dimensional diffraction patterns. Although this loss of information due to the projection of 3-D data to 1-D is a disadvantage of powder x-ray diffraction, there are also some advantages. Sample preparation is much easier in powder diffraction, measurement times are much shorter than in single crystal experiments, specimen structures are determined during measurement, and multiple phases maybe analyzed. For more details, please seek out the references focussed on this topic [3, 8].

2.3 Perovskites

Oxides form one important class of ceramic materials due to the elemental abundance of oxygen at the Earth's surface [9]. Of the many oxide ceramics, perovskites form an important subclass due to their many applications and relative abundance. The first perovskite, $CaTiO_3$, was discovered by Gustav Rose in 1839 in Russia and named after the Russian mineralogist Count Lev Perovski. The formula of perovskites is represented by $A^{VII,2+}B^{VI,4+}X_3^{2-}$, where A and B are cations in 12-fold and 6-fold coordination, respectively, and X is the anion in 6-fold coordination. The structure consists of an array of face-centered anions, O^{2-} in general, surrounding a small cation occupying the center octahedral hole, while a larger cation sits at the cell corners [10, 11], otherwise known as the dodecahedral holes [12]. The perovskite structure, along two different orientations, for $CaTiO_3$ is shown in Fig. 2.3.

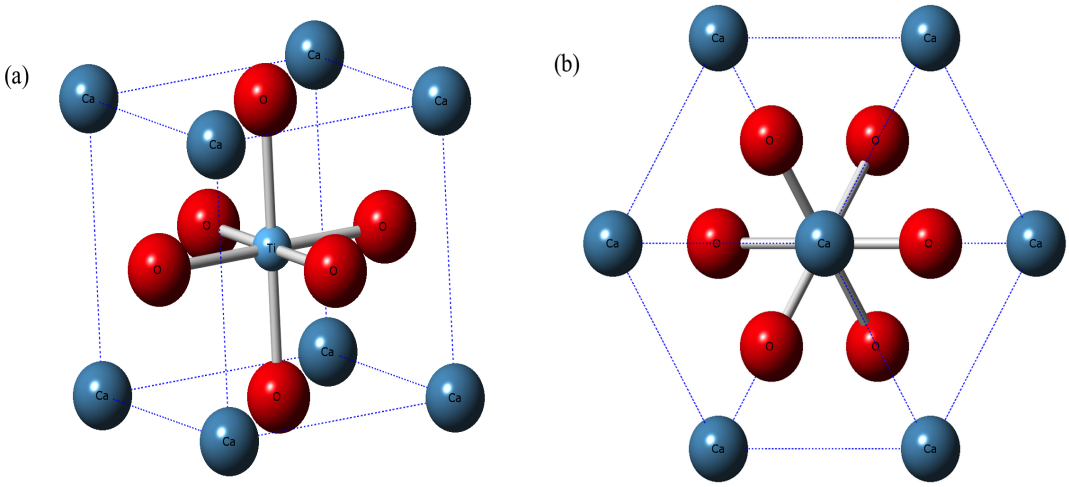

FIGURE 2.3: The perovskite structure of $CaTiO_3$, **(a)** random orientation, **(b)** [111] direction.

Despite a formula of ABO_3, with A^{2+} and B^{4+}, any solid solution with cationic charge adding up to 6+ could potentially form a perovskite crystal structure. Common perovskites include bismuth in 12-fold coordination with a charge of 3+. With

the valence of 3+ for the B-site cation, the chemical formula in this case is $A^{3+}B^{3+}O_3$. In the general case, a mixture of cations in the A-site, B-site, or both sites simultaneously is presented as: $(A'A'')^{VII}(B'B'')^{VI}O_3$. The electrostatic repulsion between anions and the metal cations narrows down the range of possible solid solutions that will form the perovskite structure. A simple relationship was proposed by Goldschmidt to represent this restriction in the form of Eq. 2.4 called the perovskite tolerance factor, t, [12, 13]

$$t = \frac{(R_A + R_O)}{\sqrt{2}\,(R_B + R_O)} \tag{2.4}$$

where R_A, R_B, and R_O, the ionic radii of the A-site cation, B-site cation, and oxygen anion respectively. When $t < 0.71$, $R_A \approx R_B$ and the structure is no longer perovskite but instead ilmenite, an example of which is $FeTiO_3$. This structure is an ordered derivative of the corundum structure. The Fe^{2+} and the Ti^{4+} ions occupy alternating layers of the cation lattice unlike in alumina, where Al^{2+} ions occupy 2/3 of the octahedral positions in the cation lattice. When the tolerance factor lies between 0.71 and 0.9, the perovskite structure distorts through tilting of the B-site octahedral to accommodate the relatively small A-site cations. This tilting distortion results in perovskite structure with either orthorhombic or rhombohedral symmetry [14, 15]. With a tolerance factor between 0.9 and 1.0, an ideal cubic perovskite forms and when $t > 1.0$ the A-site cations begins to exceed the size limits of the dodecahedral holes leading to either hexagonal symmetry, or a tetragonal distortion of the unit cell [12, 14, 15]. Ferroelectric perovskites tend toward tolerance factors slightly above 1.0 and a tetragonal symmetry [12].

The Goldschmidt tolerance factor is a useful tool to determine the phase stability of perovskite materials; however, the principle assumption of Eq. 2.4, is a hard sphere model where covalent bonding is ignored [12]. In reality, chemical bonding in ceramics combine both ionic and covalent bonding. Therefore, Eq. 2.4 does not

adequately predict whether a solid will form the perovskite structure. Electronegativity differences between the ions accounts for the covalent bonding character in perovskites. Stable perovskites tend to exhibit larger electronegativity differences. Equation 2.5 is the electronegativity difference between the A-site cation and oxygen, X_{A-O}, and the difference between the B-site cation and oxygen, X_{B-O}.

$$\Delta\text{EN} = \frac{(X_{A-O} + X_{B-O})}{2} \tag{2.5}$$

In $PbTiO_3$, Eq. 2.4 and Eq. 2.5 yields t = 1.02 and EN = -1.51 respectively; the calculated values for another common perovskite, $SrTiO_3$, are t = 1.00 and EN = -2.20 respectively. The previous calculations state $PbTiO_3$ is a tetragonal and stable perovskite ferroelectric while $SrTiO_3$ is non-ferroelectric. The amount of ionic bonding in a perovskite is proportional to Eq. 2.5 [16]. In this discussion, a single composition was assumed, however, Eqns. 2.4 and 2.5 can also be used to estimate perovskite phase stability in solid solutions.

2.4 Defect Chemistry

Nothing in life is perfect, the same is true in crystals. Some say the defects in crystals make them interesting and worth investigating. In the discussion of crystal structure, x-ray diffraction, and perovskite crystal structure, perfect crystals were assumed; however, polycrystalline materials contain defects. The boundaries between individual crystallites are called grain boundaries, and in terms of dimension, are two dimensional defects. Ceramic materials also contain point defects (0-D), line defects (1-D) such as cracks, and voids (3-D or volume defects). All of these defects play different roles in the performance of piezoelectric and ferroelectric materials, e.g. cracks and other linear defects are important in the study of electrical fatigue of ferroelectrics and grain boundaries affect electrical properties in ferroelectrics such

as the piezoelectric coefficient and other macroscopic properties. In the upcoming discussion of defect chemistry, point defects will be the focus simply because they are the easiest defects to deal with. At different points in this thesis, all the defects will be mentioned in relation to some observed macroscopic property.

Defect chemistry is the study of the departure of a crystal structure from the perfect lattice. Examples include alumina, which is a colorless and hard refractory solid; however, when a small fraction of Al^{3+} is replaced with Cr^{3+}, ruby is formed. Semiconductors are also affected by defects in crystal structure. When dopants are added to silicon, the defects generate either electrons (n-type) or holes (p-type). These charge carriers generate a current in p-n junctions used in the semiconductor industry. Defects and dislocations are also the cause of mechanical failure in materials and for certain applications engineers seek to avoid defects as much as possible. This is difficult as defects in small concentrations are thermodynamically favorable in a perfect crystal. Although the lattice energy of a crystal is dependent primarily on the chemical bonding and periodicity of a crystal, the free energy of a system includes an entropy term, which causes a minimum in the free energy. Following a proof by Smyth [17], the change in the Gibb's free energy can be related to the number, n, of defects in a solid as a function of temperature,

$$n = Nexp\left(\frac{\Delta S}{k}\right)exp\left(\frac{-\Delta H}{kT}\right) \tag{2.6}$$

where k is Boltzmann's constant, N is the number of lattice sites in a perfect crystal, ΔH [J] is the change in enthalpy, and ΔS [J/K] is the change in entropy. For Schottky defects, anion and cation vacancies are created; whereas in Frenkel defects, a vacancy and an interstitial atom are created, Eq. 2.6 changes to,

$$n = N\ exp\left(\frac{-\Delta H_S}{2kT}\right) \tag{2.7}$$

$$n = \left(NN'\right)^{1/2} \; exp\left(\frac{-\Delta H_F}{2kT}\right) \tag{2.8}$$

where Eq. 2.7 is the number of Schottky defects and Eq. 2.8 is the number of Frenkel defects [17–19]. The N′ is the equilibrium number of interstitial sites. The entropy term from Eq. 2.6 can be dropped as the enthalpy term is the dominate term [17].

Schottky, cation Frenkel, and anion Frenkel disorder; are all considered intrinsic defects. Extrinsic defects in a ceramic are caused by an impurity ion, such as charge generation after doping a ceramic. Generally, one intrinsic mechanism dominates depending on which mechanism has the lowest enthalpic cost and is used as a model for the creation of Kröger-Vink diagrams. Examples of Kröger-Vink diagrams for ceramic materials can be found in the work by Smyth [17]. An example is shown in Fig. 2.4 for Fe-doped $SrTiO_3$ [20]. Kröger-Vink diagrams are useful for determining defect concentrations at different partial pressures of oxygen. These diagrams become more complex when extrinsic defects are introduced into a ceramic.

Chemical equations in defect chemistry follow the Kröger-Vink notation. Some examples of the use this notation are found in an excellent introduction to defect chemistry by Smyth [17]. A bullet, $\bullet$, in the superscript stands for one positive charge, $'$ is a negative charge, an X is a neutral charge. Symbols in the subscript relate to the original species in a lattice position, e.g. i in the subscript stands for an interstitial. Examples of Kröger-Vink notation include: Sr substituting Ba in $BaTiO_3$ (Sr_{Ba}^{X}), cation vacancy in CaF_2 (V''_{Ca}), cation interstitial in AgBr ($Ag_I^{\bullet}$), and an oxygen vacancy ($V_O^{\bullet\bullet}$).

Impedance spectroscopy (IS) is an important tool for determining the effect of point defects on the complex electrical response of dielectric materials. All materials react to an applied electric field in different ways. Of course metals generally conduct, insulators generally insulate, and semiconductors fall in the middle in terms of electrical conductance (or resistance). The ability of a material to conduct electrical

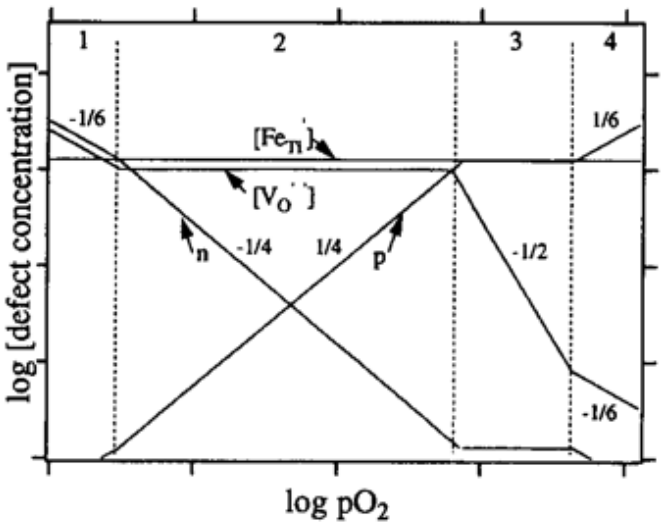

FIGURE 2.4: Kröger-Vink diagram of $SrTiFeO_3$. Reprinted from the Journal of Physics and Chemistry of Solids; Vol. 58; Svein Stinsvik *et al.*; The Defect Structure of $SrTi_{1-x}Fe_xO_{3-y}$ (x = 0-0.8) Investigated by Electrical Conductivity Measurements and Electron Energy Loss Spectroscopy (EELS); 969-976. © (1997), with permission from Elsevier.

charge is related to chemical bonding (i.e. electron states). Of course all materials are made up of a vast collection of atoms, so the number of chemical bonds and the number of possible electronic states are large. These electronic states form into bands of occupied and unoccupied electron states corresponding to the four quantum numbers (principle, n, azimuthal, l, magnetic, m_l, and spin, s). Each band is separated from each other by a region of forbidden energy states known as a band gap. Most important here, is the band gap separating the highest occupied band (commonly called the valence band) from the lowest unoccupied band (conduction band). Figure 2.5 is a simple diagram of this concept with the ordinate axis in terms of energy and the abscissa as the axis of momentum.

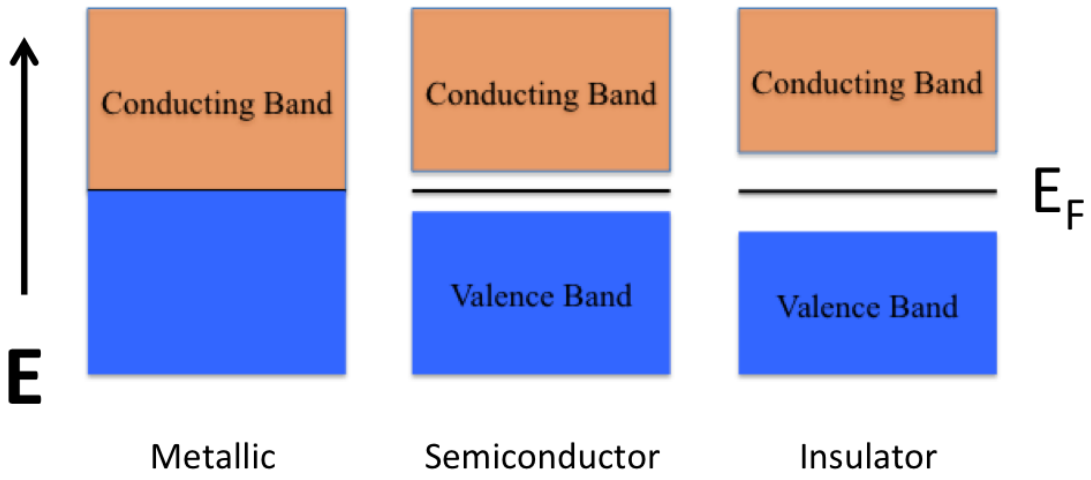

FIGURE 2.5: Diagram of bands of allowed and forbidden electron states related to chemical bonding.

In conductors, there are states available for electrons to move into the same band, i.e. the highest occupied band is partially filled. In insulators, the highest occupied band is completely filled meaning there are no available states for electrons to jump into without the addition of enough energy to surmount the band gap. There exists a band in semiconductors; however, it is small in comparison to insulators. In conductors at thermodynamic equilibrium, half the total probability of a state being occupied is known as the Fermi point. In insulators and semiconductors, the Fermi point lies in the band gap. Generally, ferroelectrics are excellent insulators with large bang gap, e.g. polycrystalline $BaTiO_3$ has a band gap of ≈ 3.2 eV at room temperature [21]. Impedance spectroscopy is used to determine the conducting species in insulators that at standard temperature and pressure would be near perfect insulators but at high temperatures conduct.

In this thesis, impedance spectroscopy is used to determine the depolarization temperature (T_d). In the following sections, short reviews of dielectric properties, piezoelectric, pyroelectric and ferroelectric properties follow. In Section 2.6, electromechanical coupling factor is discussed and in Sec. 2.9, the poling treatment of

a ferroelectric polycrystalline material is discussed. These two topics are related in that the electromechanical coupling coefficients (energy transfer between mechanical input and electric output and visa versa) is determined by first finding the resonant frequency of a poled ferroelectric ceramic. This frequency is found by measuring the impedance of the ceramic over a predetermined range of frequencies.

2.5 Dielectric Properties

Free electrons in the presence of an electric field will accelerate unimpeded towards a source of positive charge. In a solid, electrons interact with other electrons, phonons, and nuclei. In a conductor, the highest occupied energy band is partially filled, leading to electron conduction throughout the material. In an insulator, the top most energy band is unoccupied and electrons are bound to the atoms within the solid. In the presence of an electric field, electrons within a conductor accelerate in the direction of the field. In contrast, an insulator resists the electrical field up to the breakdown voltage of the material. In dielectrics, a subset of insulators, the electrons and the nuclei they surround separate under the influence of the electric field leading to a displacement of charges otherwise known as an induced dipole. Like the electric field, displacement is a vector and represents the displacement field, which is directly proportional to the electric field. In addition, the displacement is defined in terms of charges with units of charge per unit area as in Eq. 2.9.

$$D = \frac{Q}{A} \tag{2.9}$$

The distance separating the positive and negative charges in a dipole is defined as the dipole moment. In terms of macroscopic properties, the dipole moment per unit volume is defined as the polarization. In the atomic array, an overall polarization of charges in dielectrics generates a secondary field opposing the electric field and an

equilibrium separation is created between positive and negative charges. Equation 2.10 represents the polarization density,

$$P = \epsilon_o \chi_e E \tag{2.10}$$

where ϵ_o is the permittivity of free space and χ_e is the electric susceptibility. The electric susceptibility contains dielectric information about the material. Dielectric properties are represented by the permittivity and losses in the material. From electric susceptibility,

$$\chi_e = \frac{\epsilon}{\epsilon_o} - 1 = \epsilon_r - 1 \tag{2.11}$$

$$\frac{\epsilon}{\epsilon_o} = \epsilon_r \tag{2.12}$$

where ϵ_r is the relative permittivity, a measurable quantity. The product of the relative permittivity, ϵ_r, and the permittivity of free space, ϵ_o, gives the total permittivity of the dielectric, ϵ. Dielectrics are often used in capacitors, where the dielectric material is placed in between conducting material as in Fig. 2.6. It should be noted here that the preceding equations are only valid for isotropic materials. For many materials, properties are anisotropic and thus are not scalar properties but tensor properties of some rank dependent on the resultant and applied forces. Electrical susceptibility for instance, is a 2^{nd} rank tensor as the polarization and electric fields are vector quantities (i.e. 1^{st} rank tensors).

So far in the discussion of dielectrics and capacitance, static fields or direct currents were assumed. In many applications; however, capacitors are subject to alternating currents and the relationships from the previous section need to be ex-

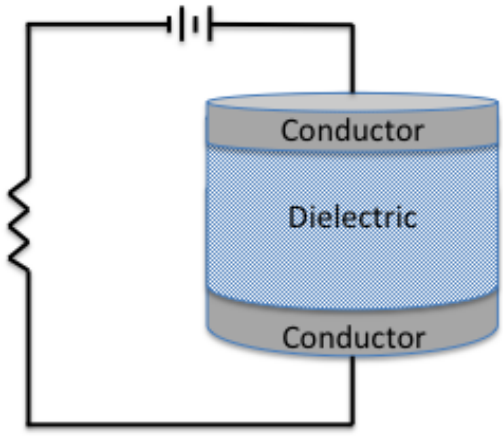

FIGURE 2.6: A simple resistor-capacitor (RC) circuit with a dielectric between two electrodes in the capacitor.

amined in the frequency domain. The permittivity, Eq. 2.12, is a complex number shown as,

$$\epsilon = \epsilon' + i\epsilon'' \tag{2.13}$$

where ϵ' is the real part and ϵ" is the imaginary part. When an alternating field is applied, the dielectric reacts by switching polarity along with the electric field. Several mechanisms are responsible for the polarization of a dielectric in an alternating field: electronic, ionic, dipolar, and space charge. Each mechanism contributes to the real permittivity of a material; however, as the frequency is increased, electric field switching becomes too fast for polarization mechanisms to keep pace and their influence on the permittivity becomes negligible. The following figure (Fig. 2.7) produced by Moulson and Herbert shows the change in permittivity as frequency is increased [18]. Each peak represents the resonant frequency of each dipole mechanism, e.g.

resonant frequency of $\approx 10^{-13}$ Hz for ionic dipoles. In the bottom half of Fig. 2.7, the imaginary component is plotted with respect to frequency. The imaginary part of the complex permittivity represents the dissipative loss of a material. Imagine a phasor diagram of a complex number, it can be seen that if the imaginary part of a complex number is zero, the complex number is completely in phase with the real part; however, when the imaginary part has a non-zero value, a phase angle separates the real and imaginary components. Taking the tangent of the angle δ gives a ratio of the imaginary and real components as in Eq. 2.14,

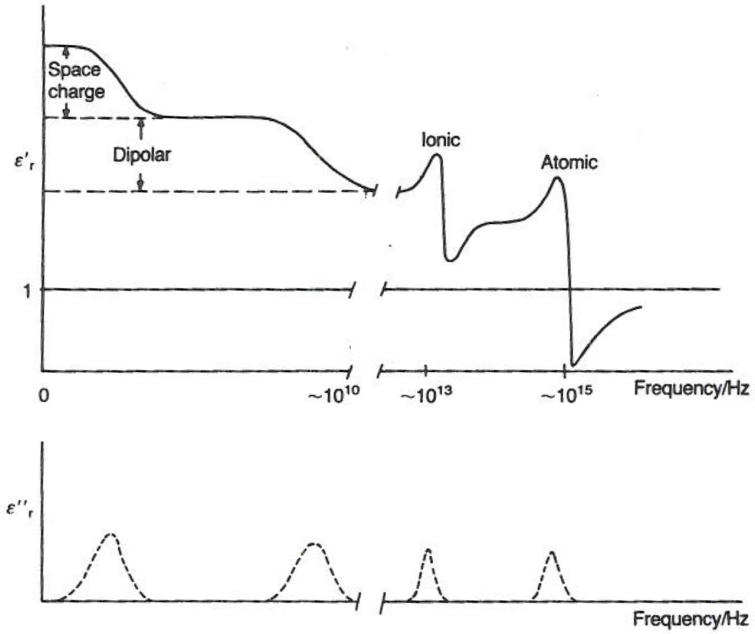

FIGURE 2.7: The dielectric spectrum showing the polarization mechanisms contributions to permittivity and loss. Reprinted, with permission, from A. J. Moulson and J. M. Herbert; Electroceramics: Materials, Properties, Applications, 2nd Edition; John Wiley and Sons; © (2003), John Wiley and Sons [18].

where ϵ' and ϵ" are the real and imaginary permittivity respectively. Equation 2.14 is known as the loss tangent and quantifies the energy loss of a dielectric material [10,

12].

$$tan\delta = \frac{\epsilon''}{\epsilon'} \tag{2.14}$$

2.6 Piezoelectricity

Piezoelectricity is the transformation of mechanical energy to electrical energy, known as the direct piezoelectric effect, and the inverse transformation of electrical energy to mechanical energy is the converse piezoelectric effect. The brothers Pierre and Jacques Curie discovered the direct piezoelectric effect in 1880. The converse effect was theorized by Gabriel Lippmann and confirmed by the Curie brothers a year later. Among the first piezoelectric materials studied included: quartz, topaz, tourmaline, and potassium sodium tartrate or Rochelle salt. Among these early known piezoelectric materials, quartz is still used due to its relatively high piezoelectric coefficient. Quartz is used as a clock standard, as the piezoelectric effect is used to change the resonant behavior of the crystal under a load and once the load is removed, the crystal returns to its original state. Along with quartz, a large number of piezoelectric materials are used in many applications.

All solids experience a strain under a load; however, in piezoelectric materials, an additional change in energy arises due to the rise of an electric field under stress. Figure 2.8 shows a ceramic piezoelectric pellet acted on by: Fig. 2.8 (a), a mechanical force compressing or extending the pellet resulting in an electrical current, and Fig. 2.8 (b), an electric field applied across the pellet causing expansion or contraction in the pellet. The 20 piezoelectric point groups lack a center of symmetry, which is responsible for the polarizability of piezoelectric materials, where polarization is defined as the strength of the separation of positive and negative charges in a dipole. Many piezoelectric ceramics also experience a mechanical strain along axes

perpendicular to an applied electric field and visa versa due to an inherent anisotropy in material properties.

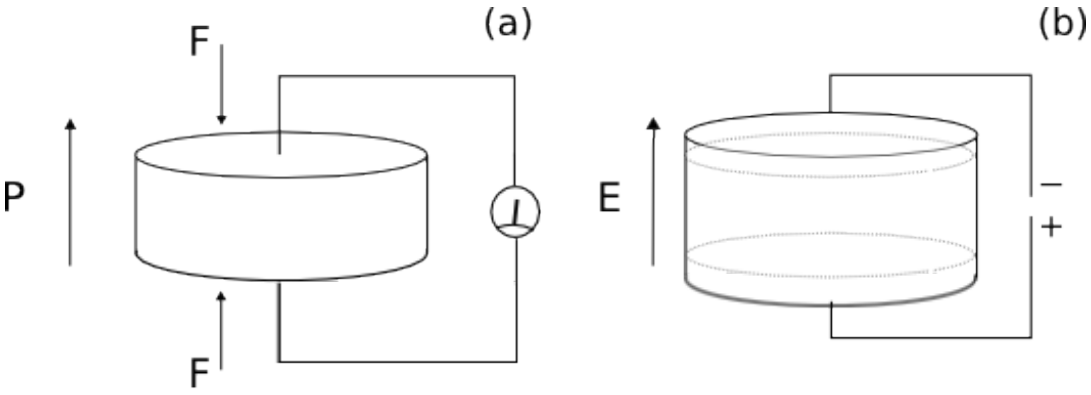

FIGURE 2.8: Exaggerated picture of the energy transformation in piezoelectric ceramics via (a) the direct piezoelectric effect and (b) the converse effect.

Piezoelectricity is quantified by several parameters: electric displacement (D), electric field (E), stress (T), and strain (S). These parameters are related to each other through equations of state describing the electronic and stress states of a piezoelectric. Stress and electric field are thus coupled and the equation of state for the direct piezoelectric effect is stated as follows in Eq. 2.15,

$$D = \mathrm{d}T + \epsilon^{T}E \tag{2.15}$$

where d is the piezoelectric coefficient and T in the superscript of permittivity represents constant stress. The piezoelectric coefficient is defined as the strength of a polarization due to an applied stress. For the converse effect, an applied field causes the material to strain. This strain through a similar argument as the direct effect is described by a coupled equation,

$$S = s^{E}T + \mathrm{d}^{*}E \tag{2.16}$$

In Eq. 2.16, d*, is the converse or indirect piezoelectric coefficient. The superscript E in the first term, represents zero or constant electric field on the compliance, *s* [12]. Polarization and electric field are both vector quantities, or first rank tensors. The stress and the strain are both second rank tensors, so in reality, T and S are matrix equations. Therefore, both coefficients are third rank tensors with 27 components.

Since application of stress on a piezoelectric induces a polarization, like in Fig. 2.8 (a), P will be used instead of D. The polarization is directly related to the electric displacement and field through Eq. 2.12 and so it is directly related to the stress on the piezoelectric as follows,

$$P_i = \mathrm{d}_{\mathrm{ijk}} T_{jk} \tag{2.17}$$

where $\mathrm{d}_{\mathrm{ijk}}$ is the direct piezoelectric coefficient (low field) with units of pC/N. Equation 2.17 assumes the only tensor applied is stress and the electric field is zero. For the converse effect, Fig. 2.8 (b), the material is strained under an applied electric load. The strain is proportional to the applied electric field represented in Eq. 2.18,

$$S_{ij} = \mathrm{d}^*_{ijk} E_k \tag{2.18}$$

where $\mathrm{d}_{\mathrm{ijk}}$* is the converse, or indirect, piezoelectric coefficient (high field) with units of pm/V. The subscripts used in Eqs. 2.17, 2.18: *i*, *j*, *k*; represent the directions along a material that a stress or field is applied and the directions of the response. The indices 1-3 denote stress or strain in directions normal to the unit cell as in Fig. 2.9. The indices 4-6 represent shear stresses on the piezoelectric again as shown in Fig. 2.9. Because of the crystal symmetry in many materials, many of these indices can be

ignored simplifying the representative tensors.

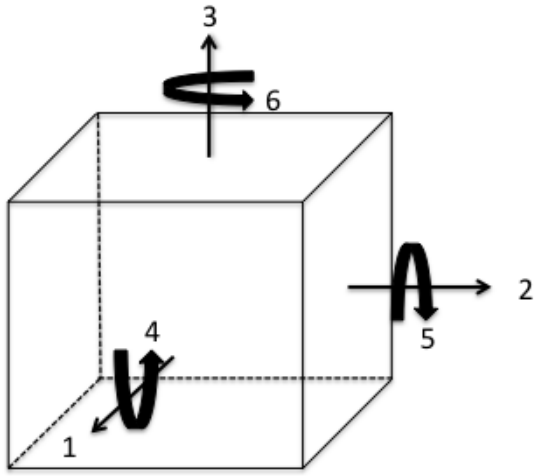

FIGURE 2.9: Normal and shear stress components on a piezoelectric unit cell.

Despite the complexity of the third rank tensor piezoelectric coefficients, simplifications can be made due to symmetry relations. The indices j and k are equal, and a new set of indices, jk, include: $11 \rightarrow 1$; $22 \rightarrow 2$; $33 \rightarrow 3$; $23 \rightarrow 4$; $13 \rightarrow 5$; $12 \rightarrow 6$, leading to 18 independent components (d_{ij}) of the piezoelectric tensor [13–16]. This notation is known as Voigt notation and reduces the order of higher rank tensors to lower order matrix forms. As a result, the matrix forms of Eqns. 2.17 and 2.18 can be written in a palatable way as,

$$\begin{pmatrix} P_1 \\ P_2 \\ P_3 \end{pmatrix} = \begin{pmatrix} \mathrm{d}_{11} & \mathrm{d}_{12} & \mathrm{d}_{13} & \mathrm{d}_{14} & \mathrm{d}_{15} & \mathrm{d}_{16} \\ \mathrm{d}_{21} & \mathrm{d}_{22} & \mathrm{d}_{23} & \mathrm{d}_{24} & \mathrm{d}_{25} & \mathrm{d}_{26} \\ \mathrm{d}_{31} & \mathrm{d}_{32} & \mathrm{d}_{33} & \mathrm{d}_{34} & \mathrm{d}_{35} & \mathrm{d}_{36} \end{pmatrix} \begin{pmatrix} T_1 \\ T_2 \\ T_3 \\ T_4 \\ T_5 \\ T_6 \end{pmatrix} \tag{2.19}$$

$$\begin{pmatrix} S_1 \\ S_2 \\ S_3 \\ S_4 \\ S_5 \\ S_6 \end{pmatrix} = \begin{pmatrix} d_{11}^* & d_{12}^* & d_{13}^* & d_{14}^* & d_{15}^* & d_{16}^* \\ d_{21}^* & d_{22}^* & d_{23}^* & d_{24}^* & d_{25}^* & d_{26}^* \\ d_{31}^* & d_{32}^* & d_{33}^* & d_{34}^* & d_{35}^* & d_{36}^* \end{pmatrix} \begin{pmatrix} E_1 \\ E_2 \\ E_3 \end{pmatrix} \tag{2.20}$$

The axis labeled 3 is commonly referred to as the poling axis. Poling is a procedure where piezoelectric domains are oriented along an applied field to maximize polarization of a ceramic, which will be discussed in more detail in later sections. Simplification of Eqns. 2.19 and 2.20 can be made to take into account the constant fields (short-circuit) and poling procedure to give Eq. 2.21,

$$\begin{pmatrix} 0 & 0 & 0 & 0 & d_{15} & 0 \\ 0 & 0 & 0 & d_{15} & 0 & 0 \\ d_{31} & d_{31} & d_{33} & 0 & 0 & 0 \end{pmatrix} \tag{2.21}$$

where the converse coefficient is simply the transpose of Eq. 2.21. For example, if a stress is applied along the poling axis, a polarization along an axis orthogonal to the poling axis, axis 1 or 2, arises and the piezoelectric coefficients $d_{31} = d_{32}$ is calculated. The following Eqns. 2.22 - 2.25 are constants, including the piezoelectric coefficients commonly studied in piezoelectric materials.

$$d_{ij} = \left(\frac{\partial P_i}{\partial T_j}\right)^E, d^*_{ij} = \left(\frac{\partial S_i}{\partial P_j}\right)^T \tag{2.22}$$

$$e_{ij} = \left(\frac{\partial P_i}{\partial S_j}\right)^E, e^*_{ij} = -\left(\frac{\partial T_i}{\partial E_j}\right)^S \tag{2.23}$$

$$g_{ij} = -\left(\frac{\partial E_i}{\partial T_j}\right)^E, g^*_{ij} = \left(\frac{\partial S_i}{\partial P_j}\right)^T \tag{2.24}$$

$$h_{ij} = -\left(\frac{\partial E_i}{\partial S_j}\right)^E, h^*_{ij} = -\left(\frac{\partial T_i}{\partial P_j}\right)^S \tag{2.25}$$

The other piezoelectric constants are (e_{ij}) the elastic coefficient, (g_{ij}) the voltage coefficient, and (h_{ij}) the piezoelectric coefficient. For piezoelectric sensors and actuators, the piezoelectric strain and voltage coefficients are commonly used. For actuators, a high d coefficient is desired, and for sensors, a high voltage coefficient g_{ij} is required.

It had been stated several times earlier that any cubic or any centrosymmetric crystal can not be piezoelectric. The proof needs only simple symmetry arguments without any analytical work. If there is crystal with a center of symmetry, apply a stress to it along any of the orthogonal axes. Since stress itself is a 2nd rank tensor with a center of symmetry [22] and the crystal has a center of symmetry, then the polarization vector would remain unchanged except for a reversal of direction, i.e. P_i = - P_i. The polarization can only be equal to its opposite if P = 0. Therefore, any centrosymmetric crystal cannot be a piezoelectric material. One cannot apply a general stress to NaCl and find a polarization in response.

In real systems, it is often desirable to measure the efficiency of a piezoelectric material. The electromechanical coupling factor, k, is used to measure the transformation of energy from an applied force, either mechanical or electrical, to the other form. The coupling factor is written as shown in Eqns. 2.26 and 2.27,

$$k^2 = \frac{\text{electrical energy converted to mechanical energy}}{\text{input electrical energy}} \tag{2.26}$$

$$k^2 = \frac{\text{mechanical energy converted to electrical energy}}{\text{input mechanical energy}} \tag{2.27}$$

Just as with the piezoelectric constants, k is dependent on direction. The above equations relate to an effective coupling factor. Coupling factors along different axes can be calculated and are referenced in the IEEE standard on Piezoelectricity [10]. Before continuing the discussion on functional properties, a brief look at an important topic, morphotropic phase boundaries (MPB), which in solid solutions of many piezoelectric materials today are those compositions with optimized properties at this phase boundary.

2.7 Morphotropic Phase Boundary (MPB)

In solid solutions, such as lead zirconate titanate (PZT), the chemical stoichiometry is adjusted to optimize dielectric and piezoelectric properties, such as doping the B-site with Nb^{5+} cations leading to increased dielectric constants and mechanical quality factor but with reduced T_C [23]. Another common example is the isovalent substitution of barium with strontium in $BaTiO_3$. This substitution lowers the Curie temperature while increasing the dielectric peak compared to pure $BaTiO_3$ [12]. In high-temperature piezoelectrics, the goal is to increase T_C, therefore stoichiometric control and proper substitutions in PT-based piezoelectrics are critical. Mentioned in Chap. 1, combination of tetragonal ferroelectric PT and the orthorhombic anti-ferroelectric PZ leads to the solid solution PZT. With more than 90 wt% PZ, PZT functions in an anti-ferroelectric orthorhombic phase. On the other end of the phase diagram, PZT functions in a ferroelectric tetragonal phase. Common functional compositions of PZT are found in the middle of the phase diagram, near compositions with a nearly equal amount of PT and PZ, as shown in Fig. 2.10 [24].

The line compound in Fig. 2.10 is labeled (MPB) and refers to the morphotropic phase boundary and marks the change between the PZ-rich ferroelectric rhombohedral phase and the PT-rich tetragonal ferroelectric phase. When the percentage of PZ

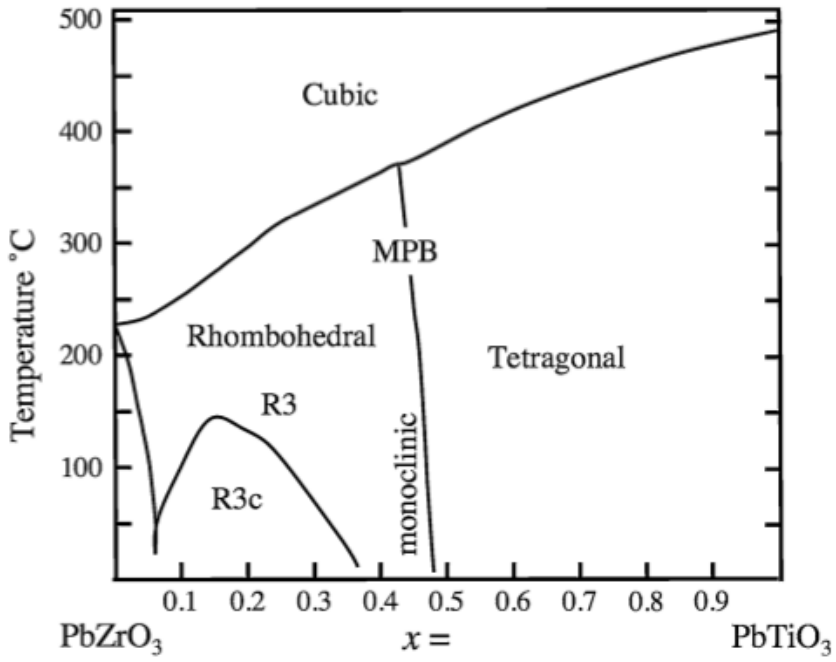

FIGURE 2.10: Phase diagram of PZT. Springer and Metallurgical and Materials Transactions A, 41, 2009; 1110-1118; Monte Carlo Simulation Study of Diffuse Scattering in PZT, Pb(Zr,Ti)O_3; T.R. Welberry *et al.*; Figure 1; © (2009) Springer, with kind permission from Springer Science and Business Media.

drops below 90%, PZT transitions to the ferroelectric rhombohedral phase. When x ≈ 0.48, both the rhombohedral and tetragonal phases are equally favorable. At the MPB, the electrical domains (see Sec. 2.9.2) orient along any of the equivalent directions for both rhombohedral (8 directions) and tetragonal symmetry (6 directions). As a result, domains align along 14 equally favorable directions.

2.8 Pyroelectricity

Materials with built-in dipoles are known as polar materials. Of the 20 piezoelectric point groups, 10 are polar point groups. Figure 2.11 shows the crystal classes

that are either piezoelectric or both piezoelectric and polar [25]. These ten crystal classes (1, 2, m, mm2, 4, 4mm, 3, 3m, 6, and 6mm) contain a unique polar axis and exhibits a phenomenon known as pyroelectricity. The dipoles may be spontaneous, but any polarity in the crystallites may be masked by twinning of adjacent grains or cancelled by large enough charges at the surface or electrode interface [26]. Pyroelectricity is the phenomenon of a change in spontaneous polarization with a change in temperature. This phenomenon should not be confused with the thermoelectric effect which is the generation of electric charge with the application of a temperature gradient.

The spontaneous polarization inherent in all polar materials is a result of naturally occurring dipoles. Cations within the dipoles lie in an asymmetric energy well due to the increase in the cations potential energy [27]. Here, asymmetric means one side of the well goes to infinite energy and the other side has a low maximum, so the energy required to surmount one side of the energy well is small as compared to the other. In pyroelectric materials, a change in temperature will perturb the dipoles and change the potential energy of the cations and in turn change the polarization of the material. The spontaneous polarization is of course also effected by an external electric field and polar materials are by definition non-centrosymmetric, therefore pyroelectric materials are also piezoelectric; however, piezoelectric materials are not generally pyroelectric.

Pyroelectricity can be explained quantitatively as the difference in the spontaneous polarization vector with a change in temperature as shown in Eq. 2.28,

$$\Delta P_S = p\Delta T \tag{2.28}$$

where p is the pyroelectric coefficient tensor. The direction of ΔP_S is defined by the point group of the material, e.g. materials in the tetragonal groups, 4 and 4mm, the direction of the polarization is along the unique polar axis [27]. Pyroelectric

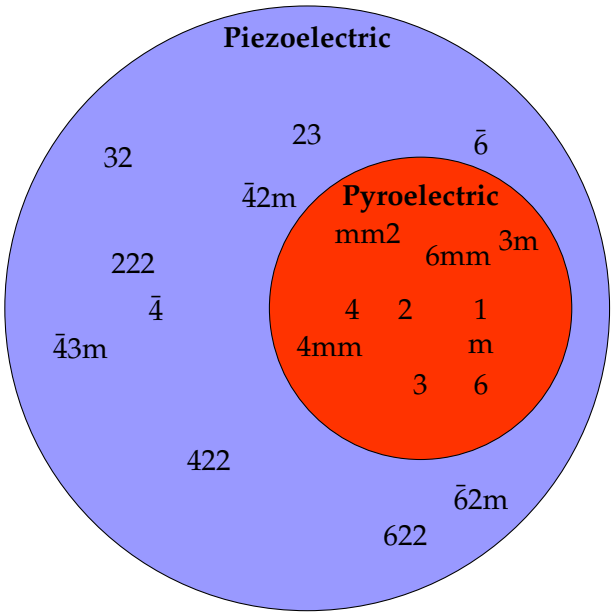

FIGURE 2.11: Venn diagram of the 20 piezoelectric point groups, 10 of which are polar or pyroelectric and contained within the red circle. All ferroelectric materials are pyroelectric and fall in the group of polar materials.

materials have an inherent spontaneous polarization without application of a stress and develop an electric charge with a change in temperature. The charge manifests on the surface and if the pyroelectric is connected to an external circuit, a current is detected.

There are a number of pyroelectric materials such as: tourmaline, CdS, ZnO, and $Li_2SO_4 \bullet 2H_2O$. The largest pyroelectric activity is seen in ferroelectric materials such as PZT, $BaTiO_3$, and $LiTaO_3$ which are discussed in more detail in the next section. Pyroelectric materials are primarily used as detectors, especially in the the infrared wavelengths where pyroelectric devices have been utilized as highly sensitive thermal imaging detectors [28]. Fusion by pyroelectricity has also been achieved using the perovskite $LiTaO_3$ single crystals. A piece of lithium tantalite is placed in a vacuum chamber and cooled to 240 K and then heated to 265 K (ΔT = 25 ^{o}K). The uniform change in temperature of the pyroelectric created large electrostatic fields that was

concentrated by an attached tungsten probe. The electric field produced was sufficient to create an ion beam of adequate energy to cause D + D $\rightarrow$ ^{3}He fusion in a deuterated target [29]. Once the temperature change takes place the pyroelectric discharges, so a periodic heating and cooling treatment must be performed for continuous operation of a pyroelectric device.

As mentioned in previous discussions, ferroelectric materials exhibited the highest pyroelectric activity (as well as piezoelectric performance). This is partially related to the ability of ferroelectric materials to switch the orientation of the spontaneous polarization. This switching does not occur in non-ferroelectric pyroelectric materials. Also, depending on the pyroelectric material (tourmaline is an example), the dipoles may require fields higher than the dielectric breakdown strength in order to completely reverse the polarization. It is this reversal of polarization that separates pyroelectric materials from ferroelectric materials discussed in the next section.

2.9 Ferroelectricity

Ferroelectricity is a material phenomenon where polarization is reversible by application of a strong electric field below the breakdown strength [12]. The materials studied in this work are ferroelectric solid solutions. Some ferroelectric materials have already been identified such as PZT, $BaTiO_3$, $LiTaO_3$, and PT-BS. Chapter 3 contains a broader review of ferroelectric materials, most in solid solution with those materials previously mentioned. There are materials other than ceramics which exhibit ferroelectricity, some polymers exhibit ferroelectricity such polyvinylidene difluoride (PVDF), but only in certain phases after both mechanical and electrical poling [30]. This section will cover a brief history and a physics review of ferroelectricity and end with the difference between normal, diffuse, anti-, and relaxor ferroelectric materials.

2.9.1 Brief History of Ferroelectrics

Potassium sodium tartrate ($KNaC_4H_4O_6 \bullet 4H_2O$ and colloquially known as Rochelle salt) is a naturally occurring mineral that was first discovered in La Rochelle, France in the 17th century [31]. Rochelle salt was found to be piezoelectric 200 years later and ferroelectric by Joseph Valasek in 1921 [32]. The crystal exhibited hysteresis in polarization when the applied field was alternated between positive and negative bias, an indication of ferroelectricity. In 1935, another potassium salt, monopotassium phosphate (KH_2PO_4), was found to be ferroelectric [31]. During World War II, demand was high for materials with high dielectric constants. Researchers from several countries observed ferroelectricity in single crystals of $BaTiO_3$ to have high dielectric constant due to ferroelectricity [31]. Towards the end of the war, ferroelectricity was observed in polycrystalline $BaTiO_3$ after a point treatment. A DC electrical field was applied to an electrode ferroelectric ceramic. Over time, randomly oriented domains aligned to the direction of the applied field. Before this discovery, ceramics of ferroelectric single crystals were soon to be inert and incapable of exhibiting ferroelectricity or piezoelectricity.

One decade after the discovery of ferroelectricity in $BaTiO_3$ and that poling treatments turn polycrystalline materials into ferroelectrics, compositions of the solid solution of $PbTiO_3$ and $PbZrO_3$, PZT, were found to exhibit high piezoelectric coefficient, excellent electromechanical coupling factor, and relatively high Curie temperature [31]. Finding $BaTiO_3$, PZT, and all the other polycrystalline ferroelectric ceramics depended on four critical discoveries: the observation of the hysteresis in polarization in Rochelle salt, the discovery of high dielectric permittivity in $BaTiO_3$, the linking of this high dielectric constant to the ferroelectricity in $BaTiO_3$, and the discovery that the poling process in polycrystalline materials could reorient domains and lead to ferroelectricity in ceramic materials [33]. As a result, today, ferroelectrics are employed in many devices such as: piezoelectric transducers used in sonar, ultrasonic, and medical applications; communication filters; and pyroelectric surveillance

devices detecting changes in ambient heat [31].

Since the discovery of ferroelectric materials, researchers have attempted to come up with a theory for the large piezoelectric properties of materials such as PZT or $BaTiO_3$. Before the development of PZT (and as a whole, MPB-based solid solutions), a phenomenological theory for the polymorphic phase transitions in $BaTiO_3$ was developed by Devonshire in 1954 around the same time PZT was being developed [26]. In the Devonshire theory, thermodynamic relationships between temperature, stress, strain, polarization, electric field, etc. were derived from free energy considerations. Maxwell relations derived from the thermodynamic relationships lead to some of the piezoelectric coefficients discussed towards the end of Sec. 2.6. Theories for the phase transitions discussed later in this section were derived from the elastic Gibb's free energy term which depends on temperature, polarization, and stress.[1] This phenomenology was later extended to explain the composition dependent phase transition (close to the MPB) of PZT [34].

Since early theory development surrounding ferroelectric phase transitions, experimental work determining the properties of PZT have dominated the field. This has been the case until recently with development of new high-temperature ferroelectric solid solutions. In addition, regulations of the use of Pb enacted in the last decade have led to increased focus on Pb-free piezoelectric materials. Many of these new materials exhibit phenomenon not fully explained by the Landau-Ginzberg-Devonshire (LGD) phenomenological theory. New theories have since been proposed to encompass the relaxor ferroelectric materials and even diffuse phase transition ferroelectric materials. The following is a brief overview of the physics of ferroelectricity. A more detailed treatment of the thermodynamics, touched on in this section, can be found in multiple texts [26, 34–37].

[1] Although the stress was assumed to be zero so that the elastic free energy could be expanded in terms of polarization [26].

2.9.2 Physics of Ferroelectrics

The fundamental requirements for ferroelectricity include a material with a non-centrosymmetric unit cell, i.e. without an inversion center. Since a non-centrosymmetric crystal structure is responsible for piezoelectricity, a ferroelectric is a piezoelectric; however, piezoelectric materials are not necessarily ferroelectric, the material must also contain a polar axis. This further restricts the number of point groups to those 10 pyroelectric points groups shown in Fig. 2.11. Another characteristic of ferroelectricity is switching of polarization in response to a switching electric field. The energy of switching can be represented simply by an energy diagram shown in Fig. 2.12 with $BaTiO_3$ as a representative material. The B-site cation is switched between a negative and positive polarization with respect to the center of the tetragonal unit cell following the field switching between negative and positive bias. Overall, the potential is represented by a double potential well with a small energy barrier to the switching. For materials in a paraelectric phase, the B-site cation will only exist in the center position, represented by the green dotted line in Fig. 2.12.

Figure 2.12 is a simplified view of the energy associated with polarization switching. Equilibrium properties increase the number of solutions to equations relating free energy and polarization (more on this topic later). It is also assumed that all B-site cations move in phase with the field; however, the B-site cation is not the only atom of the unit cell that moves with the field, the oxygen anions and the A-site cations also change position. These lattice vibrations are represented by soft phonons whose frequency decreases with increasing temperature up to T_C. The phase transition from the high symmetry paraelectric phase to the low symmetry ferroelectric phase can then be represented by the freezing in of switching of phonons between optical and acoustic modes [36]. The cited reference provides a complete treatment of soft modes and the relationship to phase transitions in ferroelectrics.

Ferroelectric ceramics have regions within individual grains with ionic dis-

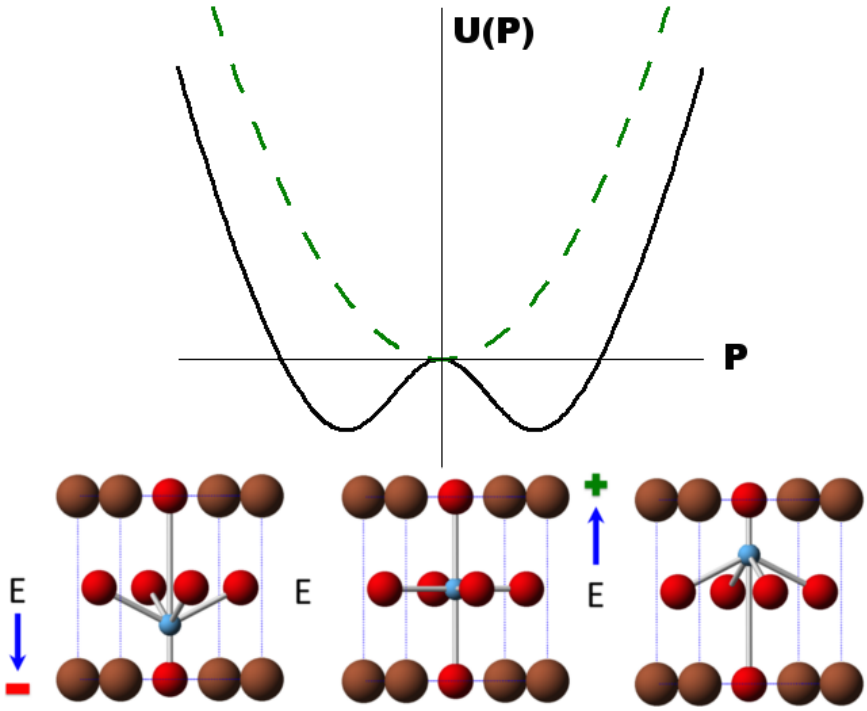

FIGURE 2.12: Energy diagram of ferroelectric switching using $BaTiO_3$ as an example. The green line represents the potential of a material in the paraelectric state.

placements in different directions known as domains. Another critical element in the ferroelectricity of ceramics such as PZT is the poling process, which involves applying large DC electric fields across a ferroelectric material in a parallel plate capacitor arrangement, i.e. disk or square ceramic with two parallel surfaces with electrodes. Domains align parallel to the field as much as possible. Once the field across a ceramic is removed, some of the domains will relax and the parallel component of the polarization vector in relaxing domains will decrease. A simple diagram of this process is presented in Fig. 2.13.

In polycrystalline materials, crystallographic grains contain ferroelectric domains with random orientation. The origin of these domains is related to the change in structure of the ceramic upon cooling. When cooling below T_C, a large amount of elastic energy arises due to the mechanical constraints of the grains. In addition, de-

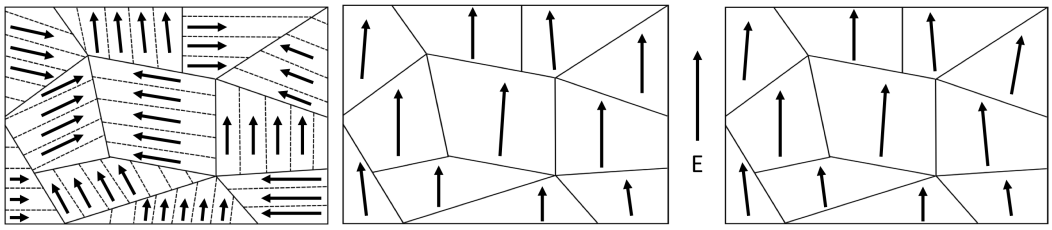

FIGURE 2.13: Schematic representation of a ceramic grain structure. Each grain contains domains **(a)** before, **(b)** during, and **(c)** after application of an electric field.

polarizing fields arise due to an in-homogenous distribution of polarization caused by a decrease in polarization to zero at the grain boundaries or the electrodes. The electrostatic and elastic energies built up during the transition from a high-temperature paraelectric state to a low-temperature ferroelectric state can be minimized by the formation of ferroelectric domains or the splitting of domains. Domains will reorient in directions dictated by crystal structure (tetragonal ⟨001⟩, rhombohedral ⟨110⟩, and orthorhombic ⟨111⟩) and orientation angles between domains: 90° domains for tetragonal crystallites and both 71° and 109° domains in rhombohedral crystals [12]. Domains also orient themselves in anti-parallel arrangement, i.e. 180° domains. So in a tetragonal crystal such as $PbTiO_3$, upon cooling below T_C, both 180° and 90° form.

Different domains have contributions from both ferroelectric and ferroelastic[2] components. The 180° domains are ferroelectric only, as the domains only component is along the polarization vectors with no components parallel to stress that arises during cooling below T_C. The 90° domains contain components along both polarization and stress vectors, therefore 90° domains are both ferroelectric and ferroelastic. In general, non-180° domains are both ferroelectric and ferroelastic. This means that purely ferroelastic domains will switch only with a mechanical input

[2]Ferroelasticity is the mechanical analogue to ferroelectricity and ferromagnetism.

and purely ferroelectric domains will rotate with only an electrical input; however non-180^o domains will respond to both an electric field and a stress field [35].

The number of possible domain orientation directions in a unit cell is: 6, 8, and 12 for tetragonal, rhombohedral, and orthorhombic unit cells respectively. The fraction of grains polarized is: 0.831, 0.921, and 0.866 for tetragonal, rhombohedral, and orthorhombic unit cells respectively. The fraction of grains distorted ideally in tetragonal and rhombohedral crystal systems is 0.368 and 0.424 respectively [12]. Most importantly, the number of equivalent directions for domains to align is partially responsible for the high polarizability of PZT. These values are tabulated in Table 2.2. The morphotropic phase boundary was elaborated on in Sec. 2.7.

TABLE 2.2: Equivalent directions and fraction of grains oriented by poling field. Reprinted from Academic Press Inc. (London) Ltd., Bernard Jaffe, William R. Cook Jr., and Hans Jaffe, Piezoelectric Ceramics, Page 17, © (1971), with permission from Elsevier [12].

Crystal symmetry and polar axis	Number of equivalent directions	Fraction of grain polarization that can be realized ideally	Fraction of grain distortion that can be realized ideally
Tetragonal [001]	6	0.831	0.368
Orthorhombic [110]	12	0.912	Not calculated
Rhombohedral [111]	8	0.866	0.424

One common crystallographic point group of ferroelectric materials is *(4mm)*. The ferroelectrics $PbTiO_3$ and $BaTiO_3$ both form crystal structures in this point group when in a ferroelectric phase. Upon poling, an initially isotropic ferroelectric ceramic changes alignment of domains to a high symmetry order represented in point group

terms as ∞mm [12]. Responsibility for the observable polarization in ferroelectrics is partially due to domain wall motion. Depending on the direction polarization is measured and the fraction of domains aligned parallel to this direction, polarizations of varying strength are observed. Although piezoelectrics and paraelectric materials exhibit a change in the polarization, charge separation occurs in all dielectrics, ferroelectrics experience a hysteresis in polarization with field switching. An example of the hysteretic behavior in ferroelectrics is presented in Fig. 2.14.

In Figure 2.14 (a), a ferroelectric begins with randomly oriented domains [Fig. 2.13 (a)]. As the field increases, the polarization increases up to the maximum applied field. As the field strength is decreased from the maximum, a small fraction of domains relax back to their original states; however, a majority of domains stay aligned parallel to the field. The polarization at maximum field is known as the saturation polarization, P_{SAT}, and the maximum number of 180° domains have been reached [Fig. 2.13 (b)]. Leveling of the hysteresis curve at high fields indicates saturation of the polarization; higher electric field strengths no longer translate to higher polarizations. The spontaneous polarization, P_S, is determined by extrapolating the curve from the point of saturated polarization back to zero electric field [Fig. 2.13 (c)]. The point where the polarization curve crosses the vertical axis (zero field) is known as the remanent polarization, P_r, and is the domain orientation that remains in the ferroelectric after the field is removed. Higher remanent polarization is desirable in ferroelectrics. In single crystals, P_S and P_r will be equal if there are no defects; however, in polycrystalline ceramics, a significant number of defects coupled with randomly oriented grains decreases the energy barrier to domain realignment as the field is decreased to zero. When the polarity of the field is reversed and increased in the opposite direction, the polarization also follows the field to a negative saturation and similar values of P_{SAT}, P_S, and P_r with negative values. The coercive field, E_C, is the energy required to switch domains by 180° and is the point where the hysteresis curve crosses the horizontal axis.

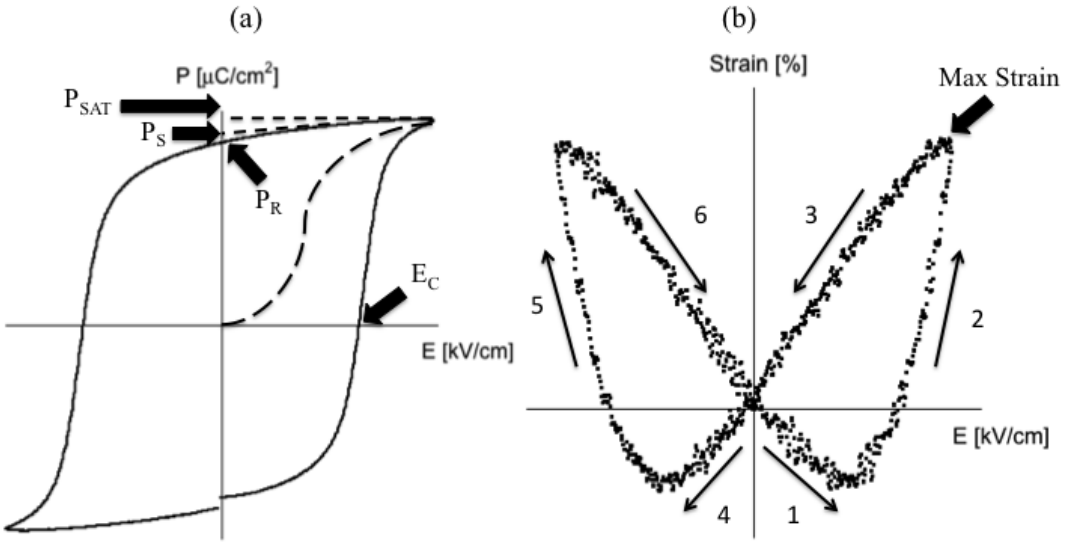

FIGURE 2.14: In **(a)**, polarization hysteresis loop of the ternary ferroelectric composition 50PT-25BS-25BNiT. In **(b)**, strain hysteresis loops otherwise known as "butterfly loops," of the 80PT-10BS-10BZnT.

Most ferroelectric materials exhibit both polarization hysteresis and electromechanical strain (ferroelastic behavior). A notable exception is in $LiNbO_3$ which contain only 180^o domains [38]. Figure 2.14 (b) represents the electromechanical strain produced during electrical field switching. Domains move and nucleate with a field much like grains with temperature. Domain wall motion contributes to the deformation in ferroelectrics and since domains are oriented in different directions, strain is caused with application of an electric field. This property is known as electrostriction, an inherent material property in all dielectrics. In normal dielectrics, the strain is proportional to the square of the field and in fact, in low applied fields, an unpoled ferroelectric will deform proportional to the square of the applied field. Conversely, in piezoelectric materials the strain will be linear with the electric field. Following the arrows in Fig. 2.14 (b), an unpoled tetragonal ferroelectric is subjected to an increasing field. Deformation initially begins in a direction independent of the field as seen by the quadratic curve of strain; however, once the field is high enough, the

deformation grows linearly and domains begin to align parallel to the field, i.e. 180º domains. Ideally, once past the coercive field, domain switching comes exclusively from 180º domains, not a mixture of 180º and 90º domains [39]. If the maximum applied field is high enough, the strain would level off as saturation is reached. Strain returns to zero once field is zero and follows a reverse path when field direction is in the opposite direction.

Polarization hysteresis and strain loops are related to the movement of domains, specifically, non-180º domain walls [40–42]. Domain wall movement is dependent on: the crystallographic structure of the unit cell, density of grains and domains within each grain, domain wall structure (e.g. combination of 71º and 109º domains in a rhombohedral crystallite), domain wall mobility, and the average size of the grains. All of these different dependencies are related to the concentration of point defects, either dopants or impurities [42]. One major effect in hard PZT [3], is the pinning of domain walls via oxygen vacancies resulting in lower mobility leading to lower remanent polarization and piezoelectric coefficients. Generally, the impact of domain wall motion on these properties is known as the domain contribution (sometimes referred to as extrinsic contribution) to the dielectric and piezoelectric properties. Intrinsic contributions to the piezoelectric coefficients come primarily from the lattice itself, i.e. switching at the unit cell level.

2.9.3 Asymmetric Loops

Information can be gleaned from the shape of the hysteresis and strain loops. Shown in Fig. 2.15, for the composition 52PT-24BS-24BNiT, are polarization and strain loops. In Figure 2.15 (a), there is a slight shift to the left or right in the coercive field attributed to an internal bias field. Equation 2.29 represents this internal bias. In

[3]The term "hard" here means electrically hard not mechanically hard. In this context, hard PZT ceramics are difficult to pole or depole in comparison to un-doped PZT or soft PZT. Hard PZT ceramics are doped with an acceptor dopant in either the A-site (Pb^{2+}) or B-site (Ti^{4+} or Zr^{4+}). Sec. 3.3 will go into greater details on both soft and hard PZT.

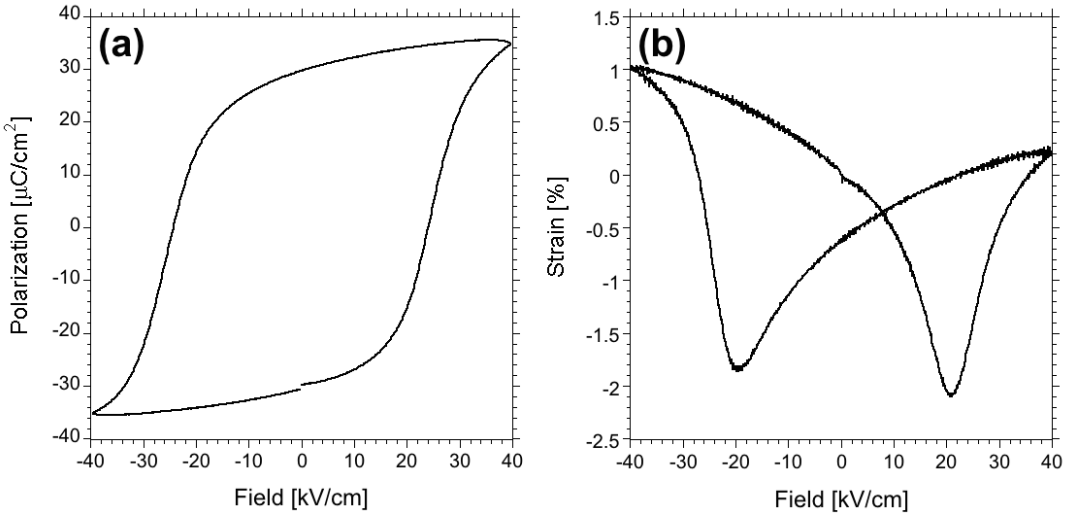

FIGURE 2.15: In **(a)**, polarization hysteresis loop of poled ternary ferroelectric composition 52PT-24BS-24BNiT. In **(b)**, strain hysteresis loop also of the composition 52PT-24BS-24BNiT. These loops are representative of asymmetric polarization and strain loops respectively.

Figure 2.15 (b), there is a dramatic asymmetry in the strain loop for this composition (especially when compared to the strain loop in Fig. 2.14 (b)). The asymmetry in these strain loops can be quantified by Eq. 2.30 [43, 44]. Internal bias field is a result of individual defects or defect clusters pinning domain walls in poled hard ferroelectric materials. Asymmetric strain loops are also a result of domain wall pinning. For an applied field parallel to the internal field, domain wall movement is unrestricted and larger strains result while the opposite applied field direction leads to restriction of domain wall movement and lower strains. Internal bias is observed in soft ferroelectrics, because of a lack of pinning of domain walls, applying fields greater than E_C in soft ferroelectrics will erase polarization build-up.

$$E_{bias} = \frac{E_C^+ - E_C^-}{2} \tag{2.29}$$

$$\gamma_S = \frac{\Delta S^+ - \Delta S^-}{\Delta S^+ + \Delta S^-} \tag{2.30}$$

The internal bias field is an effect of aging or the degradation of a materials properties with time. Aging is not the same as electrical fatigue[4] which is the degradation of a ferroelectric materials properties with field cycling. Despite the effects of aging on poled hard ferroelectric materials, a number of applications take advantage of the internal bias field and strain asymmetry. For high power applications, materials with a high internal bias is desired. For applications where high precision in the strain is required or where a DC bias is not required, strain asymmetry is desired [38].

The movement of domain walls has a huge impact on the response of a ferroelectric material. Temperature also affects the properties of a ferroelectric, with the important temperatures being the Curie temperature, T_C, and the depolarization temperature, T_d. Electromechanical coupling falls to zero at T_C. The piezoelectric coefficient also falls off at T_C, unless the material has a diffuse phase transition in which case piezoelectric properties fall off at T_d, or is relaxor ferroelectric with a complicated temperature response. In the dielectric properties, a maximum in permittivity occurs at T_C for a group of ferroelectrics with a first order phase transition. In such ferroelectrics, the permittivity will be discontinuous across T_C. In other ferroelectrics, a diffuse phase transition to the high-temperature paraelectric state is evident in broad dielectric permittivity peaks. In the following section, the differences between normal ferroelectrics (those materials with a first order phase transition), diffuse phase transition ferroelectrics, relaxor ferroelectrics, and anti-ferroelectric materials will be explained.

[4]Entire books have been written on electrical fatigue which an important limitation in PZT; however, a number of Pb-free piezoelectric solid solutions appear to exhibit fatigue-free performance [45].

2.10 Classification of Ferroelectric Materials

2.10.1 Normal Ferroelectrics

For ferroelectric behavior, an energy barrier to dipole reversal has to be surmounted with an energy level low enough to avoid breakdown. One condition for ferroelectricity is an operating temperature low enough to maintain the ferroelectric phase. If the temperature is sufficiently high, energy exists in the system to destroy dipole ordering and the material is in a paraelectric phase [11, 12, 46]. The transition from the high symmetry phase to the low symmetry phase is also accompanied by the appearance of a spontaneous polarization which was alluded to earlier in this chapter. In normal ferroelectrics, this paraelectric to ferroelectric solid phase transition is modeled on thermodynamic quantities such as free energy. An example of a normal ferroelectric is $BaTiO_3$ (shown in Fig. 2.16) where upon cooling, the material transitions from a higher symmetry paraelectric cubic phase to a lower symmetry tetragonal ferroelectric phase (*P4mm*).

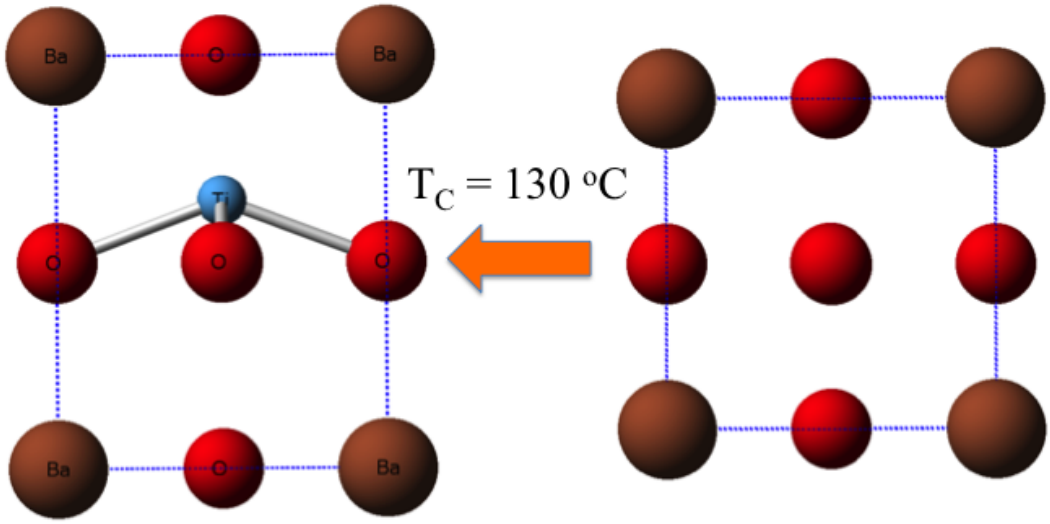

FIGURE 2.16: Phase transition from paraelectric cubic phase to lower symmetry ferroelectric tetragonal phase.

In 1937, Dr. Lev Landau developed a theory on the phase transition between two or more solid phases. The theory stated the phase transitions can be represented by an order parameter [47]. Polarization is the order parameter in ferroelectric materials. According to Landau's theory, the free energy density commonly labelled, $g(T,P)$, as a function of temperature and polarization in ferroelectrics near T_C can be expanded into a power series of even powers of the polarization (i.e. power series of the order parameter in general). Odd powers of polarization go to zero so that the free energy density has the symmetry of the paraelectric phase which must be invariant to the order parameter, i.e. the paraelectric phase does not change symmetry upon polarization reversal [36, 47]. Integrating the free energy density in terms of volume gives the free energy for a ferroelectric. If instead, $g(T,P)$ is differentiated in terms of polarization, then,

$$\left(\frac{\partial g(T,P)}{\partial P}\right) = a_1(T)P + a_2(T)P^3 + a_3(T)P^5 + \cdots \tag{2.31}$$

where a_i are functions of temperature and power series coefficients of the free energy density.

Taking the partial derivative of Eq. 2.31 with respect to the spontaneous polarization gives the inverse of the electric susceptibility. The second derivative of the free energy density is equivalent to differentiating the electric field in Eq. 2.31 with respect to the polarization. The susceptibility must be greater than zero, otherwise its inverse is infinite and the phase is unstable [26, 36], this is the stability condition of ferroelectric phase transitions. In the paraelectric phase, the spontaneous polarization is zero and the first coefficient of Eq. 2.31, $a(T)$, is inversely related to the electric susceptibility. This coefficient may be expanded in terms of a Taylor series assuming the temperature is above a stability temperature, T_o, so that $a(T) = a'(T - T_o)$. These results combined with Eq. 2.11 lead to the Curie-Weiss law (Eq. 2.32), originally

developed for ferromagnetic materials.

$$\epsilon_r = \frac{C}{T - T_o} + 1 \tag{2.32}$$

where the constant, C, is known as the Curie constant and is equal to $1/a'$. Through Eq. 2.11, susceptibility is related to the permittivity of a dielectric material. A complete derivation of the free energy density in terms of spontaneous polarization to the Curie-Weiss law for dielectric materials can be found elsewhere [26, 36, 47].

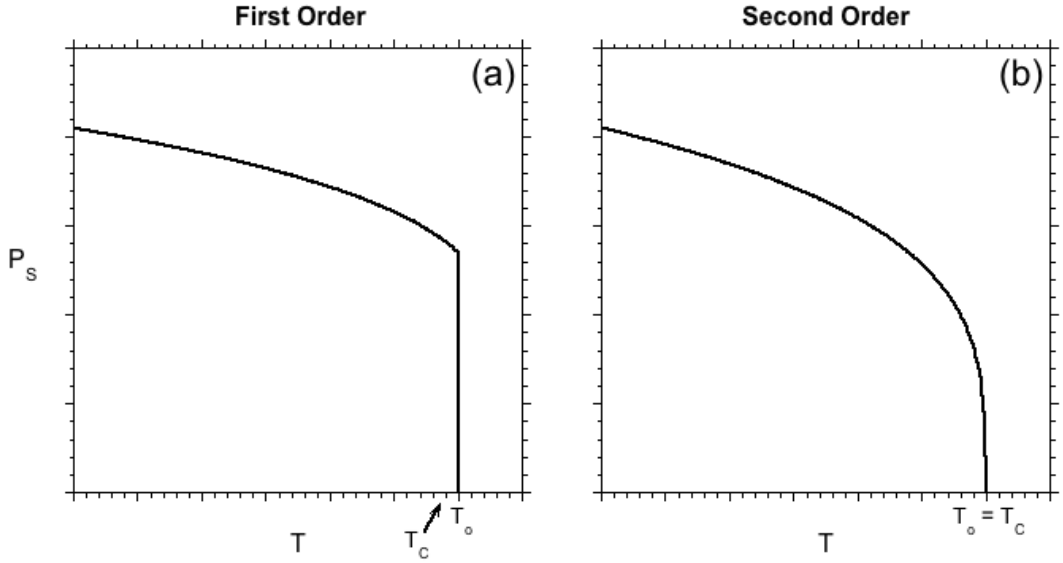

FIGURE 2.17: Examples of spontaneous polarization in normal ferroelectrics with, **(a)**, first order or, **(b)**, second order phase transitions.

Determining C is important in determining the order of the phase transition, either first or second order, a method for calculating C will be discussed in Chap. 4. What is important now is the difference between a first and second order phase transition in ferroelectrics. In first order phase transitions, a sharp discontinuous change in permittivity and spontaneous polarization (shown in Fig. 2.17 (a)) with temperature is observed around the Curie point and $T_C \neq T_o$. The Curie temperature

is different than the stability temperature by more than 10^o. If the ferroelectric has a second order phase transition, permittivity and polarization (shown in Fig. 2.17 (b)) change continuously with temperature and $T_C = T_o$ [11, 12, 26, 36, 47]. One final note, high permittivity is observed in ferroelectrics with a second order transition. In first order transitions, high permittivities are not necessary [48].

2.10.2 Anti-Ferroelectrics

Anti-ferroelectric materials exhibit ferroelectricity in separate lattices, or sub-lattices, where the polarization of each sub-lattice is anti-parallel. The polarization is the order parameter of ferroelectric materials, in anti-ferroelectric materials the order parameter is the sub-lattice polarization. In ferroelectric materials in the low temperature ferroelectric phase, there is a measurable spontaneous polarization while in anti-ferroelectrics the opposing polarization vectors cancel each other out and zero polarization or structural distortion is detected (at zero field). Models for the behavior of anti-ferroelectricity is grounded in a thermodynamic treatment similar to normal ferroelectrics; however, the principal difference between the two classes is obviously the lack of a spontaneous polarization in anti-ferroelectrics. As a result, piezoelectricity is not possible in an anti-ferroelectric. Another difference lies in the fact that there are two polarizations in anti-ferroelectricity, P_1 and P_2, which replace P in Eq. 2.31. These two polarizations manifest in polarization versus electric field plots as double hysteresis loops. For dielectric properties, large dielectric constants are not a requirement of either first or second order phase transitions. The same is true in ferroelectrics only for first order phase transitions, i.e. second order phase transitions will be "large" in ferroelectrics [48]. Even with the non-piezoelectricity, there are applications for anti-ferroelectric materials such as $PbZrO_3$ or Zr-rich PZT, and $GdFeO_3$. These applications include: high strain transducers, pyroelectric-based thermal sensors, high-energy capacitors, and electrocaloric cooling [49].

2.10.3 Relaxor Ferroelectrics

First researched by Smolenskii in the 1950's [50], another broad class of ferroelectrics (known as relaxor ferroelectrics) exhibit dielectric permittivity with a diffuse phase transition opposite the behavior of traditional ferroelectrics. This diffuse behavior is frequency dependent in permittivity and loss, the temperature of maximum permittivity, T_m, increases with increasing frequency and the maximum in loss decreases with increasing frequency. This behavior is attributed to nanometer size polar domains otherwise known as polar nano-regions (PNR). These regions contribute to the polarization within the relaxor past the temperature of maximum permittivity (T_m) and up to the Burn's temperature (T_B)[5]. Neither temperature is related to a structural transition like T_C in normal ferroelectrics. Macroscopically, the relaxor is in a high symmetry paraelectric phase within the temperature range between T_m and T_B. These PNRs exist throughout the ceramic with sizes ranging from $\approx$ 1.5 nm to 10 nm inversely related to temperature for PMN up to the Burn's temperature [51]. Cooling below T_m, the PNRs form short-range order which grow as the temperature continues to decrease until fluctuations in polarization are frozen in at the freezing temperaure, T_f.

Relaxor ferroelectrics do not follow the Curie-Weiss law around T_m. Instead relaxors follow a quadratic version of the Curie-Weiss law,

$$\frac{\epsilon'_{max}}{\epsilon'(f,T)} = 1 + \frac{(T - T_m(f))^{\gamma}}{\delta} \tag{2.33}$$

where if the parameter, $\gamma = 1$, Eq. 2.33 reduces to Eq. 2.32, the Curie-Weiss law, and the ferroelectric is normal. Relaxor ferroelectrics do follow Curie-Weiss behaviors at very high temperatures near the Burns temperature, T_B. Figure 2.18 compares the

[5]The temperature at which a paraelectric relaxor ferroelectric begins to nucleate polar nano regions upon cooling is known as the Burn's temperature.

dielectric and ferroelectric properties of normal, anti-, and relaxor ferroelectrics.

Between T_f and T_m exists another transition temperature in some relaxors known as the ergodic transition commonly seen in BNT-based solid solutions [52]. As the temperature decreases from T_m, an extra dielectric anomaly occurs indicating this transition from a high temperature ergodic state to a low temperature non-ergodic state. The importance in the ergodic nature of some relaxors is the effect that high applied electric fields play on the PNRs. In an ergodic state, applying large fields will generate large polarizations and strains; however, both will decrease to zero once the field is removed. Once the temperature in the material decreases below the transition, an applied field will induce a ferroelectric state with remanent polarization and negative strains associated with 180^o to 90^o domain switching.

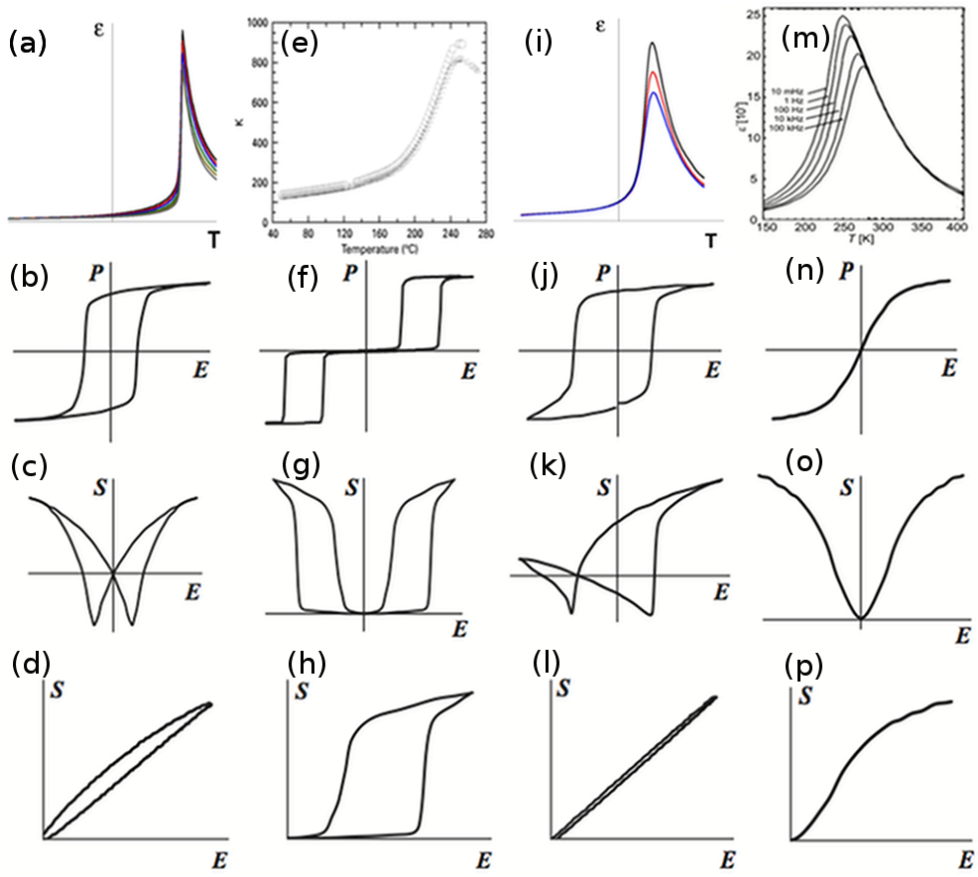

FIGURE 2.18: Comparison of the material properties between normal ferroelectrics **[(a) - (d)]**, anti-ferroelectrics **[(e) - (h)]**, hard ferroelectrics **[(i) - (l)]**, and relaxor ferroelectrics **[(m)-(p)]**. Anti-ferroelectric permittivity in **(e)** reprinted with permission from Springer and the Journal of Materials Science; 32; 1997; 5169 - 5176; Structural and electrical properties of antiferroelectric lead zirconate thin films prepared by reactive magnetron co-sputtering; K. Yamakawa et al.; Fig. 8, © (1997) Springer, with permission from Springer Science and Business Media [53]. Relaxor ferroelectric permittivity in (m) reprinted with permission from Vladmir V. Shvartsman and Doru C. Lupascu; Journal of the American Ceramic Society; John Wiley and Sons; © (2011) The American Ceramic Society [51]. Hysteresis **[(b), (f), (j), (n)]** and both bipolar **[(c), (g), (k), (o)]** and unipolar strain loops **[(d), (h), (l), (p)]** are reprinted with permission from L. Jin et al.; Journal of the American Ceramic Society; John Wiley and Sons; © (2013) The American Ceramic Society [38].

2.11 Summary

This chapter was written to provide brief descriptions of the science behind ferroelectric and piezoelectric materials. Topics included crystal structure, x-ray diffraction, and other topics in basic crystallography. Also covered was an introduction to perovskites, defect chemistry, dielectric properties, piezoelectricity, MPB, and pyroelectric properties in that order, and lastly a short primer on ferroelectricity. The reason so much time was devoted to the topic of ferroelectricity was because ferroelectric materials exhibit the highest piezoelectric performance due to the large remanent polarizations obtained.

In the following chapter, some well known piezoelectric materials will be discussed. Barium titanate and PZT will be covered and then the topic of materials for high-temperature actuators will be expanded on first by discussing the solid solution $PbTiO_3$-$BiScO_3$ (PT-BS). Then other binary and ternary solid solutions based on $PbTiO_3$ will be discussed in terms of piezoelectric coefficient, electromechanical coupling, and transition temperature (either T_C or T_d or both). The final section will cover Pb-free piezoelectric solid solutions and device applications. Later chapters will go into experimental methods, high temperature results, and device applications in depth.

2.12 References

1. Callister Jr., W. D. *Material Science and Engineering: An Introduction* 7th ed. (Wiley, 2007).
2. Sands, D. E. *Introduction to Crystallography* (Dover Publications, Inc., 1969).
3. Schwarzenbach, D. & Pinkerton, A. A. (*Crystallography* English (John Wiley & Sons Ltd, 1996).

4. Eckert, M. Max von Laue and the discovery of X-ray diffraction in 1912. *Ann. Phys. (Berlin)* **524,** A83–A85 (2012).

5. Bragg, W. L. The Diffraction of Short Electromagnetic Waves by a Crystal. *Proceedings of the Cambridge Philosophical Society* **17,** 43–57 (1913).

6. Kelly, A. & Groves, G. W. *Crystallography and Crystal Defects* (Longman Group Limited, 1970).

7. Rahman, K., Khan, A., Muhammad, N. M., Jo, J. & Choi, K.-H. Fine-resolution patterning of copper nanoparticles through electrohydrodynamic jet printing. *J. Micromech. Microeng.* **22,** 1–8 (2012).

8. Cullity, B. D. & Stock, S. R. *Elements of X-Ray Diffraction* 3rd ed. 664 pp. (Prentice Hall, 2001).

9. Greenwood, N. N. & Earnshaw, A. *Chemistry of the Elements* 2nd ed. (Butterworth-Heinemann, 1998).

10. *ANSI/IEEE 176-1987, IEEE Standard on Piezoelectricity* (IEEE, New York, 1987).

11. Kittel, C. *Introduction to Solid State Physics* 8th ed. (John Wiley & Sons Ltd, 2005).

12. Jaffe, B., Cook, W. R. & Jaffe, H. *Piezoelectric Ceramics* 1st ed. 317 pp. (Academic Press, New York, 1971).

13. Goldschmidt, V. M. Die Gesetze der Krystallochemie. **21,** 471–485 (1926).

14. Glazer, A. Classification of Tilted Octahedra in Perovskites. *Acta Crystallogr. Sect. B* **28,** 3384–3392 (1972).

15. Glazer, A. Simple Ways of Determining Perovskite Structures. *Acta Crystallogr. Sect. A* **31,** 756–762 (1975).

16. Halliyal, A., Gururaja, T., Kumar, U. & Safari, A. in *Applications of Ferroelectrics* Sixth IEEE International Symposium. **437** (IEEE, 1986).

17. Smyth, D. M. *The Defect Chemistry of Metal Oxides* (Oxford University Press, 2000).

18. Moulson, A. J. & Herbert, J. M. *Electroceramics* 2nd ed. (John Wiley & Sons Ltd, 2003).

19. Tilley, R. *Understanding Solids* (John Wiley & Sons Ltd, 2004).

20. Steinsvik, S., Bugge, R., GjØnnes, J., TaftØ, J. & Norby, T. The Defect Structure of $SrTi_{1-x}Fe_xO_{3-y}$ (x = 0-0.8) Investigated by Electrical Conductivity Measurements and Electron Energy Loss Spectroscopy (EELS). *J Phys Chem Solids* **58,** 969–976 (1997).

21. Suzuki, K. & Kijima, K. Optical Band Gap of Barium Titanate Nanoparticles Prepared by RF-plasma Chemical Vapor Deposition. *Jpn. J. Appl. Phys.* **44,** 2081–2082 (2005).

22. Nye, J. F. *Physical Properties of Crystals: Their Representation by Tensors and Matrices* (Oxford University Press, 1985).

23. Kulcsar, F. Electromechanical Properties of Lead Titanate Zirconate Ceramics Modified with Certain Three- or Five-VaIent Additions. *J. Am. Ceram. Soc.* **42,** 343–349 (1959).

24. Welberry, T. R., Goossens, D. J., Withers, R. L. & Baba-Kishi, K. Z. Monte Carlo Simulation Study of Diffuse Scattering in PZT, $Pb(Zr,Ti)O_3$. *Metall Mater Trans A* **41A,** 1110–1118 (May 2010).

25. Pecharsky, V. K. & Zavalij, P. Y. *Fundamentals of Powder Diffraction and Structure Characterization of Materials* 2nd ed. (Springer Science+Business Media, LLC, 2009).

26. Devonshire, A. F. Theory of Ferroelectrics. *Adv. Phys.* **3,** 86–130 (1954).

27. Whatmore, R. W. Pyroelectric devices and materials. *Rep. Prog. Phys.* **49,** 1335–1386 (1986).

28. Lang, S. B. Pyroelectricity: From Ancient Curiosity to Modern Imaging Tool. *Physics Today* **58,** 32–36 (2005).

29. Naranjo, B., Gimzewski, J. K. & Putterman, S. Observation of nuclear fusion driven by a pyroelectric crystal. *Nature* **434,** 1115–1117 (2005).

30. Kochervinskii, V. V. Piezoelectricity in Crystallizing Ferroelectric Polymers: Poly(vinylidene fluoride) and Its Copolymers (A Review). *Crystallography Reports* **48,** 649–675 (2003).

31. Haertling, G. H. Ferroelectric Ceramics: History and Technology. *J. Am. Ceram. Soc.* **82,** 797–818 (1999).

32. Valasek, J. Piezo-Electric and Allied Phenomena in Rochelle Salt. *Phys. Rev.* **17,** 475–481 (1921).

33. Jaffe, H. Piezoelectric Ceramics. *J. Am. Ceram. Soc.* **41,** 494–498 (11 1958).

34. Heitmann, A. A. & Rossetti Jr., G. A. Thermodynamics of Ferroelectric Solid Solutions with Morphotropic Phase Boundaries. *Adv. Phys.* **3,** 86–130 (1954).

35. Damjanovic, D. Ferroelectric, dielectric and piezoelectric properties of ferroelectric thin films and ceramics. *Rep. Prog. Phys.* **61,** 1267–1324 (1998).

36. Blinc, R. & Žekš, B. *Soft Modes in Ferroelectrics and Antiferroelectrics* 1st (North-Holland Publishing Company, 1974).

37. Chandra, P. & Littlewood, P. B. in *Physics of Ferroelectrics: A Modern Perspective* (eds Rabe, K. M., Ahn, C. H. & Triscone, J.-M.) chap. A Landau Primer for Ferroelectrics (Springer Publishing Company, New York City, NY, USA, 2007).

38. Jin, L., Li, F. & Zhang, S. Decoding the Fingerprint of Ferroelectric Loops: Comprehension of the Material Properties and Structures. *J. Am. Ceram. Soc.* **97,** 1–27 (1 2013).

39. Patterson, E. *Development. Characterization. and Piezoelectric Fatigue Behavior of Lead-Free Perovskite Piezoelectric Ceramics* PhD thesis (Oregon State University, 2012).

40. Damjanovic, D. & Demartin, M. The Rayleigh law in piezoelectric ceramics. *J. Phys. D: Appl. Phys.* **29,** 2057–2060 (1996).

41. Damjanovic, D. Stress and frequency dependence of the direct piezoelectric effect in ferroelectric ceramics. *J. Appl. Phys.* **82,** 1788–1797 (1997).

42. Jin, L., Porokhonskyy, V. & Damjanovic, D. Domain wall contributions in Pb(Zr, Ti)O_3 ceramics at morphotropic phase boundary: A study of dielectric dispersion. *Appl. Phys. Lett.* **96,** (2010).

43. Balke, N., Lupascu, D. C., Granzow, T. & Rödel, J. Fatigue of Lead Zirconate Titanate Ceramics. I: Unipolar and DC Loading. *J. Am. Ceram. Soc.* **90,** 1081–1087 (2007).

44. Balke, N., Lupascu, D. C., Granzow, T. & Rödel, J. Fatigue of Lead Zirconate Titanate Ceramics II: Sesquipolar Loading. *J. Am. Ceram. Soc.* **90,** 1088–1093 (2007).

45. Lupascu, D. C. *Fatigue in Ferroelectric Ceramics and Related Issues Materials Science* **61** (Springer, 2004).

46. Ashcroft, N. W. & Mermin, N. D. *Solid State Physics* (Saunders College Publishing, 1976).

47. Landau, L. On the Theory of Phase Transitions. *Zh. Eksp. Teor. Fiz.* **7,** 19–32 (1937).

48. Kittel, C. Theory of Antiferroelectric Crystals. *Phys. Rev.* **82,** 729–732 (1951).

49. Jiang, A. Q., Lin, Y. Y., Tang, T. A. & Zhang, Q. Asymmetry of domain forward switching and multilevel relaxation times of domain backswitching in antiferroelectric $Pb_{0.99}Nb_{0.02}(Zr_{0.84}Sn_{0.12}Ti_{0.04})_{0.98}O_3$ thin films. *Appl. Phys. Lett.* **90,** (2007).

50. Smolenskii, G. A., Isupov, V. A., Agranovskaya, A. I. & Popov, S. N. Ferroelectrics with Diffuse Phase Transitions. *Sov. Phys. Solid State* **2,** 2584–2594 (1961).

51. Shvartsman, V. V. & Lupascu, D. C. Lead-Free Relaxor Ferroelectrics. *J. Am. Ceram. Soc.* **95,** 1–26 (2012).

52. Kumar, N. & Cann, D. P. Electromechanical strain and bipolar fatigue in $Bi(Mg_{1/2}Ti_{1/2})O_3$-$(Bi_{1/2}Na_{1/2})TiO_3$-$(Bi_{1/2}K_{1/2})TiO_3$ ceramics. *J. Appl. Phys.* **114,** (2013).

53. Yamakawa, K., Gachigi, K. W., Trolier-McKinstry, S. & Dougherty, J. P. Structural and electrical properties of antiferroelectric lead zirconate thin films prepared by reactive magnetron co-sputtering. *J. Mater. Sci.* **32,** 5169–5176 (1997).

3 Literature Review of Piezoelectric Solid Solutions and their Applications

3.1 Introduction

This chapter will be a broad review of various topics in piezoelectric solid solution ceramics beginning with barium titanate, then PZT and PT-BS, other high temperature binary and ternary solid solutions, Pb-free solid solutions, and device applications of these ceramics. The overarching theme is development of ceramic materials with high T_C or T_d with excellent piezoelectric properties. Additionally, materials with high electromechanical coupling are described and some of the correlations used to predict MPB compositions are discussed.

3.2 Barium Titanate

Developed during the early 1940's [1, 2], $BaTiO_3$ was one of the first materials where ferroelectricity was observed partly due to its large coupling factor (k_{33} = 0.560 [3]) and its high permittivity ($\epsilon_r \approx$ 2000 - 10000) [4] relative to other piezoelectric materials [5]. The simplicity of the crystal structure and easily accessible transition temperatures also make $BaTiO_3$ an ideal material to characterize and model. Barium titanate takes the form of a perovskite ceramic with a tolerance factor of t = 1.06 and an electronegativity of ΔEN = -2.23 both indicating a stable and tetragonal perovskite. The ceramic is tetragonal over the temperature range (0 ^oC - 130 ^oC) [4, 5]. Above 130 ^oC, the Curie temperature, $BaTiO_3$ is in a paraelectric cubic phase. Below 0 ^oC, $BaTiO_3$ transforms into an orthorhombic phase and below -90 ^oC, $BaTiO_3$ transforms into a rhombohedral phase [4, 5]. The three polymorphs below T_C, are all ferroelectric and shown in Fig. 3.1 [4].

As stated earlier, the simple structure of $BaTiO_3$ led to a large volume of research in the dielectric and piezoelectric properties of unmodified and doped $BaTiO_3$.

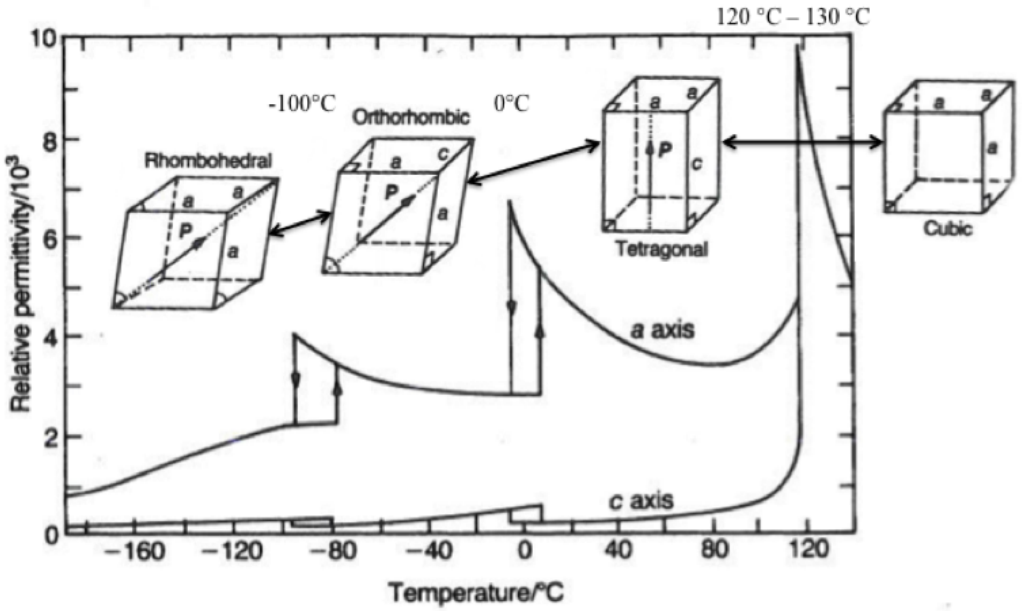

FIGURE 3.1: Relative permittivity in $BaTiO_3$ with inserted unit cells corresponding to different temperature ranges. Phase diagram of $BaTiO_3$ after [6]. Unit cell insets after [4] inserted, with permission, from A. J. Moulson and J. M. Herbert; Electroceramics: Materials, Properties, Applications, 2nd Edition; John Wiley and Sons; copyright © (2003), John Wiley and Sons.

The defect chemistry of $BaTiO_3$ is important to understand due to the use of $BaTiO_3$ in a variety of applications and the relative simplicity of the material compared to other perovskites like lead zirconate titanate (PZT). After normal processing conditions, i.e. in air, un-doped $BaTiO_3$ is a lightly colored insulator used as a capacitor. However, if processed in a low oxygen atmosphere, the ceramic is a semiconductor [7]. Equations 3.1 and 3.2 show the defect chemistry that low and high oxygen levels have respectively on $BaTiO_3$ [7],

$$O_O \iff 1/2O_2 + V_O^{\bullet\bullet} + 2e' \tag{3.1}$$

$$1/2O_2 + V_O^{\bullet\bullet} \iff O_O + 2h^{\bullet} \tag{3.2}$$

where *e* and *h* represent electrons and holes, respectively.

Equation 3.2 suggests that un-doped $BaTiO_3$ is already prone to non-stoichiometry and appears as an acceptor-doped material. Equation 3.1 is an example of reduction leading to conduction while Equation 3.2 shows oxidation (the filling of the oxygen vacancies) and leads to insulation. Despite the widespread use of $BaTiO_3$ and its decent piezoelectric properties, the ceramic's low Curie temperature restricts its application to just above the boiling point of water. Fortunately, soon after the discovery of $BaTiO_3$ came the development of PZT.

3.3 Lead Zirconate Titanate

Although $BaTiO_3$ was discovered a decade before PZT, the Pb-based piezoceramic commands a higher percentage of the piezoelectric market than $BaTiO_3$ or any other piezoelectric materials.[6] This is because of its high transition temperature, $T_C \approx$ 370 ^oC, high piezoelectric coefficient of d_{33} = 500 pC/N [5] and transverse piezoelectric coefficient of d_{31} = -100 pC/N, and is a prototypical MPB solid solution. Lead zirconate titanate, first reported in the middle of the 20^{th} century, is a binary solid solution system of $PbTiO_3$ (PT) and $PbZrO_3$ (PZ). The mechanical Q factor and frequency constant both increase with decreasing temperature while the piezoelectric coupling and dielectric constant decrease with decreasing temperature [9].

To access high piezoelectric properties and electromechanical coupling, PZT ceramics must be properly poled, freshly sintered PZT ceramics are not piezoelectric. Only after poling does PZT acquire its piezoelectric and ferroelectric characteristics.

[6] Lead zirconate titanate makes up nearly 98% of the piezoelectric actuator and motor market worth nearly $12.8 billion annually [8].

The MPB in PZT is also nearly independent with temperature, except at high temperatures, therefore the ferroelectric phase of PZT remains up to the relatively high T_C of approximately 370 ^oC. In addition to the tetragonal and rhombohedral phases in the MPB composition, recent studies have shown a monoclinic phase. The exact nature of the interaction between the three phases at the MPB is unknown; however, it has been suggested that the monoclinic phase provides a bridge for the transition of domains from the higher symmetry *P4mm* to the lower *R3c* rhombohedral symmetry. Compositions of MPB solid solutions are a continuing focus of research to find high performing materials like PZT.

Looking back to Fig. 2.10, in the phase diagram of PZT at high temperatures, PZT ceramics are in the paraelectric cubic phase (*m3m*). Cooling below T_C, the crystal structure in the PT-rich side is tetragonal (*P4mm*) and piezoelectric with $T_C \approx 490\ ^oC$, while PZ is an anti-ferroelectric orthorhombic phase (*mmm*), a state that is maintained up to ≈ 8 mol% PZ. In between the PT-rich tetragonal phase and the PZ-rich orthorhombic phase lies a rhombohedral phase (*R3m*). Below room temperature, no phase changes are observed down to liquid helium temperatures. Above room temperature and at the MPB composition, a nearly vertical phase boundary exists between the tetragonal and rhombohedral phases.

For a long time, it was thought that only the tetragonal and rhombohedral phases existed in this small region; however, recent work on PZT revealed two structures with the same monoclinic phase [8, 10]. It is not entirely known how or why these phases exist; however, it has been speculated that the monoclinic phase aids in the transition between the tetragonal and rhombohedral phases [11]. Ballaiche *et al.* proposed a mechanism for the high piezoelectric properties in PZT (later called the polarization-rotation model) where the mirror plane of the monoclinic phase allows Pb cations to displace in any orientation allowed by the monoclinic phase [12]. Evidence for this model was published by Guo *et al.* using high resolution synchrotron x-ray powder diffraction of PZT ceramics [13]. Another model proposed

domain wall movement as the principle component of the piezoelectric response [14]. More recent work from pair distribution function (PDF) fitting to neutron diffraction data, showed the existence of two monoclinic structures, labelled by Zhang *et al.* as M_A and M_B. Both structure share the same monoclinic phase, *Cm*. The only difference is in the effects on Pb displacements. In the M_A structure, Pb cations have more room to displace as compared to the monoclinic M_B [8]. The study performed by Zhang *et al.* explored the complex local structure of PZT.

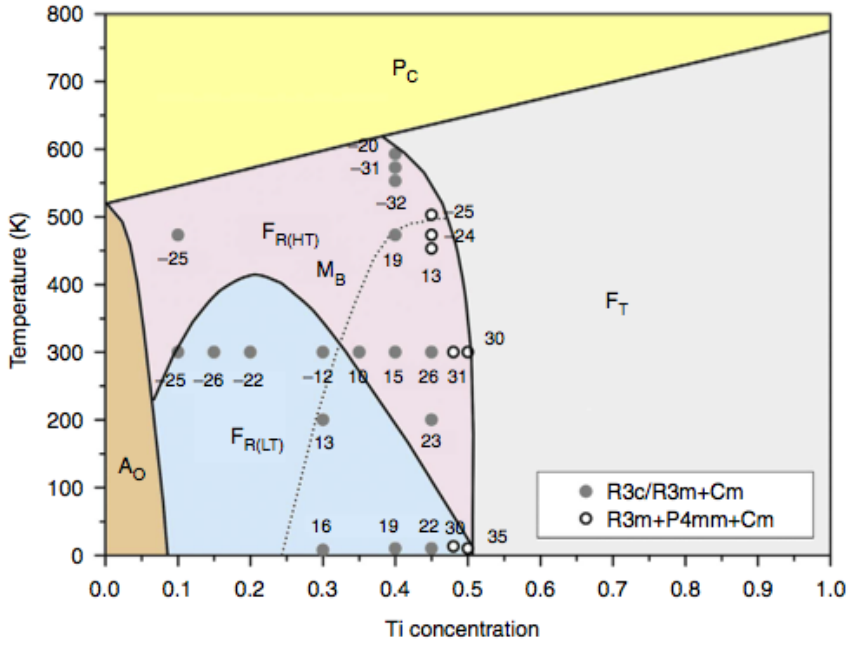

FIGURE 3.2: Updated phase diagram of the PZT perovskite system including two monoclinic structures, the transition between the two structures and rhombohedral compositions tested. Reprinted by permission from Macmillan Publishers Ltd: Journal Communications [8], copyright © (2014) Nature Publishing Group, Nature Communications website.

Other recent work on thin films of PZT used in micro-electromechanical systems (MEMS) for energy harvesting cantilevers, non-volatile memories already mentioned

with FeRAM, micro-actuators, etc. Although implementation has been delayed due to problems integrating PZT with silicon in circuit architecture, i.e. PZT of high quality cannot be grown directly on silicon. Recent advances in PZT MEMS show decent piezoelectric and dielectric properties as compared to other dielectrics and bulk PZT [15]. Although these properties are relatively low compared to bulk PZT values, the electric fields needed for device operation are very low, on the order of most circuit voltages making these thin films ideal for circuit applications.

In bulk ceramic materials, lead vacancies are created in normally processed, undoped PZT, i.e. via the standard solid-state reaction method. This Pb loss is due to Pb volatility around 700 ^{o}C, a temperature normally below the calcination temperature for most Pb-based electronic ceramics. These Pb vacancies, because of electrical neutrality, must be balanced by two positive charges (holes) as Pb cations have a valence of 2+. Lead deficient PZT is a p-type semiconductor in which electrical resistivity decreases as oxygen partial pressure increases during calcining. In contrast, when donor dopants are added, electrical resistivity increases. Thermoelectric measurements on PZT gives a positive Seebeck coefficient [16]. It was also shown that doping of PZT with donor cations did not affect the conductivity type despite improving the resistivity.

As a general rule, replacing a parent atom with more than 5 at% of another cation is considered a solid solution while less than 5 at% is doping. Doping either the A-site or B-site with an acceptor cation gives "hard" PZT, which compared to undoped PZT, exhibits lower piezoelectric coefficients, lower dielectric permittivities but also lower losses, lower resistivity, lower elastic compliance, and higher transition temperatures. Doping with a donor cation results in "soft" PZT, which has much higher piezoelectric coefficients, higher dielectric permittivity and higher loss, improved poling and depoling conditions, and higher resistivity. Table 3.1 lists the properties of undoped, hard and soft PZT, $BaTiO_3$, and $PbTiO_3$. An example of hard PZT is PZT-4 used for high power actuation applications. Examples of soft PZT

include PZT-5A and PZT-5H, which are used in sensor applications.

TABLE 3.1: Table of density, Curie temperature, and dielectric data of $BaTiO_3$ compared to PZT, both undoped and doped and MPB PT-BS.

Composition	Density [g/cm^3]	T_C [^{o}C]	K	tan δ	Ref.
$BaTiO_3$	5.7	115	1700	0.5	[2]
PZT (48-52) undoped	-	386	750	0.4	[5]
PZT-4	7.5	328	1300	0.4	[2]
PZT-5A	7.8	365	1700	2.0	[2]
PZT-5H	7.5	193	3400	4.0	[2]
$PbTiO_3$	7.5	470	190	-	[17]
PT-BS (64-46)	7.6	450	2000	2.5	[18, 19]

TABLE 3.2: Table of electromechanical properties of $BaTiO_3$ compared to PZT, both undoped and doped and MPB PT-BS.

Composition	k_p	k_{33}	d_{33} [pC/N]	d_{31} [pC/N]	S_{11}^E [x10^{-12} m^2/N]	Ref.
$BaTiO_3$	0.36	0.50	190	-78	9.1	[2]
PZT (48-52) undoped	0.52	0.67	223	-93	13.8	[5]
PZT-4	0.58	0.70	289	-123	12.3	[2]
PZT-5A	0.60	0.71	374	-171	16.4	[2]
PZT-5H	0.65	0.75	593	-274	16.5	[2]
$PbTiO_3$	-	-	56	-	-	[17]
PT-BS (64-46)	0.56	-	460	-	-	[18, 19]

Despite the high performance of PZT ceramics and the extensive work on understanding the phenomenological and microscopic mechanisms for the piezoelectric response, the material has its limits. First, it contains Pb which is toxic and governments around the world are increasingly placing restrictions on commercial products containing Pb. Lead zirconate titanate is also very susceptible to electrical fatigue, or the irreversible change to the domain state of the piezoelectric. Finally, the relatively low maximum operating temperatures of PZT make the material undesirable for some high temperature applications, principally actuator devices.

3.4 Lead Titanate - Bismuth Scandate (PT-BS)

High-temperature (piezoceramics with $T_C > 400^oC$) piezoelectric sensors and actuators are of interest for a variety of different applications ranging from commercial turbine engines to deep-sea drilling and interplanetary probes. Extreme environments such as the surface of Venus, with temperatures in excess of 400 ^oC, require materials that maintain a polarization state to function as designed. Due to weight or size restrictions, cooling systems for these functional materials may not be possible. Therefore, finding piezoelectric materials with higher transition temperatures and materials that performs as intended under extreme conditions is an important engineering goal. Ferroelectric ceramics based on PT, like PZT, have been widely used as high-temperature piezoelectric sensors and actuators due to their excellent dielectric properties and large piezoelectric coefficients up to relatively high transition temperatures (both Curie temperature (T_C) and depolarization temperature (T_D)). Unfortunately, the maximum operating temperature of PZT is approximately 150 ^oC - 180 ^oC [20], well below the Curie point. Therefore, the focus in this section is on piezoelectric materials with higher transition temperatures and comparable piezoelectric properties to PZT.

The tolerance factor from Sec. 2.3, stated in Equation 2.4, was used to formulate

potential alternatives to PZT [21]. It was found that as the tolerance factor of the end-member in solid solution with PT decreased, T_C increased at the MPB composition as shown in 3.4. It was also found that Bi-based perovskites generally exhibited lower tolerance factors than Pb containing perovskites. The addition of the smaller Bi^{3+} cation, which has a similar electronic structure to Pb^{2+}, results in a decrease in the tolerance factor. For these reasons, the solid solution of PT with a Bi-based perovskite end-member, $BiScO_3$, was predicted to have higher T_C than PZT or other Pb-based binary solid solutions. Eitel *et al.* developed the solid solution $PbTiO_3$-$BiScO_3$ (PT-BS) [21], and a host of other binary solid solutions with PT, as potential alternatives to PZT. From investigation of the tolerance factor with respect to the T_C at the MPB composition, it was found that PT-BS had a $t \approx 0.980$ and a $T_C = 450\ ^oC$. These findings prompted further investigation of PT-BS, a solid solution of tetragonal PT and rhombohedral BS. At the MPB composition (≈ 64 % PT): large values of d_{33}, k_p, and P_r were observed, similar to values for PZT [21]. The solid solution PT-BS solved two problems associated with PZT: reducing the amount of lead in solution and exhibiting a $T_C > 400\ ^oC$ as well as exhibiting piezoelectric coefficients larger than undoped PZT ($d_{33} \approx 500$ pC/N).

Over the next decade, further research into PT-BS was conducted. Eitel *et al.* studied grain morphology and dielectric, piezoelectric, and electromechanical properties and confirmed the MPB composition as 64 % PT with $T_C = 450\ ^oC$, $d_{33} = 450$ pC/N, $d_{33}^* = 700$ pm/V, and $k_p = 0.56$ [23]. It was also shown that PT-BS ceramics sintered at 1200 ^oC led to denser ceramics as opposed to pellets sintered at lower temperatures. Using percolation theory, Shimojo *et. al.* argued that the dielectric performance of PT-BS ceramics (where PT content ranged from 60 % to 80 %) was related to the growth of ScO_6 octahedrons in a network of TiO_6 octahedrons, i.e. ScO_6 octahedrons are initially isolated at high PT content, but as the PT content decreases, ScO_6 octahedrons percolate linkages causing disorder in the system around the MPB region [43, 44]. Single crystals of PT-BS composition (57/43) were produced by Zhang

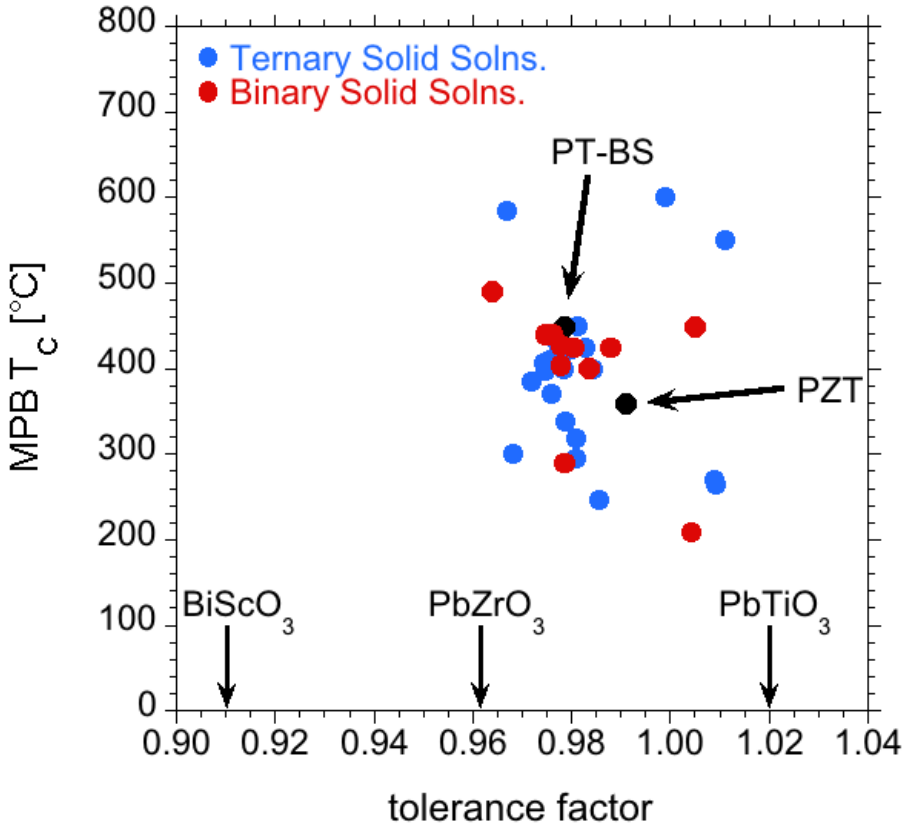

FIGURE 3.3: Tolerance factor of binary (red dots) solid solutions [5, 19, 21–33] and ternary (blue dots) solid solutions [34–42] versus the Curie temperature of the MPB compositions of represented solid solutions. The solid solutions for the MPB compositions of PT-BS and PZT are in black and the tolerance factors of the end-members: PT, PZ, and BS are arrowed at the bottom.

et al. with d_{33} = 1200 pC/N at room temperature, T_C = 404 °C, and $k_{33} \approx 90$ % [45]. The phase diagram of the PT-BS system was developed from dielectric data [18, 43], calorimetry data [18], single crystal data and tilt transition data [18].

What will be seen in later chapters is a trend of searching for MPB compositions in solid solutions with PT. There is, in PT-based solid solutions, a tetragonal phase that exists in high PT-content compositions identified by x-ray diffraction and dielectric

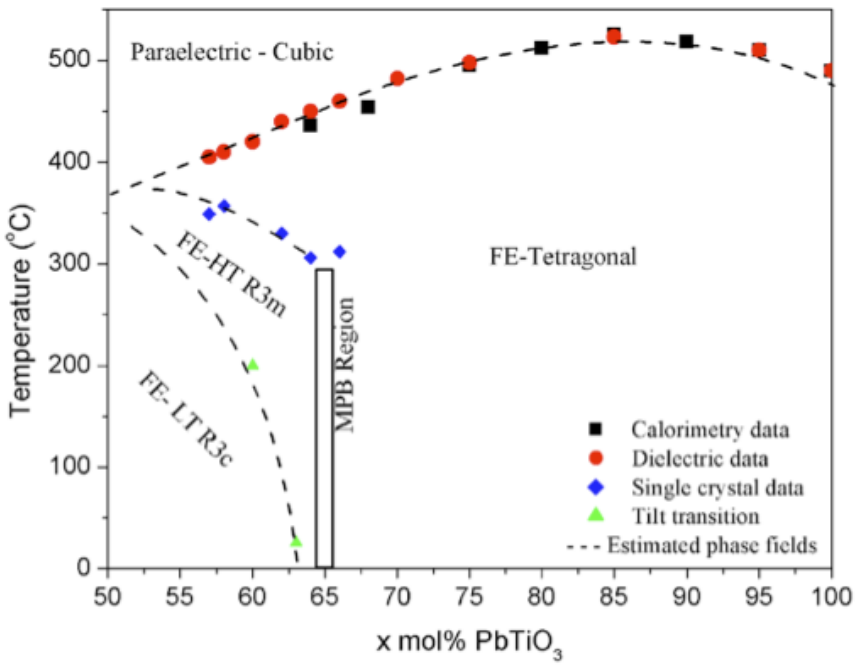

FIGURE 3.4: Phase diagram of the PT-BS perovskite solid solutions. Reprinted with permission from R.E. Eitel *et al.*, Journal of Applied Physics, 96 [5], 2828-2831 (2004). Copyright © (2004) AIP Publishing LLC.

permittivity. This tetragonal phase is identified by peak splitting of the *(100)*, *(110)*, and *(200)* peaks. This peak splitting disappears as the amount of PT decreases. The same is true in the PT-BS system [21]. An MPB region separates the high PT content tetragonal (*P4mm*) phase region from a ferroelectric rhombohedral (*R3m*). From in-situ TEM data, another rhombohedral phase is observed (*R3c*) in compositions with 50 - 60 % PT. This lower PT content rhombohedral phase is a result of anti-phase octahedral tilting in the oxygen octahedra of the perovskite structure [18, 46]. The tilting is $a^-a^-a^-$ and identified through the intensity of a superlattice peak [18] and is observed in compositions up to ≈ 63% PT at room temperature. As the PT content increases, a transition is observed between the two rhombohedral phases by the decrease and disappearance of the superlattice peak indicating a loss in octahedral

tilting. This octahedral tilting is observed in a number of other PT-based piezoelectric solid solutions to include: PT-BF, PT-BFS, PT-BMT, and PZT [47]. Despite the excellent properties of PT-BS, Sc_2O_3 (one of the components of PT-BS) is very expensive, what follows is a look at other PT-based high temperature piezoelectric solid solutions without scandium.

3.5 Other High-Temperature Piezoelectric Solid Solutions

3.5.1 Correlations

The work of Eitel *et al.* showed the correlation between the tolerance factor and the Curie temperature of the MPB composition of solid solutions with PT. Another potential correlation was found between the molecular mass difference between A-O bonds and B-O bonds. The larger the difference, the higher the value of the electromechanical coupling [48]. Lead zirconate titanate MPB composition has a measured k_p of ≈ 0.7 and a mass difference of ≈ 136 g/mol. Yamashita *et al.* used the trend to predict two materials: $Pb[(Al_{0.5}Nb_{0.5})_{1-x}Ti_x]O_3$ (PANT) and $Pb[(Ga_{0.5}Nb_{0.5})_{1-x}Ti_x]O_3$ (PGNT) with k_p higher than PZT [48]. Unfortunately, producing these materials was difficult due to the refractoriness of Al_2O_3, Ga_2O_3, and Nb_2O_5. Bismuth bearing solid solutions are also shown to not obey the trend despite the similarity in ionic masses of Pb and Bi.

Electronegativity difference is briefly discussed in the previous chapter; however, information given is complimentary to tolerance factor in that both factors give information on phase and stability. Tetragonal materials have a larger ΔEN difference than rhombohedral materials. Perhaps a better way of finding excellent piezoelectric materials is by calculating c/a ratio. The c/a ratio is the ratio between the c and a lattice parameters of a tetragonal crystal unit cell. Those compositions with a c/a ration close to 1 are MPB compositions as the rhombohedral crystal structure has only one lattice parameter, a. So, calculating the useful correlations, tolerance factor

and the c/a ratio, directs effort towards potential MPB compositions of solid solutions with potentially excellent piezoelectric properties. In the next section, a number of binary solid solutions and properties of MPB compositions is discussed.

3.5.2 High-Temperature Binary Solid Solutions

Taking the general formula of $PbTiO_3$-$Bi(M^{3+})O_3$, where M^{3+} are trivalent B-site metal cations, a number of solid solutions have been developed. The solid solution of (*R3c*) rhombohedral bismuth ferrite (BF) and (*P4mm*) PT leads to the MPB PT-BF, where the MPB is found at compositions between 27 and 34% PT. Still, because of conductive losses, poling of PT-BF is difficult [49]. Another concern in PT-BF is the high c/a ratio, an indicator of the degree of tetragonality in the crystal structure. From a practical standpoint a higher c/a ratio results in increased difficulty in poling. Manganese oxide was investigated as a potential dopant in PT-BMn, but with frustration due to the Jahn-Teller effect of Mn^{3+} ion in an octahedral environment, only a pseudo-cubic structure was observed. Additionally, a high conductivity precluded the possibility for poling and ferroelectricity [29].

For solid solutions with the formula PT-BMe, with all trivalent ions for Me such as Ga, In, Yb, La, and Al ions, only Sc^{3+} appears to produce excellent ferroelectric properties. For the majority of PT-based piezoceramics, limitations in the solid solubility inhibits the formation of MPB compositions from being observed such as in PT-BGa. In other cases like with Fe and Mn, conductive losses inhibit effective poling of these piezoceramics. Another class of solid solutions was developed to take advantage of ferroelectrically active cations with valences other than three and as will be seen, greater success in obtaining stable, insulating ferroelectric ceramics.

Piezoelectric ceramics with the formula $PbTiO_3$-$Bi(B'B'')O_3$, where B' and B'' are metal cations with different valences, constitute another class of piezoceramics. Many metal cations with a net charge of 3+ are available to create different solid solutions based on this formula. Many such solid solutions have been investigated

over the past decade. Commonly cited systems include: $PbTiO_3$-$Bi(Zn_{1/2}Ti_{1/2})O_3$ (PT-BZT) [27], $PbTiO_3$-$Bi(Mg_{1/2}Ti_{1/2})O_3$ (PT-BMT) [25], and $PbTiO_3$-$Bi(Ni_{1/2}Ti_{1/2})O_3$ (PT-BNiT) [32], where the Ti^{4+} cations occupy half of the octahedral sites shared with the second cation (Zn, Mg, Ni) all in the 2+ valence state. Phase transitions were found in PT-BMT and PT-BNiT with an increase in tetragonality with decreasing PT content; however no MPB was observed in PT-BZT resulting in values of T_C as high as 700 ^oC [27]. Many other binary complex systems have been studied and their tolerance factors and T_C are schematically shown in Fig. 3.4 (based on data from references [5, 17, 25, 27, 29, 31, 32, 49–51]).

Many other PT-based solid solutions have been investigated; however, none have surpassed the piezoelectric properties of PT-BS or PZT in terms of d_{33}, k_{33}, and T_C. Current work is focused on doping, modification, and processing methods of PT-BS and PZT to improve properties. Concurrently, other work is focused on developing new ternary solid solutions based on PT-BS and PZT.

3.5.3 High-Temperature Ternary Solid Solutions

A number of ternary high-temperature piezoelectric solid solutions are based on PT-BS with the addition of a third perovskite end member. These ternaries include PT-BS-BZT [52], PT-BS-BMT [52], PT-BS-BNiT [53–55], PT-BS-$(Ba,Sr)TiO_3$ [39], PT-BS-$Bi(Zn_{1/2}Zr_{1/2})O_3$ (PT-BS-BZZ) [36, 37], and the quaternary PT-BS-BMT-BF [40]. Other ternary compositions with scandium completely removed such as PT-BZT-BMT [35] were less successful in terms of piezoelectric performance.

This thesis covers the first several ternary systems just mentioned. In PT-BS-$(Ba,Sr)TiO_3$, increasing both barium and strontium content shifted the MPB to higher PT content. The dielectric and piezoelectric properties decreased as the MPB was shifted. The Curie temperature also decreased with increasing tetragonality and increasing barium and strontium content. Because of the increasing complexity of the system, i.e. increasing amount of metal cations, diffuse phase transitions were

observed with increasing barium and strontium content. Compared to Pb-based relaxor systems with complex B-sites; however, the T_m in this system was high [39]. Kowalski *et al.* showed in the PT-BS-BZZ system with compositions close to the MPB of the PT-BS binary, small additions of BZZ (2.5 wt %) increased room temperature d_{33} up to 520 pC/N with T_C = 430 °C and T_d = 394 °C. Also observed, was gradual increase in the diffuseness of the system with increasing BZZ content [37]. In the quaternary system PT-BS-BMT-BF, lower piezoelectric properties and electromechanical coupling was observed compared to PT-BS and the other ternary systems mentioned. Compositions possessing the highest properties were observed at lower PT-content meaning less Pb in decent piezoelectric ceramics [40]. In the PT-BZT-BMT system, low remanent polarization was observed in as-sintered samples. Upon reheating and subsequent quenching, remanent polarization and strain was observed [35]. Some other ternary systems include: PT-PZ-BNiT with diffuse phase transitions, high d_{33}, and T_C < 400 °C [41]; the solid solution of PT-BF and $BaZrO_3$ with a maximum d_{33} of 270 pC/N, T_C = 270 °C, $T_d \approx$ 150 °C, and wide range of compositions with anti-ferroelectric properties in temperatures between T_C and T_d [42]; and the PT-$BiYbO_3$-$Pb(Zn_{1/3}Nb_{2/3})O_3$ system with $T_C \approx$ 400 °C and d_{33} = 80 pC/N [38]. Figure 3.5 is a plot d_{33} with MPB Curie temperature for both binary and ternary compositions previously referred to in this chapter and some high T_C bismuth layered ceramics for comparison [56–58].

In Figure 3.5, there is trend in that the room temperature d_{33} decreases exponentially with an increase in temperature. Materials based on PT with a lower T_C were modified compositionally to obtain high dielectric constants and, as a result, high piezoelectric coefficients. This comes at the cost of polarization instability at a lower temperature [59]. For most of these ternary systems, piezoelectric coefficient decreased, T_C decreased, $T_d \neq T_C$, diffuse phase transitions were observed, and as the complexity of compositions increased, i.e. the number of metal cations increased, the diffuseness in phase transition increased in addition to a separation between T_C

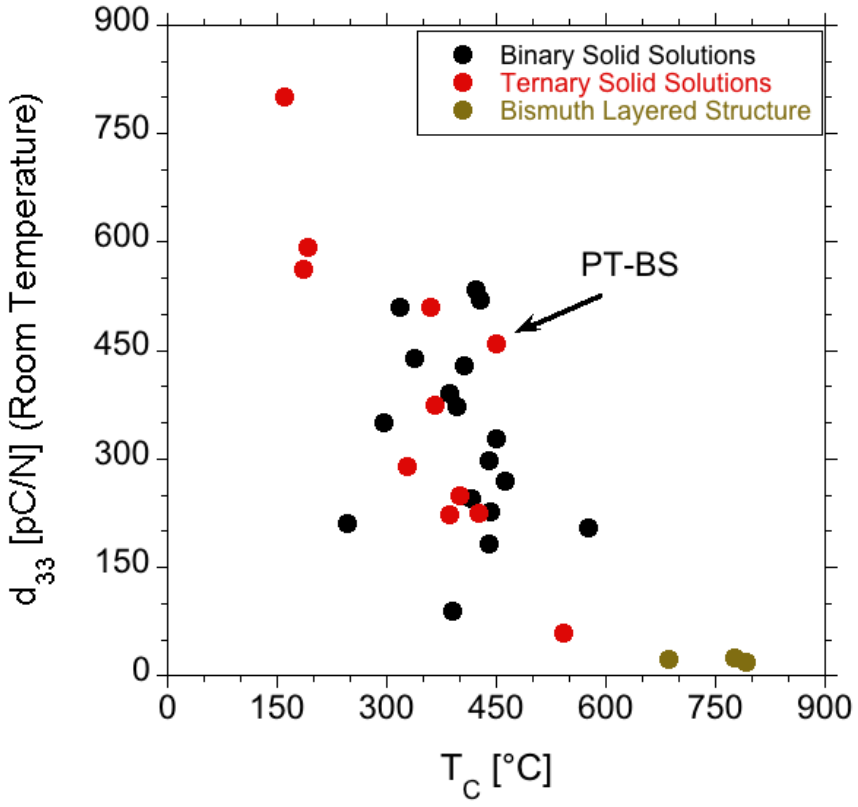

FIGURE 3.5: Room temperature piezoelectric coefficient versus T_C of binary, ternary, and bismuth layered structure materials.

and T_d. These behaviors will be seen in the PT-BS-BZT, PT-BS-BMT, and PT-BS-BNiT systems. Piezoelectric properties generally increased with increasing temperature; however, because of the diffuse nature of the phase transitions in many of the more complex systems, d_{33} often drops off before T_C. In fact, one definition of T_d is the temperature at the inflection point of the downward slope in d_{33} (T_d marked as red line in Fig. 3.6) with temperature [60]. It is this upper most temperature which dictates the maximum operating temperature of piezoelectric actuators.

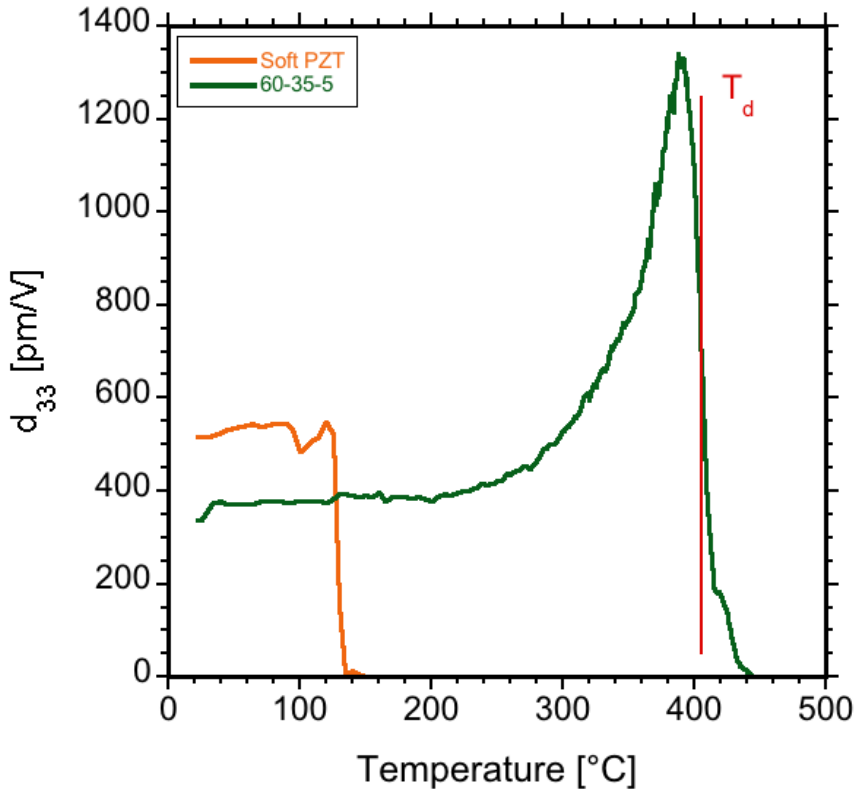

FIGURE 3.6: Depolarization temperature for 65PT-35BS-5BNiT marked by red line.

3.6 Pb-Free Piezoelectric Solid Solutions

Many Pb-free piezoelectric materials, e.g. $(Bi_{1/2}Na_{1/2})TiO_3$ (BNT)-based solid solutions, exhibit multiple dielectric anomalies associated with multiple events which may not necessarily be a phase transition. Many Pb-free materials are also relaxor ferroelectrics with the associated frequency dependent diffuse dielectric peaks. Some solid solutions, such as $(K_{1-x}Na_x)NbO_3$ (KNN), exhibit temperature dependent phase transition otherwise known as a polymorphic phase transition (PPT). For these reasons, researchers are not concerned with T_C so much as T_d, T_m, T_f, and T_B. Three primary Pb-free families of solid solutions have been extensively researched: $BaTiO_3$-based, KNN-based, and $(Bi_{1/2}Na_{1/2})TiO_3$ - $(Bi_{1/2}K_{1/2})TiO_3$ (BNT-BKT)-based solid solutions.

In barium titanate based solid-solutions, including BT-BNT, investigators have found a morphotropic phase boundary (MPB) [61] with compositions which exhibit respectable piezoelectric coefficients, high electromechanical coupling coefficients [62], and low dielectric loss with high permittivity [63]. Ongoing research in this system concerns the phase diagram of the MPB compositions and the behavior of a transition between an anti-ferroelectric phase and normal ferroelectric phase.

At room temperature in the KNN system, depending on composition, phases present are ferroelectric orthorhombic, monoclinic, or orthorhombic anti-ferroelectric (pure $NaNbO_3$) [64]. This system also contains several PPT zones separating phases with temperature not composition. In some undoped compositions of KNN, d_{33} values range from 80 - 160 pC/N [64–67]. Doping of ferroelectric compositions can improve the piezoelectric coefficient up to 300 pC/N [68]. Processing of this system however, is quite difficult due to highly volatile chemical species (Na_2CO_3 and K_2CO_3), poor densification, and chemical inhomogeneity [64]. So KNN is often seen in solid solution with other Pb-free systems such as $BaTiO_3$ or BNT-BKT.

In BNT-based systems, depolarization occurs at temperatures $T_d < 200\ ^oC$. Just above this temperature, a rhombohedral phase (*R3c*) transitions to a tetragonal phase (*P4bm*) between 200 and 320 ^oC often exhibited by a sharp and local increase in permittivity. Between 320 and 540 ^oC, the ceramic transitions to a high temperature cubic phase ($Pm\bar{3}m$) [64, 69]. For the solid solution of BNT-BKT, these piezoceramics have been extensively studied for their high temperature of maximum permittivity, T_m, relatively high piezoelectric properties [70], high coupling factors, and favorable dielectric properties all coinciding at a MPB of ≈ 16 - 20 % BKT [70]. Ternary compositions based on BNT-BKT have been developed here at OSU. Those solid solutions include either $Bi(Zn_{1/2},Ti_{1/2})O_3$ (BZT) in solution with BNT-BKT [71, 72], or $Bi(Mg_{1/2},Ti_{1/2})O_3$ (BMT) in solution with BNT-BKT [73, 74]. Both BZT-BNT-BKT and BMT-BNT-BKT ternary systems exhibited high field induced strain, low (or zero) electrical fatigue, and ergotic relaxor behavior [72, 73]. Because of the fatigue re-

sistance and high field induced strains, compositions of both ternary systems have shown promise as replacement materials for PZT in device applications.

3.7 Summary

This chapter covered various ferroelectric ceramic solid solutions including Pb-free systems. The Pb-free ceramics were included to highlight some of the high temperature piezoelectric ceramics, especially BNT-based systems. Still, the PT-based solid solutions exhibited the highest T_C and T_d and so are the materials of choice for high temperature actuator applications. Of the various PT-based solid solutions, PT-BS solid solutions exhibited the highest piezoelectric properties with the highest transition temperatures. With small additions of other perovskite end-members, systems like PT-BS-BZZ exhibited excellent properties with T_C = 430 ^oC. In general however, ternary solid solutions exhibited diffuse phase transitions with reduced piezoelectric coefficients as compared to PT-BS or PZT. In Chapters 5-8, three additional PT-based ternary solid solution systems will be explored. It will be shown that compositions close to pure PT-BS exhibit high T_C and high piezoelectric coefficients and that as the concentration of the three end-members come close to equality, the phase transition becomes more and more diffuse.

3.8 References

1. Thurnauer, H. Reflections. *Am Ceram Soc Bull* **56,** 861–866 (1977).
2. Haertling, G. H. Ferroelectric Ceramics: History and Technology. *J. Am. Ceram. Soc.* **82,** 797–818 (1999).
3. Bhattacharya, K. & Ravichandran, G. Ferroelectric perovskites for electromechanical actuation. *Acta Mater* **51,** 5941–5960 (2003).

4. Moulson, A. J. & Herbert, J. M. *Electroceramics* 2nd ed. (John Wiley & Sons Ltd, 2003).

5. Jaffe, B., Cook, W. R. & Jaffe, H. *Piezoelectric Ceramics* 1st ed. 317 pp. (Academic Press, New York, 1971).

6. Merz, W. J. The Electric and Optical Behavior of $BaTiO_3$ Single-Domain Crystals. *Phys. Rev.* **76,** 1221–1225 (8 1949).

7. Smyth, D. M. *The Defect Chemistry of Metal Oxides* (Oxford University Press, 2000).

8. Zhang, N. *et al.* The missing boundary in the phase diagram of $PbZr_{1-x}Ti_xO_3$. *Nat. Commun.* **5,** 5231–5239 (2014).

9. Gerson, R. Piezoelectric and Dielectric Properties of Lead Titanate Zirconate Ceramics at Low Temperatures. *J. Appl. Phys.* **33,** 830–832 (1962).

10. Noheda, B. *et al.* A monoclinic ferroelectric phase in the $Pb(Zr_{1-x}Ti_x)O_3$ solid solution. *Appl. Phys. Lett.* **74,** 2059–2061 (1999).

11. Noheda, B. Structure and high-piezoelectricity in lead oxide solid solutions. *Curr Opin Solid State Mater Sci* **6,** 27–34 (2002).

12. Ballaiche, L., García, A. & Vanderbilt, D. Finite-Temperature Properties of $Pb(Zr_{1-x}Ti_x)O_3$ Alloys from First Principles. *Phys. Rev. Lett.* **84,** 5427–5430 (2000).

13. Guo, R. *et al.* Origin of the High Piezoelectric Response in $PbZr12xTi_xO_3$. *Phys. Rev. Lett.* **84,** 5423–5426 (2000).

14. Jin, Y. M., Wang, Y., Khachaturyan, A. G., Li, J. F. & Viehland, D. Conformal miniaturization of domains with low domain-wall energy: monoclinic ferroelectric states near the morphotropic phase boundaries. *Phys. Rev. Lett.* **91,** 197601–1 (2003).

15. Muralt, P. PZT Thin Films for Microsensors and Actuators: Where Do We Stand? **47,** 903–915 (2000).

16. Gerson, R. & Jaffe, H. Electrical Conductivity in Lead Titanate Zirconate Ceramics. *J. Phys. Chem. Solids* **24,** 979–984 (1963).

17. Zhang, S. J. & Yu, F. Piezoelectric materials for high temperature sensors. *J. Am. Ceram. Soc.* **94,** 3153–3170 (2011).

18. Eitel, R. E., Zhang, S. J., Shrout, T. R. & Randall, C. A. Phase Diagram of the Perovskite System (1-x)$BiScO_3$-x$PbTiO_3$. *J. Appl. Phys.* **96,** 2828–2831 (2004).

19. Jiang, Y. *et al.* Microstructure and Electric Properties of (1-x)Bi($Sc_{0.75}Zn_{0.125}Ti_{0.125}$)$O_3$-x$PbTiO_3$ Ceramics. *Ferroelectrics* **380,** 130–134 (2009).

20. Stringer, C. J., Shrout, T. R., Randall, C. A. & Reaney, I. Classification of Transition Temperature Behavior in Ferroelectric $PbTiO_3$-Bi(Me'Me")O_3 Solid Solutions. *J. Appl. Phys.* **99,** 0241061–0241064 (2006).

21. Eitel, R. E. *et al.* New High Temperature Morphotropic Phase Boundary Based on Bi(Me)O_3-$PbTiO_3$ Ceramics. *Jpn. J. Appl. Phys.* **40,** 5999–6002 (2001).

22. Sehirlioglu, A., Sayir, A. & Dynys, F. Doping of $BiScO_3$-$PbTiO_3$ Ceramics for Enhanced Properties. *J. Am. Ceram. Soc.* **93,** 1718–1724 (2010).

23. Eitel, R. E., Randall, C. A., Shrout, T. R. & Park, S.-E. Preparation and Characterization of High Temperature Perovskite Ferroelectrics in the Solid-Solution (1-x)$BiScO_3$-x$PbTiO_3$. *Jpn. J. Appl. Phys.* **41,** 2099–2104 (2002).

24. Leist, T. *et al.* Temperature Dependence of the Piezoelectric Coefficient in $BiMeO_3$-$PbTiO_3$ (Me = Fe, Sc, ($Mg_{1/2}Ti_{1/2}$)) Ceramics. *J. Am. Ceram. Soc.* **95,** 711–715 (2012).

25. Suchomel, M. R. & Davies, P. K. Predicting the position of the morphotropic phase boundary in high temperature $PbTiO_3$Bi(B'B")O_3 based dielectric ceramics. *J Appl Phys* **96,** 4405–4410 (2004).

26. Randall, C. A. *et al.* Investigation of a high T_C piezoelectric system: (1-x)Bi($Mg_{1/2}$ $Ti_{1/2}$)O_3-(x)$PbTiO_3$. *J. Appl. Phys.* **95,** 3633–3639 (2004).

27. Suchomel, M. R. & Davies, P. K. Enhanced Tetragonality in (x)$PbTiO_3$-(1-x)$Bi(Zn_{1/2}Ti_{1/2})O_3$ and Related Solid Solution Systems. *Appl. Phys. Lett.* **86,** 2629051–2629053 (2005).

28. Sterianou, I. *et al.* High-temperature (1-x)$BiSc_{1/2}Fe_{1/2}O_3$-x$PbTiO_3$ piezoelectric ceramics. *Appl. Phys. Lett.* **87,** 242901 (2005).

29. Woodward, D. & Reaney, I. A structural study of ceramics in the $(BiMnO_3)$x-$(PbTiO_3)$1-x solid solution series. *J Phys Condens Matter* **16,** 8823–8834 (2004).

30. Cheng, J. R., Zhu, W., Li, N. & Cross, L. Fabrication and characterization of x$BiGaO_3$-(1-x)$PbTiO_3$: a high temperature reduced Pb-content piezoelectric ceramic. *Mater. Lett.* **57,** 2090–2094 (2003).

31. Cheng, J. R., Li, N. & Cross, L. Structural and dielectric properties of Ga-modified $BiFeO_3$-$PbTiO_3$ crystalline solutions. *J. Appl. Phys.* **94,** 5153–5158 (2003).

32. Choi, S. M., Stringer, C. J., Shrout, T. R. & Randall, C. A. Structure and Property Investigation of a Bi-based Perovskite Solid Solution: (1-x)$Bi(Ni_{1/2}Ti_{1/2})O_3$-x$PbTiO_3$. *J. Appl. Phys.* **98,** 0341081–0341084 (2005).

33. Takenaka, T. & Yamada, M. Solid-Solution $(Bi_{1-x}Pb_x)(Ni_{(1+x)/2}Ti_{(1+x)/2})O_3$ for New Piezoelectric Ceramics. *Jpn. J. Appl. Phys.* **32,** 4218–4222 (1993).

34. Stein, D. M., Grinberg, I., Rappe, A. M. & Davies, P. K. Multiple dielectric transitions in the $PbTiO_3$-$Bi(Zn_{1/2}Ti_{1/2})O_3$-$BI(Mg_{1/2}Ti_{1/2})O_3$ system. *J. Appl. Phys.* **110,** 074110 (2011).

35. Dwivedi, A., Randall, C. A. & Rossetti, G. A. J. Thermal history induced variable relaxor behavior in the high T_C ternary ferroelectric $0.6(Mg_{1/2}Ti_{1/2})O_3$-$0.05Bi(Zn_{1/2}Ti_{1/2})O_3$-$0.35PbTiO_3$. *Mater. Lett.* **65,** 3034–3036 (2011).

36. Kang, H., Chen, J., Liu, L., Fang, L. & Xing, X. Temperature dependences of the ferroelectric and dielectric properties of high curie temperature $PbTiO_3$-$BiScO_3$-$Bi(Zn_{1/2}Zr_{1/2})O_3$. *Mater. Res. Bull.* **48,** 2006–2009 (2013).

37. Kowalski, B. A., Sehirlioglu, A., Dynys, F. W. & Sayir, A. Characterization of the High-Temperature Ferroelectric (100-x-y)$BiScO_3$-(x)$Bi(Zr_{0.5}Zn_{0.5})O_3$-(y)$PbTiO_3$ Perovskite Ternary Solid Solution. *J. Am. Ceram. Soc.* **97,** 490–497 (2014).

38. Shi, L., Liao, Q., Zhang, B., Zhang, J. & Guo, D. Structure and electrical properties of (1-x)(0.1$BiYbO_3$-0.9$PbTiO_3$)-x$Pb(Zn_{1/3}Nb_{2/3})O_3$ high-temperature ternary piezoelectric ceramics. *Mater. Lett.* **114,** 100–102 (2014).

39. Song, T. H., Eitel, R. E., Shrout, T. R., Randall, C. A. & Hackenberger, W. Piezoelectric Properties in the Perovskite $BiScO_3$-$PbTiO_3$-(Ba,Sr)TiO_3 Ternary System. *Jpn. J. Appl. Phys.* **42,** 5181–5184 (2003).

40. Sebastian, T. *et al.* High temperature piezoelectric ceramics in the $Bi(Mg_{1/2}Ti_{1/2})O_3$-$BiFeO_3$-$BiScO_3$-$PbTiO_3$ system. *J. Electroceram.* **25,** 130–134 (2010).

41. Kang, H. *et al.* Structure and enhanced piezoelectric response by chemical doping in $PbTiO_3$-$PbZrO_3$-$Bi(Ni_{1/2}Ti_{1/2})O_3$. *Inorganic Chemistry Communications* **31,** 66–68 (2013).

42. Fan, L. *et al.* Enhanced piezoelectric and ferroelectric properties in the $BaZrO_3$ substituted $BiFeO_3$-$PbTiO_3$. *Appl. Phys. Lett.* **102,** (2013).

43. Shimojo, Y., Wang, R., Sekiya, T., Nakamura, T. & Cross, L. MPB Phase Diagram and Ferroelectric Properties in the $PbTiO_3$-$BiScO_3$ System. *Ferroelectrics* **284,** 121–128 (2003).

44. Stauffer, D. & Aharony, A. *Introduction to Percolation Theory* 2^{nd} (Taylor & Francis Inc, 1992).

45. Zhang, S. J., Randall, C. A. & Shrout, T. R. High Curie temperature piezocrystals in the $BiScO_3$-$PbTiO_3$ perovskite system. *Appl. Phys. Lett.* **83,** 3150–3152 (2003).

46. Randall, C. A., Eitel, R. E., Shrout, T. R., Woodward, D. & Reaney, I. Transmission Electron Microscopy Investigation of the High Temperature $BiScO_3$-$PbTiO_3$ Piezoelectric Ceramic System. *J. Appl. Phys.* **93,** 9271–9274 (2003).

47. Reaney, I. M. Octahedral tilting, domain structure and piezoelectricity in perovskites and related ceramics. *J. Electroceram.* **19,** 1–8 (2006).

48. Yamashita, Y., Hosono, Y., Harada, K. & Ichinose, N. Effect of Molecular Mass of B-site Ions on Electromechanical Coupling Factors of Lead-Based Perovskite Piezoelectric Materials. *Jpn. J. Appl. Phys.* **39,** 5593–5596 (2000).

49. Woodward, D., Reaney, I., Eitel, R. E. & Randall, C. A. Crystal and domain structure of the $BiFeO_3$-$PbTiO_3$ solid solution. *J Appl Phys* **94,** 3313–3318 (2003).

50. Duan, R., Speyer, R. F., Alberta, E. F. & Shrout, T. R. High Curie temperature perovskite $BiInO_3$-$PbTiO_3$ ceramics. *J Mater Res* **19,** 2185–2193 (2004).

51. Yu, H., Ren, W. & Ye, Z. G. Structural, Dielectric, and Ferroelectric Properties of the (1-x)$PbTiO_3$-x$BiAlO_3$ Solid Solution. *IEEE Trans. Ultra. Ferro. Freq. Control* **57,** 2177–2181 (2010).

52. Ansell, T. Y., Cann, D. P., Nikkel, J. & Sehirlioglu, A. High Temperature Piezoelectric Ceramics based on x$PbTiO_3$-(1-x)$Bi(Sc_{1/2}Me_{1/4}Ti_{1/4})O_3$ (Me = Zn, Mg) Ternary Perovskites. *Jpn. J. Appl. Phys.* **51,** 101802 (2012).

53. Ansell, T. Y. & Cann, D. P. High temperature piezoelectric ceramics based on (1 - x)[$BiScO_3$ + $Bi(Ni_{1/2}Ti_{1/2})O_3$] - x$PbTiO_3$. *Mater. Lett.* **80,** 87–90 (2012).

54. Ansell, T. Y. & Cann, D. P. Piezoelectric properties of the high temperature MPB x$PbTiO_3$ - (1-x)[$BiScO_3$ + $Bi(Ni_{1/2}Ti_{1/2})O_3$] composition. *J Electroceram* **31,** 159–167 (2013).

55. Ansell, T. Y., Cann, D. P., Sapper, E. & Rödel, J. Thermal Depolarization in the High-Temperature Ternary Piezoelectric System x$PbTiO_3$-y$BiScO_3$-z$Bi(Ni_{1/2}Ti_{1/2})O_3$. *J. Am. Ceram. Soc.* 1–9 (2014).

56. Zhou, Z., Li, Y., Hui, S. & Dong, X. Effect of tungsten doping in bismuth-layered $Na_{0.5}Bi_{2.5}Nb_2O_9$ high temperature piezoceramics. *Appl. Phys. Lett.* **104,** (2014).

57. Peng, Z., Chen, Q., Chen, Y., Xiao, D. & Zhu, J. Microstructure and electrical properties in W/Nb co-doped Aurivillius phase $Bi_4Ti_3O_{12}$ piezoelectric ceramics. *Mater. Res. Bull.* **59,** 125–130 (2014).

58. Sun, L. *et al.* Dielectric and piezoelectric properties of cerium-doped $(NaBi)_{0.49}[\ ]_{0.02}Bi_2Nb_{1.98}Ta_{0.02}O_9$-based piezoceramics. *Ceramics International* **40,** 14159–14163 (2014).

59. Zhang, S. J., Xia, R. & Shrout, T. R. Lead-free piezoelectric ceramics vs. PZT? *J. Electroceram.* **19,** 251–257 (2007).

60. Anton, E. M., Jo, W., Damjanovic, D. & Rödel, J. Determination of depolarization temperature of $(Bi_{1/2}Na_{1/2})TiO_3$-based lead-free piezoceramics. *J. Appl. Phys.* **110,** 094108–14 (2011).

61. Takenaka, T., Maruyama, K.-i. & Sakata, K. $(Bi_{1/2}Na_{1/2})TiO_3$-$BaTiO_3$ System for Lead-Free Piezoelectric Ceramics. *Jpn. J. Appl. Phys.* **30,** 2236 (1991).

62. Takenaka, T., Hazumi, A., Hata, T. & Sakata, K. Mechanical properties of $(BiNa)_{1/2}TiO_3$-based piezoelectric ceramics. *Silicates Industrials* **7,** 136–142 (1993).

63. Chu, B.-J., Chen, R., Li, G.-R. & Yin, Q.-R. Electrical Properties of $Na_{1/2}Bi_{1/2}TiO_3$-$BaTiO_3$ ceramics. *J. Europ. Ceram. Soc.* **22,** 2115–2121 (2002).

64. Rödel, J., Jo, W., Seifert, K. T. P., Anton, E. M. & Granzow, T. Perspective on the Development of Lead-free Piezoceramics. *J. Am. Ceram. Soc.* **92,** 1153 (2009).

65. Birol, H., Damjanovic, D. & Setter, N. Preparation and Characterization of (K0.5Na0.5)NbO3 Ceramics. *J. Eur. Ceram. Soc.* **26,** 861–866 (2006).

66. Egerton, L. & Dillon, D. M. Piezoelectric and Dielectric Properties of Ceramics in the System Potassium Sodium Niobate. *J. Am. Ceram. Soc.* **42,** 438–442 (1959).

67. Du, H. L. *et al.* Preparation and Piezoelectric Properties of $(K_{0.5}Na_{0.5})NbO_3$ Lead-Free Piezoelectric Ceramics with Pressure-Less Sintering. *Mater. Sci. Eng. B* **131,** 83–87 (2006).

68. Saito, Y. *et al.* Lead-Free Piezoceramics. *Nature* **432,** 84–87 (2004).

69. Hiruma, Y., Nagata, H. & Takenaka, T. Phase diagrams and electrical properties of $(Bi_{1/2}Na_{1/2})TiO_3$-based solid solutions. *J. Appl. Phys.* **104,** 124106 (2008).

70. Sasaki, A., Chiba, T., Mamiya, Y. & Otsuki, E. Dielectric and Piezoelectric Properties of $(Bi_{0.5}Na_{0.5})TiO_3$-$Bi_{0.5}K_{0.5})TiO_3$ Systems. *Jpn. J. Appl. Phys.* **38,** 5564–5567 (1999).

71. Patterson, E. *Development. Characterization. and Piezoelectric Fatigue Behavior of Lead-Free Perovskite Piezoelectric Ceramics* PhD thesis (Oregon State University, 2012).

72. Patterson, E. A., Cann, D. P., Pokorny, J. & Reaney, I. M. Electromechanical strain in $Bi(Zn_{1/2}Ti_{1/2})O_3$-$(Bi_{1/2}Na_{1/2})TiO_3$-$(Bi_{1/2}K_{1/2})TiO_3$ solid solutions. *J. Appl. Phys.* **111,** (2012).

73. Kumar, N. & Cann, D. P. Electromechanical strain and bipolar fatigue in $Bi(Mg_{1/2}Ti_{1/2})O_3$-$(Bi_{1/2}Na_{1/2})TiO_3$-$(Bi_{1/2}K_{1/2})TiO_3$ ceramics. *J. Appl. Phys.* **114,** (2013).

74. Kumar, N., Ansell, T. Y. & Cann, D. P. Role of point defects in bipolar fatigue behavior of $Bi(Mg_{1/2}Ti_{1/2})O_3$ modified $(Bi_{1/2}Na_{1/2})TiO_3$-$(Bi_{1/2}K_{1/2})TiO_3$ relaxor ceramics. *J. Appl. Phys.* **115,** (2014).

4 Experimental Methods

4.1 Materials Synthesis

All compositions are synthesized using a standard solid-state oxide method. Compositions, in the PT-BS-BXT ternaries, are initially calculated to include 2.0-mol% Pb excess to account for lead volatility. Appropriate amounts of oxide and carbonate powders are then mixed together with ethanol and yttria stabilized zirconia (YTZ) milling media (TOSOH corporation), and vibratory milled for six hours, after which, the batched powders are dried in an oven at 100 ^{o}C for approximately 8 - 12 hours. The dried batched powder is then calcined at temperatures of 800 - 1000 ^{o}C depending on composition for four hours. The calcined powders are then re-milled in ethanol for another six hours and dried. In both milling steps, the powders and ethanol make up the slurry where roughly 85 % of the volume is ethanol and the rest are the mixed powders.

Once dried, calcined powders are weighed and mixed with 3.0 wt% solution of Polyvinyl Butyral (PVB) binder; the ratio of PVB to calcined powder is 0.5 g PVB for every 1.0 g powder. Mixing in a mortar and pestle, the mixture is ground until a fine powder is produced. The powder is then poured into a circular cast and uniaxially cold pressed at pressures of 34.5 MPa for 3 min into thin discs roughly 15 mm thick and 1.4 mm in diameter. Further densification of the "green" ceramics occurs by sintering; first the ceramics are heated in a furnace to 400 ^{o}C for four hours to burn off the binder and any other organics; then the ceramics are heated to temperatures up to 1150 ^{o}C for another four hours depending on composition.The heating rate for both calcination and sintering steps is set at a constant 3 - 5 ^{o}C/min rate for both heating and cooling. The sintered pellets are then polished, using various grit sandpaper and ethanol, down to $\approx$ 0.800 mm thickness. Depending on characterization, i.e. X-ray diffraction (XRD), scanning electron microscopy (SEM), etc.; the pellets are either left

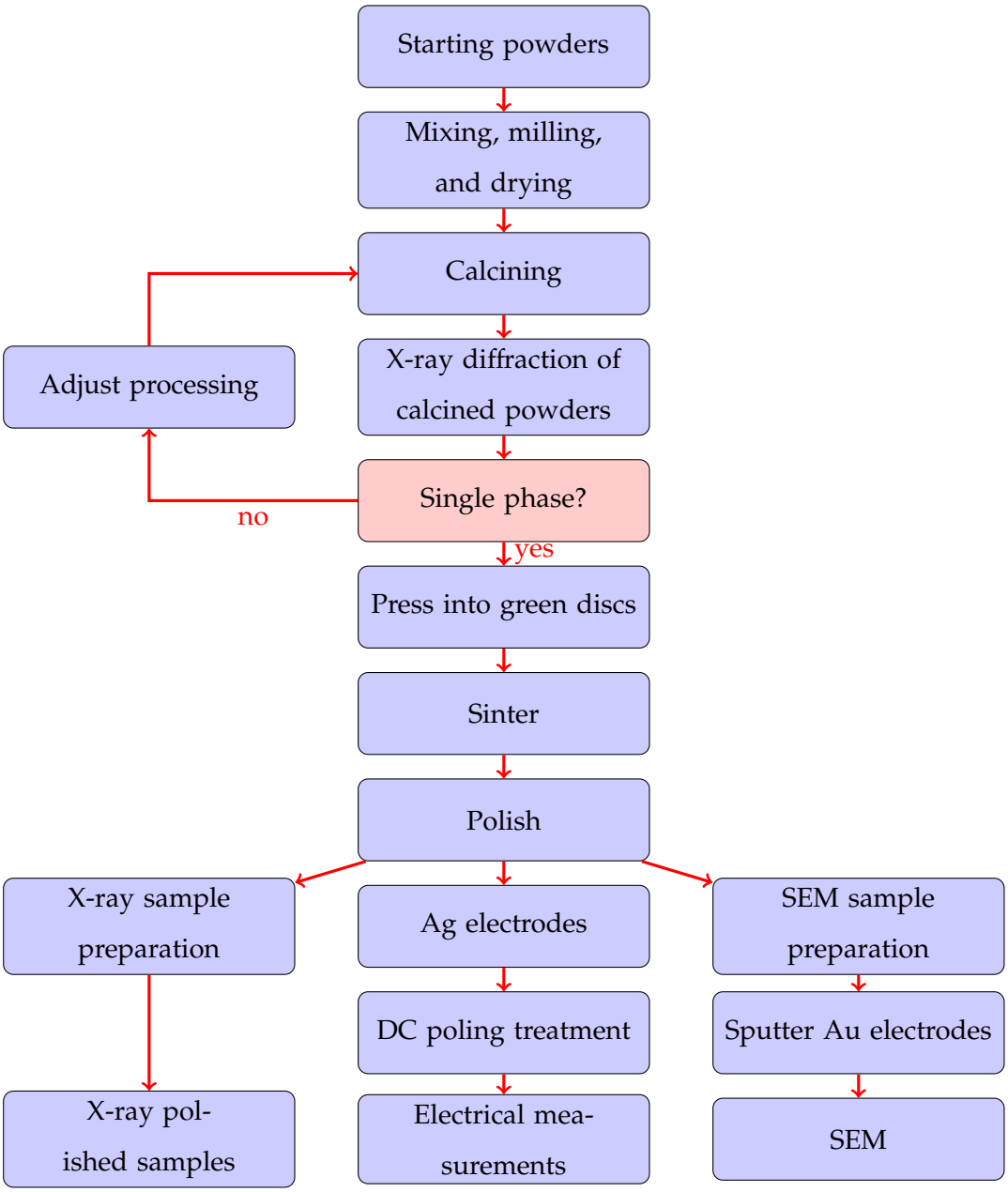

FIGURE 4.1: Flow diagram of processing and characterization of ceramics.

without electrodes; silver electrodes are painted and dried on pellets; or gold electrodes are sputtered onto pellets. Especially for SEM, polishing includes polishing with 1200 grit sandpaper and an alumina polish slurry followed with a thermal anneal

at 1000 ^{o}C/1 h. Figure 4.1 is a flow chart of all processing steps and characterization steps.

4.2 Structural Characterization

Structural identification of ceramics is done by XRD with a (D8 Discover, Bruker AXS) and/or SEM with a (Quanta TM 600 FEG SEM, FEI Company). The following is the procedure used in the D8 to produce the x-rays. Applying a 40 mA current to a tungsten filament, electrons are knocked off and accelerated through a 40 kV potential in the x-ray tube. At the end of the tube is a copper metal target and the high-energy electrons are absorbed by the Cu target. The decelerating electrons transfer energy to valence electrons bound to the Cu atoms. The excited electrons transition down to the lowest available energy level and in the process x-rays are produced. The characteristic wavelength of radiation emanating from copper is $\approx$ 1.54 Å, this is on the same order of magnitude as the atomic separation (also unit cell size) in most crystalline materials. Multiple electron transitions, or x-ray emission energies occur depending on electron transition between different energy shells.

The primary emission lines seen in this research include: Kα1, Kα2, Kβ Lα1, Lα2, and Lβ1 lines. The Lα and Lβ arises from M-shell to L-shell electron transitions. These transition lines are undesirable and are filtered out when the x-ray beam passes through a Ni filter. Electrons dropping from the L-shell to K shell correspond to the Kα transition line while a M-shell to K-shell transition corresponds to the Kβ lines. The Kα line is a doublet and corresponds to different 2p orbital transitions depending on electron spin and orbital momentum quantum numbers. The Kβ line that appears in copper relates to a 3p (M3) to 1s (K1) transition [1, 2], and are filtered out by software proprietary to Bruker. Once past the Ni filter, the x-rays are collimated into a parallel beam by passing through a Göbel mirror. The x-rays are then diffracted off the sample into a detector (Lynkeye) made of metal strips, each acting as an individual detector.

Phase identification of ceramics is accomplished in a range of 20° - 80° in 2θ.

A complimentary structural characterization technique to XRD is electron microscopy or scanning electron microscopy (SEM). Samples are prepared by polishing down to ≈ 0.8 mm with fine grit (1200) paper and an alumina polish. Polished samples are then thermally annealed in air at 1000 °C for one hour, cooled down to room temperature, and coated with a thin gold electrode. The gold is sputtered onto ceramics using a sputtering unit (Scancoat Six, BOC Edwards). A low vacuum is created in the sample chamber and argon gas is introduced. The electric potential is then increased up to 10 kV and gold is deposited onto samples for about 30 seconds. The pellets are then brought to a SEM (Quanta TM 600 FEG SEM, FEI Company). Samples are placed within the chamber and the chamber is evacuated to pressures as low as ≈ 6 - 10 atm. Then potential fields of up to 30 kV accelerate electrons toward sample. After the electron microscopy is complete, the Abrams Three-Circle procedure, stated in the standard testing methods of the American Society for Testing and Materials is applied to SEM images to determine the average grain sizes [3]. According to the ASTM standard, a percentage relative accuracy of no more than 10 % is acceptable when presenting grain size measurements.

4.3 Electrical Characterization

For electrical testing, silver paste (Heraeus C1000) is applied to samples and fired on at 700 °C for 30 minutes. After electrodes are fired on, samples are placed in between two Pt electrodes within an alumina tube (NorECs AS ProbostatTM) and heating samples up to 600 °C for one hour and a heating rate of 3 °C/min. Using a LCR meter (Agilent 4263B), the dielectric permittivity and loss are measured as a function of temperature, measured by a temperature reader (Dpi32-C24, Omega Engineering, Inc.). Dielectric testing is conducted by passing a low field through the sample at a number of frequencies (10 Hz up to 1 MHz, 3 frequencies per decade).

To test the piezoelectric properties, the same silver electrodes, as with dielectric testing, are applied to ceramic samples and fired. Poling of specimens is conducted inside an environmental chamber (Delta Design Inc.). Samples are placed between two electrodes and heated up to 100 ^{o}C for one hour. A DC electric field of 40 kV/cm is applied across a sample for 30 minutes. After which, the ceramics are taken out and aged for one day. The direct piezoelectric coefficient, d_{33}, is then measured in a d_{33} meter (Sinoceramics Inc., Shanghai, China). Hysteresis and electromechanical strain measurements were taken inside a standard ferroelectric testing system (Radiant Technologies, Premier Precision II) at room temperature. The field applied was 40 kV/cm and the hysteresis measurement frequency was 1 Hz following similar bulk ferroelectric measurement applications [4, 5]. Strain measurements were averaged over five loops while using an MTI-2100 Fotonic Sensor (MTI Instruments Inc.). The converse piezoelectric coefficient (d^*_{33} [pm/V]) is calculated from the ratio of the maximum unipolar strain and the maximum applied electric field [6, 7].

For the ternary system PT-BS-BMgT, temperature dependent polarization and strain was measured at NASA Glenn Research Center, Cleveland, OH. Samples were poled in a sample holder (aixACCT) filled with silicon oil and with the same poling conditions previously mentioned. After one day aging, samples were again placed in the sample holder and a high DC field of 40 kV was applied across samples to measure temperature dependent piezoelectric properties at: 25 ^{o}C, 50 ^{o}C, 75 ^{o}C, 100 ^{o}C, 125 ^{o}C, and 150 ^{o}C. Polarization hysteresis, bipolar electromechanical strain, and unipolar strain are then measured and plotted as functions of field. All data conducted in Ohio were averaged over five cycles. Temperature dependent piezoelectric characterization was also carried out on compositions of the ternary PT-BS-BNiT in a similar setup (aixACCT) in Technische Universität (TU) Darmstadt, Darmstadt, Hessen, Germany. All parameters were the same as before, but with only polarization and bipolar strain measurements up to 190 ^{o}C with the same 25 ^{o}C steps. Further studies of properties with temperature involved a look at depolarization of samples,

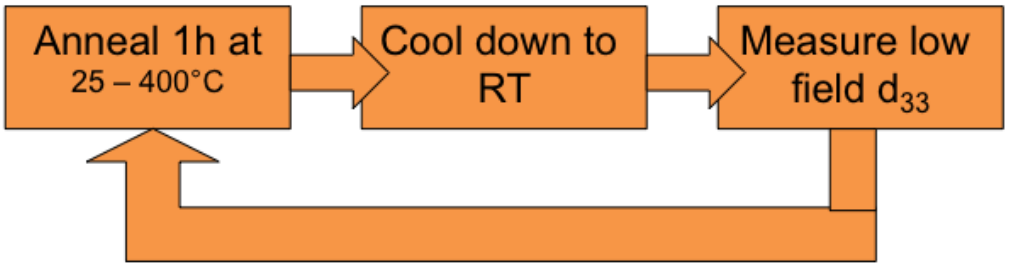

FIGURE 4.2: Diagram of the process for the ex-situ d_{33} measurement.

i.e. changes of domain structure with increasing temperature.

Three different methods were used to measure the depoling temperature, T_d, in Oregon: an ex-situ d_{33} technique (Fig. 4.2), analysis of the dielectric loss in log scale, and impedance spectroscopy. For the ex-situ d_{33} approach, poled samples were placed in a furnace and heated to temperatures ranging from 100 to 350 ^{o}C in 25 ^{o}C steps, and held at the measurement temperature for one hour. After each, the samples were cooled down to room temperature and the direct piezoelectric coefficient (d_{33} [pC/N]) was measured using a YE2730A d_{33} meter (Sinoceramics Inc.). Although a cheap and easy method to investigate T_d, the ex-situ d_{33} method is limited. The piezoelectric coefficient should increase close to T_d related to changes in several coupled parameters: electrostrictive coefficient Q, polarization P, and permittivity ϵ [8, 9]. Another simple method of finding T_d is analysis of dielectric data on poled specimens. Looking at the tanδ data of poled samples and noting a local maximum corresponding to the inflection point in the ϵ' curve, the maximum corresponds to T_d in poled samples [9]. Following the resonance method set by the IEEE standard on piezoelectrics [10], poled samples were placed in the same set-up as the dielectric measurements and heated to incrementally higher temperatures from room temperature up to 400 ^{o}C. The samples were allowed to soak at predetermined temperatures for an hour after which an impedance spectrum is measured for frequencies from 1 Hz - 1 MHz.

Due to the limitations of the ex-situ d_{33} method, two additional techniques

were utilized for the observation of depolarization in ferroelectric materials: in-situ d_{33} and thermally stimulated depolarization current (TSDC); these measurements were conducted at TU Darmstadt. In a custom built chamber, an alumina plate with a hole $\approx$ 11.2 mm in diameter, samples are placed and covered with alumina cylinders which act to lightly press the sample down. Pinholes were drilled into the alumina cylinders to allow light from a laser interferometer through. An outer metal cylinder is placed over the alumina cylinders to seal the interior and protect against stray electric fields. Heating of the chamber occurs by resistive heating where a resistor lies underneath the sample chamber. To measure the temperature, a thermocouple is placed in between the bottom alumina plate and alumina cylinder. Two silver electrodes are placed in electrical contact with the sample to measure a signal. A schematic diagram of the setup is presented in Fig. 4.3 [9].

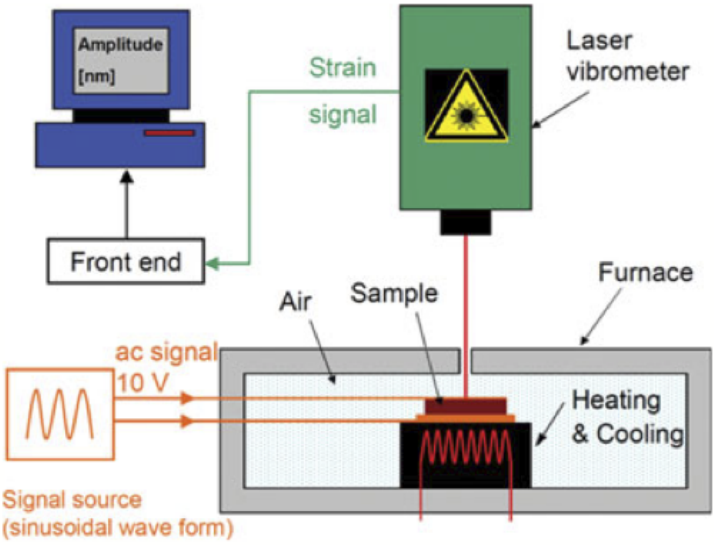

FIGURE 4.3: Schematic representation of the experimental setup used for both the in-situ d_{33} and TSDC measurements. Leist et al., Journal of the American Ceramic Society, John Wiley and Sons [9]. Copyright © (2011) The American Ceramic Society.

For the in-situ piezoelectric coefficient measurement, poled samples were placed

in the chamber and a laser vibrometer (Polytec sensor OFV-505) connected to a laser source (Polytec VDD-E-600) were used to measure the intensity of reflected light. As the temperature increases, the piezoelectric coefficient will increase and the piezoelectric will apply increasing amount of force on a spring sitting over the material. The spring in turn will move a reflecting plate and the intensity of reflected light will change. The electrical signal is a 10 V, 1 kHz signal sent to the electrodes and supplied by a function generator (Hameg HM8131-2).

The same experimental setup is used for TSDC measurements. Again placing a poled sample in the chamber and closing the chamber. No laser interferometry is needed nor is the function generator required, instead a high precision ampere meter (Keithley Electrometer, 6517B) is used to send a high signal to the samples and measure the current response. The current is measured, however, calculating the current density and in turn, the polarization loss is much more useful in determining T_d from TSDC measurements. Polarization and temperature are related thermodynamically to the pyroelectric effect as in Eq. 2.28 and rearranged in Eq. 4.1,

$$p = \frac{\partial P_S}{\partial T} \tag{4.1}$$

where P_S is the spontaneous polarization [8]. If the only thermally activated mechanism is polarization reversal [11], then the P_{Loss} can be calculated from Equation 4.1 by,

$$P_{Loss} = \int J_{depole} dt \tag{4.2}$$

Calculation of Eq. 4.2 was approximated by using the trapezoid method of integration. Taking the current of the sample and dividing by the sample area to get the current density, and then applying the trapezoid method of adding successive rectangles underneath the curve of J_{depole}, the polarization loss values are calculated. All five methods to the depolarization temperature should correspond with each other and

any differences may be attributed to error in measurement, experimental error, etc. The results of these experiments are shown and discussed in the next four chapters.

4.4 References

1. Bearden, J. A. X-Ray Wavelengths. *Rev Mod Phys* **39,** 78–124 (1967).
2. Thompson, A. *et al. X-ray Data Booklet* DE-AC02-05CH11231 (U.S. Department of Energy, Center for X-ray Optics Advanced Light Source, Lawrence Berkeley National Laboratory, Oct. 2009), 1–176.
3. *Standard Test Methods for Determining Average Grain Size* Standard E112-10 (American Society for Testing and Materials, ASTM International, 100 Barr Harbor Drive, PO Box C700, West Conshohocken, PA 19428-2959. United States, 2010).
4. Shimojo, Y., Wang, R., Sekiya, T., Nakamura, T. & Cross, L. MPB Phase Diagram and Ferroelectric Properties in the $PbTiO_3$-$BiScO_3$ System. *Ferroelectrics* **284,** 121–128 (2003).
5. Inaguma, Y. *et al.* High-pressure synthesis and ferroelectric properties in perovskite -type $BiScO_3$-$PbTiO_3$ solid solution. *J. Appl. Phys.* **95,** 231–235 (2004).
6. Haertling, G. H. Ferroelectric Ceramics: History and Technology. *J. Am. Ceram. Soc.* **82,** 797–818 (1999).
7. Eitel, R. E., Shrout, T. R. & Randall, C. A. Nonlinear contributions to the dielectric permittivity and converse piezoelectric coefficient in piezoelectric ceramics. *J. Appl. Phys.* **99,** 124110 (2006).
8. Anton, E. M., Jo, W., Damjanovic, D. & Rödel, J. Determination of depolarization temperature of $(Bi_{1/2}Na_{1/2})TiO_3$-based lead-free piezoceramics. *J. Appl. Phys.* **110,** 094108–14 (2011).

9. Leist, T. *et al.* Temperature Dependence of the Piezoelectric Coefficient in $BiMeO_3$-$PbTiO_3$ (Me = Fe, Sc, ($Mg_{1/2}Ti_{1/2}$)) Ceramics. *J. Am. Ceram. Soc.* **95,** 711–715 (2012).

10. *ANSI/IEEE 176-1987, IEEE Standard on Piezoelectricity* (IEEE, New York, 1987).

11. Damjanovic, D., Bhalla, A. S. & Cross, L. Dielectric and Pyroelectric Properties of Triglycerol - Gelatin Films. *IEEE Trans. Ultra. Ferro. Freq. Control* **138** (Nov. 1991).

5 High Temperature Piezoelectric Ceramics Based on $xPbTiO_3$-(1-x)$Bi(Sc_{1/2}Me_{1/4}Ti_{1/4})O_3$ (Me = Zn, Mg) Ternary Perovskites

Troy Y. Ansell, Jason Nikkel, and David P. Cann

Materials Science, School of Mechanical, Industrial, and Manufacturing Engineering, Oregon State University, Corvallis, OR, 97331, U.S.A.

Alp Sehirlioglu

Department of Materials Science and Engineering, Case Western Reserve University, Cleveland, OH 44106, U.S.A.

Published in

Japanese Journal of Applied Physics

Volume 51, 101802 (2012)

5.1 Abstract

Polycrystalline $xPbTiO_3$-(1-x)$Bi(Sc_{1/2}Me_{1/4}Ti_{1/4})O_3$ (PT-BS-BMeT) ceramics, where Me = Mg (M) or Zn (Z), were studied for development of high temperature piezoelectrics. Ceramics were processed using standard mixed oxide procedure at various temperatures. X-ray diffraction at room temperature revealed that the tetragonality of PT-BS-BZT decreased as $PbTiO_3$ content decreased from x = 0.90 to 0.60 and tetragonality of PT-BS-BMT decreased as $PbTiO_3$ content decreased from x = 0.60 to 0.40. A transition was observed in PT-BS-BMT within compositions x = 0.42 - 0.50. Dielectric properties revealed permittivites up to $\epsilon_r \approx 20000$ and transition temperatures up to 540 ^oC. Hysteresis measurements showed full saturation below 50 mol% $PbTiO_3$ content with remanent polarization of $P_r = 32.8\ \mu C/cm^2$ and coercive field of 23.0 kV/cm. Converse piezoelectric coefficients (d_{33}*) calculated from unipolar strain measurements revealed values between 240 and 313 pm/V. Depolarization temperatures were measured between 320 and 390 ^oC.

5.2 Introduction

Ferroelectric ceramics based on lead titanate ($PbTiO_3$, PT) or lead zirconium titanate [$xPbTiO_3$-(1-x)$PbZrO_3$, PZT] solid solutions have been widely used in sensor and actuating applications, in industries such as the automotive and aerospace fields [1], due to their excellent dielectric properties and large piezoelectric coefficients. PZT, especially, has come to dominate the electroceramics market due to the perovskite's large piezoelectric coefficient of d_{33} = 233 pC/N for undoped PZT [2], d_{33} = 750 pC/N for Navy Type IV/PZT 5H, or d_{33} = 375 pC/N for Navy Type II/PZT 5A [3]. The Navy Type IV/PZT 5H also known as soft PZT has very high response but low transition temperature of T_C = 195 ^oC [3]. High permittivities and piezoelectric coefficients occur in materials near a structural transition or where two different crystallographic structures exist in the material at the same time. Such a structural

transition occurs at the morphotropic phase boundary (MPB) with a change in composition of the solid solution. MPB in PZT exists in the vicinity of x = 0.50 mol% PT [3]. The MPB is nearly temperature independent and PZT remains ferroelectric up to a transition temperature of ≈ 390 ^{o}C [4–6]. However, despite the relatively high transition temperature known as the Curie temperature (T_C) of PZT ceramics, many applications in automotive, aeronautical and space industries require sensors and/or actuators which can withstand operating temperatures up to 400 ^{o}C or higher [6], which is a temperature much higher than commercially available PZT materials can reliably operate at (150 ^{o}C) [7]. High temperature dielectric materials based on ferroelectrics are also required for insulation and capacitor applications. Any good piezoelectric or dielectric material must maintain excellent properties at these higher temperatures to be considered as a candidate material for use in such demanding environments. Therefore, it is necessary to find materials with transition temperatures higher than PZT, and at the same time, maintain or exceed its high piezoelectric coefficients, high dielectric permittivities, and low dielectric loss.

To achieve these requirements, several groups have researched $xPbTiO_3$-(1-x)$BiScO_3$ (PT-BS) [1, 3–12], $xPbTiO_3$-(1-x)$Bi(Zn_{0.5}Ti_{0.5})O_3$ (PT-BZnT) [12–15], $xPbTiO_3$-(1-x)$Bi(Mg_{0.5}Ti_{0.5})O_3$ (PT-BMgT) [11, 16, 17], and $xPbTiO_3$-(1-x)$Bi(Ni_{0.5}Ti_{0.5})O_3$ (PT-BNiT) solid solutions [18, 19]. Eitel et al. [4] and Gotmare et al. [11] showed the existence of a MPB composition in the PT-BS binary at x = 0.64. Shimojo et al. showed that the PT-BS system remained single phase down to x = 0.625 PT and that the peak dielectric constant at T_C and T_C itself decreased with decreasing PT content [8]. Eitel et al. also showed the PT-BS system has a transition temperature of 450 ^{o}C with a large piezoelectric coefficient of d_{33} > 460pC/N, high relative permittivity, and low dielectric loss in the frequency range 1kHz to 100kHz for composition x = 0.64, the MPB composition [5]. For the PT-BZnT system, with single-phase compositions x = 0.60 to 1.00, high permittivities were measured with transition temperatures reaching 700 ^{o}C for x = 0.60 [13]. Ternary perovskite compositions of $xPbTiO_3$-(1-

x)Bi(Sc0.5Zn.0.25Ti0.25)O_3 (PTBSZ), where x = 0.50-0.60, have been investigated. The MPB composition found at x = 0.56, had measured values of planar electromechanical coupling factor of (k_p)= 0.47, d_{33} = 320 pC/N, and T_C = 445 ^oC [6]. In the PT-BMgT binary, Sharma et al. showed a transition from tetragonal to rhombohedral structures occurred with PT content around 35 mol% and also observed two temperature induced phase transformations in dielectric data indicating relaxor ferroelectric to antiferroelectric to paraelectric transitions in the temperature range of 150 - 300 ^oC [16]. R. Rai et al., also studying the PT-BMgT binary, observed a transition around x = 0.32 - 0.34 with a maximum remnant polarization of $P_r \approx 7.9\ \mu C/cm^2$ [17]. Choi et al. developed the PT-BNiT solid solution and found a T_C near 400 ^oC and a d_{33} coefficient of ≈ 260 pC/N at room temperature for the MPB composition at 0.49PT-0.51BNiT [19].

Further research into ferroelectric systems has led to the study of several ternary solid solution systems. Song et al. studied the MPB of the ternary x[(1-y)$PbTiO_3$-y($Ba_{0.294}Sr_{0.706}$)TiO_3]-(1-x)$BiScO_3$, where x = 0.60, and found d_{33} and k_p values decreased with increasing amounts of barium and strontium substitution [20]. Sehirlioglu et al. combined the MPB composition in the PT-BS system (at 65/45) and the MPB composition in the PT-PZ system (i.e. PZT at 52/48) to form the ternary PT-PZ-BS system. This material system exhibited a T_C of approximately 400 ^oC and the d_{33} values greater than 400 pm/V [21]. Stein et al. investigated compositions in the ternary system $PbTiO_3$-Bi(Zn1/2Ti1/2)O_3-Bi(Mg1/2Ti1/2)O_3 and found an MPB composition at 0.338PT-0.112BZT-0.550BMgT [22]. Sebastian et al. investigated the pseudo quaternary system $PbTiO_3$-Bi($Mg_{1/2}Ti_{1/2}$)O_3-$BiFeO_3$-$BiScO_3$ and observed a piezoelectric constant d_{33} = 328 pC/N and a transition temperature of T_C = 450 ^oC [23].

In this report, two ternary systems were developed, x$PbTiO_3$ - (1-x)Bi($Sc_{1/2}Zn_{1/4}$-$Ti_{1/4}$)O_3 (PT-BS-BZnT) and x$PbTiO_3$ - (1-x)Bi($Sc_{1/2}Mg_{1/4}Ti_{1/4}$)O_3 (PT-BS-BMT). The phase diagrams of the PT-BS-BZnT and PT-BS-BMT are shown in Figs. 5.1 and 5.2, respectively. Reported compositions of PT-BS, PT-BZnT, PT-BMgT binary systems,

as well as the ternary PT-BS-BZnT and PT-BS-BMgT compositions reported in this work are marked on the phase diagram. The purpose of this paper is to study the structure, characterize the dielectric, ferroelectric and piezoelectric properties, and determine the phase transition temperatures of the ternary perovskite ferroelectrics in PT-BS-BZnT and PT-BS-BMgT systems.

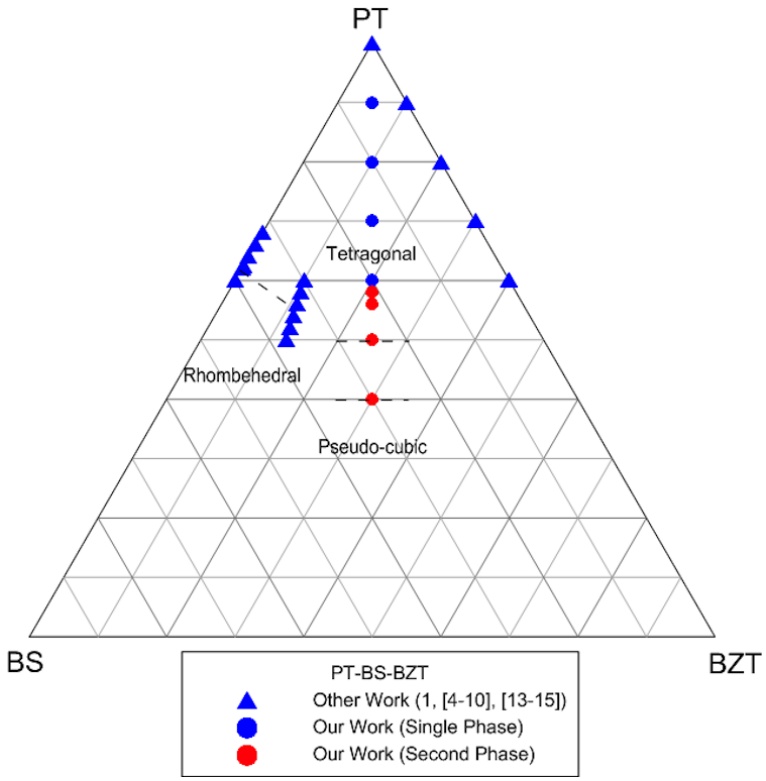

FIGURE 5.1: Ternary phase diagram of the PT-BS-BZnT system.

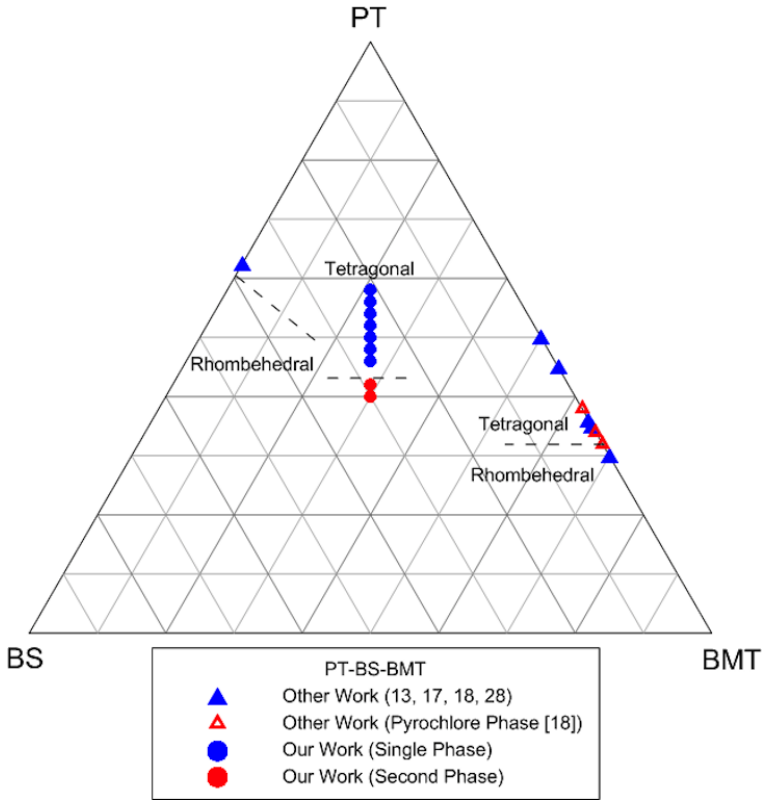

FIGURE 5.2: Ternary phase diagram of the PT-BS-BMgT system.

5.3 Methods

All ceramic samples were prepared with the use of standard metal oxide powder processing. Starting materials of high purity metal oxides and carbonates included from Sigma-Aldrich: PbO (99.9%), Bi_2O_3 (99.9%), TiO_2 (99.0%), and $MgCO_3$, and from Alfa-Aesar: ZnO (99.9%) and Sc_2O_3 (99.9%). Oxide powders were weighed to obtain $xPbTiO_3$-(1-x)$Bi(Sc_{1/2}X_{1/4}Ti_{1/4})O_3$ compositions. ZnO and $MgCO_3$ were used as the Zn and Mg source in the BZnT and BMgT systems, respectively. 2% molar excess of PbO was added to each composition to prevent Pb loss during calcination and sintering. A vibratory milling machine was used to grind and mix the prepared batches for 6 hours. The batches were then dried and calcined in an alumina

crucible between 950 and 1000 °C for BMgT samples, and between 800 and 1100 °C depending on composition for the BZnT system. Prior to the sintering stage, the calcined powders were again mixed in the vibratory mill for 6 hours, and then dried. The powders were finally uniaxially pressed at 34.5 MPa into thin discs. The resulting pellets were sintered in an alumina crucible for 4 h at 950 - 1080 °C for BMgT and 900 - 1150 °C for BZnT again depending on composition, generally the higher the PT mol%, the higher the sintering temperature. The diameter of the sintered ceramics was > 10mm. Sintered ceramics were polished down to around ≈ 0.800 mm thickness to obtain an aspect ratio > 10:1. Silver electrodes were fired onto ceramics at 700 °C for high temperature dielectric measurements and gold electrodes were deposited onto ceramics for hysteresis measurements.

X-ray diffraction (Bruker AXS D8 Discover) was used to determine the phase purity and crystal structure. Ceramic samples were placed into a sample holder (NorECs AS Probostat) in between two Pt electrodes to measure the temperature dependence of the dielectric properties via an LCR meter (Agilent 4263B) from room temperature up to ≈ 650 °C. Dielectric measurements were conducted on unpoled ceramics.

Specimens were poled at NASA Glenn Research Center, Cleveland, OH. Ceramic samples were placed inside a bulk ceramics sample holder (aixACCT), heated up to 100 °C. A poling field of 40 kV/cm was applied for 15 min after which samples were cooled down for another 30 minutes while field was still applied. After aging poled samples for 24 h, both unipolar and bipolar ferroelectric and piezoelectric behavior was characterized at 25, 50, and 100 °C. Strain measurements, both unipolar and bipolar drive, were carried out using a laser dopplermeter (Polytec OFV-5000) and all ferroelectric data was analyzed using a ferroelectric analyzer (aixACCT) at frequencies of 0.1 and 1 Hz. Strain data presented in this manuscript were averaged over five cycles. The direct piezoelectric constants, hereafter referred as low-field d_{33} constant (pC/N), were measured using a YE2730A d_{33} meter (Sinoceramics Inc.,

Shanghai, China). The converse piezoelectric coefficients were determined from unipolar data by taking the maximum strain and calculating the coefficient relating strain and the electric field [24, 25]. For the rest of this paper, the converse piezoelectric coefficient is referred to as the high field d_{33}* coefficient (pm/V).

The depolarization temperature was measured indirectly by measuring the resonance spectrum, i.e. real impedance versus frequency, of poled ceramics at temperatures starting at room temperature up to 400 ^{o}C at 5 ^{o}C intervals, using an Agilient 4294A impedance anaylzer and following the resonance method based on IEEE Standards [26].

5.4 Results and Discussion

5.4.1 Structural and dielectric properties of PT-BS-BZnT

X-ray diffraction (XRD) results show the dependence of structure on composition in the PT-BS-BZnT ternary (Fig. 5.3). Above x = 60 mol% PT, perovskite structure formed with no secondary phases. Below 60PT, a minor second phase was observed with 100% peak around $2\theta = 28^{o}$. This second phase was identified as bismuth oxide that has not been incorporated into the crystal structure. The relative intensity of the second phase peak increased with decreasing PT content. Presence of unreacted powder makes it hard to determine the exact composition of the MPB. Tetragonality of the unit cell increased with increasing PT content as seen from the peak splitting observed for the (100) and (110) peaks. This peak splitting is characteristic of a tetragonal perovskite phase and is observed in all PT-BS-BZnT compositions studied. Calculation of c/a ratios, as seen in the inset of Fig. 5.3, shows a downward trend toward a pseudo-cubic or rhombehedral structure with decreasing PT content. When the c/a = 1 below T_C, the crystal has pseudo-cubic or rhombohedral structure.

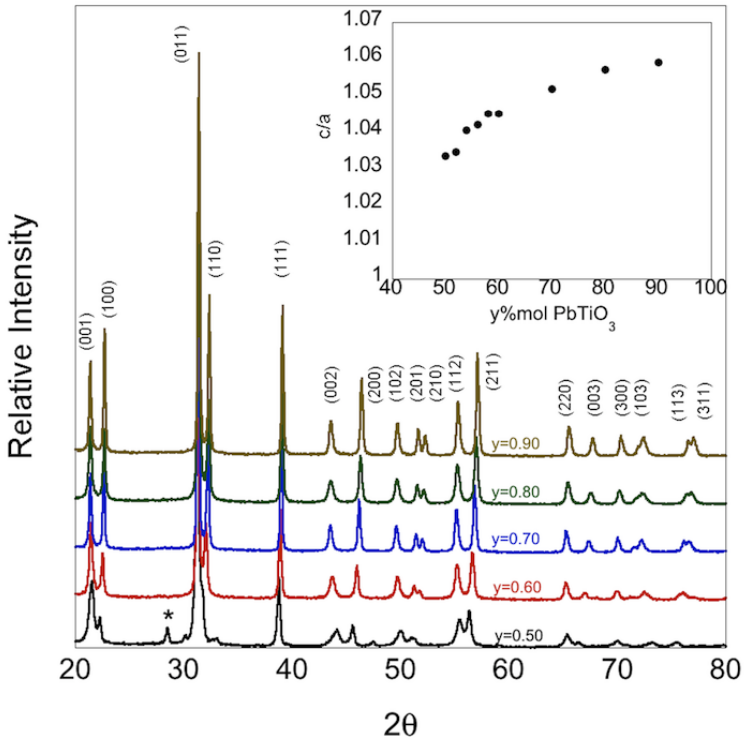

FIGURE 5.3: Structural determination of the PT-BS-BZnT system by XRD. The asterisk indicates second phase. The inset is c/a ratios calculated for all compositions above 50 mol% $PbTiO_3$.

Phase pure compositions with > 60% PT content exhibited high relative permittivities and acceptable dielectric losses. Table 5.1 lists dielectric constants and losses measured at room temperature and 100 °C. Figure 5.4 shows dielectric constant and dielectric loss for compositions with x = 0.90 [Fig. 5.4 (a)], 0.80 [Fig. 5.4 (b)], 0.70 [Fig. 5.4 (c)], and 0.60 [Fig. 5.4 (d)]. The relative permittivity decreased with increasing PT content from $\epsilon_r \approx 20000$ for x = 0.60 down to $\epsilon_r \approx 10000$ for x = 0.70 and 0.80 and then back up to $\epsilon_r \approx 15000$ for the x = 0.90 composition. Permittivities were also highest at all frequencies measured for the composition x = 0.60. As the PT content decreased, the dielectric peak associated with transition from a ferroelectric

to a paraelectric phase broadened. However, transition temperature did not exhibit dependency on measurement frequency. The peak of x = 0.60 is relatively broad as compared to the sharp transition of the x = 0.90 composition due to the influence of local inhomogeneities. The transition temperature, T_C, also increased with increasing PT content with $T_C \approx 520$ °C at x = 0.90, pure PT has its transition around 500 °C.

TABLE 5.1: Dielectric properties of the PT-BS-BZT ternary at room temperature and 100 °C, and a frequency of 1kHz.

	25 °		100 °	
Composition (mol% $PbTiO_3$)	Dielectric constant ϵ_r	Dielectric loss tanδ	Dielectric constant ϵ_r	Dielectric loss tanδ
0.60	460	0.032	580	0.054
0.70	270	0.016	325	0.029
0.80	210	0.035	260	0.062
0.90	170	0.110	230	0.115

In most PT based binaries, T_C decreases as PT content decreases [4,5,7,17]. However, in this BZnT ternary near pure PT, the Curie temperature increases for x = 0.90 and then decreases for lower mol % PT compositions. Suchomel et al. observed this behavior in the PT-BZnT binary, T_C increased from a low of 500 °C at pure PT to a high of 700 °C at x = 0.60 [13]. It was proposed that the increasing transition temperature was due to large tetragonal distortions caused by ferroelectrically active cations in the B-site coupling with A-site cations, Zn and Ti among the proposed cations [13, 14]. All four BZnT compositions approximately followed the Curie-Weiss Law for the ferroelectric to paraelectric transition in ferroelectric crystals. Despite

the large dielectric permittivities and high Curie temperatures in the PT-BS-BZnT ternary, the high losses and large secondary phases made further research in this system undesirable.

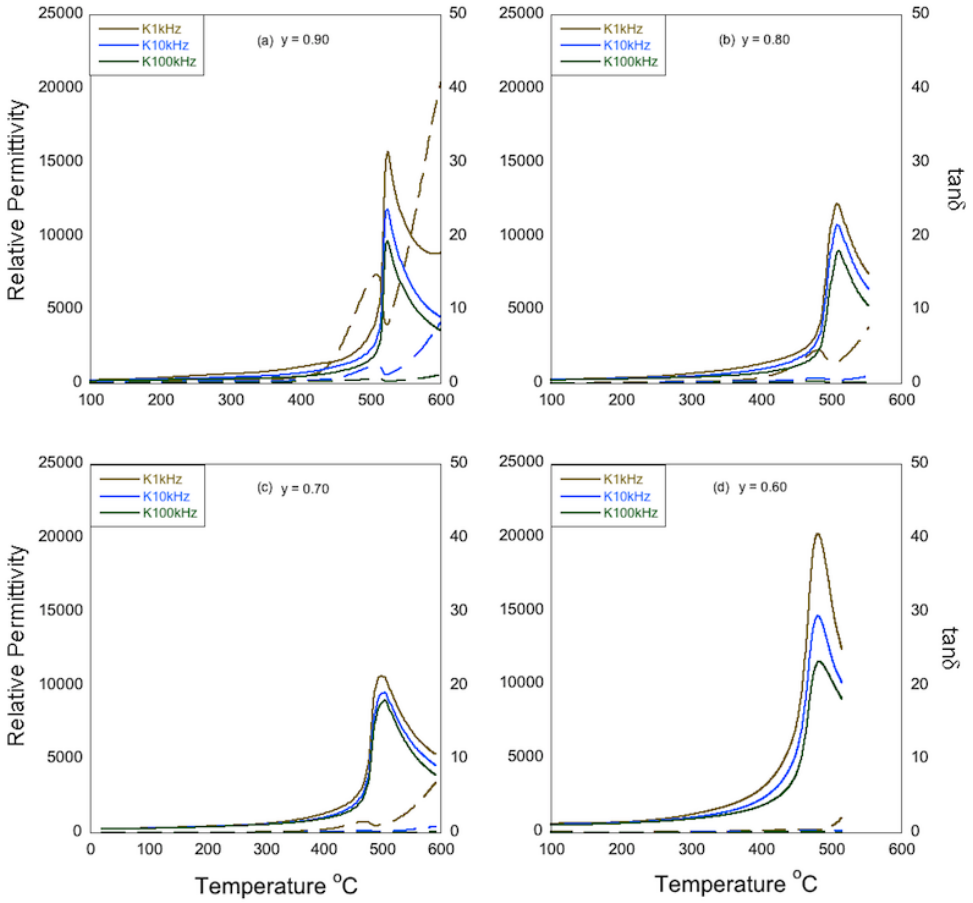

FIGURE 5.4: Dielectric constant and loss tangent as a function of temperature for: (a) x = 0.90, (b) x = 0.80, (c) x = 0.70, and (d) x = 0.60 compositions of the BZnT system.

5.4.2 Structural and electric properties of PT-BS-BMgT

Unlike the BZnT system, PT-BS-BMgT compositions were processed as phase pure perovskite structure to a much wider range of compositions along the %BS = %BMT line (Fig. 5.2). XRD scans and c/a ratios for the BMgT ternary are shown

in Fig. 5.5. When the PT content was below x = 0.48, a minor impurity phase formed with 100 % peak around 2θ = 28°, corresponding to unreacted Bi_2O_3, just as in the BZnT system. In the range of compositions between x = 0.40 and 0.50, a mixture of rhombehedral and tetragonal phases were observed. As the PT content decreased, peak splitting associated with a tetragonal phase disappears (inset in Fig. 5.5). However, as in the BZnT system, a true MPB composition was not observed due to solubility limits [27]. Compositions with greater PT content (> 50%) than the transition region (40% - 50%) exhibited splitting of the (100) and (110) peaks, characteristic of tetragonal

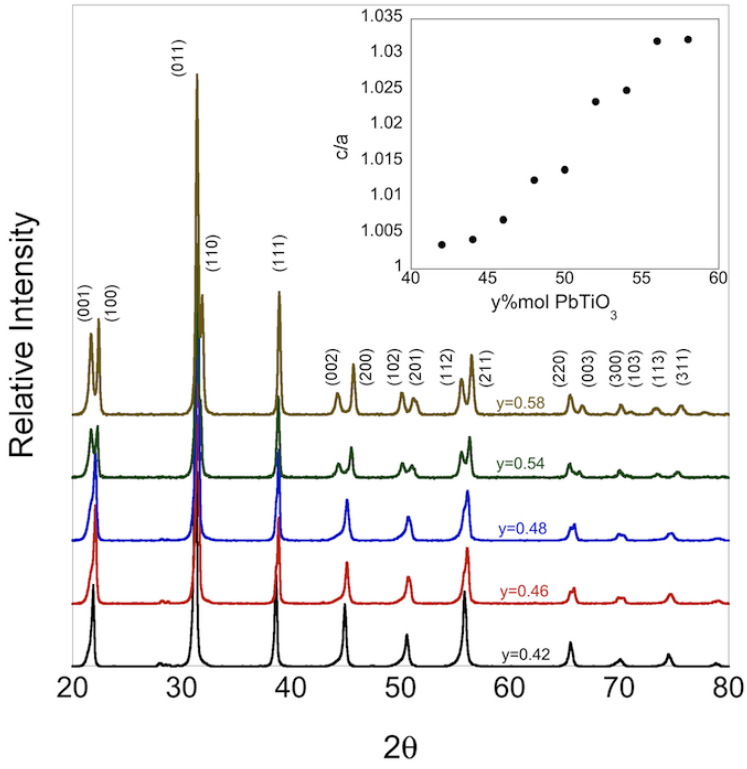

FIGURE 5.5: Structural determination of PT-BS-BMgT system by XRD. The asterisk indicates second phase. Inset, c/a ratios of x = 0.42 to 0.58 compositions.

perovskite phase. In the transition region, the (111) peak began to split into two peaks. Concurrent with the (111) splitting, all tetragonally split peaks such as the (001) and (100) or the (102) and (201) peaks combine which is characteristic of the formation of a rhombohedral phase. The diffuse nature of the (100), (200), (201), (211), and (220) peaks in compositions x = 0.42 and 0.46 may be due to the presence of both tetragonal and rhombohedral phases [27]. A structural transformation was taking place between x = 0.40 and 0.50 mol% PT, however for the compositions with x ≤ 0.40, the second phase peaks grew upwards of 5% in intensity with respect to the (011) peak; the 100% peak of the perovskite phase.

TABLE 5.2: Dielectric properties of the PT-BS-BMT ternary at room temperature and 100 °C, and a frequency of 1kHz.

	25 °		100 °	
Composition (mol% $PbTiO_3$)	Dielectric constant ϵ_r	Dielectric loss tanδ	Dielectric constant ϵ_r	Dielectric loss tanδ
0.42	520	0.031	930	0.038
0.46	530	0.020	790	0.035
0.48	590	0.015	860	0.029
0.50	570	0.016	790	0.026
0.52	740	0.016	1030	0.025
0.54	750	0.014	1080	0.034
0.56	760	0.054	940	0.022
0.58	640	0.011	810	0.023

Table 5.2 tabulates the dielectric permittivities and losses for the PT-BS-BMgT

ternary for compositions x = 0.42 to x = 0.58 mol% PT at both room temperature and 100 °C. Compositions x = 0.42, 0.48, and 0.54, were measured at temperatures up to 650 °C at three different frequencies: 1 kHz, 10 kHz, and 100 kHz (Fig. 5.6). The dielectric maximum observed at a phase transformation was dependent on the measurement frequency. For composition with x = 0.42, Fig. 5.6 (a), a high temperature phase transition was observed at 480 °C. For x = 0.48, Fig. 5.6 (b), measurement at 1 kHz reveals two peaks, the first occurs at a temperature of around 400 °C and the second occurs at a temperature of 540 °C. The second peak is likely due to the high losses at these high temperatures. The same two peak behavior in the permittivity was also observed in the x = 0.54 composition; again the second peak is likely due to the high losses. For composition x = 0.54, the transition occurred at a temperature around 445 °C.

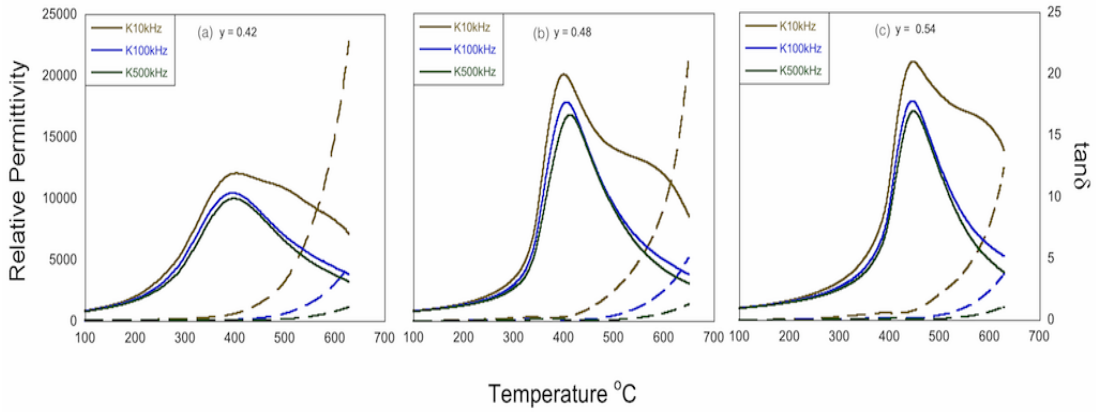

FIGURE 5.6: Dielectric constant and loss tangent as a function of temperature for the BMgT system.

5.4.3 Ferroelectric and piezoelectric properties of PT-BS-BMgT

Figure 5.7 shows ferroelectric hysteresis of compositions x = 0.56, 0.48, and 0.42 at 100 °C after poling according to the procedure summarized in experimental section. The composition x = 0.56 did not form a saturated hysteresis loop indicating

incomplete poling of the system due to large strain associated with rotation of tetragonal compositions with larger c/a ratios. Increasing poling field resulted in breakdown of the specimens indicating that the field required for polarization rotation in these highly tetragonal systems was higher than the breakdown strength of the ceramic. For compositions with lower PT content, polarization dramatically increased. However, for x = 0.48 the ferroelectric loops exhibited high loss, therefore the measured remanent polarization at 100 °C is unlikely to be accurate. The remanent polarization was also measured at room temperature and P_r = 30.0 μC/cm^2 for composition x = 0.48. For the composition x = 0.42, a saturated loop was observed with low loss, allowing the measurement of remanent polarization ($P_r \approx 32.8$ μC/cm^2) and coercive field ($E_C \approx 23.0$ kV/cm).

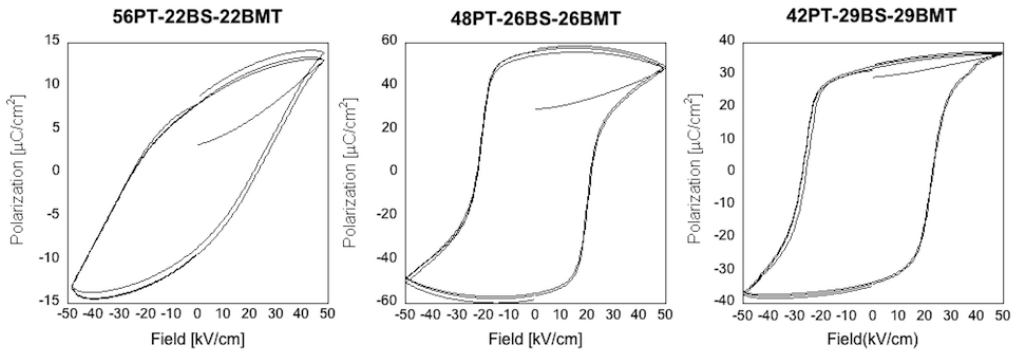

FIGURE 5.7: Ferroelectric hysteresis loops of various PT-BS-BMgT samples at a frequency of 1 Hz.

The field induced strain behavior of a series of PT-BS-BMgT compositions under a 1 Hz bipolar driving field at 100 °C is shown in Fig. 5.8. All compositions showed domain rotation with some asymmetry in the strain data indicating domain wall pinning. The low-field d_{33} values measured on poled samples increased as the PT content decreased to a maximum value of 280 pC/N for the x = 0.42 composition. Unipolar strain data is shown in Fig. 5.9. While the x = 0.56 composition showed large field induced strains, a significant amount of hysteresis was observed due

to insufficient poling conditions. The high-field d_{33}* values, calculated from the maximum strain value at the maximum applied electric field, were highest for the x = 0.42 composition at a value of 313 pm/V.

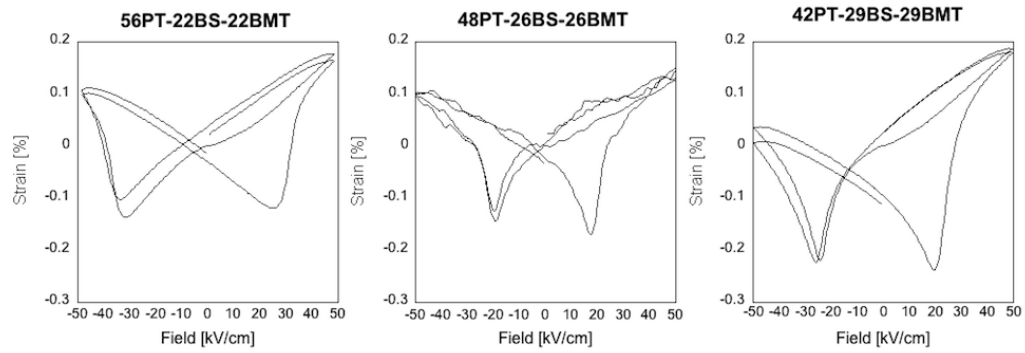

FIGURE 5.8: Bipolar field induced strain data measured at a frequency of 1Hz and at 100 °C.

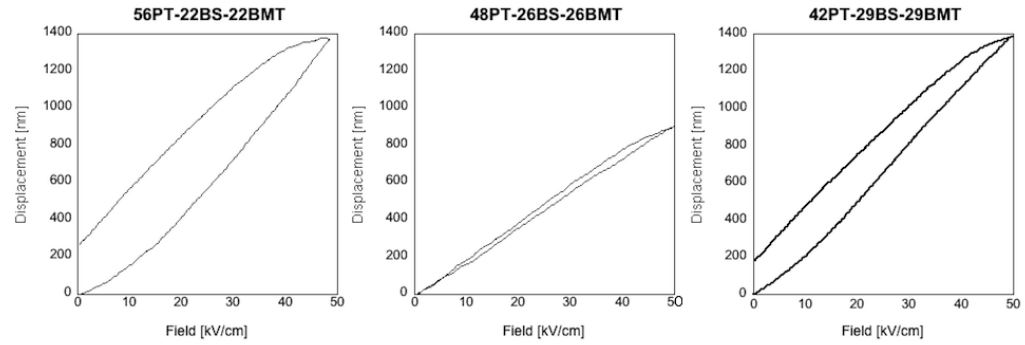

FIGURE 5.9: Unipolar field induced strain data measured at a frequency of 1Hz and at 100 °C.

The resonance method [26], was utilized to measure the planar coupling factor k_p and Table 5.3 lists the measured resonant and anti-resonant frequencies of various BMgT compositions used to calculate the k_p. The highest value of k_p = 0.150 occurred for the composition x = 0.48. The low value of k_p maybe due to low resistivity of samples leading to inefficient poling of the ceramic discs [28, 29]. The same method

was used to indirectly observe the de-poling of poled ceramics. The depolarization temperature of poled samples of PT-BS-BMgT was determined by measuring the degradation of the phase angle at resonance. Once the temperature approached the depolarization temperature, both the phase angle and the resonant and anti-resonant peaks disappeared indicating depolarization. Another way of looking at depolarization is at the point where the electromechanical coupling disappears, the ceramic is said to be de-poled. The x = 0.50 composition exhibited a depolarization temperature of approximately 380 ^{o}C and the x = 0.48 composition exhibited a depolarization temperature of approximately 320 ^{o}C.

TABLE 5.3: Room temperature impedance data of poled PT-BS-BMT ceramics.

Composition (mol% $PbTiO_3$)	Resonant frequency f_r (kHz)	Anti-resonant frequency f_a (kHz)	Electromechanical coupling factor k_p
0.42	225	231	0.054
0.48	213	229	0.150
0.50	220	231	0.110
0.52	218	228	0.100

5.5 Conclusion

Two ternary ceramic systems, PT-BS-BZnT and PT-BS-BMgT, were studied in order to determine the structural, electrical, and piezoelectric properties. Structural transitions were observed for the BMgT system in the range of x = 0.42 - 0.50 mol% PT, while the MPB for the BZnT system could not be accessed because of the limited solid solubility of both $BiScO_3$ and $Bi(Zn_{1/2}Ti_{1/2})O_3$. The x = 0.42 composition exhibited the largest polarization values of $P_r \approx 32.8$ $\mu C/cm^2$ with a coercive field

of $E_C \approx 23.0$ kV/cm at 100 ^oC. Both the BZnT and BMgT systems showed high relative permittivities, with low loss, and high transition temperatures up to $T_C = 540$ ^oC. The optimum piezoelectric properties were obtained for the 42PT-29BS-29BMgT composition with a low-field d_{33} value of 280 pC/N and a high-field d_{33}* value of 310 pC/N, despite a planar factor of only 0.054. The highest coupling factor of 0.150 was obtained for the 48PT-26BS-26BMgT composition indicating that poling conditions were optimum for the possible MBP composition. The depolarization temperature of poled samples in the PT-BS-BMgT system varied between 320 ^oC and 390 ^oC. Based on these properties, these materials have excellent potential for high temperature piezoelectric applications.

5.6 Acknowledgement

The authors would like to acknowledge this work was supported in part through NASA / Oregon Space Grant Consortium, grant NNX10AK68. Dr. Alp Sehirlioglu would like to acknowledge AFOSR grant FA9550-06-1-0260.

5.7 References

1. Zhang, S. J., Randall, C. A. & Shrout, T. R. High Curie temperature piezocrystals in the $BiScO_3$-$PbTiO_3$ perovskite system. *Appl. Phys. Lett.* **83,** 3150–3152 (2003).
2. Jaffe, B., Cook, W. R. & Jaffe, H. *Piezoelectric Ceramics* 1st ed. 317 pp. (Academic Press, New York, 1971).
3. Sehirlioglu, A., Sayir, A. & Dynys, F. Doping of $BiScO_3$-$PbTiO_3$ Ceramics for Enhanced Properties. *J. Am. Ceram. Soc.* **93,** 1718–1724 (2010).
4. Eitel, R. E. *et al.* New High Temperature Morphotropic Phase Boundary Based on $Bi(Me)O_3$-$PbTiO_3$ Ceramics. *Jpn. J. Appl. Phys.* **40,** 5999–6002 (2001).

5. Eitel, R. E., Zhang, S. J., Shrout, T. R. & Randall, C. A. Phase Diagram of the Perovskite System (1-x)$BiScO_3$-x$PbTiO_3$. *J. Appl. Phys.* **96,** 2828–2831 (2004).

6. Jiang, Y. *et al.* Microstructure and Electric Properties of (1-x)Bi($Sc_{0.75}Zn_{0.125}Ti_{0.125}$)$O_3$-x$PbTiO_3$ Ceramics. *Ferroelectrics* **380,** 130–134 (2009).

7. Eitel, R. E., Randall, C. A., Shrout, T. R. & Park, S.-E. Preparation and Characterization of High Temperature Perovskite Ferroelectrics in the Solid-Solution (1-x)$BiScO_3$-x$PbTiO_3$. *Jpn. J. Appl. Phys.* **41,** 2099–2104 (2002).

8. Inaguma, Y. *et al.* High-pressure synthesis and ferroelectric properties in perovskite -type $BiScO_3$-$PbTiO_3$ solid solution. *J. Appl. Phys.* **95,** 231–235 (2004).

9. Leist, T. *et al.* Temperature Dependence of the Piezoelectric Coefficient in $BiMeO_3$-$PbTiO_3$ (Me = Fe, Sc, ($Mg_{1/2}Ti_{1/2}$)) Ceramics. *J. Am. Ceram. Soc.* **95,** 711–715 (2012).

10. Yu, G., Chen, X., Cao, F., Wang, G. & Dong, X. Dynamic ferroelectric hysteresis scaling behavior of 40$BiScO_3$-60$PbTiO_3$ bulk ceramics. *Solid State Commun* **150,** 1045–1047 (2010).

11. Gotmare, S. W., Leontsev, S. O. & Eitel, R. E. Thermal Degradation and Aging of High-Temperature Piezoelectric Ceramics. *J. Am. Ceram. Soc.* **93,** 1965 (2010).

12. Stringer, C. J., Shrout, T. R., Randall, C. A. & Reaney, I. Classification of Transition Temperature Behavior in Ferroelectric $PbTiO_3$-Bi(Me'Me")O_3 Solid Solutions. *J. Appl. Phys.* **99,** 0241061–0241064 (2006).

13. Suchomel, M. R. & Davies, P. K. Enhanced Tetragonality in (x)$PbTiO_3$-(1-x)Bi($Zn_{1/2}Ti_{1/2}$)O_3 and Related Solid Solution Systems. *Appl. Phys. Lett.* **86,** 2629051–2629053 (2005).

14. Grinberg, I. *et al.* Structure and Polarization in the High T_C Ferroelectric Bi(Zn, Ti)O_3-$PbTiO_3$ Solid Solutions. *Phys. Rev. Lett.* **98,** 107601 (2007).

15. Zhang, X. D., Kwon, D. & Kim, B. G. Structural evolution of a high T_C ferroelectric (x)Bi($Zn_{1/2}Ti_{1/2}$)O_3-$PbTiO_3$ solid solution. *Appl. Phys. Lett.* **92,** 082906 (2008).

16. Sharma, S. & Hall, D. A. Ferroelectric and Antiferroelectric Polarization Switching Characteristics of Bi($Mg_{0.5}Ti_{0.5}$)O_3-$PbTiO_3$ Ceramics. *J. Mater. Sci.: Mater. Electron.* **21,** 405–409 (2010).

17. Rai, R., Sinha, A., Sharmac, S. & Sinha, N. K. P. Investigation of structural and electrical properties of (1-x) $Bi_{0.5}Mg_{0.5}TiO_3$-(x)$PbTiO_3$ ceramic system. *J. Alloys Compd.* **486,** 273–277 (2009).

18. Takenaka, T. & Yamada, M. Solid-Solution ($Bi_{1-x}Pb_x$)($Ni_{(1+x)/2}Ti_{(1+x)/2}$)O_3 for New Piezoelectric Ceramics. *Jpn. J. Appl. Phys.* **32,** 4218–4222 (1993).

19. Choi, S. M., Stringer, C. J., Shrout, T. R. & Randall, C. A. Structure and Property Investigation of a Bi-based Perovskite Solid Solution: (1-x)Bi($Ni_{1/2}Ti_{1/2}$)O_3-x$PbTiO_3$. *J. Appl. Phys.* **98,** 0341081–0341084 (2005).

20. Song, T. H., Eitel, R. E., Shrout, T. R., Randall, C. A. & Hackenberger, W. Piezoelectric Properties in the Perovskite $BiScO_3$-$PbTiO_3$-(Ba,Sr)TiO_3 Ternary System. *Jpn. J. Appl. Phys.* **42,** 5181–5184 (2003).

21. Sehirlioglu, A., Sayir, A., Dynys, F., Nittala, K. & Jones, J. Structure and Piezoelectric Properties Near the Bismuth Scandium Oxide-Lead Zirconate-Lead Titanate Ternary Morphotropic Phase Boundary. *J. Am. Ceram. Soc.* **94,** 788–795 (2011).

22. Stein, D. M., Grinberg, I., Rappe, A. M. & Davies, P. K. Multiple dielectric transitions in the $PbTiO_3$-Bi($Zn_{1/2}Ti_{1/2}$)O_3-BI($Mg_{1/2}Ti_{1/2}$)O_3 system. *J. Appl. Phys.* **110,** 074110 (2011).

23. Sebastian, T. *et al.* High temperature piezoelectric ceramics in the Bi($Mg_{1/2}Ti_{1/2}$)O_3-$BiFeO_3$-$BiScO_3$-$PbTiO_3$ system. *J. Electroceram.* **25,** 130–134 (2010).

24. Eitel, R. E., Shrout, T. R. & Randall, C. A. Nonlinear contributions to the dielectric permittivity and converse piezoelectric coefficient in piezoelectric ceramics. *J. Appl. Phys.* **99,** 124110 (2006).

25. Haertling, G. H. Ferroelectric Ceramics: History and Technology. *J. Am. Ceram. Soc.* **82,** 797–818 (1999).

26. *ANSI/IEEE 176-1987, IEEE Standard on Piezoelectricity* (IEEE, New York, 1987).

27. Randall, C. A. *et al.* Investigation of a high T_C piezoelectric system: (1-x)Bi($Mg_{1/2}$ $Ti_{1/2}$)O_3-(x)$PbTiO_3$. *J. Appl. Phys.* **95,** 3633–3639 (2004).

28. Zhang, S. J., Alberta, E. F., Eitel, R. E., Randall, C. A. & Shrout, T. R. in *IEEE Transactions on Ultrasonics, Ferroelectrics, and Frequency control* **52** (IEEE, 2005), 11.

29. Zhang, S. J. & Yu, F. Piezoelectric materials for high temperature sensors. *J. Am. Ceram. Soc.* **94,** 3153–3170 (2011).

6 High Temperature Piezoelectric Ceramics based on (1-x)[$BiScO_3$ + $Bi(Ni_{1/2}Ti_{1/2})O_3$] - x$PbTiO_3$

Troy Y. Ansell and David P. Cann

Materials Science, School of Mechanical, Industrial, and Manufacturing Engineering, Oregon State University, Corvallis, OR, 97331, U.S.A.

Published in

Materials Letters

Volume 80, 87 - 90 (2012)

6.1 Abstract

High temperature ferroelectrics are an important aspect of piezoelectric materials research for many energy related applications. Some of the desired properties are high Curie temperature, large remanent polarization, and large piezoelectric coefficients. Polycrystalline perovskite ceramics of the composition (1-x)[$BiScO_3$+$Bi(Ni_{1/2}Ti_{1/2})O_3$] - x$PbTiO_3$ (BS-BNiT-PT), were synthesized using standard solid state processing. Room temperature x-ray diffraction revealed a perovskite phase with an observed transition from tetragonal to pseudo-cubic symmetry over the compositional range x = 0.50 - 0.60. Compositions rich in $PbTiO_3$ showed strong tetragonal distortions with characteristic first-order phase transitions. As the $PbTiO_3$ content decreased dielectric measurements revealed large permittivities ($\epsilon_r' \approx$ 16,000) with relaxor characteristics up to 400 ^oC. Ferroelectric hysteresis measurements revealed remanent polarizations as high as 31 $\mu C/cm^2$ at x = 0.52 with relatively low coercive fields of 25 kV/cm. The piezoelectric coefficients, mechanical quality, and planar coupling factors of the x = 0.54 composition were 376 pC/N, 13.4, and 0.148, respectively.

6.2 Introduction

High temperature piezoelectric actuators are of current interest for a variety of different applications ranging from commercial turbine engines to interplanetary probes. Currently, lead zirconate titanate or PZT has been the most widely used actuator material due its exemplary properties, such as d_{33} = 233 pC/N for undoped PZT [1], d_{33} = 750 pC/N for Navy Type IV/PZT 5H, or d_{33} = 375 pC/N for Navy Type II/PZT 5A [2]. Despite the excellent electrical properties, the relatively low Curie temperature and operating temperature prohibits the use of PZT from some of the more demanding actuator applications. A number of studies have been conducted to develop materials with comparable properties to PZT with transition temperatures higher than 400 ^oC. Several groups have studied the binary composition (1-x)$BiScO_3$

- $xPbTiO_3$ (BS-PT) and found a morphotropic phase boundary (MPB) at x = 0.65 with ferroelectric properties comparable to PZT [2–6][2Ð6]. Another promising binary composition is $(1-x)Bi(Ni_{0.5},Ti_{0.5})O_3$ - $x\ PbTiO_3$ (BNT-PT) with a rhombehedral - tetragonal MPB between x = 0.40 and 0.50 and moderately high piezoelectric and mechanical properties with a ferroelectric to paraelectric transition above 400 °C [7, 8].

The effects of doping by various oxides on these binaries have also been studied. Sehirlioglu et al. observed that doping with Zr for Sc onto the B-site of BS-PT increased the depolarization temperature while decreasing the Curie temperature. In addition, they observed that the remanent polarization increased and the coercive field decreased [2]. Zhang et al. showed that Mn_2O_3 doping decreased the dielectric loss of BS-PT [6]. Doping of the BNT-PT system by Mn_2O_3 also showed a decreased dielectric loss, however, at the cost of a decreased d_{33} constant [8]. Another technique to improve materials properties is to include excess amounts of the volatile element in the solid solution such including excess PbO or Bi_2O_3 in the batch composition. Sehirlioglu et al. showed that 5 at% excess Bi_2O_3 effectively increased the resistivity of BS-PT while excess PbO increased the AC conductivity [3]. In this work, the latter approach is taken to investigate the ternary ferroelectric composition $(1-x)[BiScO_3+Bi(Ni_{1/2}Ti_{1/2})O_3]$ - $xPbTiO_3$ (BS-BNiT-PT).

6.3 Experimental

All ceramic samples were prepared with the use of standard metal oxide powder processing. Starting materials of high purity metal oxides and carbonates including PbO (99.9%), Bi_2O_3 (99.9%), TiO_2 (99.0%), NiO (99.9%), and Sc_2O_3 (99.9%) were weighed according to the compositions $(1-x)[BiScO_3+Bi(Ni_{1/2}Ti_{1/2})O_3]$ - $xPbTiO_3$. Excess Pb (2 mol%) was added to each composition to prevent Pb loss during calcinations and sintering. A vibratory milling machine was used to grind and mix the

prepared batches for 6 h. The batches were then dried and calcined in an alumina crucible at 950 ^{o}C for 4 - 6 h. Prior to the sintering stage, the calcined powders were again mixed in the vibratory mill for 6 h, and then dried. The powders were finally uniaxially cold and dry pressed at 34.5 MPa for 3 min into thin discs. The resulting pellets were sintered in an alumina crucible for 4 h at 1100 - 1150 ^{o}C depending on composition. Sintered ceramics were polished down to around $\approx$ 0.800 mm thickness. Silver electrodes were fired onto ceramics at 700 ^{o}C for high temperature dielectric and ferroelectric testing.

X-ray diffraction (Bruker AXS Inc. D8 Discover, Madison, WI, USA) was used to determine the phase purity and crystal structure. Ceramic samples were placed into a sample holder (NorECs AS ProbostatTM, Oslo, Norway) in between two Pt electrodes. The temperature dependence of permittivity and dissipation was then measured using an LCR meter (Agilent 4263B, Santa Clara, CA) from room temp up to $\approx$650 ^{o}C. Samples were poled at 40 kV/cm and 100 ^{o}C for 30 min inside a 9023 chamber furnace (Delta Design Inc., San Diego, CA), then taken outside the box for 30 min while under continued electromechanical poling. Polarization and electromechanical strain were measured at an electric field of 40 kV/cm at room temperature by a standard ferroelectric test system (Radiant Technologies RT66A, Albuquerque, New Mexico) coupled with a fiber-optic sensor (MTI-2100 Fotonic Sensor, MTI Instruments Inc., Albany, NY) at room temperature.

6.4 Results and Discussion

A number of compositions in the (1 - x)(0.5BS-0.5BNiT) - xPT ternary system were prepared via solid-state synthesis techniques. As shown in Fig. 6.1, compositions from x = 0.50 to 0.60 were found to form a single perovskite phase within the limits of x-ray diffraction. Compositions below 50 mol% $PbTiO_3$ included a significant fraction of secondary phases composed of unincorporated Bi_2O_3. Therefore

the perovskite stability limit for this ternary system is near x = 0.50. The XRD data also revealed a transition in symmetry over the solubility range, between x = 0.50 and 0.54. At high $PbTiO_3$ content as in x = 0.58 and 0.56, a high degree of tetragonal splitting is observed in the (100) and (110) reflections which is characteristic of perovskite tetragonal symmetry. As the $PbTiO_3$ content decreased, the peak splitting decreased in all reflections. At the solubility limit, some minor peak distortions were observed which could indicate pseudo-cubic symmetry or the co-existence of multiple perovskite phases [7] (Fig. 6.2).

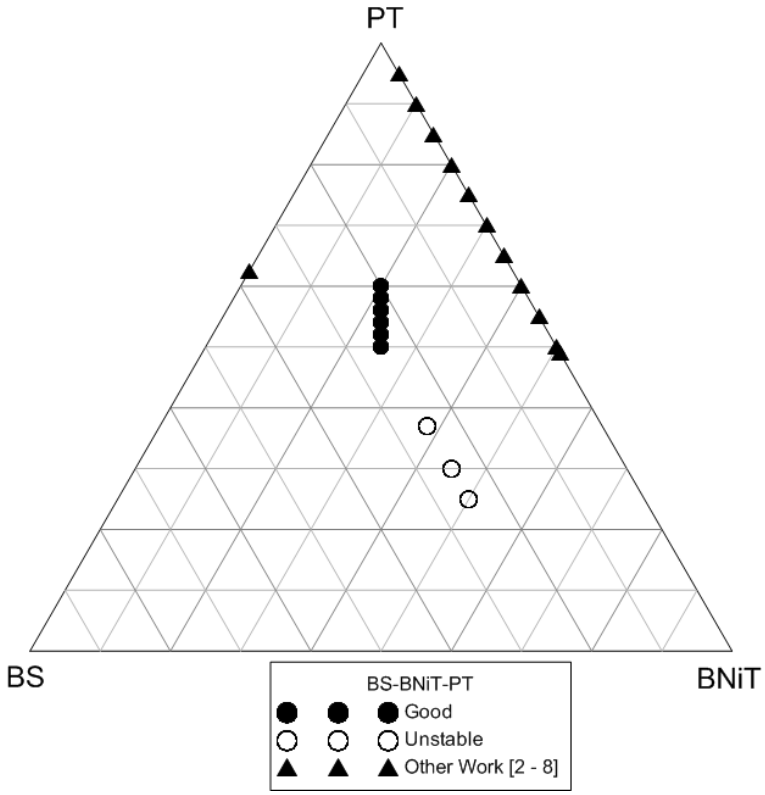

FIGURE 6.1: Ternary phase diagram of the BS-BNiT-PT ternary perovskite compositions in this study.

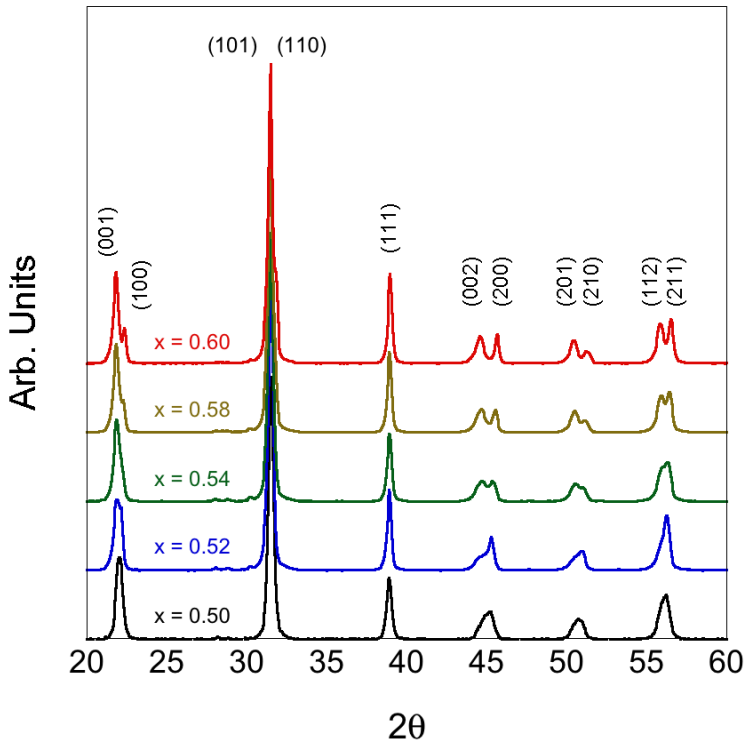

FIGURE 6.2: XRD data for ceramic specimens of x=0.50 to 0.58 compositions indexed to a perovskite unit cell.

The dielectric properties were measured for compositions over the range of x = 0.52 to x = 0.60. In Fig. 6.3 (a - c), the permittivity and the dielectric loss at 1 kHz, 10 kHz, and 100 kHz were measured from 100 °C to 600 °C. Figure 6.3 (d) compares the relative permittivity and loss, at 10 kHz, for compositions x = 0.52 to 0.60. A high dielectric constant and low loss were observed for the 60 mol% $PbTiO_3$ composition with a sharp phase transition at 415 °C typical of a tetragonal-to-cubic transition. As the $PbTiO_3$ content decreased, the transition temperature decreased and became more diffuse. At the composition x = 0.54, a noticeable broadening of the transition and a decrease in the transition temperature to approximately 370 °C was observed. In Fig. 6.3 (c), the dielectric maximum for the x = 0.52 composition was around 335 °C with a further broadening in the transition.

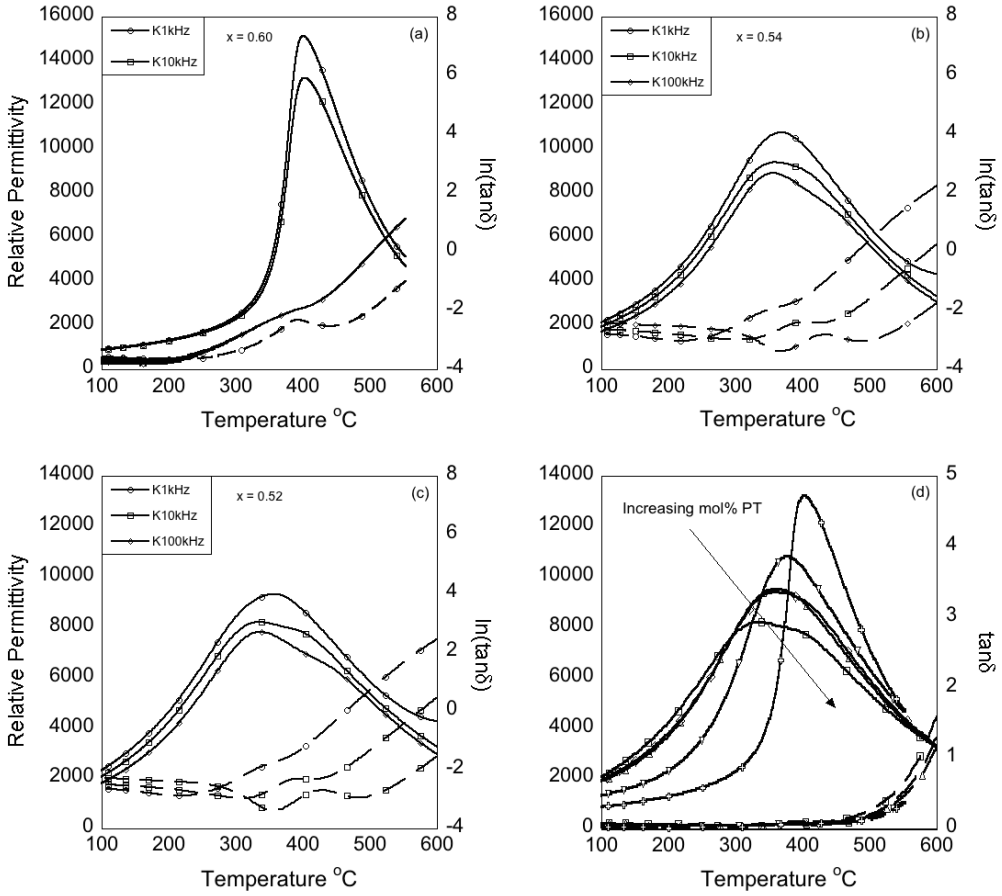

FIGURE 6.3: Dielectric measurements on: (a) x = 0.60, (b) x = 0.54, and (c) x = 0.52 compositions. Dielectric permittivity and loss are plotted in (d) for compositions x = 0.52 to 0.60 at a frequency of 10 kHz.

In Fig. 6.4, bipolar polarization versus electric field on ceramic specimens reveal remanent polarizations in these compositions decreased from approximately 30 to 20 $\mu C/cm^2$ as the $PbTiO_3$ content increased. Furthermore, as the $PbTiO_3$ content increased, the coercive field increased such that compositions rich in PbTiO3 became increasingly difficult to achieve saturation. The remanent polarization saw a maximum of 31.4 $\mu C/cm^2$ for x = 0.52 shrinking down to 4.9 $\mu C/cm^2$ for the x = 0.60 composition.

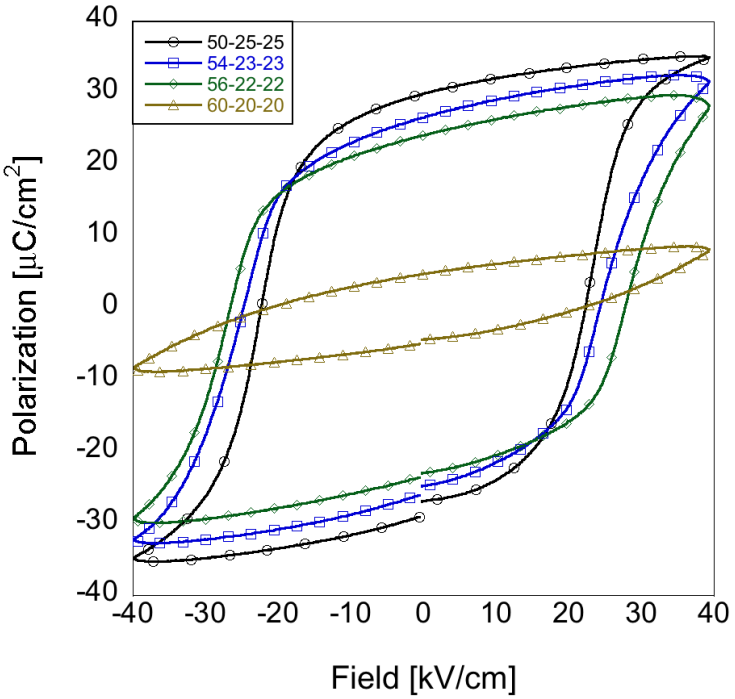

FIGURE 6.4: Polarization versus electric field for compositions x = 0.50 to 0.60.

Bipolar electromechanical strain measurements on poled specimens shown in Fig. 6.5 (a) - 6.5 (c) show characteristic asymmetry due to the strain on poled ceramics. Compositions rich in $PbTiO_3$, e.g. x = 0.58 (Fig. 6.5 (a), had relatively low strain values due to the high coercive field. As the $PbTiO_3$ content decreased larger strain values could be attained. In Figs. 6.5 (d) - 6.5 (f), unipolar strain data show large relative strains for the x = 0.54 composition. Low field d_{33} measurements revealed large piezoelectric coefficients for the compositions with 52 and 54 mol% $PbTiO_3$ with d_{33} = 349 pC/N and d_{33} = 376 pC/N, respectively. Remanent polarizations also show a maximum with 31.4 $\mu C/cm^2$ and 26.4 $\mu C/cm^2$ for x = 0.52 and 0.54 compositions, respectively. The piezoelectric coefficient d_{33} and remanent polarizations show that optimum properties coincide with the transition in perovskite symmetry seen in the XRD data between x = 0.52 and 0.54. This suggests that an MPB exists near this

composition or there is a coexistence of multiple perovskite phases.

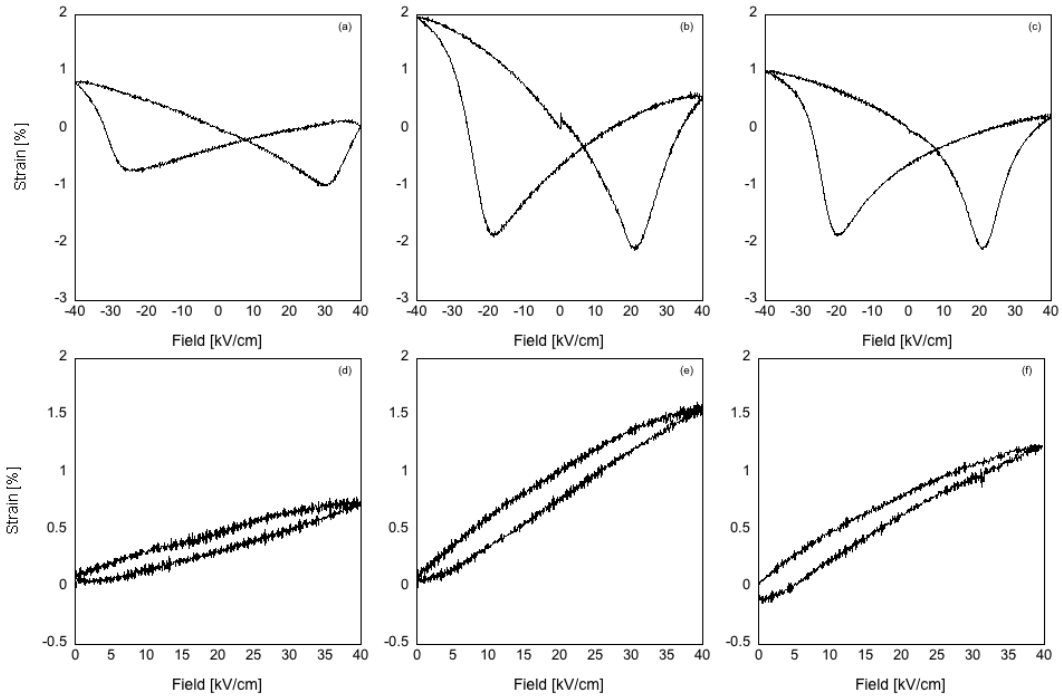

FIGURE 6.5: Bipolar and unipolar electromechanical strain data for compositions x = 0.58 (a, d), 0.54 (b, e), and 0.52 (c, f).

6.5 Conclusion

This investigation into the ternary perovskite system (PT-BS-BNiT) revealed new ferroelectric materials with great promise for use as high temperature piezoelectric actuators. X-ray diffraction data revealed stable perovskite phases in compositions with $x \geq 0.50$ and transition in symmetry from tetragonal distortions to pseudo-cubic symmetry over the compositional range $x = 0.50$ and $x = 0.54$. Dielectric measurements showed a shift from relaxor behavior at $x = 0.50$ to a first order ferroelectric transition at $x = 0.60$ with relatively high Curie temperatures. Ferroelectric and electromechanical strain measurements revealed large piezoelectric strains

and optimal piezoelectric properties for the x = 0.54 composition with d_{33} = 376 pC/N, Q_M = 14.9, and k_p = 0.13. These data suggest that excellent piezoelectric properties are tied to the transition in the perovskite symmetry over the compositional range x = 0.52 and 0.54.

6.6 Acknowledgements

The authors would like to acknowledge this work was supported in part through NASA / Oregon Space Grant Consortium, grant NNX10AK68. Dr. Alp Sehirlioglu would like to acknowledge AFOSR grant FA9550-06-1-0260.

6.7 References

1. Jaffe, B., Cook, W. R. & Jaffe, H. *Piezoelectric Ceramics* 1st ed. 317 pp. (Academic Press, New York, 1971).
2. Sehirlioglu, A., Sayir, A. & Dynys, F. Doping of $BiScO_3$-$PbTiO_3$ Ceramics for Enhanced Properties. *J. Am. Ceram. Soc.* **93,** 1718–1724 (2010).
3. Sehirlioglu, A., Sayir, A. & Dynys, F. Microstructural-Property Relationships in Liquid Phase-Sintered High-Temperature Bismuth Scandium Oxide-Lead Titanate Piezoceramics. *J. Am. Ceram. Soc.* **91,** 2910–2916 (2008).
4. Gotmare, S. W., Leontsev, S. O. & Eitel, R. E. Thermal Degradation and Aging of High-Temperature Piezoelectric Ceramics. *J. Am. Ceram. Soc.* **93,** 1965 (2010).
5. Jiang, Y. *et al.* Microstructure and Electric Properties of (1-x)$Bi(Sc_{0.75}Zn_{0.125}Ti_{0.125})O_3$-x$PbTiO_3$ Ceramics. *Ferroelectrics* **380,** 130–134 (2009).
6. Zhang, S. J., Alberta, E. F., Eitel, R. E., Randall, C. A. & Shrout, T. R. in *IEEE Transactions on Ultrasonics, Ferroelectrics, and Frequency control* **52** (IEEE, 2005), 11.

7. Takenaka, T. & Yamada, M. Solid-Solution $(Bi_{1-x}Pb_x)(Ni_{(1+x)/2}Ti_{(1+x)/2})O_3$ for New Piezoelectric Ceramics. *Jpn. J. Appl. Phys.* **32,** 4218–4222 (1993).

8. Choi, S. M., Stringer, C. J., Shrout, T. R. & Randall, C. A. Structure and Property Investigation of a Bi-based Perovskite Solid Solution: (1-x)$Bi(Ni_{1/2}Ti_{1/2})O_3$-x$PbTiO_3$. *J. Appl. Phys.* **98,** 0341081–0341084 (2005).

7 Piezoelectric properties of the high temperature MPB $xPbTiO_3$ - (1 - x)[$BiScO_3$ + $Bi(Ni_{1/2}Ti_{1/2})O_3$] composition

Troy Y. Ansell and David P. Cann

Materials Science, School of Mechanical, Industrial, and Manufacturing Engineering, Oregon State University, Corvallis, OR, 97331, U.S.A.

Published in

Journal of Electroceramics

Volume 31, 159 - 167 (2013)

7.1 Abstract

The ternary perovskite $xPbTiO_3$ - (1 - x)[$BiScO_3$ + $Bi(Ni_{1/2}Ti_{1/2})O_3$] (PT-BS-BNiT), where x = 0.54 is the morphotropic phase boundary composition, was studied for high temperature ferroelectric applications. Polycrystalline ceramics were prepared using the standard solid-state methods. The stoichiometric ceramic was found to have room temperature dielectric permittivity and loss values at 1 kHz of 1490 and 0.049 respectively. Piezoelectric properties, of the stoichiometric composition, measured included: P_r = 31.0 μC/cm^2, E_C=25.0 kV/cm, d_{33}=340 pC/N, d_{33}* = 896 pm/V, and a bipolar electromechanical strain of 0.25 %. From these data, the Curie temperature was T_C = 370 ^{o}C and the depoling temperature was T_D = 325 ^{o}C. Processing ceramics with excess bismuth improved the low field piezoelectric coefficients with a maximum of d_{33} = 445 pC/N, while increasing the lead content increased the transition temperatures. The depoling and Curie temperatures of all compositions were measured to be between 275 and 400 ^{o}C.

7.2 Introduction

Since the discovery of ferroelectricity in Rochelle salt in 1921 [1], many materials exhibiting ferroelectric behavior have been discovered. The most widely used and studied ferroelectric materials include barium titanate ($BaTiO_3$) and lead zirconium titanate ($xPbTiO_3$-(1-x)$PbZrO_3$) or PZT. The latter, PZT, has been used extensively for several ferroelectric applications including ferroelectric random access memory (FeRAM) [2], as a heat sensor and other pyroelectric applications [3], in piezoelectric sensor applications such as in battery and tire pressure sensors [4], and piezoelectric actuator applications such as piezoelectric microelectromechanical (MEMS) systems [5]. In the field of high temperature piezoelectric transducers, PZT remains the standard material though its operating temperature is limited by depolarization processes that become prevalent at temperatures near 150 - 200 ^{o}C [6–8].

High temperature piezoelectric sensors and actuators are of interest for a variety of different applications ranging from commercial turbine engines to deep-sea drilling and interplanetary probes. The dominance of PZT in piezoelectric applications is due to its excellent properties including large piezoelectric coefficients (d_{33}, d_{31}, and d_{15}), high dielectric constant and low dielectric loss, high polarizability, a relatively high transition temperature, and a large degree of solubility which allows a selection of dopants with PZT to engineer the properties of the final device [9].

The composition at the morphotropic phase boundary or MPB (52PT-48PZ) possesses the largest piezoelectric coefficients and coupling factors [10]. The piezoelectric properties of PZT at the MPB include d_{33} = 233 pC/N, d_{31} = - 93.5 pC/N, and d_{15} = 494 pC/N for the un-doped MPB composition [9]. Mechanical coupling in un-doped MPB PZT was measured to be $k_p = 0.52$, $k_{33} = 0.67$, $k_{31} = 0.31$, and $k_{15} = 0.69$ [9]. Relatively high dielectric constants and a low dissipation factor of 0.004 were also measured for the MPB PZT composition [9]. Relatively high transition temperature or Curie temperature was also reported for MPB PZT at T_C = 386 ^oC [9]. Doping and substitution of PZT causes substantial changes in the macroscopic properties previously listed. Donor doping of PZT, such as a soft PZT like Navy typeIV/PZT 5H, leads to higher piezoelectric response, d_{33} = 750 pC/N, but lowers the transition temperature to $T_C \approx 195\ ^oC$ as compared to un-doped PZT. Acceptor doping, such as in a hard PZT like Navy type II/PZT 5A, also leads to a higher piezoelectric coefficient of d_{33} = 375 pC/N, but again the transition temperature is lowered to T_C = 370 ^oC [9–11]. Despite these impressive properties, the Curie temperature of PZT, in both doped and un-doped form, is too low for many high temperature applications. Especially, the rapid degradation of piezoelectric properties of PZT beyond a temperature of $\approx 200\ ^oC$ effectively limits the use of PZT at elevated temperatures [12]. Therefore, new materials have been developed with the goal of achieving the same or improved piezoelectric properties of PZT with transition temperatures exceeding 400 ^oC.

Because transition temperatures of PZT-based compositions do not typically

exceed 400 ^{o}C, alternative families of high temperature piezoelectric perovskite ceramics based on solid solutions with PT have been developed. Some examples of PT based piezoelectric ceramics include binary solid solutions such as ($xPbTiO_3$ -(1-x)$BiScO_3$, PT-BS) [11–20], ($xPbTiO_3$-(1-x)Bi(M',Ti)O_3, PT-BMT) [12, 21–25], where M' = Zn, Mg, or Ni, and ($xPbTiO_3$-(1-x)[Bi($Mg_{1/2}Ti_{1/2}$)O_3- $BiFeO_3$-$BiScO_3$], PT-BMTFS) [26]. The MPB composition of PT-BS at $x \approx 0.65$ [13–15, 19, 20], exhibited a high Curie temperature (T_C = 460 ^{o}C), high piezoelectric constants (d_{33} = 450 pC/N), and dielectric properties comparable to PZT [15, 19]. Added to these impressive improvements over PZT, the upper operating temperature of PT-BS, otherwise known as the depoling temperature, T_D, was found to be approximately 350 ^{o}C [12, 18]. Despite these outstanding properties, the expense of Sc_2O_3 makes it desirable to develop a material with the similar improvements over PZT in piezoelectric properties with the same high transition temperatures, T_C and T_D, as PT-BS while replacing scandium in part or in full with another ferroelectrically active cation. For example, Sebastian et al. developed the PT-BMTFS system replacing Sc_2O_3 with Fe_2O_3 to lower the cost of piezoelectric material [26–28].

In previous work, a number of PT based ternary perovskite piezoelectric systems were developed for high temperature applications including ($xPbTiO_3$ - (1-x)[$BiScO_3$ + Bi($Zn_{1/2}Ti_{1/2}$)O_3], PT-BS-BZnT), ($xPbTiO_3$ - (1-x)[$BiScO_3$ + Bi($Mg_{1/2}Ti_{1/2}$)-O_3], PT-BS-BMgT), and ($xPbTiO_3$ - (1-x)[$BiScO_3$ + Bi($Ni_{1/2}Ti_{1/2}$)O_3], PT-BS-BNiT) [29]. The PT-BS-BNiT ternary system showed the most promise in achieving high piezoelectric performance with a high T_C and T_D. The MPB composition at x=0.54 (54PT-23BS- 23BNiT), exhibited the highest piezoelectric coefficient of d_{33} = 376 pC/N and highest remanent polarization of P_r = 29.0 μC/cm^2 [29] respectively. This paper will investigate the piezoelectric properties and depolarization temperature of PT-BS-BNiT ternary ceramics as well as to examine the influence of the Bi^{3+} and Pb^{2+} stoichiometry.

7.3 Experimental

The focus of this work is on the composition xPT-(1-x)[BS-BNiT] with x = 0.54 with varying Bi and Pb stoichiometries in order to account for the effects of volatility. Ceramic samples were prepared by the standard solid-state reaction method. Starting powders of PbO (99.9 %, Sigma-Aldrich), Bi_2O_3 (99.9 %, Sigma-Aldrich), TiO_2 (99.0 %, Sigma-Aldrich), NiO (99.99 %, Sigma-Aldrich), and Sc_2O_3 (99.995 %, Stanford Materials Corp.) were batched and milled with yttria-stabilized zirconia milling pellets for 6 h in a vibratory milling machine. Batched powders were then dried in an oven at 100 ^oC, after which dried samples were calcined at 950 ^oC for 4 h; heating and cooling rates were 3 ^oC/minute. Calcined powders were milled for another 6 h and dried. Powders were then pressed, ≈ 34.5 MPa, into green discs with polyvinyl butyral (PVB) used as the binder. Discs were then heated to 400 ^oC at a 5 ^oC/minute heating rate, and held for 4 h to burn off the binder, after which the discs were heated up to 1150 ^oC at a 3 ^oC/minute heating rate and held for four hours. Newly sintered ceramic samples were then polished down to a thickness of approximately 0.800 mm to obtain an approximate diameter to thickness ratio of approximately 10:1.

The crystal structure of polished ceramics was determined by x-ray diffraction (Bruker AXS Inc. D8 Discover, Madison, WI, USA). Silver paste was then applied to samples and electrodes were fired at 700 ^oC for 30 min. Samples were then placed in between two Pt electrodes within an alumina tube (NorECs AS ProbostatTM, Oslo, Norway) and heated up to 650 ^oC for 1 h. Using a LCR meter (Agilent 4263B, Santa Clara, CA), the dielectric permittivity and loss were measured on un-poled samples, as a function of temperature, measured by a temperature reader (Dpi32 - C24, Omega Engineering, Inc., Stamford, CT).

Poling of specimens was conducted inside an environmental chamber (Delta Design Inc., San Diego, CA). Samples were place between two electrodes and heated up to 100 ^oC for 1 h. A DC electric field of 40 kV/cm was then applied across the samples for 30 min. After 30 min, the ceramics were taken out of the furnace and

allowed to cool down to room temperature while the field was still applied for another 30 min. Hysteresis and electromechanical strain measurements were taken inside a standard ferroelectric testing system (Radiant Technologies, Premier Precision II, Albuquerque, New Mexico) at room temperature. The field applied was 40 kV/cm and the hysteresis measurement frequency was 1 Hz following similar bulk ferroelectric measurement applications [19, 30]. Strain measurements were averaged over five loops while using a fiber-optic sensor (MTI-2100 Fotonic Sensor, MTI Instruments Inc., Albany, NY). The converse piezoelectric coefficient (d_{33}* [pm/V]) is calculated from the ratio of the maximum unipolar strain and the maximum applied electric field [10, 31].

Three different methods were used to measure the depoling temperature T_D: an ex-situ d_{33} technique, analysis of the dielectric loss in log scale, and impedance spectroscopy. For the ex-situ d_{33} approach, poled samples were placed in a furnace and heated to temperatures ranging from 100 ^{o}C to 350 ^{o}C in 25 ^{o}C steps, and held at the measurement temperature for 1 h. After which the samples were cooled down to room temperature and the direct piezoelectric coefficient (d_{33} [pC/N]) was measured using a YE2730A d_{33} meter (Sinoceramics Inc., Shanghai, China). Following the resonance method set by the IEEE standard on piezoelectrics [32], poled samples were placed in the same set-up as the dielectric measurements and heated to incrementally higher temperatures from room temperature up to 400 ^{o}C. The samples were allowed to soak at predetermined temperatures for an hour after which an impedance spectrum is measured for frequencies from 1 Hz to 1 MHz.

Measurements of grain size started with the microstructural imaging by the field emission scanning electron microscope (SEM) Quanta TM 600 FEG SEM (FEI Company, Hillsboro, OR, USA). Afterwards the Abrams Three-Circle procedure, stated in the standard testing methods of the American Society for Testing and Materials was applied to SEM images to determine the average grain sizes [33]. According to the ASTM standard, a % relative accuracy of no more than 10 % is acceptable when

presenting grain size measurements.

7.4 Results

7.4.1 Structural and dielectric properties

In previous work [29], the authors studied the MPB composition of the ternary PT-BS-BNiT system. Compositions were made with 2% extra Pb added to avoid lead loss. As will be seen later, single-phase compositions were obtained for different amounts of lead or bismuth added or removed. Samples were produced with at least 94% theoretical density. The microstructure of the stoichiometric composition as well as the Pb and Bi excess compositions are shown in Fig. 7.1. The micrographs confirm the high sintered densities with very little porosity. The estimated average grain sizes are listed in Table 7.1 with the corresponding percent relative accuracy (%RA) referenced in the ASTM standard [33]. Figure 7.2 shows the diffraction patterns for compositions with varying bismuth and lead stoichiometries for the MPB composition. An increase in the tetragonal splitting of the (00*l*) reflections was observed for compositions deficient in Bi. The perovskite compound $BiScO_3$ was shown to be the rhombohedral analog to $PbZrO_3$ in the PZT system [9, 13]. Therefore, in PT-BS-BNIT, it appears that introducing Bi deficiency near the MPB shifts the overall composition to the tetragonal side of the MPB. This is consistent with the results shown in Fig. 7.2 (b), where an increase in the tetragonal splitting was observed for an increase in Pb content.

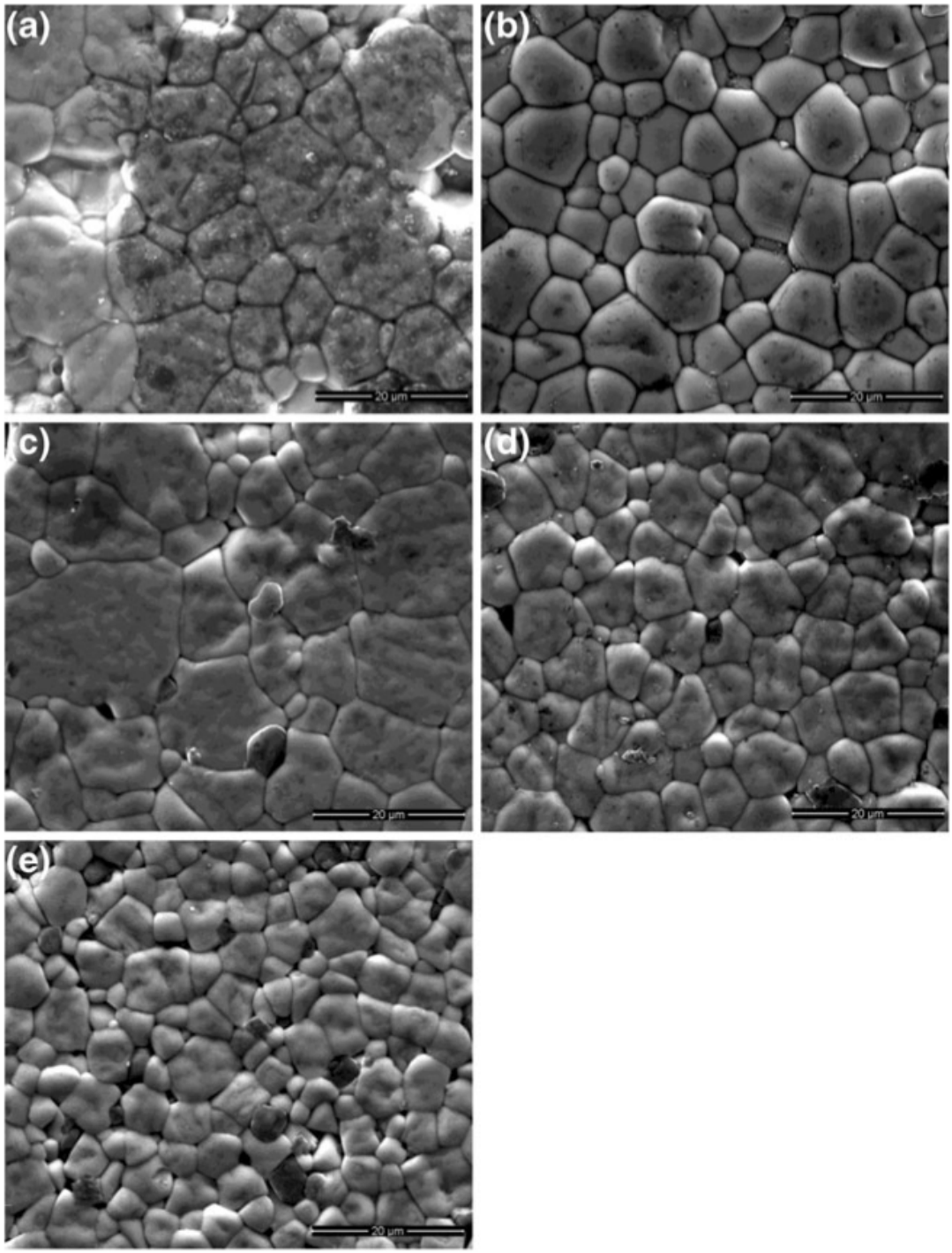

FIGURE 7.1: Electron microscope images of Pb and Bi excess compositions, (a) 5 % Pb excess, (b) 2 % Pb excess, (c) stoichiometric, (d) 2 % Bi excess, and (e) 5 % Bi excess samples.

TABLE 7.1: Average grain sizes and % relative accuracy for bismuth and lead excess compositions and the stoichiometric sample [33].

	5 % Pb excess	2 % Pb excess	stoichiometric	2 % Bi excess	5 % Bi excess
Average Grain Size [μm]	18.0	12.7	20.1	12.6	9.31
% Relative Accuracy	8.1	10.0	8.7	9.5	5.8

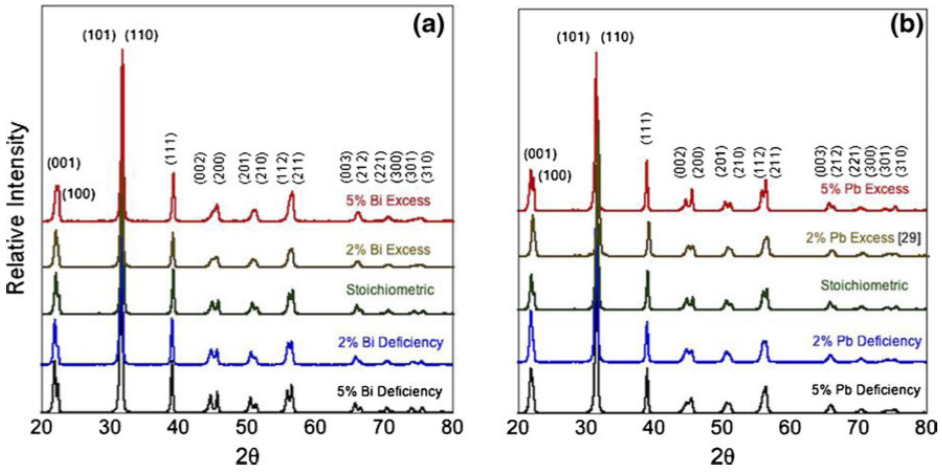

FIGURE 7.2: X-ray diffraction of samples of MPB composition with varying stoichiometries: a Bi-deficient or Bi-excess samples compared to XRD scan of the stoichiometric composition and b likewise for changes to Pb content compared to stoichiometric MPB composition.

In order to determine the Curie temperature of the samples, dielectric measurements were carried out on un-poled samples. The results at 10 kHz are plotted in Fig. 7.3, with the stoichiometric composition compared to compositions with 2 % and 5 % excess Pb and Bi. Both bismuth excess samples and the 2 % Pb excess sample were shown to have a relatively low T_C of approximately 350 ^oC. There were some noted

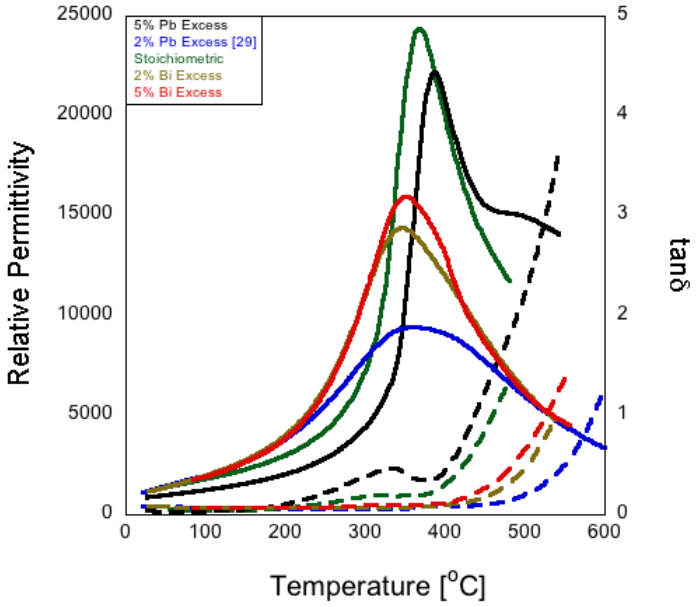

FIGURE 7.3: X-ray diffraction of samples of MPB composition with varying stoichiometries: (a) Bi-deficient or Bi-excess samples compared to XRD scan of the stoichiometric composition and (b) likewise for changes to Pb content compared to stoichiometric MPB composition.

differences in the diffuseness of the phase transition, with the 2 % Pb excess composition being the most diffuse. The 5 % Pb excess and the stoichiometric samples had transition temperatures of 390 °C and 370 °C, respectively. The dielectric loss remained below the 0.1 % threshold up until 220 °C except for the 5 % Pb excess sample in which the loss increased above 0.1 % around 200 °C. Table 7.2 lists the dielectric properties measured at 1 kHz at temperatures of 25 °C and 100 °C.

7.4.2 Ferroelectric and piezoelectric properties

The ferroelectric hysteresis properties were measured on poled samples and plotted in Fig. 7.4. Samples with varying Bi stoichiometry, shown in Fig. 7.4 (a), show a coercive field between 24 and 25 kV/cm for all samples except 5 % Bi-

TABLE 7.2: Dielectric properties of the MPB ($xPbTiO_3$-(1-x)[$BiScO_3$ + $Bi(Ni_{1/2}Ti_{1/2})O_3$] ternary at room temperature and 100 °C

Stoichiometry	25 °C		100 °C	
	Dielectric constant ϵ_r	Dielectric loss $tan\delta$	Dielectric constant ϵ_r	Dielectric loss $tan\delta$
5 % Pb-excess	920	0.033	1310	0.061
2 % Pb-excess [34]	1290	0.070	2150	0.062
2 % Pb-deficient	1330	0.067	2100	0.061
5 % Pb-deficient	1410	0.046	2590	0.071
Stoichiometric	1490	0.049	1915	0.053
5 % Bi-excess	1320	0.067	2070	0.064
2 % Bi-excess	1310	0.068	2170	0.062
2 % Bi-deficient	1345	0.062	2000	0.052
5 % Bi-deficient	1250	0.035	1700	0.038

deficient sample, which had a coercive field of 28 kV/cm. All hysteresis loops show saturation at an applied field of 40 kV/cm except for the 5 % Bi-deficient sample, which showed decreased saturation polarization and remanent polarization compared to the stoichiometric sample. With an increased amount of bismuth, the remanent polarization increased to values of 36.5 $\mu C/cm^2$ and 40.5 $\mu C/cm^2$ for the 2 % and 5 % Bi-excess compositions, respectively. The remanent polarization of the 2 % Bi-deficient sample was 33.0 μC/cm2 while the 5 % Bi-deficient had a remanent polarization of 27.9 $\mu C/cm^2$. Both bismuth excess compositions and the 2 % Bi-deficient sample had a higher remanent polarization than the stoichiometric composition of P_r = 31.0 $\mu C/cm^2$. As shown in Fig. 7.4 (b), all of the lead excess compositions showed

significantly lower remanent polarizations than the bismuth excess compositions. The remanent polarizations of the 5 % and 2 % Pb-excess samples were 22.5 μC/cm^2 and 26.4 μC/cm^2 respectively [29]. For the lead deficient compositions, the remanent polarizations were P_r = 31.0 μC/cm^2 and P_r = 30.2 μC/cm^2 for 5 % and 2 % Pb-deficient samples, respectively. The coercive field for the lead excess and deficient samples exhibited a wider range of values from 21 to 28 kV/cm as compared to the bismuth compositions.

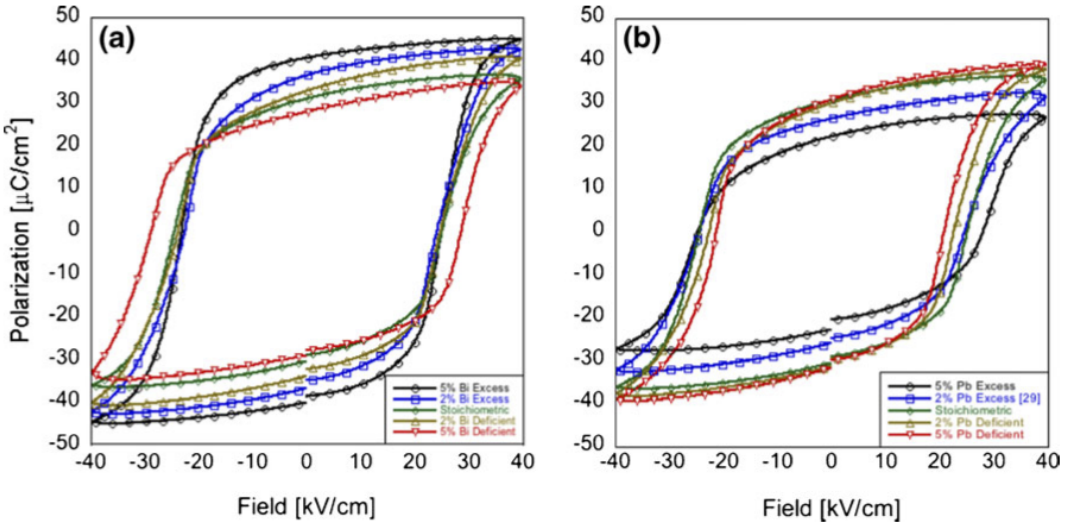

FIGURE 7.4: Polarization hysteresis of Bi (a) and Pb (b) deficient and excess samples compared to the stoichiometric composition.

Figure 7.5 shows both bipolar and unipolar electromechanical strain measurements on bismuth and lead samples poled at 40 kV/cm at 100 ^{o}C for 30 min. In Fig. 7.5 (a), the bipolar strain behavior of bismuth deficient and excess compositions showed the characteristic asymmetric "butterfly" loops due to degradation of poled domains as result of field switching. The bismuth excess compositions showed the highest amount of strain at approximately 0.35 %. Bismuth deficient samples exhibited similar strain values to the stoichiometric composition between 0.2 % and

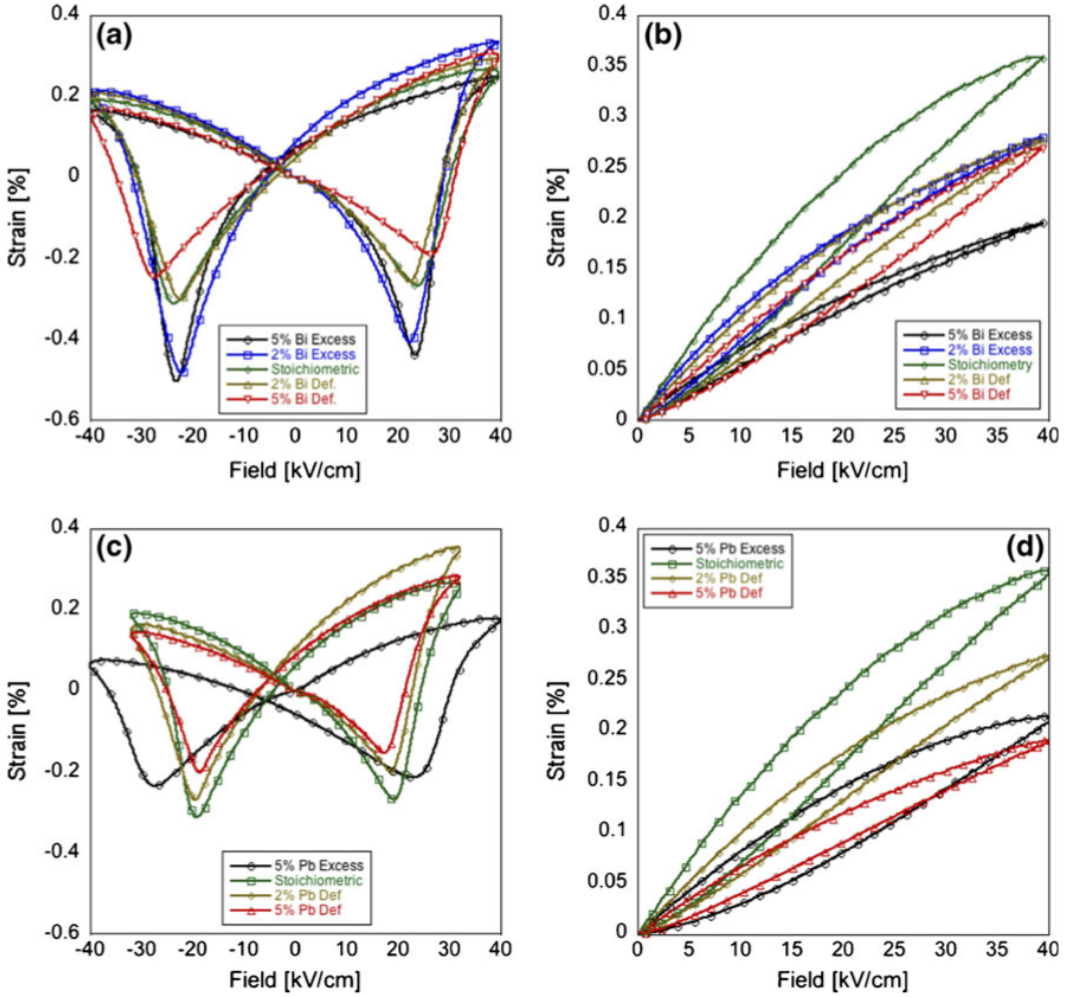

FIGURE 7.5: Electromechanical strain, both bipolar (a) and unipolar (b), of the stoichiometric composition compared to the 2 % and 5 % bismuth excess and deficient samples. Electromechanical strain, both bipolar (c) and unipolar (d), of the stoichiometric composition compared to the 2 % and 5 % lead deficient samples and 5 % lead excess sample. The 2 % Pb-excess sample was created in a previous work, which the reader is directed to [29].

0.3 %. In Fig. 7.5 (c), lead excess and deficient samples showed strains of about 0.25 % for the 2 % Pb-deficient and 5 % Pb-excess samples while the 5 % Pb-deficient

sample exhibited strain values close to 0.2 %. In Fig. 7.5 (b) and (d), unipolar strain measurements are presented for bismuth and lead respectively in order to calculate the high field d_{33}* constants. The d_{33}* values of the stoichiometric composition was approximately 900 pm/V and compositions with variations in bismuth and lead stoichiometry varied between 470 and 700 pm/V. The results for all compositions are compiled in Table 7.3.

TABLE 7.3: Room temperature piezoelectric coefficient measured from d_{33} meter (direct) and calculated from unipolar strain (converse).

Stoichiometry	d_{33} [pC/N]	d_{33}* [pm/V]
5 % Pb-excess	171	549
2 % Pb-excess [34]	376	547
2 % Pb-deficient	370	688
5 % Pb-deficient	380	473
Stoichiometric	340	896
5 % Bi-excess	413	492
2 % Bi-excess	445	701
2 % Bi-deficient	425	695
5 % Bi-deficient	343	682

7.4.3 Depoling temperature

From measurement of the dielectric constant versus temperature (Fig. 7.3), the Curie temperature was observed to be between 350 ^{o}C and 390 ^{o}C depending on the composition. However, a local maximum in the dielectric loss was observed at temperatures 10 to 20 ^{o}C below T_C for all samples. Plotting the value for tanδ in a log scale as shown in Fig. 7.6, the dielectric anomaly corresponding can be more

easily determined. Using the approach outlined by Leist et al. [12], the depolarization temperature (T_D) for the stoichiometric composition was approximately 320 °C compared to the maximum measured at 400 °C for the 2 % Pb excess composition [29]. As the bismuth content increased the depolarization temperature dropped to 324 °C and 305 °C for the 2 % and 5 % Bi excess samples, respectively. To confirm the depolarization temperature obtained from the dielectric data, two other methods were utilized: an ex-situ d_{33} measurement and analysis of the piezoelectric coupling coefficient from high temperature impedance spectra.

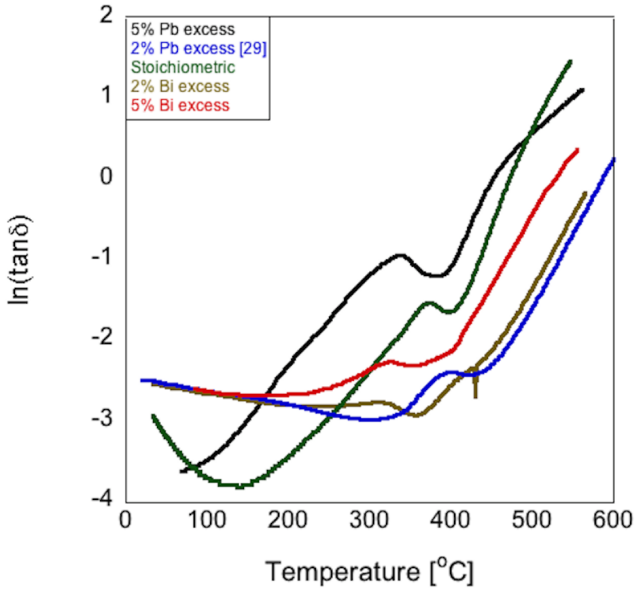

FIGURE 7.6: Dielectric dissipation plotted again in log scale for lead and bismuth excess samples compared to the stoichiometric composition; measurements taken at 10 kHz.

The ex-situ d_{33} data is presented in Fig. 7.7. The depolarization temperatures are determined from the temperature at which the piezoelectric coefficient experienced a significant decrease; below this temperature, the piezoelectric constant should remain independent of temperature. The highest piezoelectric coefficient ob-

served was 445 pC/N for the 2 % Bi excess sample, which remained constant up to a temperature of approximately 275 °C. At approximately 300 °C, the piezoelectric constant decreased to zero, therefore $T_D \approx 300$ °C for the 2 % Bi-excess composition. For the stoichiometric composition, the piezoelectric coefficient saw an initial decrease to 250 pC/N and remained constant up to 325 °C. The depolarization temperature measured from this ex-situ approach and the dielectric data were very similar for the stoichiometric sample: 320 °C and 325 °C, respectively. In Fig. 7.7(b), both Pb-excess and Pb-deficient samples maintained low piezoelectric coefficients between 150 pC/N and 250 pC/N depending on composition up to temperatures of approximately 300 °C. One notable exception was the 5 % Pb-deficient composition, which had a piezoelectric coefficient of 375 pC/N and a depolarization temperature of only 250 °C.

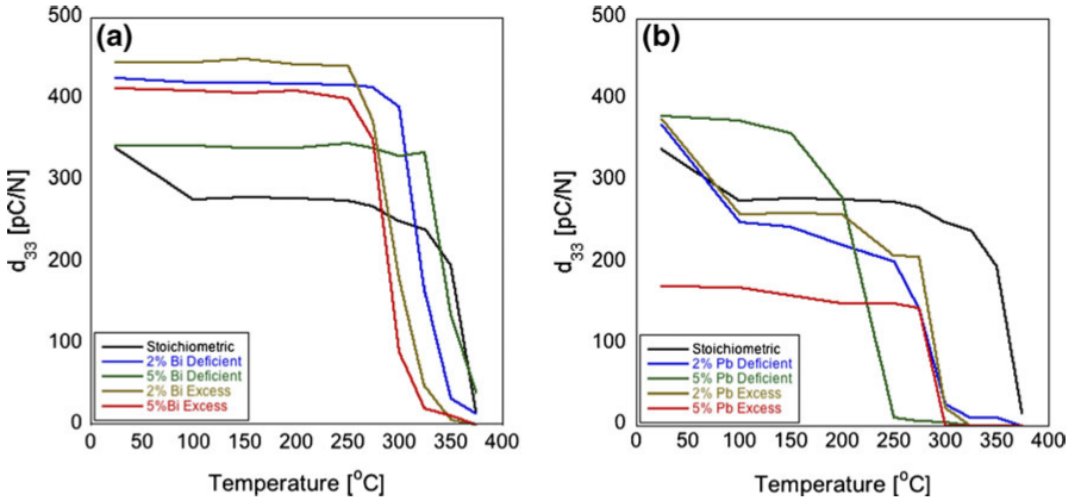

FIGURE 7.7: Ex-situ d_{33} plots of the various stoichiometries of the MPB composition, a Bi-excess and Bi-deficient on the left hand side and b Pb-excess and Pb-deficient on the right hand side.

Another method for determining the depolarization temperature involved measuring the impedance spectra as a function of temperature and then, by following

the IEEE standard [32], calculating the planar mechanical coupling factor, k_p. For the stoichiometric composition, 2 % Bi excess and deficient, and 5 % Pb excess and deficient samples, the impedance was measured up to 400 ^oC. Here, as with the ex-situ d_{33} method, the depolarization temperature was determined from the temperature at which a decrease in the value of k_p was observed. Most of the compositions exhibited a decrease in k_p at temperatures between 300 ^oC and 325 ^oC. The only exception was the 5 % Pb-deficient composition, which observed a decrease in k_p at 225 ^oC. The results of all three methods of determining the depolarization temperature for different Pb and Bi stoichiometry are summarized in Table 7.4.

TABLE 7.4: Depolarization temperatures (^oC) measured through dielectric data, ex-situ d_{33}, and high temperature impedance.

Stoichiometry	Dielectric loss (10 kHz) in log scale	Ex-situ d_{33}	High temperature impedance
5 % Pb-excess	334	275	300
2 % Pb-excess	400	275	-
2 % Pb-deficient	345	275	-
5 % Pb-deficient	325	200	225
Stoichiometric	320	325	325
5 % Bi-excess	305	300	-
2 % Bi-excess	324	300	300
2 % Bi-deficient	340	325	310
5 % Bi-deficient	345	325	-

7.5 Discussion

As seen in Table 7.3, samples with excess bismuth exhibited higher low-field piezoelectric constants, however, the stoichiometric composition exhibited the highest d_{33}* value. Dielectric loss and permittivities listed in Table tab:7-2 for both Pb and Bi excess samples were similar, however, the 5 % Pb excess and stoichiometric compositions had lower dielectric loss at both room temperature and at 100 ^{o}C. The average grain sizes for the stoichiometric, and all the lead and bismuth excess compositions fell into the range of 10 - 21 μm. The stoichiometric composition had the largest grain size with an average grain size of 20.1 μm. Possibly due to the larger grain size in the stoichiometric composition, the dielectric and piezoelectric properties were improved relative to the properties of the compositions with excess oxides.

As grain sizes increased, the number of grains decreased and thus the volume of grain boundaries also decreased, leading to an increase in resistivity. Research conducted on liquid phase-sintered PT-BS by Sehirlioglu et al. showed an increase in resistivity led to an improvement in poling conditions and in turn, an improvement in piezoelectric properties [35]. Sehirlioglu also found that increasing the amount of PbO in PT-BS increased the grain-boundary conductivity leading to a decrease in piezoelectric properties while adding Bi_2O_3 improved the resistivity and piezoelectric properties of PT-BS. Liquid phase sintering was not specifically part of the present study, however, the larger grain sizes that resulted from the stoichiometric composition led to higher dielectric and high field piezoelectric constants and lower dielectric losses. The replacement of lead by bismuth on the A-site and/or the creation of lead vacancies alone may be responsible for the improved resistivity and the improved low field piezoelectric coefficients for the Bi excess samples [35]. The Pb excess compositions exhibited an increased tetragonality, which led to an increase in T_C and T_D [24].

7.6 Conclusion

The MPB composition of the ternary perovskite PT-BS-BNiT was studied extensively to determine the transition temperature and depolarization temperature. Other important ferroelectric properties were also characterized including: both low and high field d_{33} and d_{33}* constants, dielectric permittivity and loss, polarization hysteresis, and electromechanical strain. The stoichiometry of the MPB composition was adjusted by changing the A-site occupancy of Bi and Pb to optimize the depoling temperature and the ferroelectric properties. It was found that the addition of 2 % Bi led to improved low field piezoelectric properties with the Curie temperature, T_C = 346 ^oC, and more importantly the depolarization temperature, T_D = 300 ^oC, remained relatively high. Room temperature permittivity of the 2 % Bi-excess sample was 1320 at 1 kHz with a loss of 0.067. The highest low field piezoelectric coefficient was observed for the 2 % Bi-excess sample with d_{33} = 445 pC/N while the stoichiometric composition had the highest high field coefficient with d_{33}*=896 pm/V. The remanent polarization of the stoichiometric and the 2 % Bi-excess compositions were 31.0 $\mu C/cm^2$ and 36.4 $\mu C/cm^2$, respectively, while the maximum remanent polarization was observed for the 5 % Bi- excess sample with P_r = 41.0 $\mu C/cm^2$. Bipolar electromechanical strain applied to the 2 % Bi-excess sample caused strains up to 0.5 % compared to strains of 0.25 % of the stoichiometric composition under an applied field.

7.7 Acknowledgements

The authors would like to acknowledge this work was supported in part through NASA/Oregon Space Grant Consortium, grant NNX10AK68.

7.8 References

1. Valasek, J. Piezo-Electric and Allied Phenomena in Rochelle Salt. *Phys. Rev.* **17,** 475–481 (1921).
2. Yamakawa, K. *et al.* Novel Pb(Ti,Zr)O_3 (PZT) Crystallization Technique Using Flash Lamp for Ferroelectric RAM (FeRAM) Embedded LSIs and One Transistor Type FeRAM Devices. *Jpn. J. Appl. Phys.* **41,** 2630–2634 (2002).
3. Malmonge, L. F., Malgonge, J. A. & Sakamoto, W. K. Study of Pyroelectric Activity of PZT/PVDF-HFP Composite. *Mater. Res.* **6,** 469–473 (2003).
4. Makki, N. & Pop-Iliev, R. Battery-and wire-less tire pressure measurement systems (TPMS) sensor. *Microsyst Technol* **18,** 1201–1212 (2012).
5. Matsushita, S., Kanno, I., Adachi, K., Yokokawa, R. & Kotera, H. Metal-based piezoelectric microelectromechanical systems scanner composed of Pb(Zr, Ti)O_3 thin film on titanium substrate. *Microsyst Technol* **18,** 765–771 (2012).
6. Turner, R., Fuierer, P., Newnham, R. & Shrout, T. R. Materials for high temperature acoustic and vibration sensors: A review. *Appl. Acoust.* **41,** 299 (1994).
7. Shrout, T. R. & Zhang, S. J. Lead-Free Piezoelectric Ceramics: Alternative for PZT? *J. Electroceram.* **19,** 111–124 (2007).
8. Jiang, Y. *et al.* Microstructure and Electric Properties of (1-x)Bi($Sc_{0.75}Zn_{0.125}Ti_{0.125}$)$O_3$-x$PbTiO_3$ Ceramics. *Ferroelectrics* **380,** 130–134 (2009).
9. Jaffe, B., Cook, W. R. & Jaffe, H. *Piezoelectric Ceramics* 1st ed. 317 pp. (Academic Press, New York, 1971).
10. Haertling, G. H. Ferroelectric Ceramics: History and Technology. *J. Am. Ceram. Soc.* **82,** 797–818 (1999).
11. Sehirlioglu, A., Sayir, A. & Dynys, F. Doping of $BiScO_3$-$PbTiO_3$ Ceramics for Enhanced Properties. *J. Am. Ceram. Soc.* **93,** 1718–1724 (2010).

12. Leist, T. *et al.* Temperature Dependence of the Piezoelectric Coefficient in $BiMeO_3$-$PbTiO_3$ (Me = Fe, Sc, $(Mg_{1/2}Ti_{1/2})$) Ceramics. *J. Am. Ceram. Soc.* **95,** 711–715 (2012).

13. Eitel, R. E. *et al.* New High Temperature Morphotropic Phase Boundary Based on $Bi(Me)O_3$-$PbTiO_3$ Ceramics. *Jpn. J. Appl. Phys.* **40,** 5999–6002 (2001).

14. Eitel, R. E., Zhang, S. J., Shrout, T. R. & Randall, C. A. Phase Diagram of the Perovskite System (1-x)$BiScO_3$-x$PbTiO_3$. *J. Appl. Phys.* **96,** 2828–2831 (2004).

15. Eitel, R. E., Randall, C. A., Shrout, T. R. & Park, S.-E. Preparation and Characterization of High Temperature Perovskite Ferroelectrics in the Solid-Solution (1-x)$BiScO_3$-x$PbTiO_3$. *Jpn. J. Appl. Phys.* **41,** 2099–2104 (2002).

16. Stringer, C. J., Shrout, T. R., Randall, C. A. & Reaney, I. Classification of Transition Temperature Behavior in Ferroelectric $PbTiO_3$-Bi(Me'Me")O_3 Solid Solutions. *J. Appl. Phys.* **99,** 0241061–0241064 (2006).

17. Zhang, S. J., Randall, C. A. & Shrout, T. R. High Curie temperature piezocrystals in the $BiScO_3$-$PbTiO_3$ perovskite system. *Appl. Phys. Lett.* **83,** 3150–3152 (2003).

18. Sehirlioglu, A., Sayir, A. & Dynys, F. High Temperature Properties of $BiScO_3$-$PbTiO_3$ Piezoelectric Ceramics. *J. Appl. Phys.* **106,** 0141021–0141027 (2009).

19. Shimojo, Y., Wang, R., Sekiya, T., Nakamura, T. & Cross, L. MPB Phase Diagram and Ferroelectric Properties in the $PbTiO_3$-$BiScO_3$ System. *Ferroelectrics* **284,** 121–128 (2003).

20. Randall, C. A., Eitel, R. E., Shrout, T. R., Woodward, D. & Reaney, I. Transmission Electron Microscopy Investigation of the High Temperature $BiScO_3$-$PbTiO_3$ Piezoelectric Ceramic System. *J. Appl. Phys.* **93,** 9271–9274 (2003).

21. Takenaka, T. & Yamada, M. Solid-Solution $(Bi_{1-x}Pb_x)(Ni_{(1+x)/2}Ti_{(1+x)/2})O_3$ for New Piezoelectric Ceramics. *Jpn. J. Appl. Phys.* **32,** 4218–4222 (1993).

22. Choi, S. M., Stringer, C. J., Shrout, T. R. & Randall, C. A. Structure and Property Investigation of a Bi-based Perovskite Solid Solution: (1-x)$Bi(Ni_{1/2}Ti_{1/2})O_3$-x$PbTiO_3$. *J. Appl. Phys.* **98,** 0341081–0341084 (2005).

23. Chen, J. *et al.* Structure and lattice dynamics in $PbTiO_3$-$Bi(Zn_{1/2}Ti_{1/2})O_3$ solid solutions. *J. Appl. Phys.* **105,** 044105 (2009).

24. Suchomel, M. R. & Davies, P. K. Enhanced Tetragonality in (x)$PbTiO_3$-(1-x)$Bi(Zn_{1/2}Ti_{1/2})O_3$ and Related Solid Solution Systems. *Appl. Phys. Lett.* **86,** 2629051–2629053 (2005).

25. Sharma, S. & Hall, D. A. Ferroelectric and Antiferroelectric Polarization Switching Characteristics of $Bi(Mg_{0.5}Ti_{0.5})O_3$-$PbTiO_3$ Ceramics. *J. Mater. Sci.: Mater. Electron.* **21,** 405–409 (2010).

26. Sebastian, T. *et al.* High temperature piezoelectric ceramics in the $Bi(Mg_{1/2}Ti_{1/2})O_3$-$BiFeO_3$-$BiScO_3$-$PbTiO_3$ system. *J. Electroceram.* **25,** 130–134 (2010).

27. Sterianou, I. *et al.* High-temperature (1-x)$BiSc_{1/2}Fe_{1/2}O_3$-x$PbTiO_3$ piezoelectric ceramics. *Appl. Phys. Lett.* **87,** 242901 (2005).

28. Sterianou, I., Sinclair, D. C., Reaney, I. M., Comyn, T. & Bell, A. J. Investigation of high Curie temperature (1-x)$BiSc_{1-y}Fe_yO_3$-x$PbTiO_3$ piezoelectric ceramics. *J. Appl. Phys.* **106** (2009).

29. Ansell, T. Y., Cann, D. P., Nikkel, J. & Sehirlioglu, A. High Temperature Piezoelectric Ceramics based on x$PbTiO_3$-(1-x)$Bi(Sc_{1/2}Me_{1/4}Ti_{1/4})O_3$ (Me = Zn, Mg) Ternary Perovskites. *Jpn. J. Appl. Phys.* **51,** 101802 (2012).

30. Inaguma, Y. *et al.* High-pressure synthesis and ferroelectric properties in perovskite -type $BiScO_3$-$PbTiO_3$ solid solution. *J. Appl. Phys.* **95,** 231–235 (2004).

31. Eitel, R. E., Shrout, T. R. & Randall, C. A. Nonlinear contributions to the dielectric permittivity and converse piezoelectric coefficient in piezoelectric ceramics. *J. Appl. Phys.* **99,** 124110 (2006).

32. *ANSI/IEEE 176-1987, IEEE Standard on Piezoelectricity* (IEEE, New York, 1987).

33. *Standard Test Methods for Determining Average Grain Size* Standard E112-10 (American Society for Testing and Materials, ASTM International, 100 Barr Harbor Drive, PO Box C700, West Conshohocken, PA 19428-2959. United States, 2010).

34. Ansell, T. Y. & Cann, D. P. High temperature piezoelectric ceramics based on (1 - x)[$BiScO_3$ + $Bi(Ni_{1/2}Ti_{1/2})O_3$] - x$PbTiO_3$. *Mater. Lett.* **80,** 87–90 (2012).

35. Sehirlioglu, A., Sayir, A. & Dynys, F. Microstructural-Property Relationships in Liquid Phase-Sintered High-Temperature Bismuth Scandium Oxide-Lead Titanate Piezoceramics. *J. Am. Ceram. Soc.* **91,** 2910–2916 (2008).

8 Thermal depolarization in the high temperature ternary piezoelectric system $xPbTiO_3$ - $yBiScO_3$ - $zBi(Ni_{1/2}Ti_{1/2})O_3$

Troy Y. Ansell and David P. Cann

Materials Science, School of Mechanical, Industrial, and Manufacturing Engineering, Oregon State University, Corvallis, OR, 97331, U.S.A.

Eva Sapper and Jürgen Rödel Institute of Materials Science, Technische Universität Darmstadt, Darmstadt 64287, Germany.

Published in

Journal of the American Ceramic Society

Published online (13 Oct, 2014), doi: 10.1111/jace.13268

8.1 Abstract

In the high temperature ternary perovskite piezoelectric system $xPbTiO_3$ - $yBiScO_3$ - $zBi(Ni_{1/2},Ti_{1/2})O_3$ (PT-BS-BNiT), the addition of bismuth to the A-site and nickel to the B-site leads to compositions that exhibit diffuse relaxor-like behavior. For these, depolarization temperature, not Curie point, is the critical value of temperature. Depolarization temperature (T_d) is defined as the temperature at which the steepest loss in polarization occurs. This temperature is observed in poled materials through two different methods: loss tangent measurements and in-situ d_{33}. Across the ternary system, multiple dielectric anomalies occurred which was observed in dielectric tests where the dielectric peak broadens and becomes frequency dependent as BNiT content increased. For different compositions, the value of T_d ranged between 275 ^oC - 375 ^oC. Values for the piezoelectric coefficient increased with temperature up to $d_{33} \approx 1000$ pC/N during in-situ d_{33}. High temperature (up to 190 ^oC) and high field (up to 40 kV/cm) were also applied to test ferroelectric properties in these regimes.

8.2 Introduction

High temperature piezoelectric materials are used as actuators and sensors in a variety of applications from deep oil well drilling operations to motor control and monitoring in deep space probes. One example includes an ultrasonic transducer in a rock driller for the in-situ Venus lander [1]. Any actuator or sensor made from a piezoelectric material placed in such an environment must remain functional at temperatures exceeding 400 ^oC. Additional high temperature applications include fuel injectors for automotive and jet engines. Perovskite materials especially have dominated this field of study due to a crystal structure that is amenable to polarization. Additionally, Pb-based solid solutions dominate high temperature piezoceramics research due to a number of factors including the high polarizability of Pb^{2+} due to its large radius and large effective number of electrons, and the lone pair of electrons

in Pb^{2+} [2].

The dominant high temperature piezoceramic material is the ubiquitous lead zirconate titanate ($PbTiO_3$ - $PbZrO_3$, PZT). Made of a solid solution of lead titanate ($PbTiO_3$, PT) and lead zirconate ($PbZrO_3$, PZ), un-doped PZT (0.48PT-0.52PZ) features a Curie temperature of $T_C \approx 390\ ^oC$, room temperature piezoelectric coefficients $d_{33} \approx 233$ pC/N [3], $d_{31} \approx -100$ pC/N [4], and $d_{15} \approx 500$ pC/N [4], a room temperature permittivity $\epsilon \approx 1600$ [5] and a large temperature stability due to the nearly vertical phase boundary, otherwise known as the morphotropic phase boundary (MPB), separating the P4mm tetragonal and R3m rhombohedral ferroelectric phases [3]. Without a detailed description, PZT ceramics with donor cation substitutions lead to a softening effect where dielectric permittivity, electromechanical coupling, and piezoelectric coefficients increase [3]. Electrical hardening occurs due to acceptor doping and is observed when loss tangent decreases and mechanical Q and coercive field increase [3, 6]. Despite the relatively high Curie temperature of PZT, the maximum operating temperature of PZT; soft, hard, or undoped lies below 200 ^oC [7]. New materials were investigated to find T_C values higher than 400 ^oC with comparable piezoelectric properties to those of PZT. The solid solution of lead titanate and bismuth scandate (PT-BS) has proved to be extremely promising with $T_C \approx 450\ ^oC$ and a piezoelectric coefficient of $d_{33} \approx 460$ pC/N [8].

Studying a number of solid solution systems modeled after $PbTiO_3$ - $BiB'O_3$, Eitel et al. found an increase in T_C with a decrease in B-site cationic radii for B' = Sc (BS), In (BI), and Yb (BY) [8]. At the MPB composition (0.64PT-0.36BS), bismuth scandate exhibited a high $T_C \approx 450\ ^oC$ [6, 8–10], high piezoelectric coefficients d_{33} = 335 - 450 pC/N [6, 8–10], and high coupling factors $k_p \approx 0.55$ close to that of PZT [8]. Also observed in this system was a temperature independent MPB up to 300 ^oC suggesting a wide range of temperature stability similar to PZT [10]. Numerous additional studies of PT-BS were conducted to further increase T_C and piezoelectric properties through isovalent modifications [11, 12], aliovalent doping [6, 13–15],

stoichiometric modifications [16, 17], and varying processing [16–18] with limited success. Notwithstanding the excellent properties of PT-BS, some disadvantages of this solid solution exist: modification of the piezoceramic is limited as compared to PZT [6], octahedral tilting occurring at a relatively high PT content (≈ 62 %) limits the functional range of PT-BS to compositions near the MPB [10], and compared to other oxides used in PT-BS, Sc_2O_3 is quite expensive.

Table 8.1 lists alternative solid solutions also modeled after $PbTiO_3$ - $BiB'O_3$. The majority of systems listed were studied for exceptionally high Curie temperatures; however, piezoelectric data was missing for most due to various reasons discussed later in this section. Piezoelectric coefficients were observed for two of these solid solutions, xPT-(1-x)BMT and $xPbTiO_3$ - (1-x)$Bi(Ni_{1/2}Ti_{1/2})O_3$ and are highlighted in Table 8.1. In the PT-BMT system, an MPB was observed at x = 0.35, T_C = 425 ^oC, and d_{33} = 260 pC/N [19–21]. In the PT-BNiT system, an MPB formed at x = 0.51, T_C = 400 ^oC, and d_{33} = 260 pC/N at room temperature [22]. Electromechanical coupling factors k_{33} and k_{31} for the x = 0.50 composition was found to be 0.503 and 0.238 respectively [23]. Despite the many different systems investigated and the many solid solutions that have been studied, none so far have matched the high piezoelectric performance of the PT-BS binary system or the high performance and low cost of PZT.

A number of metal cation substitutions have been investigated in solid solution with PT with the goal of replacing Sc on the B-site including In [8, 24], Yb [8], Al [25], Ga [26], Fe [27, 28], and Mn [29]. None of these solid solutions have been able to achieve a high piezoelectric response comparable to PT-BS. In general, with the addition of low tolerance factor compounds there are limitations in range of perovskite stability, which inhibits the formation of stable MPB compositions in studies on In, Yb, Al, and Ga-containing systems. In Mn and Fe-containing systems, high conductive losses inhibited the effectiveness of poling processes.

TABLE 8.1: List of PT-based Perovskite Binary Solid Solutions and Curie Temperatures. Materials where Piezoelectric Coefficients and Other Properties were measured are highlighted.

PT-based solid soln.	B-site cation in BiB'_3 end-member	T_C [^oC]	Ref.
PT-BI	In	581	[8, 24]
PT-BA	Al	460	[25]
PT-BG	Ga	485	[26]
PT-BF	Fe	632	[27, 28]
PT-BMn	Mn	450	[29]
PT-BZT	Zn^{2+}, Ti^{4+}	700	[30]
PT-BZZ	Zn^{2+}, Zr^{4+}	520	[30]
PT-BZS	Zn^{2+}, Sn^{4+}	510	[30]
PT-BMT	Mg^{2+}, Ti^{4+}	405	[31]
PT-BMZ	Mg^{2+}, Zr^{2+}	300	[19]
PT-BNT	Ni^{2+}, Ti^{4+}	400	[22, 23]
PT-BZW	Zn^{2+}, W^{6+}	530	[32]

In order to reduce both the Pb (reduce toxicity) and Sc (reduce cost) content in piezoelectric ceramics, while maintaining the excellent piezoelectric properties and relatively high Curie temperature, a ternary solid solution was developed that combined PT-BS with PT-BNiT. In previous work on the ternary PT-BSNiT, compositional modifications accomplished by including excess Bi led to a maximum in low-field d_{33} = 445 pC/N (the direct effect) and a maximum in high-field d_{33}^* ≈ 900 pm/V (the converse effect), however, the Curie temperature never exceeded 400 ^oC and k_p = 0.25 [33, 34]. Compositions studied contained equal parts BS and BNiT. In this study, the range of compositions studied is expanded to cover the entire ternary system

PT-BS-BNiT with a linkage from the PT-BS binary to the PT-BNiT binary system. The goal of this study is to examine MPB compositions in the ternary system to find compositions with high piezoelectric activity, high T_C values, and with a reduced Sc content to lower the cost of potential applications. To this end, a large number of compositions were evaluated and salient effects in terms of permittivity, small signal and large signal piezoelectric coefficients were considered. It will also be seen that T_C is not the only temperature figure of merit but also the depolarization temperature, T_d, will be important. For the remainder of this article, compositions will be referred to using the convention xPT-yBS-zBNiT. For example, a composition close to pure PT-BNiT studied is named 50PT-10BS-40BNiT or simply referred to as 50-10-40.

8.3 Experimental Methods

Specimens were prepared using the standard mixed oxide method. Starting oxide powders of Bi_2O_3 (99.9%, Sigma-Aldrich, St. Louis, MO), NiO (99.99%, Sigma-Aldrich, St. Louis, MO), TiO_2 (99.0%, Sigma-Aldrich, St. Louis, MO), PbO (99.9%, Sigma-Aldrich, St. Louis, MO), and Sc_2O_3 (99.995%, Stanford Materials Corp., Irvine, CA) were batched in ethanol and milled for six hours with yttria-stabilized zirconia milling pellets (Nikkato Corp., Sakia, Osaka, Japan). Batched powders were then dried and placed in a sealed alumina crucible. The powders were calcined at a temperature of 950 ^oC for 4 h with a ramp rate of 5 ^oC/minute both heating and cooling. After calcination, powders were milled for another 6 h and dried. Calcined powders were mixed with polyvinyl butyral (PVB, Solutia Inc., Town and Country, MO), used as a binder, and cold-pressed into green discs at a pressure of $\approx$ 34.5 MPa for 3 min using a standard experimental press. Green discs were then placed on a bed of calcined powders of the same composition and sealed in a rectangular alumina crucible for sintering. Temperature was ramped at a rate of 5 ^oC/minute to 400 ^oC and held for 4 h to burn off the binder. Then the temperature ramp rate was set at 3

°C/minute to 1150 °C and held for 4 h for sintering. Piezoelectric discs were prepared to a thickness to diameter ratio of 1:10 following the IEEE standard for piezoelectricity [35]. Therefore, sintered samples were polished to a thickness of approximately 0.800 mm.

Before any electrical measurements were made, phase identification was conducted by X-ray diffraction (XRD) to ensure a single perovskite phase (within the detection limits of XRD) using a Bruker D8 Discover (Bruker D8 Discover, Bruker Biosciences Corp., Billerica, MA). Silver electrodes, using painted on silver paste (Heraeus C1000, Heraeus Holding GmbH, Hanau, Germany), were fired onto additional samples at 700 °C for half an hour. These samples were then poled at 100 °C with a field of ≈ 40 kV/cm for 30 minutes after which the temperature was reduced to room temperature with the field still applied to lock-in domain orientation. This poling procedure was employed for all samples. Poled samples were placed in a tube furnace (NorECs AS ProbostatTM, Oslo, Norway) between two Pt electrodes. Electrical permittivity and loss were measured on poled samples using a computer connected to an LCR meter (Agilent 4263B, Santa Clara, CA), while the temperature was recorded using a temperature reader (Dpi32-C24, Omega Engineering, Inc., Stamford, CT).

Using a custom built setup [31, 36] in-situ d_{33} was measured on poled samples at temperatures between 22 °C and 400 °C with a sinusoidal excitation signal of 10 V amplitude and a heating rate of 2 °C/min. High temperature hysteresis and strain measurements were also made on poled samples using a ferroelectric analyzer (aixACCT, Aachen, Germany) up to temperatures of 190 °C. The measurement frequency was held at 1 Hz for all high temperature polarization and strain data. The measurement waveform was triangular and two pulses were applied to each sample at all temperatures measured.

8.4 Results

8.4.1 Dielectric Properties

Figure 8.1 displays the phase diagram of the PT-BS-BNiT system. X-ray diffraction, provided in Fig. 8.2, was used to confirm the phase purity of each composition. Peak splitting of the (100), (110), and (200) peaks in Fig. 8.2 decreases as the PT content decreases. Complete disappearance of peak splitting, however, only appears in compositions with less than 50 % PT content; compositions that are not phase pure.

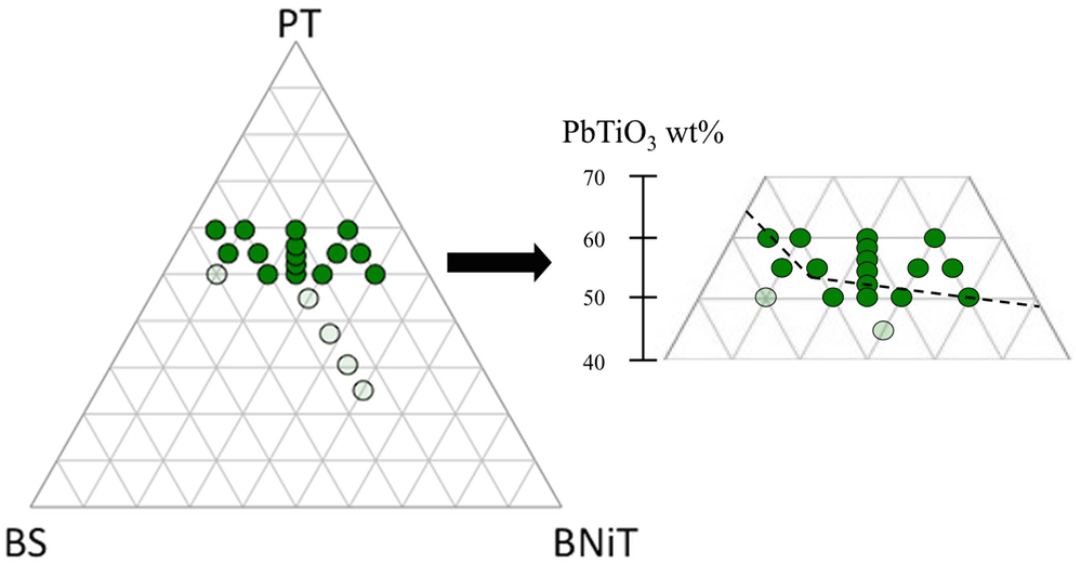

FIGURE 8.1: (a) The ternary phase diagram of the PT-BS-BNiT system. **(b)** Schematic of ternary diagram where compositions were studied. Solid green circles represent single-phase compositions, while the open circles represent compositions with an impurity phase. Dotted line represents proposed MPB line indicated from XRD and permittivity studies.

The maximum values of the relative permittivity and the room temperature piezoelectric coefficient listed in Table II were used to highlight MPB compositions (those compositions close to the dotted line in [Fig. 8.1(b)]). For compositions with PT content of 55 or 60 %, both the low temperature permittivity and the loss tangent

increased as the BS content increased. For compositions with 50 % PT, in general the opposite trend was observed for both loss tangent and relative permittivity. The relative permittivity decreased from 50-20-30 to 50-25-25 for both 25 ^{o}C and 100 ^{o}C and then increased for the composition 50-30-20. For compositions with 10 % BS content (e.g. 60-10-30), as the PT content decreased from 60 % to 50 %, relative permittivity values and loss tangent increased. However, for compositions with 30 % BS content, an initial increase and then a decrease are observed in permittivity at 25 ^{o}C, while permittivity increases at 100 ^{o}C. For both temperatures at constant 30 % BS, the loss tangent increased with decreasing PT content. The trends apparent in these results, specifically maximum values in relative permittivity, indicate that an MPB line lies in the regions indicated in [Fig. 8.1(b)]. In addition, the direct room temperature d_{33} coefficient values were higher for compositions closer to the MPB line and a clear decrease in properties was observed in compositions far away from the transition line.

The maximum values of the relative permittivity and the room temperature piezoelectric coefficient listed in Table 8.2 were used to highlight MPB compositions (those compositions close to the dotted line in [Fig. 8.1(b)]). For compositions with PT content of 55 or 60 %, both the low temperature permittivity and the loss tangent increased as the BS content increased. For compositions with 50 % PT, in general the opposite trend was observed for both loss tangent and relative permittivity. The relative permittivity decreased from 50-20-30 to 50-25-25 for both 25 ^{o}C and 100 ^{o}C and then increased for the composition 50-30-20. For compositions with 10 % BS content (e.g. 60-10-30), as the PT content decreased from 60 % to 50 %, relative permittivity values and loss tangent increased. However, for compositions with 30 % BS content, an initial increase and then a decrease are observed in permittivity at 25 ^{o}C, while permittivity increases at 100 ^{o}C. For both temperatures at constant 30 % BS, the loss tangent increased with decreasing PT content. The trends apparent in these results, specifically maximum values in relative permittivity, indicate that an

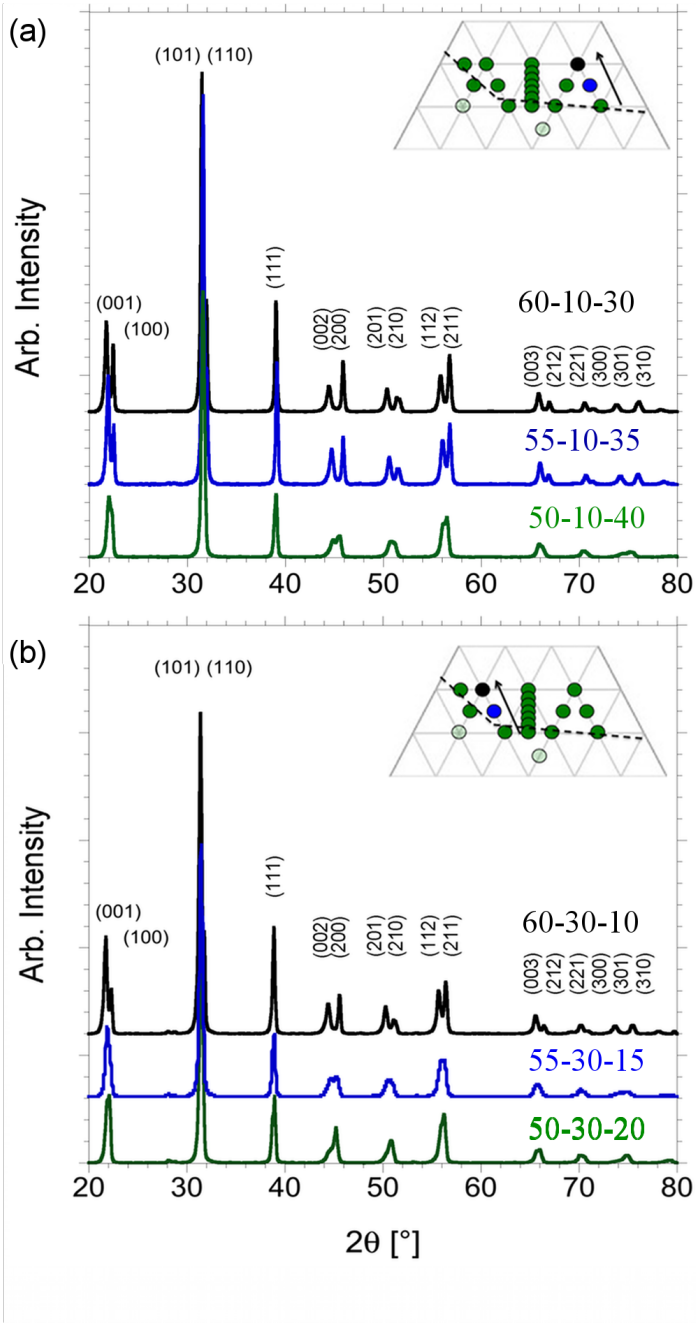

FIGURE 8.2: Room temperature x-ray diffraction of BNiT-rich compositions **(a)** and BS-rich compositions **(b)**. In both parts, an insert of the middle portion of the phase diagram is displayed with the compositions color-coded in both the insert and the XRD.

MPB line lies in the regions indicated in [Fig. 8.1(b)]. In addition, the direct room temperature d_{33} coefficient values were higher for compositions closer to the MPB line and a clear decrease in properties was observed in compositions far away from the transition line.

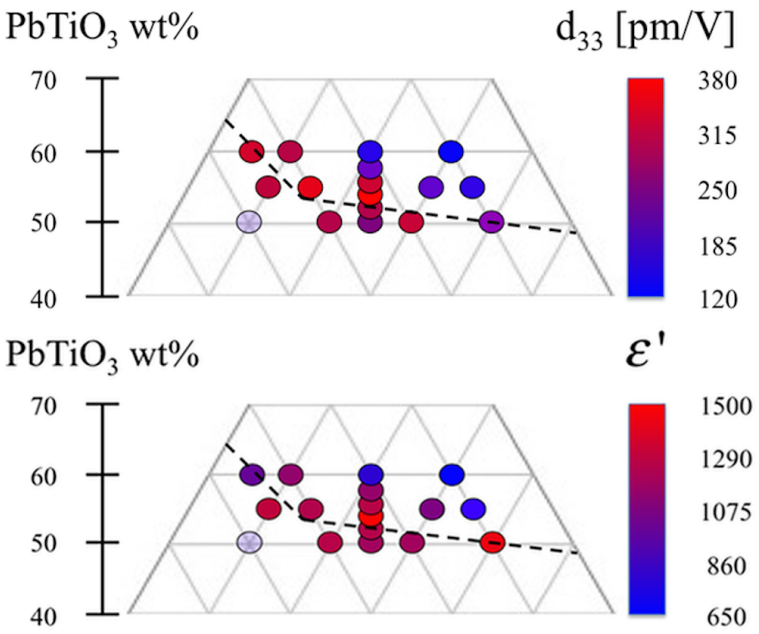

FIGURE 8.3: **(a)** Room temperature d_{33} [pm/V] and **(b)** permittivity of compositions within the PT-BS-BNiT ternary phase diagram. The composition 50-40-10 is transparent as in Fig. 8.1 indicating a second phase.

Figure 8.3 displays exploded views of the phase diagram like in [Fig. 8.1 (b)] where the values of both room temperature d_{33} [pm/V] in [Fig. 8.3 (a)] and room temperature permittivity [Fig. 8.3 (b)] are color-coded in terms of quantity. The higher the piezoelectric coefficient or permittivity, the redder the color in the corresponding figures as shown in the color bar in each figure. A trend is seen in Fig. 8.3 where compositions closer to the MPB generally exhibited higher properties. Other trends include a decrease in maximum permittivity, T_C, and T_d as the composition moved from the PT-BS binary line to the PT-BNiT binary line. An asterisk appears in Table

8.2 after the composition 50-40-10 indicating a second phase was present in this composition.

TABLE 8.2: Room Temperature Piezoelectric Coefficient, Transition Peak Diffuseness, and Dielectric Properties at 25 °C and 100 °C. The composition identified with an asterisk (*) indicates the presence of impurity peaks in the XRD data.

			25 °		100 °	
PT-BS-BNiT	d_{33} [pC/N]	γ	ϵ_r	tanδ	ϵ_r	tanδ
50-10-40	262	1.56	1427	0.072	2573	0.073
50-20-30	320	1.61	1292	0.077	2507	0.076
50-25-25	256	1.81	1187	0.075	2187	0.074
50-30-20	301	1.70	1205	0.080	2254	0.071
50-40-10*	190	1.62	824	0.064	1204	0.052
55-10-35	170	1.81	863	0.031	1153	0.031
55-15-30	218	1.75	1076	0.036	1481	0.033
55-30-15	350	1.81	1241	0.031	1944	0.031
55-35-10	310	1.55	1252	0.072	2110	0.060
60-10-30	127	1.84	671	0.017	829	0.019
60-30-10	304	1.49	1094	0.033	1440	0.030
60-35-5	331	1.72	1050	0.040	1338	0.036

Figure 8.4 provides the relative permittivity and loss tangent data of four poled compositions. In general, the dielectric properties were characterized by sharp phase transitions for compositions rich in PT, whereas compositions rich in BS and/or BNiT were characterized by diffuse phase transitions indicative of relaxor behavior. On the PT-BS rich side of the ternary, sharp first-order phase transitions were observed similar to that found in the PT-BS system with high relative permittivities such as

for the composition 60-30-10 as shown in [Fig. 8.4 (a)] [8]. In the PT-BNiT rich region, the composition 60-10-30 [Fig. 8.4 (b)] exhibited a similar sharp increase in relative permittivity near T_C in the poled sample. In compositions near the middle of the ternary system such as 50-30-20 [Fig. 8.4 (c)], small frequency dependence was observed in the vicinity of T_C (approximately 2 to 8 ^oC per decade of frequency). The occurrence of this frequency dependence became more apparent as the BNiT content increased. For example, the composition 50-10-40 [Fig. 8.4 (d)] exhibited a shift in the temperature of maximum permittivity on the order of $\approx$ 50 ^oC over the frequency range 1 kHz to 100 kHz. Therefore, instead of T_C as the transition temperature, T_m will be used following the convention for relaxor ferroelectrics. In previous work, samples with equimolar amounts of BS and BNiT (i.e. in the middle of the ternary phase diagram) were investigated and compositions with a higher PT content exhibited sharp phase transitions that broadened as the mole fraction of the Bi-containing end-members increased [26, 27]. Similar trends were observed in the compositions with substantial BS content such as 60-30-10 and 50-30-20 on the left side of the ternary diagram in Fig. 8.1. Compositions rich in BNiT and at constant PT content, exhibited relaxor-like behavior, especially in the composition 50-10-40 with strongly frequency dependent permittivity.

In general, the diffuseness of the phase transition increased as the BNiT content increased. The composition 50-30-20 exhibited a relatively narrow peak near T_m, but as the BNiT content increased relaxor-like behavior was observed with a broadening in the transition peak. The parameter γ is a quantitative measure of the diffuseness of a peak in permittivity. The parameter is measured by using a modified Curie-Weiss law and the details are described by Datta et al [37]. Table 8.2 lists γ for compositions in this system. Comparing the diffuseness of compositions in Fig. 8.4, diffuseness initially increases as the BNiT content increases. For composition 60-30-10 (10 % BNiT), γ = 1.49, for 50-30-20 (20 % BNiT), γ = 1.70, and for 50-20-30 (30 % BNiT), γ = 1.81. For composition 50-10-40 (40 % BNiT) however, the diffuseness is 1.56, which

does not follow the expected trend. This anomaly in the diffuseness is a result of the high temperature peak interfering in the calculation of the diffuseness. Choi et al. reported similar results with diffuse phase transitions in the PT-BNiT binary solid solution and described a very broad and diffuse transition peak in permittivity at the MPB composition (≈ 49 % PT) [22].

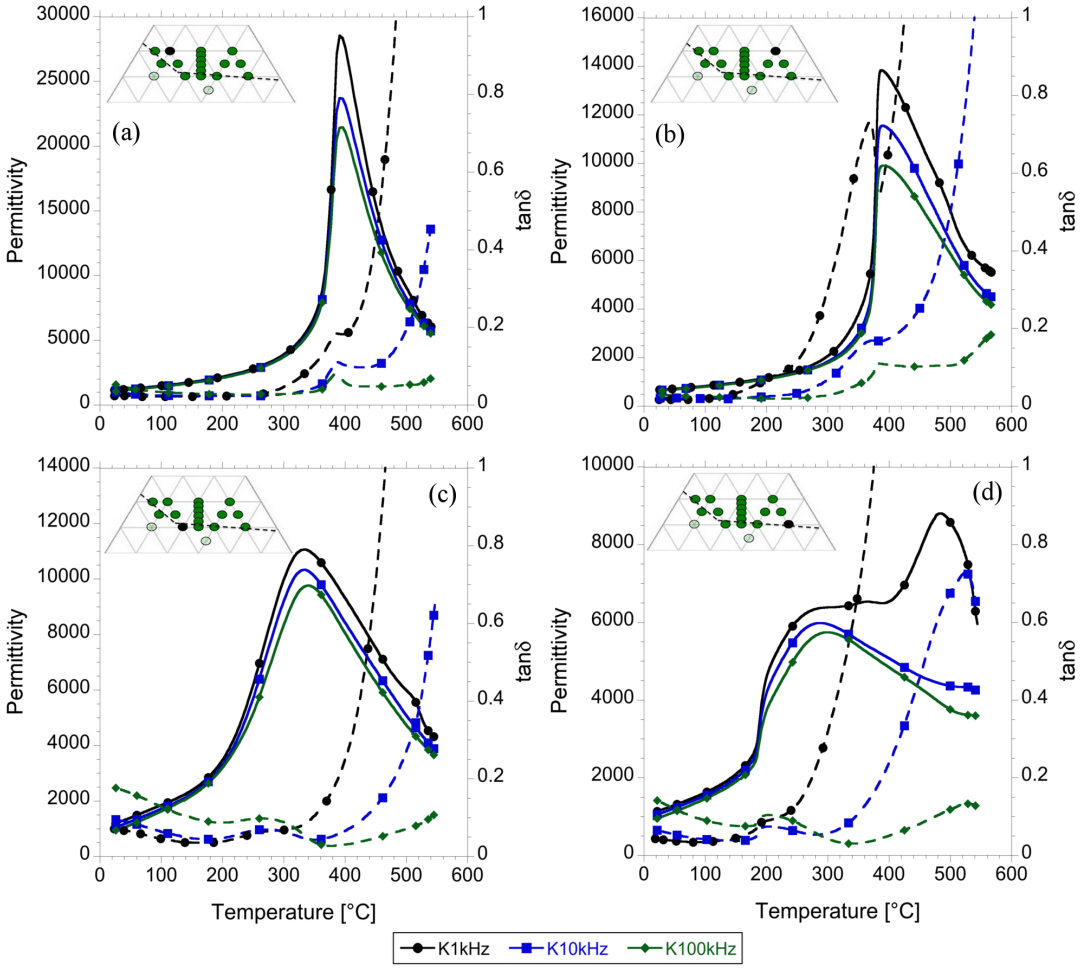

FIGURE 8.4: Relative permittivity and loss tangent of poled compositions: **(a)** 60-30-10, **(b)** 60-10-30, **(c)** 50-30-20, and **(d)** 50-10-40. Phase diagram included in inset of all four compositions with a black dot representing the compositions location in the diagram.

Because of the relaxor like behavior observed in PT-poor compositions such as the composition 50-10-40, T_C can no longer be used solely as the figure of merit for the maximum operating temperature. Even in materials such as PZT, the maximum operating temperature is generally listed as half the Curie temperature (≈ 180 °C) [3]. An alternative measure of maximum operating temperature builds on the development of lead-free piezoceramics where the observation of an ambiguity in T_C in a number of solid solutions led researchers to identify the temperature at which the sample experiences the steepest decrease in polarization as the depolarization temperature (T_d) [36]. For sufficiently poled piezoelectrics, T_d derived from dielectric data has been defined as the first peak in loss tangent during heating. Physically, this is linked to an intermediate phase region where there is a loss of long range order above T_d but at temperatures below T_C or T_m [36, 38].

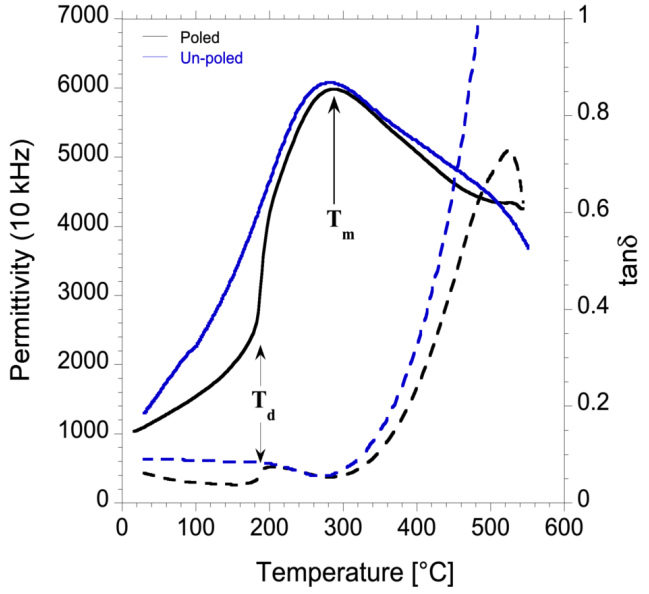

FIGURE 8.5: Relative permittivity of the composition 50-10-40 comparing both un-poled and poled specimens at 10 kHz.

At lower temperatures, application of high fields to an un-poled ferroelectric

ceramic induces long-range order in polarization. As the temperature increases past T_d, this order is broken and polarization decreases. Figure 8.5 displays the relative permittivity and loss of composition 50-10-40 for both un-poled and poled samples. In the poled sample, a dielectric anomaly is observed in addition to the permittivity peak and corresponds to the temperatures, T_d and T_m. As shown in the loss tangent data, the poled specimen experienced lower losses at temperatures lower than T_d in comparison to the un-poled specimen. Then the loss tangent increased to closely match the loss of an un-poled specimen at $T \geq T_d$. This behavior will be discussed and compared to other systems in a later section [39].

8.4.2 High Temperature Piezoelectric Properties

The depolarization temperature can also be determined more directly through the measurement of the temperature dependence of d_{33}. As the temperature is increased, the piezoelectric coefficient increased in all compositions in this study up to a maximum value, above that temperature d_{33} dropped off to zero. The inflection point in the temperature dependent d_{33} curve, at temperatures higher than the maximum in d_{33}, is defined as the depolarization temperature, T_d [36]. Figure 8.6 provides the in-situ d_{33} values of four different compositions as compared to soft PZT (PIC 151, PI Ceramics, Lederhose, Germany) and hard PZT (PIC 181, PI Ceramics, Lederhose, Germany). For the compositions 60-30-10 and 60-10-30, d_{33} decreased to zero at $T_d \approx$ 370 ^{o}C just slightly below $T_C \approx 400$ ^{o}C. In the former, d_{33} increased to a maximum of 800 pC/N, while in the latter, d_{33} increased to only 245 pm/V. In 50-30-20, d_{33} had an initial constant increase over the temperature range 75 ^{o}C - 200 ^{o}C followed by an increase in the slope up to $T_d \approx 280$ ^{o}C. Similar behavior was observed in 50-20-30, although the rate of increase generally stayed high and the maximum in d_{33} occurred at lower temperature of ≈ 190 ^{o}C. The last composition, 50-10-40, d_{33} remained at a relatively high value of about 400 pC/N up to $T_d \approx 215$ ^{o}C.

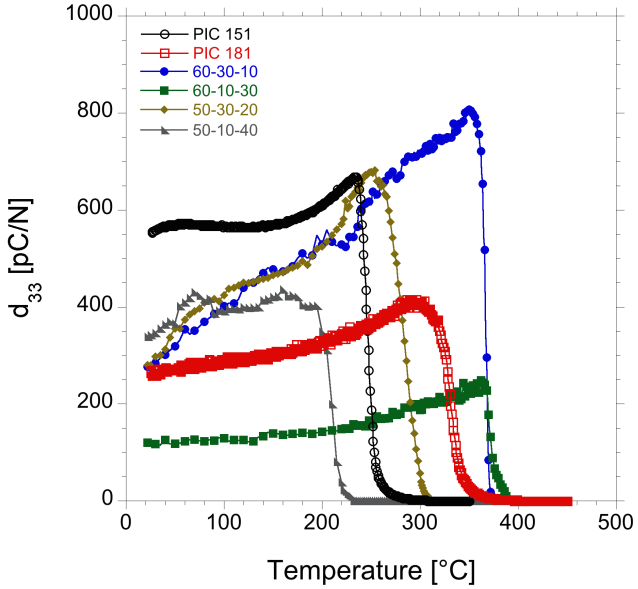

FIGURE 8.6: In-situ piezoelectric coefficients of compositions across the ternary phase diagram as compared to soft PZT.

For the majority of the compositions, the T_d values measured from dielectric data were similar to T_d values measured from the in-situ piezoelectric data. The depolarization temperatures generally increased with increasing PT-BS content. This temperature also increased with increasing PT content where the highly tetragonal compositions exhibited a higher T_d. Compositions rich in PT-BS exhibits a small difference between T_d and T_C. For those compositions closer to PT-BNiT in content, the difference in T_d and T_m was larger. Measured depolarization temperatures from both dielectric and in-situ d_{33} data are listed in Table 8.3 .

8.4.3 High Temperature Ferroelectric Properties

The depolarization and Curie temperatures are important high temperature properties of piezoelectric ceramics. These temperatures determine the maximum usable range. However, with bulk ceramics, high fields are often required to operate actuators. With high temperatures and high-applied electric fields, dielectric break-

TABLE 8.3: Depolarization Temperatures Measured by Dielectric Permittivity and in-situ d_{33}.

Composition	$T_{Dielectric}$ [°C]	$T_{in-situ}$ [°C]
50-10-40	190	215
50-20-30	230	215
50-25-25	250	278
50-30-20	280	282
55-30-15	290	288
55-35-10	290	288
60-10-30	365	370
60-30-10	380	367
60-35-5	400	400

down of the piezoelectric material is likely. In order to investigate the stability of samples, a field of 40 kV/cm was applied to various compositions across the ternary diagram at temperatures starting from room temperature up to 190 °C. This maximum temperature was selected in order to avoid issues with the breakdown of silicon oil in the sample holder.

Figure 8.7 provides the polarization and strain measurements of BNiT compositions (XRD depicted in [Fig. 8.2 (b)]) measured at temperatures 25, 50, 100, 150, and 190 °C. In [Fig. 8.7 (a)], the polarization loops of 60-30-10 at temperatures up to 190 °C is characteristic of a normal ferroelectric with saturation and minimal loss. The room temperature coercive field was measured at ≈ 34 kV/cm and the remanent polarization was at 28 μC/cm^2. As the temperature increased, the remanent polarization increased while the coercive field decreased to ≈ 14.0 kV/cm. In [Figs. 8.7 (b) and (e)]

and [Figs. 8.7 (c) and (f)], the same polarization and strain tests were carried out on the compositions 55-30-15 and 50-30-20, respectively. Both compositions had values of remanent polarization similar to 60-30-10, however, both experienced conductive loss at temperatures close to 190 ^{o}C. In [Fig. 8.7 (c)], polarization of composition 50-30-20 at 190 ^{o}C was omitted as the losses became too high. This behavior is seen to a smaller extent in [Fig. 8.7 (b)].

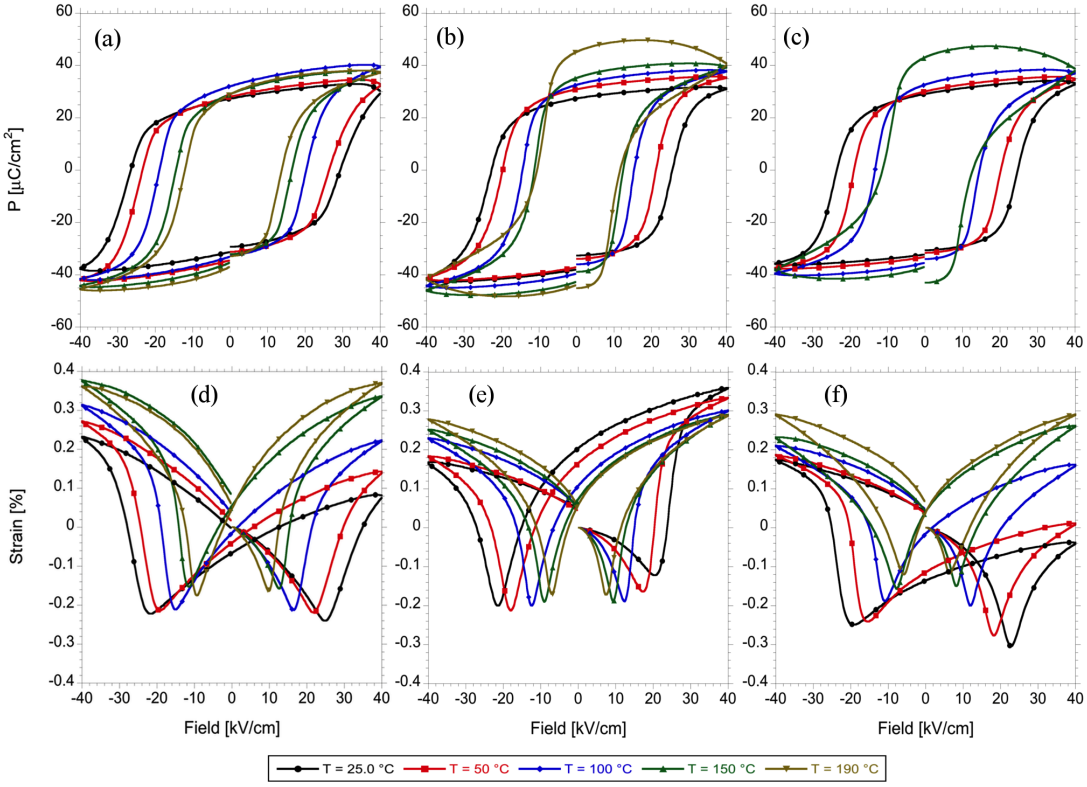

FIGURE 8.7: Plots of polarization and strain in temperature for the compositions: **(a)** and **(d)** 60-30-10, **(b)** and **(e)** 55-30-15, **(c)** and **(f)** 50-30-20.

The electromechanical strain data for the composition 60-30-10 in [Fig. 8.7 (d)] revealed a high degree of asymmetry at lower temperatures. The right hand strain loop was larger than the left hand strain loop in this composition. Similar asymmetric strain behavior was observed in composition 50-30-20 seen in [Fig. 8.7 (f)]. In the

composition 55-30-15 in [Fig. 8.7 (e)] the left hand strain loop was larger than the right. Remanent strain and polarization was also observed up to the highest measurement temperature and can be attributed to domains which have not rotated back to their original orientation at zero field [4].

8.5 Discussion

Several key features of the PT-BS-BNiT ternary were demonstrated so far: an apparent shift between normal and relaxor ferroelectric behavior (Fig. 8.4), dielectric anomaly only in poled samples (Fig. 8.5), and poled sample strain asymmetry (Fig. 8.7). The strain asymmetry may be a result of aging in the ceramic based on the poling procedure and will be discussed shortly. In Fig. 8.5, the lack of more than two dielectric anomalies indicates a broad phase transition between the ferroelectric tetragonal phases and the high temperature paraelectric cubic, with a mixture of ferroelectric tetragonal and relaxor pseudo-cubic phases at temperatures between T_d and T_m.

Figure 8.8 illustrates the trend in dielectric and piezoelectric anomalies observed in the ternary system as a function of composition. The transition temperatures of those compositions shown in Fig. 8.2 are plotted in Fig. 8.8, where T_{d1} and T_{d2} are the depolarization temperatures measured from dielectric data and in-situ d_{33} measurements, respectively. The inset in both parts of Fig. 8.8 provides the compositions represented. Overall there was a decrease in the temperature of all three anomalies as the mole fraction of BNiT increased both on the PT-BS-rich side [Fig. 8.8 (a)] and in the BNiT-rich compositions in [Fig. 8.8 (b)]. In addition, the temperature difference between T_d and T_m varied as a function of composition. Region I in Fig. 8.8 corresponds to the high temperature paraelectric phase which was cubic for all compositions. Region II represents the intermediate regime between T_d and T_m, which is also indicated in Fig. 8.5 for the poled composition 50-10-40. Region III corresponds

to the low temperature phase which was tetragonal for PT-rich compositions and pseudo-cubic or rhombohedral for compositions rich in BS and/or BNiT.

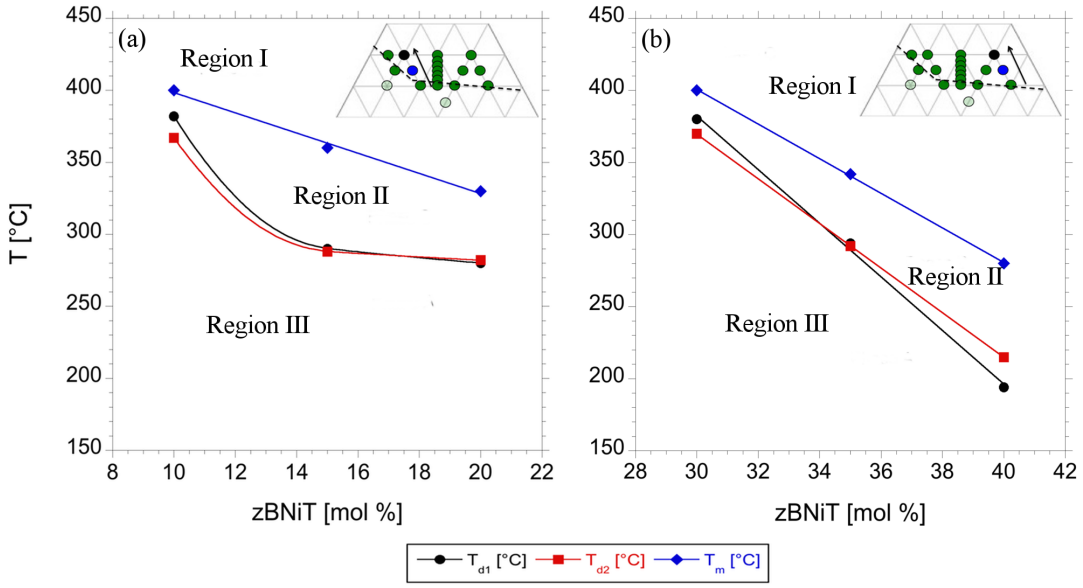

FIGURE 8.8: Comparison of the temperatures of dielectric and piezoelectric anomalies (T_{d1} from dielectric data of poled samples, T_{d2} from in-situ d_{33} data, and T_m from dielectric data) for three PT-BS rich compositions: 60-30-10, 55-30-15, and 50-30-20 in **(a)** and three PT-BNiT rich compositions: 60-10-30, 55-10-35, and 50-10-40 in **(b)**, where the x-axis is plotted in terms of zBNiT. Insets indicate where the compositions are in the phase diagram. Region I corresponds to the high temperature paraelectric phase. Region II is the intermediate regime. Region III indicates the regime for the low temperature phase.

For compositions that exhibited a sharp first-order phase transition, such as 60-30-10 [Fig. 8.4 (a)] or 60-10-30 [Fig. 8.4 (b)], T_m and T_d are approximately the same and depolarization occurred near the paraelectric-ferroelectric phase transition. As the amount of BNiT increased, a broadening in the dielectric maxima occurred and the phase transitions became increasingly diffuse. There was an apparent shift from a normal paraelectric-ferroelectric phase transition to a relaxor ferroelectric transition

as seen in BNiT rich compositions like 50-10-40 [Fig. 8.4 (d)] mentioned previously. For compositions such as 50-10-40, there was a large difference between T_d and T_m corresponding to different dielectric anomalies.

In ferroelectrics that are characterized by a diffuse phase transition such as in $Pb_{1-x}La_x(Zr_{0.65}Ti_{0.35})O_3$ (PLZT), field-induced long range order disappears upon heating through a thermal depoling temperature, defined as T_t, by Schmidt et al. [38]. This temperature was observed to be lower than T_C. Upon cooling back down through T_C, no evidence of T_d was observed. Multiple dielectric anomalies were also seen in the relaxor $(Bi_{1/2}Na_{1/2})TiO_3$ (BNT), where three different dielectric anomalies were seen at temperatures: T_d, T_{T-R}, and T_m, corresponding to the depolarization, tetragonal to rhombohedral transition, and maximum in permittivity, respectively [36, 39]. In the solid solution of BNT-$BaTiO_3$ (BNT-BT), a two-step depolarization process was observed with randomization of domain structures at a lower temperature followed by the ferroelectric-relaxor transition temperature [40]. In the composition 50-10-40 there is no phase transition (like T_{T-R} in BNT) observed between T_d and T_m. Stein et al. found multiple dielectric anomalies in compositions in the $PbTiO_3$-$Bi(Zn_{1/2}Ti_{1/2})O_3$-$Bi(Mg_{1/2}Ti_{1/2})O_3$ (PT-BZT-BMT) ternary piezoelectric system [41]. These dielectric anomalies were attributed to tetragonal distortions that persist to temperatures beyond the first dielectric anomaly. It was observed in compositions with a large mole fraction of Bi cations on the A-site and with ferroelectrically active cations (i.e. Ti, Zn, Sc, etc.) residing on the B-site [41]. In this system, the appearance of multiple dielectric anomalies corresponded to compositions with relatively high Bi content in the A-site and relatively high concentrations of Ni^{2+}, which is another ferroelectrically active cation, on the B-site. However, the second dielectric anomaly appeared only after poling, as seen in Fig. 8.5. In comparison to other systems, the PT-BS-BNiT ternary system seems to most resemble both the PT-BZT-BMT and the diffuse ferroelectric relaxors like PLZT. A large amount of Bi cations causes the relaxation in dielectric permittivity like in PT-BZT-BMT, but the multiple dielectric

anomalies occur only after a poling treatment as found in PLZT.

The discussion thus far has been focused on high temperature, low field properties. The effects of high fields on the ferroelectric properties of actuators operating at high temperatures are also important. In this study, high fields were applied to poled samples just below 200 ^{o}C. Higher temperatures were not possible due to the limitation of heating silicone oil. Throughout the ternary system, at low temperatures, normal ferroelectric behavior was observed in the polarization and strain data. The small remanent polarization values and quadratic strain loops characteristic of an ergodic relaxor ferroelectric were not observed. Instead large leakage currents resulted in deformed "lossy" polarization loops at temperatures approaching 200 ^{o}C, which is still below T_d for all compositions studied. In the strain loops, a high degree of asymmetry was observed in all compositions at low temperatures. This asymmetry is due to domain wall pinning in poled samples. Domain wall pinning is an aging effect where an initial domain orientation is stabilized during the high temperature poling treatment and is linked to the formation of an internal bias field [42]. Thus the formation of a bias field was the result of the poling treatment (DC loading) [43]. Microscopically, movement of mobile charge carriers to the domain walls generates an internal bias field, as DC loading is similar to unipolar loading, which likely induced the strain asymmetry seen in Fig. 8.7 [44].

Figure 8.9 provides the strain asymmetry [Fig. 8.9 (a)] and the bias field [Fig. 8.9 (b)] in the three compositions: 60-30-10, 55-30-15, and 50-30-20. Strain asymmetry (γ_S) and bias field (E_{bias}) were calculated using the definitions established by Balke et al. in the study of fatigue in PZT [44, 45]. In [Fig. 8.9 (a)], negative γ_S was observed in compositions 60-30-10 and 50-30-20 at low temperatures which increased to zero with increasing temperature, a slight positive γ_S was observed between 150 and 175 ^{o}C in 50-30-20. In the composition 55-30-15, a positive γ_S at low temperatures was observed which also tended toward zero as the temperature increased. These effects are related to the different magnitudes of the strain loop maxima observed in Fig. 8.7.

The large bias fields observed in the composition 60-30-10 in [Fig. 8.9 (b)] were due to the increased aging of poled samples. This might be a function of composition due

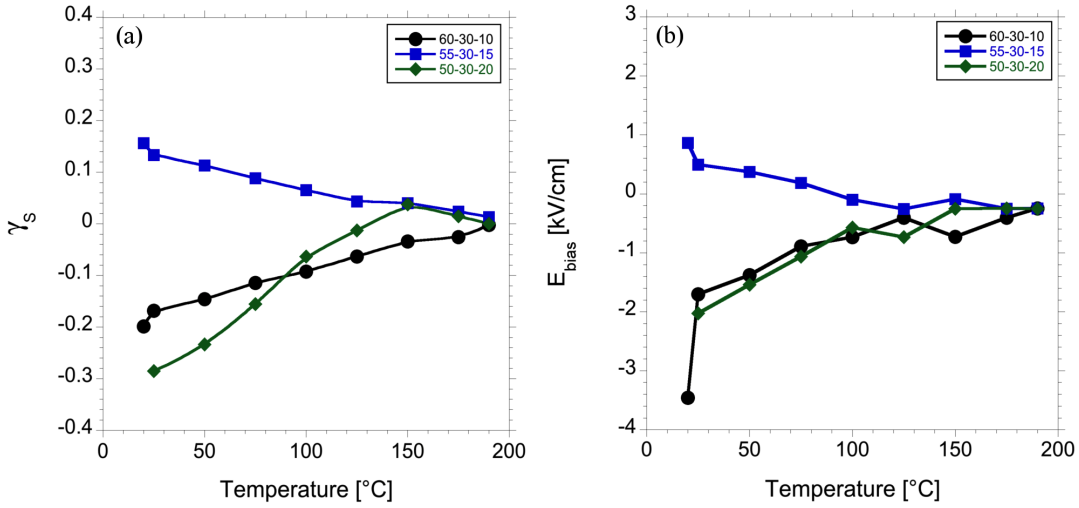

FIGURE 8.9: (a) Plot of asymmetry in strain with increasing temperature for the compositions: (a) 60-30-10, (b) 55-30-15, and (c) 50-30-20. **(b)** Bias field of same compositions shown in part (a).

to the relative distance from the MPB in this ternary system. Much lower bias fields were observed in the other two compositions. With an increase in the temperature, the strain loops became symmetric. This can be attributed to thermally assisted domain reorientation and an increase in domain wall mobility at higher temperatures due to the increased thermal energy in the system [6].

8.6 Conclusion

Ternary solid solutions based on PT-BS-BNiT were investigated as a potential alternative for high temperature piezoelectric materials based on PT-BS and PZT. With measurement of the high temperature properties of the entire BNiT ternary system, a transition line was identified by observing the following trends: an increase in d_{33}

up to 331 pC/N, an increase in P_r up to a value of 34.1 μC/cm^2, and an increase in the room temperature permittivity. It was also observed that BNiT rich compositions exhibited relaxor-like behavior in dielectric data. Therefore, T_C was found to be an inappropriate label for the transition temperature for these compositions and replaced with T_m. It was also found that polarization was reduced at temperatures (T_d) much lower than T_m. The depolarization temperature was determined using two different methods, including dielectric measurements on poled samples and an in-situ d_{33} technique. The values of T_d between the two methods differed by no more than 25 ^{o}C. As the PT-BS content increased, the difference between T_d and T_m decreased and dielectric transition peaks sharpened. The composition 60-35-5 had $T_d \approx T_m$ = 405 ^{o}C while for a composition rich in BNiT, namely 50-10-40, the depolarization temperature was $T_d \approx 200\ ^o$C. The measurement of the piezoelectric coefficient in-situ revealed the temperature dependent behavior of d_{33} with the largest values recorded over 1000 pC/N in the composition 50-20-30 close to T_d. Low temperature strain asymmetry was attributed to the rise of an internal bias field which was the result of charge agglomeration at the domain walls leading to pinning. As the temperature was increased, thermally assisted domain reorientation led to symmetric strain loops and increased remanent polarizations.

8.7 Acknowledgements

The authors would like to acknowledge funding of this work by the Deutsche Forschungsgemeinschaft (DFG) through SFB595, project D1. The authors would also like to thank Matias Acosta and Deborah Schneider for their help in experimentation and to acknowledge Kyle Webber and Florian Schader for their help in completing the final manuscript.

8.8 References

1. Bao, X. *et al.* Modeling and Computer Simulation of Ultrasonic/Sonic Driller/ Corer (USDC). **50,** 1147–1160 (2003).
2. Rödel, J., Jo, W., Seifert, K. T. P., Anton, E. M. & Granzow, T. Perspective on the Development of Lead-free Piezoceramics. *J. Am. Ceram. Soc.* **92,** 1153 (2009).
3. Jaffe, B., Cook, W. R. & Jaffe, H. *Piezoelectric Ceramics* 1st ed. 317 pp. (Academic Press, New York, 1971).
4. Damjanovic, D. Ferroelectric, dielectric and piezoelectric properties of ferroelectric thin films and ceramics. *Rep. Prog. Phys.* **61,** 1267–1324 (1998).
5. Jaffe, B., Roth, R. & Marzullo, S. Properties of Piezoelectric Ceramics in the Solid-Solution Series Lead Titanate-Lead Zirconate-Lead Oxide: Tin Oxide and Lead Titanate-Lead Hafnate. *J Res Nat Bur Stand* **55,** 239–254 (1955).
6. Sehirlioglu, A., Sayir, A. & Dynys, F. Doping of $BiScO_3$-$PbTiO_3$ Ceramics for Enhanced Properties. *J. Am. Ceram. Soc.* **93,** 1718–1724 (2010).
7. Turner, R., Fuierer, P., Newnham, R. & Shrout, T. R. Materials for high temperature acoustic and vibration sensors: A review. *Appl. Acoust.* **41,** 299 (1994).
8. Eitel, R. E. *et al.* New High Temperature Morphotropic Phase Boundary Based on $Bi(Me)O_3$-$PbTiO_3$ Ceramics. *Jpn. J. Appl. Phys.* **40,** 5999–6002 (2001).
9. Eitel, R. E., Randall, C. A., Shrout, T. R. & Park, S.-E. Preparation and Characterization of High Temperature Perovskite Ferroelectrics in the Solid-Solution (1-x)$BiScO_3$-x$PbTiO_3$. *Jpn. J. Appl. Phys.* **41,** 2099–2104 (2002).
10. Eitel, R. E., Zhang, S. J., Shrout, T. R. & Randall, C. A. Phase Diagram of the Perovskite System (1-x)$BiScO_3$-x$PbTiO_3$. *J. Appl. Phys.* **96,** 2828–2831 (2004).
11. Sterianou, I. *et al.* High-temperature (1-x)$BiSc_{1/2}Fe_{1/2}O_3$-x$PbTiO_3$ piezoelectric ceramics. *Appl. Phys. Lett.* **87,** 242901 (2005).

12. Sterianou, I., Sinclair, D. C., Reaney, I. M., Comyn, T. & Bell, A. J. Investigation of high Curie temperature (1-x)$BiSc_{1-y}Fe_yO_3$-x$PbTiO_3$ piezoelectric ceramics. *J. Appl. Phys.* **106** (2009).

13. Zhang, S. J., Alberta, E. F., Eitel, R. E., Randall, C. A. & Shrout, T. R. in *IEEE Transactions on Ultrasonics, Ferroelectrics, and Frequency control* **52** (IEEE, 2005), 11.

14. Chen, S., Dong, X., Yang, H., Liang, R. & Mao, C. Effects of Niobium Doping on the Microstructure and Electrical Properties of 0.36$BiScO_3$-0.64$PbTiO_3$ Ceramics. *J. Am. Ceram. Soc.* **90,** 477–482 (2007).

15. Eitel, R. E., Shrout, T. R. & Randall, C. A. Tailoring Properties and Performance of (1-x)$BiScO_3$-x$PbTiO_3$ Based Piezoceramics by Lanthanum Substitution. *Jpn. J. Appl. Phys.* **43,** 8146–8150 (2004).

16. Sehirlioglu, A., Sayir, A. & Dynys, F. High Temperature Properties of $BiScO_3$-$PbTiO_3$ Piezoelectric Ceramics. *J. Appl. Phys.* **106,** 0141021–0141027 (2009).

17. Sehirlioglu, A., Sayir, A. & Dynys, F. Microstructural-Property Relationships in Liquid Phase-Sintered High-Temperature Bismuth Scandium Oxide-Lead Titanate Piezoceramics. *J. Am. Ceram. Soc.* **91,** 2910–2916 (2008).

18. Zhang, S. J., Randall, C. A. & Shrout, T. R. High Curie temperature piezocrystals in the $BiScO_3$-$PbTiO_3$ perovskite system. *Appl. Phys. Lett.* **83,** 3150–3152 (2003).

19. Suchomel, M. R. & Davies, P. K. Predicting the position of the morphotropic phase boundary in high temperature $PbTiO_3$Bi(B′B")O_3 based dielectric ceramics. *J Appl Phys* **96,** 4405–4410 (2004).

20. Sharma, S. & Hall, D. A. Ferroelectric and Antiferroelectric Polarization Switching Characteristics of Bi($Mg_{0.5}Ti_{0.5}$)O_3-$PbTiO_3$ Ceramics. *J. Mater. Sci.: Mater. Electron.* **21,** 405–409 (2010).

21. Chen, J., Tan, X., Jo, W. & Rödel, J. Temperature dependence of piezoelectric properties of high-T_C Bi($Mg_{1/2}Ti_{1/2}$)O_3-$PbTiO_3$. *J. Appl. Phys.* **106,** 034109 (2009).

22. Choi, S. M., Stringer, C. J., Shrout, T. R. & Randall, C. A. Structure and Property Investigation of a Bi-based Perovskite Solid Solution: (1-x)Bi($Ni_{1/2}Ti_{1/2}$)O_3-x$PbTiO_3$. *J. Appl. Phys.* **98,** 0341081–0341084 (2005).

23. Takenaka, T. & Yamada, M. Solid-Solution ($Bi_{1-x}Pb_x$)($Ni_{(1+x)/2}Ti_{(1+x)/2}$)O_3 for New Piezoelectric Ceramics. *Jpn. J. Appl. Phys.* **32,** 4218–4222 (1993).

24. Duan, R., Speyer, R. F., Alberta, E. F. & Shrout, T. R. High Curie temperature perovskite $BiInO_3$-$PbTiO_3$ ceramics. *J Mater Res* **19,** 2185–2193 (2004).

25. Yu, H., Ren, W. & Ye, Z. G. Structural, Dielectric, and Ferroelectric Properties of the (1-x)$PbTiO_3$-x$BiAlO_3$ Solid Solution. *IEEE Trans. Ultra. Ferro. Freq. Control* **57,** 2177–2181 (2010).

26. Cheng, J. R., Zhu, W., Li, N. & Cross, L. Fabrication and characterization of x$BiGaO_3$-(1-x)$PbTiO_3$: a high temperature reduced Pb-content piezoelectric ceramic. *Mater. Lett.* **57,** 2090–2094 (2003).

27. Venevstev, Y. N. *et al. Sov. Phys. Crystallogr.* **5,** 594 (1960).

28. Woodward, D., Reaney, I., Eitel, R. E. & Randall, C. A. Crystal and domain structure of the $BiFeO_3$-$PbTiO_3$ solid solution. *J Appl Phys* **94,** 3313–3318 (2003).

29. Woodward, D. & Reaney, I. A structural study of ceramics in the ($BiMnO_3$)x-($PbTiO_3$)1-x solid solution series. *J Phys Condens Matter* **16,** 8823–8834 (2004).

30. Suchomel, M. R. & Davies, P. K. Enhanced Tetragonality in (x)$PbTiO_3$-(1-x)Bi($Zn_{1/2}Ti_{1/2}$)O_3 and Related Solid Solution Systems. *Appl. Phys. Lett.* **86,** 2629051–2629053 (2005).

31. Leist, T. *et al.* Temperature Dependence of the Piezoelectric Coefficient in $BiMeO_3$-$PbTiO_3$ (Me = Fe, Sc, ($Mg_{1/2}Ti_{1/2}$)) Ceramics. *J. Am. Ceram. Soc.* **95,** 711–715 (2012).

32. Stein, D. M., Suchomel, M. R. & Davies, P. K. Enhanced tetragonality in (x)$PbTiO_3$-(1-x)Bi(B'B'')O_3 systems: Bi($Zn_{3/4}W_{1/4}$)O_3. *Appl. Phys. Lett.* **89,** 132907 (2006).

33. Ansell, T. Y. & Cann, D. P. Piezoelectric properties of the high temperature MPB x$PbTiO_3$ - (1-x)[$BiScO_3$ + Bi($Ni_{1/2}Ti_{1/2}$)O_3] composition. *J Electroceram* **31,** 159–167 (2013).

34. Ansell, T. Y., Cann, D. P., Nikkel, J. & Sehirlioglu, A. High Temperature Piezoelectric Ceramics based on x$PbTiO_3$-(1-x)Bi($Sc_{1/2}Me_{1/4}Ti_{1/4}$)O_3 (Me = Zn, Mg) Ternary Perovskites. *Jpn. J. Appl. Phys.* **51,** 101802 (2012).

35. *ANSI/IEEE 176-1987, IEEE Standard on Piezoelectricity* (IEEE, New York, 1987).

36. Anton, E. M., Jo, W., Damjanovic, D. & Rödel, J. Determination of depolarization temperature of ($Bi_{1/2}Na_{1/2}$)TiO_3-based lead-free piezoceramics. *J. Appl. Phys.* **110,** 094108–14 (2011).

37. Datta, K., Thomas, P. A. & Roleder, K. Anomalous phase transitions of lead-free piezoelectric x$Na_{0.5}Bi_{0.5}TiO_3$-(1-x)$BaTiO_3$ solid solutions with enhanced phase transition temperatures. *Phys. Rev. B* **82,** 224105 1–6 (2010).

38. Schmidt, G. *et al.* Induced Phase Transitions in Ferroelectrics with Diffuse Phase Transitions. *Phys. Stat. Sol. (A)* **63,** 501–510 (1981).

39. Hiruma, Y., Nagata, H. & Takenaka, T. Phase diagrams and electrical properties of ($Bi_{1/2}Na_{1/2}$)TiO_3-based solid solutions. *J. Appl. Phys.* **104,** 124106 (2008).

40. Jo, W., Daniels, J., Damjanovic, D., Kleeman, W. & Rödel, J. Two-stage processes of electrically induced-ferroelectric to relaxor transition in 0.94($Bi_{1/2}Na_{1/2}$)Ti)O_3-0.06$BaTiO_3$. *Appl. Phys. Lett.* **102,** 192903 (2013).

41. Stein, D. M., Grinberg, I., Rappe, A. M. & Davies, P. K. Multiple dielectric transitions in the $PbTiO_3$-Bi($Zn_{1/2}Ti_{1/2}$)O_3-BI($Mg_{1/2}Ti_{1/2}$)O_3 system. *J. Appl. Phys.* **110,** 074110 (2011).

42. Kamel, T. M. & With, G. d. Poling of hard ferroelectric PZT ceramics. *J. Eur. Ceram. Soc.* **28,** 1827–1838 (2008).

43. Lupascu, D. C. *Fatigue in Ferroelectric Ceramics and Related Issues Materials Science* **61** (Springer, 2004).

44. Balke, N., Lupascu, D. C., Granzow, T. & Rödel, J. Fatigue of Lead Zirconate Titanate Ceramics. I: Unipolar and DC Loading. *J. Am. Ceram. Soc.* **90,** 1081–1087 (2007).

45. Balke, N., Lupascu, D. C., Granzow, T. & Rödel, J. Fatigue of Lead Zirconate Titanate Ceramics II: Sesquipolar Loading. *J. Am. Ceram. Soc.* **90,** 1088–1093 (2007).

9 Conclusion

9.1 Summary of High Temperature Piezoelectric Development

Three ternary perovskite piezoelectric solid solution families were developed for high temperature piezoelectric actuator applications. The systems studied were $PbTiO_3$ - $BiScO_3$ - $Bi(Me_{1/2}Ti_{1/2})O_3$, where Me = Zn, or Mg, or Ni. in the BZT ternary system, X-ray diffraction revealed limited solid solubility in the compositional range of 60 - 100 % PT. Although investigation in the BZT system found a high T_C of 530 ^oC at 90 % PT and large dielectric permittivities ($\approx$ 20000), dielectric loss was quite large ($\approx$ 10) near T_C in the 90 % PT composition. Poling of BZT ternary compositions was also difficult due to the high degree of tetragonality in the system. More success was found in the BMT ternary with larger solubility range down to 40 % PT and XRD revealed a transition region where tetragonal phase peak splitting disappeared. However, a rhombohedral phase was not observed as the (111) peak did not split, an indication of rhombohedral symmetry. Despite this, samples in the BMT ternary were easily poled. The composition 42PT-29BS-29BMT was revealed to have the highest low field d_{33} value in this system with d_{33} = 280 pC/N. High field measurements also revealed the 42 % PT composition to have the largest high field piezoelectric coefficient, d_{33}* = 313 pm/V. The highest values of T_C in this ternary occurred in the composition 56PT-22BS-22BMT with $T_C \approx 450\ ^oC$. The low electromechanical coupling factor prompted research in the third ternary, PT-BS-BNiT.

The ions of zinc, magnesium, titanium, and scandium were used as the B-site cations because of their empty valence shells. The same is true for Ni^{2+} with an empty 4s shell. In the BNiT ternary, an initial look in the middle of the ternary similar to the region studied in the BZT and BMT ternaries revealed a smaller solubility range down to 50PT-25BS-25BNiT. Similar to the BMT ternary, a transition region was revealed through a combination of XRD and dielectric data, where tetragonal peak splitting disappeared as the PT content decreased down to 52 or 54 % PT. Curie temperatures

decreased from 415 °C to 335 °C at the transition in the compositional range studied. Because the composition 54PT-23BS-23BNiT exhibited superior piezoelectric properties as compared to the other compositions ($d_{33} \approx 376$ pC/N), chemical modification study was conducted on this composition. It was revealed that the addition of 2 wt% Bi improved low field $d_{33} = 445$ pC/N while the stoichiometric composition exhibited high field $d_{33}^* = 896$ pm/V and the highest strains of 0.5 %. An updated version of Figure 3.5 shows how values for d_{33} compare to other high temperature piezoelectric systems in Figure 9.1.

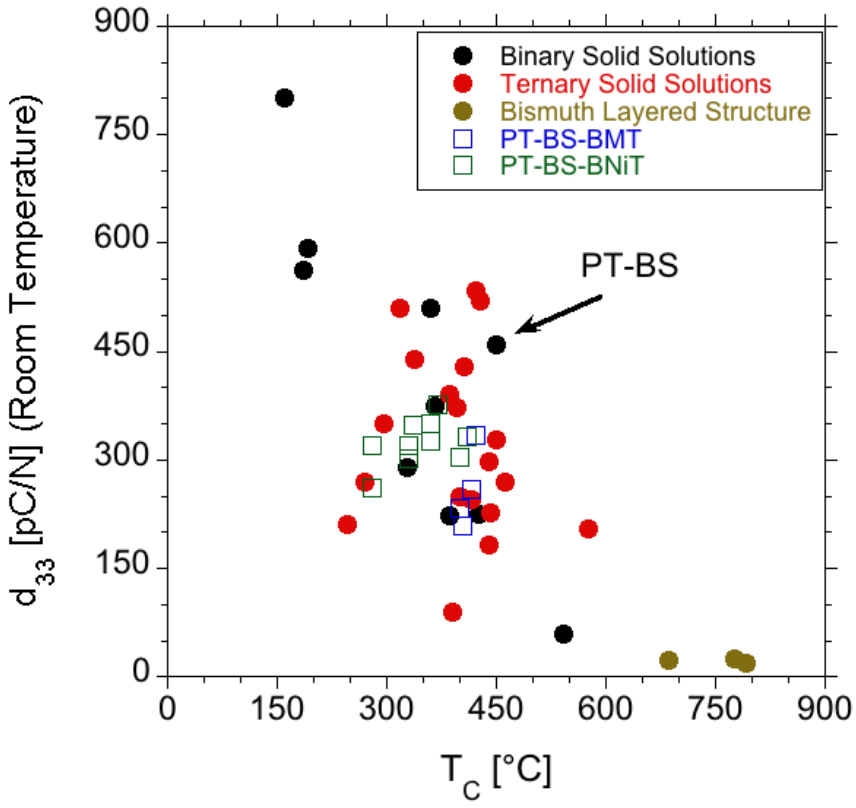

FIGURE 9.1: Room temperature piezoelectric coefficient versus T_C of binary, ternary, bismuth layered structure materials, and both the BNiT and BMT systems in comparison.

Dielectric testing on poled samples reveals dielectric maxima in loss that did not coincide with Curie temperature. Upon further study of the entire ternary system, it was found that compositions with large fractions of PT-BNiT in solution exhibited relaxor like behavior and T_C no longer became a valid figure of merit for the operational temperature range of these materials. Instead T_m and T_d were used. As the BNiT content increased, T_d decreased and the difference between T_m and T_d increased. Several models were looked at to explain the microscopic structure that exists in the phase region between T_d and T_m. The first was a phase transition between rhombohedral and tetragonal phases like in BNT-BKT but was ruled out because of a lack of rhomobohedral peaks in room temperature XRD. The second idea involved a transition between a low temperature ferroelectric phase and a high temperature relaxor phase like in BNT-BT (essentially ergodic/non-ergodic transition); however, the order of these transition are not second order as is proposed in the BNT-BT system and there is no evidence for ergodicity. In PLZT, long-range order is induced by a sufficiently high applied field and disappears upon heating through T_t. This temperature marks the onset of a ergodic phase similar to BNT-BT, but again is not observed in PT-BS-BNiT compositions. One final model suggested for the PT-BZT-BMT ternary, attributed the diffuse phase transitions to a persistence of a tetragonal phase in temperatures above T_d [1]. This was observed to occur in compositions with a significant amount of Bi in the A-site and ferroelectrically active cations in the B-site, both of which are true for BNiT-rich compositions like 50PT-10BS-40BNiT.

Another common occurrence in poled compositions of PT-BS-BNiT was the increase in d_{33} as the temperature increasing up to a maximum that occurs at a temperature just below T_d. Other perovskite ferroelectric materials exhibited this behavior. Table 9.1 tabulates T_d derived from in-situ d_{33} and the maximum d_{33} value. Generally, T_d was higher for compositions with a higher percentage of PT and those compositions exhibiting higher maximum d_{33} values had a higher wt% of BS than BNiT.

TABLE 9.1: Depolarization Temperatures from in-situ d_{33} and the maximum value in d_{33}.

Composition	$T_{in-situ}$ [°C]	Maximum d_{33} [pC/N]
50-10-40	190	437
55-10-35	292	316
55-15-30	316	402
50-20-30	230	1018
50-25-25	250	400
52-24-24	294	290
54-23-23	130	525
50-30-20	280	682
55-30-15	290	445
55-35-10	290	405
60-10-30	365	249
60-30-10	380	809
60-35-5	400	1340

Of the three ternary systems investigated, PT-BS-BNiT exhibited superior properties for several reasons: a clearly defined transition region, two MPB forming components (PT-BS and PT-BNiT), and excellent piezoelectric properties in both binary components. All three systems also decreased the amount of lead required to produce decent piezoceramics as compared to PZT and PT-BS. However, due to the expense of scandium, inferior electromechanical coupling, and piezoelectric properties of these ternaries, their use may be limited.

9.2 Future Work

9.2.1 Missing Structure in PT-BS-BNiT?

Pair distribution fitting (PDF) studies in PZT showed that a monoclinic distortion was responsible for the material's high piezoelectric activity [2]. In the PT-BS-BNiT system and other PT-based solid solutions with diffuse phase transitions, at temperatures between T_d and T_m, zero polarization is evident from a loss of piezoelectric activity; however, phase transitions that occur at T_C or T_m are the only transitions in this phase region. This is likely the result of phase mixing taking place in this temperature range. Although dissimilar responses between PZT and piezoelectric systems like PT-BS-BNiT, in-situ XRD and/or neutron scattering paired with a fitting technique such as PDF or reverse Monte-Carlo or phase-field analysis could help in determining whether tetragonal distortion persist in this undefined region or if it is another mechanism such as anti-ferroelectricity.

9.2.2 Radiation Induced Defect Studies in Ferroelectric Materials

The study of radiation damage effects in materials over the past half-century has focused mainly on metals, metal alloys, nuclear solid fuels, and moderators. These materials were used primarily in nuclear weapon systems and nuclear power plants as structural and fuel components; however, with an aging "fleet" of nuclear power plants, there is a need for the monitoring of the structural health of nuclear power plants. Research into the radiation-induced degradation of ferroelectric materials has been limited, with advancements linked to technological needs. With the development of ferroelectric materials as components in optoelectronic, optical, dielectric applications, radiation effects studies on materials including PZT and bismuth containing components is necessary for nuclear power plant structural health monitoring.

An understanding of the fundamental mechanisms that underpin radiation damage in piezoelectric materials would help guide future research into radiation

resistant materials for use in exploratory probes, satellites, and other space applications from single-event and constant radiation damage and destruction. This research could also motivate the use of piezoelectrics and ferroelectrics in the next generation nuclear power plants where in-situ structural health monitoring of reactor components in generation IV reactors with high internal temperatures and pressures will be critical. The use of piezoelectric materials such as PZT in aerospace applications is becoming more prevalent, and the proposed work will provide valuable insights into the behavior of these materials under extreme environments.

9.3 References

1. Stein, D. M., Grinberg, I., Rappe, A. M. & Davies, P. K. Multiple dielectric transitions in the $PbTiO_3$-$Bi(Zn_{1/2}Ti_{1/2})O_3$-$BI(Mg_{1/2}Ti_{1/2})O_3$ system. *J. Appl. Phys.* **110,** 074110 (2011).

2. Zhang, N. *et al.* The missing boundary in the phase diagram of $PbZr_{1-x}Ti_xO_3$. *Nat. Commun.* **5,** 5231–5239 (2014).

10 Bibliography

1. Scott, J. F., Araujo, C. A., Meadows, H. B., McMillan, L. D. & Shawabkeh, A. Radiation effects on ferroelectric thin-film memories: Retention failure mechanisms. *J. Appl. Phys.* **66,** 1444–1453 (1989).

2. Eitel, R. E. *et al.* New High Temperature Morphotropic Phase Boundary Based on Bi(Me)O_3-$PbTiO_3$ Ceramics. *Jpn. J. Appl. Phys.* **40,** 5999–6002 (2001).

3. Eitel, R. E., Randall, C. A., Shrout, T. R. & Park, S.-E. Preparation and Characterization of High Temperature Perovskite Ferroelectrics in the Solid-Solution (1-x)$BiScO_3$-x$PbTiO_3$. *Jpn. J. Appl. Phys.* **41,** 2099–2104 (2002).

4. Bao, X., Bar-Cohen, Y., Sherrit, S., Badescu, M. & Shrout, T. R. in *Proceedings of the SPIE Smart Structures and Materials/NDE Symposium* (SPIE, 2012).

5. Suchomel, M. R. & Davies, P. K. Enhanced Tetragonality in (x)$PbTiO_3$-(1-x)Bi($Zn_{1/2}Ti_{1/2}$)O_3 and Related Solid Solution Systems. *Appl. Phys. Lett.* **86,** 2629051–2629053 (2005).

6. Randall, C. A. *et al.* Investigation of a high T_C piezoelectric system: (1-x)Bi($Mg_{1/2}$ $Ti_{1/2}$)O_3-(x)$PbTiO_3$. *J. Appl. Phys.* **95,** 3633–3639 (2004).

7. Sharma, S. & Hall, D. A. Ferroelectric and Antiferroelectric Polarization Switching Characteristics of Bi($Mg_{0.5}Ti_{0.5}$)O_3-$PbTiO_3$ Ceramics. *J. Mater. Sci.: Mater. Electron.* **21,** 405–409 (2010).

8. Takenaka, T. & Yamada, M. Solid-Solution ($Bi_{1-x}Pb_x$)($Ni_{(1+x)/2}Ti_{(1+x)/2}$)O_3 for New Piezoelectric Ceramics. *Jpn. J. Appl. Phys.* **32,** 4218–4222 (1993).

9. Choi, S. M., Stringer, C. J., Shrout, T. R. & Randall, C. A. Structure and Property Investigation of a Bi-based Perovskite Solid Solution: (1-x)Bi($Ni_{1/2}Ti_{1/2}$)O_3-x$PbTiO_3$. *J. Appl. Phys.* **98,** 0341081–0341084 (2005).

10. Woodward, D., Reaney, I., Eitel, R. E. & Randall, C. A. Crystal and domain structure of the $BiFeO_3$-$PbTiO_3$ solid solution. *J Appl Phys* **94,** 3313–3318 (2003).

11. Cheng, J. R., Zhu, W., Li, N. & Cross, L. Fabrication and characterization of x$BiGaO_3$-(1-x)$PbTiO_3$: a high temperature reduced Pb-content piezoelectric ceramic. *Mater. Lett.* **57,** 2090–2094 (2003).

12. Cheng, J. R., Li, N. & Cross, L. Structural and dielectric properties of Ga-modified $BiFeO_3$-$PbTiO_3$ crystalline solutions. *J. Appl. Phys.* **94,** 5153–5158 (2003).

13. Eitel, R. E., Zhang, S. J., Shrout, T. R. & Randall, C. A. Phase Diagram of the Perovskite System (1-x)$BiScO_3$-x$PbTiO_3$. *J. Appl. Phys.* **96,** 2828–2831 (2004).

14. Sterianou, I. *et al.* High-temperature (1-x)$BiSc_{1/2}Fe_{1/2}O_3$-x$PbTiO_3$ piezoelectric ceramics. *Appl. Phys. Lett.* **87,** 242901 (2005).

15. Sterianou, I., Sinclair, D. C., Reaney, I. M., Comyn, T. & Bell, A. J. Investigation of high Curie temperature (1-x)$BiSc_{1-y}Fe_yO_3$-x$PbTiO_3$ piezoelectric ceramics. *J. Appl. Phys.* **106** (2009).

16. Sebastian, T. *et al.* High temperature piezoelectric ceramics in the $Bi(Mg_{1/2}Ti_{1/2})O_3$-$BiFeO_3$-$BiScO_3$-$PbTiO_3$ system. *J. Electroceram.* **25,** 130–134 (2010).

17. Goyer, R. A. Lead Toxicity: Current Concerns. *Environ. Health Persp.* **100,** 177–187 (1993).

18. Piomelli, S. Childhood lead poisoning. *Pediatr. Clin. N. Am.* **49,** 1285–1304 (2002).

19. Papanikolaou, N. C., Hatzidaki, E. G., Belivanis, S., Tzanakakis, G. N. & Tsatsakis, A. M. Lead toxicity update. A brief review. *Med. Sci. Monit.* **11,** RA329–RA336 (2005).

20. Rödel, J., Jo, W., Seifert, K. T. P., Anton, E. M. & Granzow, T. Perspective on the Development of Lead-free Piezoceramics. *J. Am. Ceram. Soc.* **92,** 1153 (2009).

21. Callister Jr., W. D. *Material Science and Engineering: An Introduction* 7th ed. (Wiley, 2007).

22. Sands, D. E. *Introduction to Crystallography* (Dover Publications, Inc., 1969).

23. Schwarzenbach, D. & Pinkerton, A. A. (*Crystallography* English (John Wiley & Sons Ltd, 1996).

24. Eckert, M. Max von Laue and the discovery of X-ray diffraction in 1912. *Ann. Phys. (Berlin)* **524,** A83–A85 (2012).

25. Bragg, W. L. The Diffraction of Short Electromagnetic Waves by a Crystal. *Proceedings of the Cambridge Philosophical Society* **17,** 43–57 (1913).

26. Kelly, A. & Groves, G. W. *Crystallography and Crystal Defects* (Longman Group Limited, 1970).

27. Rahman, K., Khan, A., Muhammad, N. M., Jo, J. & Choi, K.-H. Fine-resolution patterning of copper nanoparticles through electrohydrodynamic jet printing. *J. Micromech. Microeng.* **22,** 1–8 (2012).

28. Cullity, B. D. & Stock, S. R. *Elements of X-Ray Diffraction* 3rd ed. 664 pp. (Prentice Hall, 2001).

29. Greenwood, N. N. & Earnshaw, A. *Chemistry of the Elements* 2nd ed. (Butterworth-Heinemann, 1998).

30. *ANSI/IEEE 176-1987, IEEE Standard on Piezoelectricity* (IEEE, New York, 1987).

31. Kittel, C. *Introduction to Solid State Physics* 8th ed. (John Wiley & Sons Ltd, 2005).

32. Jaffe, B., Cook, W. R. & Jaffe, H. *Piezoelectric Ceramics* 1st ed. 317 pp. (Academic Press, New York, 1971).

33. Goldschmidt, V. M. Die Gesetze der Krystallochemie. **21,** 471–485 (1926).

34. Glazer, A. Classification of Tilted Octahedra in Perovskites. *Acta Crystallogr. Sect. B* **28,** 3384–3392 (1972).

35. Glazer, A. Simple Ways of Determining Perovskite Structures. *Acta Crystallogr. Sect. A* **31,** 756–762 (1975).

36. Halliyal, A., Gururaja, T., Kumar, U. & Safari, A. in *Applications of Ferroelectrics* Sixth IEEE International Symposium. **437** (IEEE, 1986).

37. Smyth, D. M. *The Defect Chemistry of Metal Oxides* (Oxford University Press, 2000).

38. Moulson, A. J. & Herbert, J. M. *Electroceramics* 2nd ed. (John Wiley & Sons Ltd, 2003).

39. Tilley, R. *Understanding Solids* (John Wiley & Sons Ltd, 2004).

40. Steinsvik, S., Bugge, R., GjØnnes, J., TaftØ, J. & Norby, T. The Defect Structure of $SrTi_{1-x}Fe_xO_{3-y}$ (x = 0-0.8) Investigated by Electrical Conductivity Measurements and Electron Energy Loss Spectroscopy (EELS). *J Phys Chem Solids* **58,** 969–976 (1997).

41. Suzuki, K. & Kijima, K. Optical Band Gap of Barium Titanate Nanoparticles Prepared by RF-plasma Chemical Vapor Deposition. *Jpn. J. Appl. Phys.* **44,** 2081–2082 (2005).

42. Nye, J. F. *Physical Properties of Crystals: Their Representation by Tensors and Matrices* (Oxford University Press, 1985).

43. Kulcsar, F. Electromechanical Properties of Lead Titanate Zirconate Ceramics Modified with Certain Three- or Five-VaIent Additions. *J. Am. Ceram. Soc.* **42,** 343–349 (1959).

44. Welberry, T. R., Goossens, D. J., Withers, R. L. & Baba-Kishi, K. Z. Monte Carlo Simulation Study of Diffuse Scattering in PZT, $Pb(Zr,Ti)O_3$. *Metall Mater Trans A* **41A,** 1110–1118 (May 2010).

45. Pecharsky, V. K. & Zavalij, P. Y. *Fundamentals of Powder Diffraction and Structure Characterization of Materials* 2nd ed. (Springer Science+Business Media, LLC, 2009).

46. Devonshire, A. F. Theory of Ferroelectrics. *Adv. Phys.* **3,** 86–130 (1954).

47. Whatmore, R. W. Pyroelectric devices and materials. *Rep. Prog. Phys.* **49,** 1335–1386 (1986).

48. Lang, S. B. Pyroelectricity: From Ancient Curiosity to Modern Imaging Tool. *Physics Today* **58,** 32–36 (2005).

49. Naranjo, B., Gimzewski, J. K. & Putterman, S. Observation of nuclear fusion driven by a pyroelectric crystal. *Nature* **434,** 1115–1117 (2005).

50. Kochervinskii, V. V. Piezoelectricity in Crystallizing Ferroelectric Polymers: Poly(vinylidene fluoride) and Its Copolymers (A Review). *Crystallography Reports* **48,** 649–675 (2003).

51. Haertling, G. H. Ferroelectric Ceramics: History and Technology. *J. Am. Ceram. Soc.* **82,** 797–818 (1999).

52. Valasek, J. Piezo-Electric and Allied Phenomena in Rochelle Salt. *Phys. Rev.* **17,** 475–481 (1921).

53. Jaffe, H. Piezoelectric Ceramics. *J. Am. Ceram. Soc.* **41,** 494–498 (11 1958).

54. Heitmann, A. A. & Rossetti Jr., G. A. Thermodynamics of Ferroelectric Solid Solutions with Morphotropic Phase Boundaries. *Adv. Phys.* **3,** 86–130 (1954).

55. Damjanovic, D. Ferroelectric, dielectric and piezoelectric properties of ferroelectric thin films and ceramics. *Rep. Prog. Phys.* **61,** 1267–1324 (1998).

56. Blinc, R. & Žekš, B. *Soft Modes in Ferroelectrics and Antiferroelectrics* 1st (North-Holland Publishing Company, 1974).

57. Chandra, P. & Littlewood, P. B. in *Physics of Ferroelectrics: A Modern Perspective* (eds Rabe, K. M., Ahn, C. H. & Triscone, J.-M.) chap. A Landau Primer for Ferroelectrics (Springer Publishing Company, New York City, NY, USA, 2007).

58. Jin, L., Li, F. & Zhang, S. Decoding the Fingerprint of Ferroelectric Loops: Comprehension of the Material Properties and Structures. *J. Am. Ceram. Soc.* **97,** 1–27 (1 2013).

59. Patterson, E. *Development. Characterization. and Piezoelectric Fatigue Behavior of Lead-Free Perovskite Piezoelectric Ceramics* PhD thesis (Oregon State University, 2012).

60. Damjanovic, D. & Demartin, M. The Rayleigh law in piezoelectric ceramics. *J. Phys. D: Appl. Phys.* **29,** 2057–2060 (1996).

61. Damjanovic, D. Stress and frequency dependence of the direct piezoelectric effect in ferroelectric ceramics. *J. Appl. Phys.* **82,** 1788–1797 (1997).

62. Jin, L., Porokhonskyy, V. & Damjanovic, D. Domain wall contributions in Pb(Zr, Ti)O_3 ceramics at morphotropic phase boundary: A study of dielectric dispersion. *Appl. Phys. Lett.* **96,** (2010).

63. Balke, N., Lupascu, D. C., Granzow, T. & Rödel, J. Fatigue of Lead Zirconate Titanate Ceramics. I: Unipolar and DC Loading. *J. Am. Ceram. Soc.* **90,** 1081–1087 (2007).

64. Balke, N., Lupascu, D. C., Granzow, T. & Rödel, J. Fatigue of Lead Zirconate Titanate Ceramics II: Sesquipolar Loading. *J. Am. Ceram. Soc.* **90,** 1088–1093 (2007).

65. Lupascu, D. C. *Fatigue in Ferroelectric Ceramics and Related Issues Materials Science* **61** (Springer, 2004).

66. Ashcroft, N. W. & Mermin, N. D. *Solid State Physics* (Saunders College Publishing, 1976).

67. Landau, L. On the Theory of Phase Transitions. *Zh. Eksp. Teor. Fiz.* **7,** 19–32 (1937).

68. Kittel, C. Theory of Antiferroelectric Crystals. *Phys. Rev.* **82,** 729–732 (1951).

69. Jiang, A. Q., Lin, Y. Y., Tang, T. A. & Zhang, Q. Asymmetry of domain forward switching and multilevel relaxation times of domain backswitching in antiferroelectric $Pb_{0.99}Nb_{0.02}(Zr_{0.84}Sn_{0.12}Ti_{0.04})_{0.98}O_3$ thin films. *Appl. Phys. Lett.* **90,** (2007).

70. Smolenskii, G. A., Isupov, V. A., Agranovskaya, A. I. & Popov, S. N. Ferroelectrics with Diffuse Phase Transitions. *Sov. Phys. Solid State* **2,** 2584–2594 (1961).

71. Shvartsman, V. V. & Lupascu, D. C. Lead-Free Relaxor Ferroelectrics. *J. Am. Ceram. Soc.* **95,** 1–26 (2012).

72. Kumar, N. & Cann, D. P. Electromechanical strain and bipolar fatigue in $Bi(Mg_{1/2}Ti_{1/2})O_3$-$(Bi_{1/2}Na_{1/2})TiO_3$-$(Bi_{1/2}K_{1/2})TiO_3$ ceramics. *J. Appl. Phys.* **114,** (2013).

73. Yamakawa, K., Gachigi, K. W., Trolier-McKinstry, S. & Dougherty, J. P. Structural and electrical properties of antiferroelectric lead zirconate thin films prepared by reactive magnetron co-sputtering. *J. Mater. Sci.* **32,** 5169–5176 (1997).

74. Thurnauer, H. Reflections. *Am Ceram Soc Bull* **56,** 861–866 (1977).

75. Bhattacharya, K. & Ravichandran, G. Ferroelectric perovskites for electromechanical actuation. *Acta Mater* **51,** 5941–5960 (2003).

76. Merz, W. J. The Electric and Optical Behavior of $BaTiO_3$ Single-Domain Crystals. *Phys. Rev.* **76,** 1221–1225 (8 1949).

77. Zhang, N. *et al.* The missing boundary in the phase diagram of $PbZr_{1-x}Ti_xO_3$. *Nat. Commun.* **5,** 5231–5239 (2014).

78. Gerson, R. Piezoelectric and Dielectric Properties of Lead Titanate Zirconate Ceramics at Low Temperatures. *J. Appl. Phys.* **33,** 830–832 (1962).

79. Noheda, B. *et al.* A monoclinic ferroelectric phase in the $Pb(Zr_{1-x}Ti_x)O_3$ solid solution. *Appl. Phys. Lett.* **74,** 2059–2061 (1999).

80. Noheda, B. Structure and high-piezoelectricity in lead oxide solid solutions. *Curr Opin Solid State Mater Sci* **6,** 27–34 (2002).

81. Ballaiche, L., García, A. & Vanderbilt, D. Finite-Temperature Properties of $Pb(Zr_{1-x}Ti_x)O_3$ Alloys from First Principles. *Phys. Rev. Lett.* **84,** 5427–5430 (2000).

82. Guo, R. *et al.* Origin of the High Piezoelectric Response in PbZr12xTi_xO_3. *Phys. Rev. Lett.* **84,** 5423–5426 (2000).

83. Jin, Y. M., Wang, Y., Khachaturyan, A. G., Li, J. F. & Viehland, D. Conformal miniaturization of domains with low domain-wall energy: monoclinic ferroelectric states near the morphotropic phase boundaries. *Phys. Rev. Lett.* **91,** 197601–1 (2003).

84. Muralt, P. PZT Thin Films for Microsensors and Actuators: Where Do We Stand? **47,** 903–915 (2000).

85. Gerson, R. & Jaffe, H. Electrical Conductivity in Lead Titanate Zirconate Ceramics. *J. Phys. Chem. Solids* **24,** 979–984 (1963).

86. Zhang, S. J. & Yu, F. Piezoelectric materials for high temperature sensors. *J. Am. Ceram. Soc.* **94,** 3153–3170 (2011).

87. Jiang, Y. *et al.* Microstructure and Electric Properties of (1-x)Bi($Sc_{0.75}Zn_{0.125}Ti_{0.125}$) O_3-x$PbTiO_3$ Ceramics. *Ferroelectrics* **380,** 130–134 (2009).

88. Stringer, C. J., Shrout, T. R., Randall, C. A. & Reaney, I. Classification of Transition Temperature Behavior in Ferroelectric $PbTiO_3$-Bi(Me'Me")O_3 Solid Solutions. *J. Appl. Phys.* **99,** 0241061–0241064 (2006).

89. Sehirlioglu, A., Sayir, A. & Dynys, F. Doping of $BiScO_3$-$PbTiO_3$ Ceramics for Enhanced Properties. *J. Am. Ceram. Soc.* **93,** 1718–1724 (2010).

90. Leist, T. *et al.* Temperature Dependence of the Piezoelectric Coefficient in $BiMeO_3$-$PbTiO_3$ (Me = Fe, Sc, $(Mg_{1/2}Ti_{1/2})$) Ceramics. *J. Am. Ceram. Soc.* **95,** 711–715 (2012).

91. Suchomel, M. R. & Davies, P. K. Predicting the position of the morphotropic phase boundary in high temperature $PbTiO_3Bi(B'B'')O_3$ based dielectric ceramics. *J Appl Phys* **96,** 4405–4410 (2004).

92. Woodward, D. & Reaney, I. A structural study of ceramics in the $(BiMnO_3)x$-$(PbTiO_3)1$-x solid solution series. *J Phys Condens Matter* **16,** 8823–8834 (2004).

93. Stein, D. M., Grinberg, I., Rappe, A. M. & Davies, P. K. Multiple dielectric transitions in the $PbTiO_3$-$Bi(Zn_{1/2}Ti_{1/2})O_3$-$BI(Mg_{1/2}Ti_{1/2})O_3$ system. *J. Appl. Phys.* **110,** 074110 (2011).

94. Dwivedi, A., Randall, C. A. & Rossetti, G. A. J. Thermal history induced variable relaxor behavior in the high T_C ternary ferroelectric $0.6(Mg_{1/2}Ti_{1/2})O_3$-$0.05Bi(Zn_{1/2}Ti_{1/2})O_3$-$0.35PbTiO_3$. *Mater. Lett.* **65,** 3034–3036 (2011).

95. Kang, H., Chen, J., Liu, L., Fang, L. & Xing, X. Temperature dependences of the ferroelectric and dielectric properties of high curie temperature $PbTiO_3$-$BiScO_3$-$Bi(Zn_{1/2}Zr_{1/2})O_3$. *Mater. Res. Bull.* **48,** 2006–2009 (2013).

96. Kowalski, B. A., Sehirlioglu, A., Dynys, F. W. & Sayir, A. Characterization of the High-Temperature Ferroelectric (100-x-y)$BiScO_3$-(x)$Bi(Zr_{0.5}Zn_{0.5})O_3$-(y)$PbTiO_3$ Perovskite Ternary Solid Solution. *J. Am. Ceram. Soc.* **97,** 490–497 (2014).

97. Shi, L., Liao, Q., Zhang, B., Zhang, J. & Guo, D. Structure and electrical properties of (1-x)$(0.1BiYbO_3$-$0.9PbTiO_3)$-x$Pb(Zn_{1/3}Nb_{2/3})O_3$ high-temperature ternary piezoelectric ceramics. *Mater. Lett.* **114,** 100–102 (2014).

98. Song, T. H., Eitel, R. E., Shrout, T. R., Randall, C. A. & Hackenberger, W. Piezoelectric Properties in the Perovskite $BiScO_3$-$PbTiO_3$-(Ba,Sr)TiO_3 Ternary System. *Jpn. J. Appl. Phys.* **42,** 5181–5184 (2003).

99. Kang, H. *et al.* Structure and enhanced piezoelectric response by chemical doping in $PbTiO_3$-$PbZrO_3$-$Bi(Ni_{1/2}Ti_{1/2})O_3$. *Inorganic Chemistry Communications* **31,** 66–68 (2013).

100. Fan, L. *et al.* Enhanced piezoelectric and ferroelectric properties in the $BaZrO_3$ substituted $BiFeO_3$-$PbTiO_3$. *Appl. Phys. Lett.* **102,** (2013).

101. Shimojo, Y., Wang, R., Sekiya, T., Nakamura, T. & Cross, L. MPB Phase Diagram and Ferroelectric Properties in the $PbTiO_3$-$BiScO_3$ System. *Ferroelectrics* **284,** 121–128 (2003).

102. Stauffer, D. & Aharony, A. *Introduction to Percolation Theory* 2^{nd} (Taylor & Francis Inc, 1992).

103. Zhang, S. J., Randall, C. A. & Shrout, T. R. High Curie temperature piezocrystals in the $BiScO_3$-$PbTiO_3$ perovskite system. *Appl. Phys. Lett.* **83,** 3150–3152 (2003).

104. Randall, C. A., Eitel, R. E., Shrout, T. R., Woodward, D. & Reaney, I. Transmission Electron Microscopy Investigation of the High Temperature $BiScO_3$-$PbTiO_3$ Piezoelectric Ceramic System. *J. Appl. Phys.* **93,** 9271–9274 (2003).

105. Reaney, I. M. Octahedral tilting, domain structure and piezoelectricity in perovskites and related ceramics. *J. Electroceram.* **19,** 1–8 (2006).

106. Yamashita, Y., Hosono, Y., Harada, K. & Ichinose, N. Effect of Molecular Mass of B-site Ions on Electromechanical Coupling Factors of Lead-Based Perovskite Piezoelectric Materials. *Jpn. J. Appl. Phys.* **39,** 5593–5596 (2000).

107. Duan, R., Speyer, R. F., Alberta, E. F. & Shrout, T. R. High Curie temperature perovskite $BiInO_3$-$PbTiO_3$ ceramics. *J Mater Res* **19,** 2185–2193 (2004).

108. Yu, H., Ren, W. & Ye, Z. G. Structural, Dielectric, and Ferroelectric Properties of the (1-x)$PbTiO_3$-x$BiAlO_3$ Solid Solution. *IEEE Trans. Ultra. Ferro. Freq. Control* **57,** 2177–2181 (2010).

109. Ansell, T. Y., Cann, D. P., Nikkel, J. & Sehirlioglu, A. High Temperature Piezoelectric Ceramics based on x$PbTiO_3$-(1-x)$Bi(Sc_{1/2}Me_{1/4}Ti_{1/4})O_3$ (Me = Zn, Mg) Ternary Perovskites. *Jpn. J. Appl. Phys.* **51,** 101802 (2012).

110. Ansell, T. Y. & Cann, D. P. High temperature piezoelectric ceramics based on (1 - x)[$BiScO_3$ + $Bi(Ni_{1/2}Ti_{1/2})O_3$] - x$PbTiO_3$. *Mater. Lett.* **80,** 87–90 (2012).

111. Ansell, T. Y. & Cann, D. P. Piezoelectric properties of the high temperature MPB x$PbTiO_3$ - (1-x)[$BiScO_3$ + $Bi(Ni_{1/2}Ti_{1/2})O_3$] composition. *J Electroceram* **31,** 159–167 (2013).

112. Ansell, T. Y., Cann, D. P., Sapper, E. & Rödel, J. Thermal Depolarization in the High-Temperature Ternary Piezoelectric System x$PbTiO_3$-y$BiScO_3$-z$Bi(Ni_{1/2}Ti_{1/2})O_3$. *J. Am. Ceram. Soc.* 1–9 (2014).

113. Zhou, Z., Li, Y., Hui, S. & Dong, X. Effect of tungsten doping in bismuth-layered $Na_{0.5}Bi_{2.5}Nb_2O_9$ high temperature piezoceramics. *Appl. Phys. Lett.* **104,** (2014).

114. Peng, Z., Chen, Q., Chen, Y., Xiao, D. & Zhu, J. Microstructure and electrical properties in W/Nb co-doped Aurivillius phase $Bi_4Ti_3O_{12}$ piezoelectric ceramics. *Mater. Res. Bull.* **59,** 125–130 (2014).

115. Sun, L. *et al.* Dielectric and piezoelectric properties of cerium-doped $(NaBi)_{0.49}[\ ]_{0.02}Bi_2Nb_{1.98}Ta_{0.02}O_9$-based piezoceramics. *Ceramics International* **40,** 14159–14163 (2014).

116. Zhang, S. J., Xia, R. & Shrout, T. R. Lead-free piezoelectric ceramics vs. PZT? *J. Electroceram.* **19,** 251–257 (2007).

117. Anton, E. M., Jo, W., Damjanovic, D. & Rödel, J. Determination of depolarization temperature of $(Bi_{1/2}Na_{1/2})TiO_3$-based lead-free piezoceramics. *J. Appl. Phys.* **110,** 094108–14 (2011).

118. Takenaka, T., Maruyama, K.-i. & Sakata, K. $(Bi_{1/2}Na_{1/2})TiO_3$-$BaTiO_3$ System for Lead-Free Piezoelectric Ceramics. *Jpn. J. Appl. Phys.* **30,** 2236 (1991).

119. Takenaka, T., Hazumi, A., Hata, T. & Sakata, K. Mechanical properties of $(BiNa)_{1/2}TiO_3$-based piezoelectric ceramics. *Silicates Industrials* **7,** 136–142 (1993).

120. Chu, B.-J., Chen, R., Li, G.-R. & Yin, Q.-R. Electrical Properties of $Na_{1/2}Bi_{1/2}TiO_3$-$BaTiO_3$ ceramics. *J. Europ. Ceram. Soc.* **22,** 2115–2121 (2002).

121. Birol, H., Damjanovic, D. & Setter, N. Preparation and Characterization of (K0.5Na0.5)NbO3 Ceramics. *J. Eur. Ceram. Soc.* **26,** 861–866 (2006).

122. Egerton, L. & Dillon, D. M. Piezoelectric and Dielectric Properties of Ceramics in the System Potassium Sodium Niobate. *J. Am. Ceram. Soc.* **42,** 438–442 (1959).

123. Du, H. L. *et al.* Preparation and Piezoelectric Properties of $(K_{0.5}Na_{0.5})NbO_3$ Lead-Free Piezoelectric Ceramics with Pressure-Less Sintering. *Mater. Sci. Eng. B* **131,** 83–87 (2006).

124. Saito, Y. *et al.* Lead-Free Piezoceramics. *Nature* **432,** 84–87 (2004).

125. Hiruma, Y., Nagata, H. & Takenaka, T. Phase diagrams and electrical properties of $(Bi_{1/2}Na_{1/2})TiO_3$-based solid solutions. *J. Appl. Phys.* **104,** 124106 (2008).

126. Sasaki, A., Chiba, T., Mamiya, Y. & Otsuki, E. Dielectric and Piezoelectric Properties of $(Bi_{0.5}Na_{0.5})TiO_3$-$Bi_{0.5}K_{0.5})TiO_3$ Systems. *Jpn. J. Appl. Phys.* **38,** 5564–5567 (1999).

127. Patterson, E. A., Cann, D. P., Pokorny, J. & Reaney, I. M. Electromechanical strain in $Bi(Zn_{1/2}Ti_{1/2})O_3$-$(Bi_{1/2}Na_{1/2})TiO_3$-$(Bi_{1/2}K_{1/2})TiO_3$ solid solutions. *J. Appl. Phys.* **111,** (2012).

128. Kumar, N., Ansell, T. Y. & Cann, D. P. Role of point defects in bipolar fatigue behavior of $Bi(Mg_{1/2}Ti_{1/2})O_3$ modified $(Bi_{1/2}Na_{1/2})TiO_3$-$(Bi_{1/2}K_{1/2})TiO_3$ relaxor ceramics. *J. Appl. Phys.* **115,** (2014).

129. Bearden, J. A. X-Ray Wavelengths. *Rev Mod Phys* **39,** 78–124 (1967).

130. Thompson, A. *et al. X-ray Data Booklet* DE-AC02-05CH11231 (U.S. Department of Energy, Center for X-ray Optics Advanced Light Source, Lawrence Berkeley National Laboratory, Oct. 2009), 1–176.

131. *Standard Test Methods for Determining Average Grain Size* Standard E112-10 (American Society for Testing and Materials, ASTM International, 100 Barr Harbor Drive, PO Box C700, West Conshohocken, PA 19428-2959. United States, 2010).

132. Inaguma, Y. *et al.* High-pressure synthesis and ferroelectric properties in perovskite -type $BiScO_3$-$PbTiO_3$ solid solution. *J. Appl. Phys.* **95,** 231–235 (2004).

133. Eitel, R. E., Shrout, T. R. & Randall, C. A. Nonlinear contributions to the dielectric permittivity and converse piezoelectric coefficient in piezoelectric ceramics. *J. Appl. Phys.* **99,** 124110 (2006).

134. Damjanovic, D., Bhalla, A. S. & Cross, L. Dielectric and Pyroelectric Properties of Triglycerol - Gelatin Films. *IEEE Trans. Ultra. Ferro. Freq. Control* **138** (Nov. 1991).

135. Yu, G., Chen, X., Cao, F., Wang, G. & Dong, X. Dynamic ferroelectric hysteresis scaling behavior of $40BiScO_3$-$60PbTiO_3$ bulk ceramics. *Solid State Commun* **150,** 1045–1047 (2010).

136. Gotmare, S. W., Leontsev, S. O. & Eitel, R. E. Thermal Degradation and Aging of High-Temperature Piezoelectric Ceramics. *J. Am. Ceram. Soc.* **93,** 1965 (2010).

137. Grinberg, I. *et al.* Structure and Polarization in the High T_C Ferroelectric Bi(Zn, Ti)O_3-$PbTiO_3$ Solid Solutions. *Phys. Rev. Lett.* **98,** 107601 (2007).

138. Zhang, X. D., Kwon, D. & Kim, B. G. Structural evolution of a high T_C ferroelectric (x)$Bi(Zn_{1/2}Ti_{1/2})O_3$-$PbTiO_3$ solid solution. *Appl. Phys. Lett.* **92,** 082906 (2008).

139. Rai, R., Sinha, A., Sharmac, S. & Sinha, N. K. P. Investigation of structural and electrical properties of (1-x) $Bi_{0.5}Mg_{0.5}TiO_3$-(x)$PbTiO_3$ ceramic system. *J. Alloys Compd.* **486,** 273–277 (2009).

140. Sehirlioglu, A., Sayir, A., Dynys, F., Nittala, K. & Jones, J. Structure and Piezoelectric Properties Near the Bismuth Scandium Oxide-Lead Zirconate-Lead Titanate Ternary Morphotropic Phase Boundary. *J. Am. Ceram. Soc.* **94,** 788–795 (2011).

141. Zhang, S. J., Alberta, E. F., Eitel, R. E., Randall, C. A. & Shrout, T. R. in *IEEE Transactions on Ultrasonics, Ferroelectrics, and Frequency control* **52** (IEEE, 2005), 11.

142. Sehirlioglu, A., Sayir, A. & Dynys, F. Microstructural-Property Relationships in Liquid Phase-Sintered High-Temperature Bismuth Scandium Oxide-Lead Titanate Piezoceramics. *J. Am. Ceram. Soc.* **91,** 2910–2916 (2008).

143. Yamakawa, K. *et al.* Novel Pb(Ti,Zr)O_3 (PZT) Crystallization Technique Using Flash Lamp for Ferroelectric RAM (FeRAM) Embedded LSIs and One Transistor Type FeRAM Devices. *Jpn. J. Appl. Phys.* **41,** 2630–2634 (2002).

144. Malmonge, L. F., Malgonge, J. A. & Sakamoto, W. K. Study of Pyroelectric Activity of PZT/PVDF-HFP Composite. *Mater. Res.* **6,** 469–473 (2003).

145. Makki, N. & Pop-Iliev, R. Battery-and wire-less tire pressure measurement systems (TPMS) sensor. *Microsyst Technol* **18,** 1201–1212 (2012).

146. Matsushita, S., Kanno, I., Adachi, K., Yokokawa, R. & Kotera, H. Metal-based piezoelectric microelectromechanical systems scanner composed of Pb(Zr, Ti)O_3 thin film on titanium substrate. *Microsyst Technol* **18,** 765–771 (2012).

147. Turner, R., Fuierer, P., Newnham, R. & Shrout, T. R. Materials for high temperature acoustic and vibration sensors: A review. *Appl. Acoust.* **41,** 299 (1994).

148. Shrout, T. R. & Zhang, S. J. Lead-Free Piezoelectric Ceramics: Alternative for PZT? *J. Electroceram.* **19,** 111–124 (2007).

149. Sehirlioglu, A., Sayir, A. & Dynys, F. High Temperature Properties of $BiScO_3$-$PbTiO_3$ Piezoelectric Ceramics. *J. Appl. Phys.* **106,** 0141021–0141027 (2009).

150. Chen, J. *et al.* Structure and lattice dynamics in $PbTiO_3$-$Bi(Zn_{1/2}Ti_{1/2})O_3$ solid solutions. *J. Appl. Phys.* **105,** 044105 (2009).

151. Bao, X. *et al.* Modeling and Computer Simulation of Ultrasonic/Sonic Driller/ Corer (USDC). **50,** 1147–1160 (2003).

152. Jaffe, B., Roth, R. & Marzullo, S. Properties of Piezoelectric Ceramics in the Solid-Solution Series Lead Titanate-Lead Zirconate-Lead Oxide: Tin Oxide and Lead Titanate-Lead Hafnate. *J Res Nat Bur Stand* **55,** 239–254 (1955).

153. Chen, S., Dong, X., Yang, H., Liang, R. & Mao, C. Effects of Niobium Doping on the Microstructure and Electrical Properties of $0.36BiScO_3$-$0.64PbTiO_3$ Ceramics. *J. Am. Ceram. Soc.* **90,** 477–482 (2007).

154. Eitel, R. E., Shrout, T. R. & Randall, C. A. Tailoring Properties and Performance of (1-x)$BiScO_3$-x$PbTiO_3$ Based Piezoceramics by Lanthanum Substitution. *Jpn. J. Appl. Phys.* **43,** 8146–8150 (2004).

155. Chen, J., Tan, X., Jo, W. & Rödel, J. Temperature dependence of piezoelectric properties of high-T_C $Bi(Mg_{1/2}Ti_{1/2})O_3$-$PbTiO_3$. *J. Appl. Phys.* **106,** 034109 (2009).

156. Venevstev, Y. N. *et al. Sov. Phys. Crystallogr.* **5,** 594 (1960).

157. Stein, D. M., Suchomel, M. R. & Davies, P. K. Enhanced tetragonality in (x)$PbTiO_3$-(1-x)Bi(B'B")O_3 systems: $Bi(Zn_{3/4}W_{1/4})O_3$. *Appl. Phys. Lett.* **89,** 132907 (2006).

158. Datta, K., Thomas, P. A. & Roleder, K. Anomalous phase transitions of lead-free piezoelectric x$Na_{0.5}Bi_{0.5}TiO_3$-(1-x)$BaTiO_3$ solid solutions with enhanced phase transition temperatures. *Phys. Rev. B* **82,** 224105 1–6 (2010).

159. Schmidt, G. *et al.* Induced Phase Transitions in Ferroelectrics with Diffuse Phase Transitions. *Phys. Stat. Sol. (A)* **63,** 501–510 (1981).

160. Jo, W., Daniels, J., Damjanovic, D., Kleeman, W. & Rödel, J. Two-stage processes of electrically induced-ferroelectric to relaxor transition in $0.94(Bi_{1/2}Na_{1/2})Ti)O_3$-$0.06BaTiO_3$. *Appl. Phys. Lett.* **102,** 192903 (2013).

161. Kamel, T. M. & With, G. d. Poling of hard ferroelectric PZT ceramics. *J. Eur. Ceram. Soc.* **28,** 1827–1838 (2008).